Factors affecting CO_2 utilisation via the reverse Boudouard reaction and Macro-thermogravimetric development for char conversion

Thesis submitted in fulfilment of the requirements for the degree of Doctor of Philosophy

in

Mechanical Engineering

to

Cardiff University,

School of Engineering

By

Ahmed Mohammed Alsawadi

May 2025

Dedication

This thesis is dedicated to the memory of my mother Khamisah Hassan Aljubairi. I wish you were still here; you would have been the first and most important person to share this with. I have lost you, but I will never forget the love you gave to our family.

It is also dedicated to the memory of my brother, Zyad. You left us too soon, but your presence remains with us always.

Rest in Peace Mam and brother.

Abstract

Carbon Capture, Utilisation and Storage (CCUS) is currently known as a key solution to reach net zero emissions, with CO_2 utilisation (CCU) via thermochemical gasification technology of renewable materials being a promising pathway. The reverse Boudouard reaction is an interesting option for CCU applications; it is a heterogeneous, endothermic reaction that typically requires temperatures above 700°C to proceed. Therefore, understanding its mechanisms and studying the factors that affect it are beneficial to increase gasification process efficiency and hence reduce risk in process up-scaling.

This thesis investigates the critical mechanisms affecting char reactivity in CO_2 gasification using biochar, hydrochar and coal char samples by measuring mineral content, porosity, crystalline mineral phases, morphology, surface elements and surface functional groups. CO_2-chemisorption measurements of the char samples measured both organic and inorganic active sites using thermogravimetric analysis. The CO_2-chemisorption method at low temperatures was implemented to quantify the amount of CO_2 adsorbed/desorbed within the char's surface and to identify its role in char reactivity. Key findings include that while the pore structure of chars is indeed a significant characteristic, porosity alone does not exert the primary influence on gasification reactivity. Gasification reactivity was well correlated with CO_2 strong chemisorption capacities. Three kinetic models Volumetric model (VM), Grain model (GM) and Random pore model (RPM) were used to describe CO_2 gasification in isothermal and non-isothermal conditions.

A novel thermogravimetric fixed bed reactor (Macro-TGA) was designed to examine the effect of using a larger char sample on the gasification reactivity. The reactor was also used to investigate the role of surface area on the reaction performance by comparing the reactivity and produce gas of 12 and 16 mm pellets with the char powder sample. In comparison with Micro-TGA, the reactivity of biochar decreased when using 5 g sample. The kinetic parameters were also lower in the Macro-TGA compared to the Micro-TGA.

Acknowledgements

Praise be to God, Lord of the Worlds, for His guidance in my life. I would like to thank and express my appreciation to the Government of the Kingdom of Saudi Arabia for funding my PhD. I am also grateful to Cardiff University for giving me the opportunity to learn and for its support throughout this period.

To my soulmate, Reham Alsawadi, thank you for your patience and understanding when I was busy, and for standing beside me during difficult times. To my sweet daughters, Wajd and Lora, I know I gave you less time than you deserved, but I hope you know your father was working hard for your future. Everything I do is for your happiness; you are my life.

This PhD would not have been possible without the direct supervision and continuous support of my supervisors, Professor Richard Marsh and Dr Julian Steer. There are no words to thank you enough. Professor Richard, thank you for your support, guidance, and patience. You always said, "keep going" and that helped me more than anything else. Dr Julian Steer, I will never forget the time we spent together in the lab and during our breaks. Both of you always listened, stayed positive, and shared even the smallest details of the work without complaint. Thank you both sincerely.

A special thanks to Mr Malcolm Seaborne for helping me build my reactor and always answering my questions without hesitation. I wish you a full and healthy recovery.

I am also grateful to many others who supported me during this project: Mr Jonathan Martin, Mr Jeff Rowlands, Mr Carl Wadsworth, Mr Aurelien Vadex, Dr Duncan Muir, Dr David Morgan, Dr Julian Herbert, Dr Chay Anthony and Dr Greg Shaw for helping me with various experiments throughout my PhD.

Last but not least, I thank my dear father, Mohamed Alsawadi, my brothers and sisters, for encouraging me during tough times and for their prayers.

Publications and conference presentations

Publications

Ahmed M. Alsawadi, Richar Marsh, Julian M. Steer, David Morgan "A study of the mechanisms associated with CO_2 utilisation via the reverse Boudouard reaction". Fuel 381 (February 2025):133448. https://doi.org/10.1016/j.fuel.2024.133448.

Chay A. Davies-Smith, Julian Herbert, Darbaz Khasraw, Ciar´an Martin, David Warren-Walker, David Bryant, Joe Gallagher, Gordon Allison, Rakesh Bhatia, Julian M. Steer, Richard Marsh, Ahmed M. Alsawadi "Hydrothermal Pretreatment: Investigating the Use of Solid Residue from a Biomass Hemicellulose Extraction Process in the Production of High-Quality Biochar for Use in the Steel Industry." Bioresource Technology (January 2025):133448. https://doi.org/10.2139/ssrn.5202509 (submitted for publication).

Conference presentations

"The influence of structural properties of biochar on CO_2 gasification reactivity", The Fuel and Energy Research Forum's 2nd FERIA "The European Conference on Fuel and Energy Research and its Applications", Monday-Wednesday 4th-6th September 2023, The Edge Conference Centre, University of Sheffield, UK.

"CO_2 and biomass: Dual conversion from waste to value -added products", The Environmental Sustainability Research Forum "The Scientific Forum: Innovative Research Horizons Towards Sustainable Environmental Biosystems", Tuesday 28th November 2023, The Cavendish Laboratory, University of Cambridge, UK.

Table of Contents

List of Figures

List of Tables

Chapter 1 Introduction

1.1 Background

Global warming refers to the increase in the Earth's temperature relative to the pre-industrial period (1800–1900). It is mainly attributed to human activities, particularly the burning of fossil fuel which increases the concentration of heat-trapping greenhouse gases (GHGs) in Earth's atmosphere [1,2]. The Intergovernmental Panel on Climate Change (IPCC) [1] has recently reported that global surface temperatures rose by 1.1°C above the pre-industrial levels during 2011–2020. Figure 1.1 illustrates how greenhouse gases such as carbon dioxide (CO_2), water vapor (H_2O), methane (CH_4) and nitrous oxide (N_2O) increase global warming by absorbing the reflected sunlight energy (heat and light) and re-emit some of them back to the earth surface. Although CH_4 and N_2O trap more heat per molecule [3], CO_2 is the largest GHG contributor to climate change and global warming because it remains in the atmosphere much longer (up to 1000 years) [3] and it is the most abundant product emitted by modern industrial activities [4].

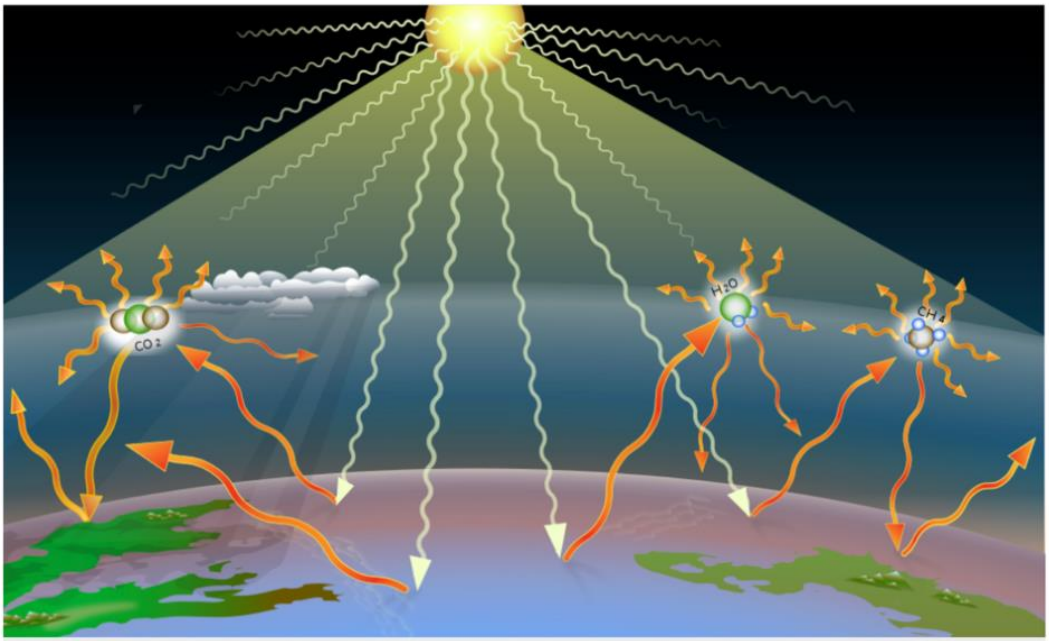

Figure 1.1: A simple illustration of the greenhouse effect: the earth converts solar energy into infrared radiation which is absorbed by GHGs and trapped, some of it back to the earth [235].

Limiting global warming and mitigating its attendant effect requires reducing emissions of heat-trapping GHGs, particularly CO_2. This has been widely recognized as an urgent action to avoid global warming consequences such as rising sea levels and extreme weather events [5]. In response to the impacts of climate change, over 196 countries agreed to the 2015 Paris Agreement outcomes under supervision of the United Nations Framework Convention on Climate Change (UNFCCC) [6]. The agreement aims to restrict the global average temperature rise below 2°C with more efforts to keep the increase within 1.5°C. Despite this international commitment, limiting global warming to 1.5°C is unlikely to be achieved before the end of this century as acknowledged by IPCC [7]. This target requires not only net zero GHG emissions but also net negative CO_2 emissions by 2050.

According to the Met Office [8], the annual growth rate of atmospheric CO_2 concentrations for 2024–2025 shows a slight decline compared to the previous record for 2023-2024. However, this still exceeds the levels projected under IPCC scenarios consistent with limiting warming to 1.5°C. The National Oceanic and Atmospheric Administration (NOAA Global Monitoring Laboratory) has released the latest updated measurements of the CO_2 atmospheric concentrations based on the Mauna Loa Observatory record in Hawaii. The CO_2 level has raised from 425.38 parts per million (ppm) in March 2024 to 428.15 ppm in March 2025 [9], as shown in Figure 1.2.

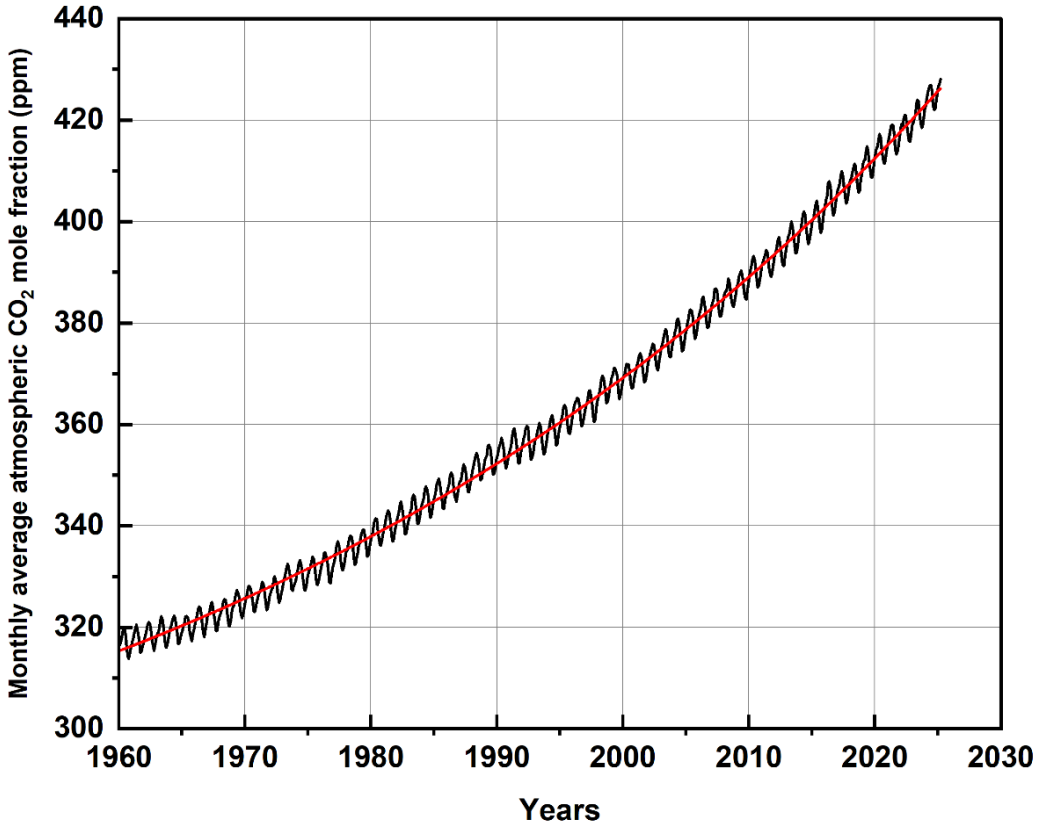

Figure 1.2: Monthly average atmospheric CO_2 concentrations (1960 -2025), according to the NOAA Global Monitoring Laboratory data [9].

The levels of CO_2 today are higher than at any time in the last 65 years as depicted in Figure 1.3. This is mainly because of the industrial revolution and the increase in population that led to extremely high energy consumption. Fuels such as natural gas, oil and coal, known as fossil fuels, account for 81% of the world's energy resources [10]. The recent International Energy Agency (IEA) report in 2023 shows a growth of CO_2 emissions related to global energy by 1.1% which is equivalent to 410 million tons [11]. Figure 1.3 presents the total CO_2 equivalent emissions of GHGs from the combustion of different fossil fuel types from 1971 to 2022. According to Olivier et al. [12], CO_2 emissions from burning fossil fuels makes up about 70% of all GHGs worldwide. There is

no debate that high energy demands from sectors such as electricity generation, heating, and transportation will exacerbate the current situation.

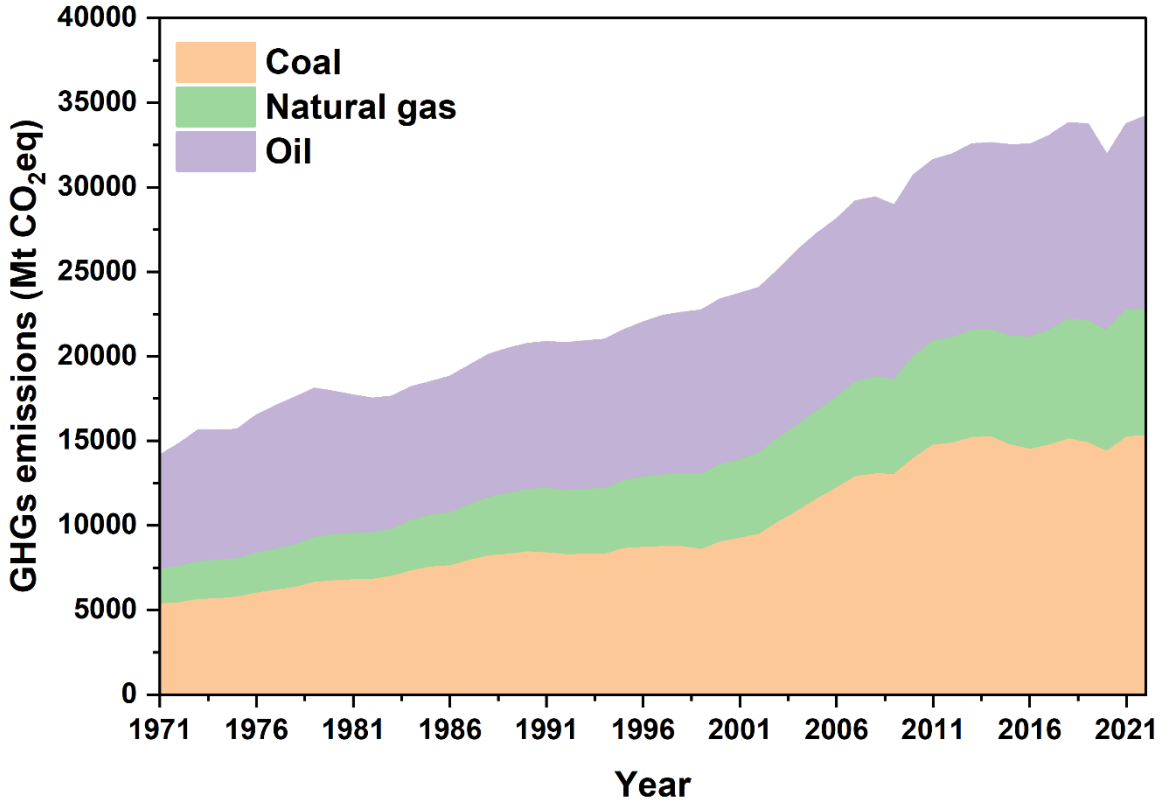

Figure 1.3: Total GHG emissions from fossil fuel combustion based on the latest 2022 data from IEA [10]. Unit is million metric tonnes (Mt).

The IPCC has outlined the potential future scenarios of CO_2 emissions and their impact on atmospheric CO_2 accumulation over the coming decades as shown in Figure 1.4. In the worst-case scenario (SSP5-8.5), atmospheric CO_2 concentration could reach nearly three times the current level of 428 ppm. This will significantly raise the global temperatures by 4°C by 2100. [1].

The deployment of effective CO_2 reduction technologies and the use of renewable energy have become essential to meet rising energy demands, reduce the impacts of climate change, and achieve net-zero emissions targets. One of the most promising approaches for CO_2 removal is Carbon Capture, Utilisation and Storage (CCUS) [13–17]. The following

sections provide an overview of CCUS technologies and the potential utilisation of CO_2 through sustainable thermochemical gasification.

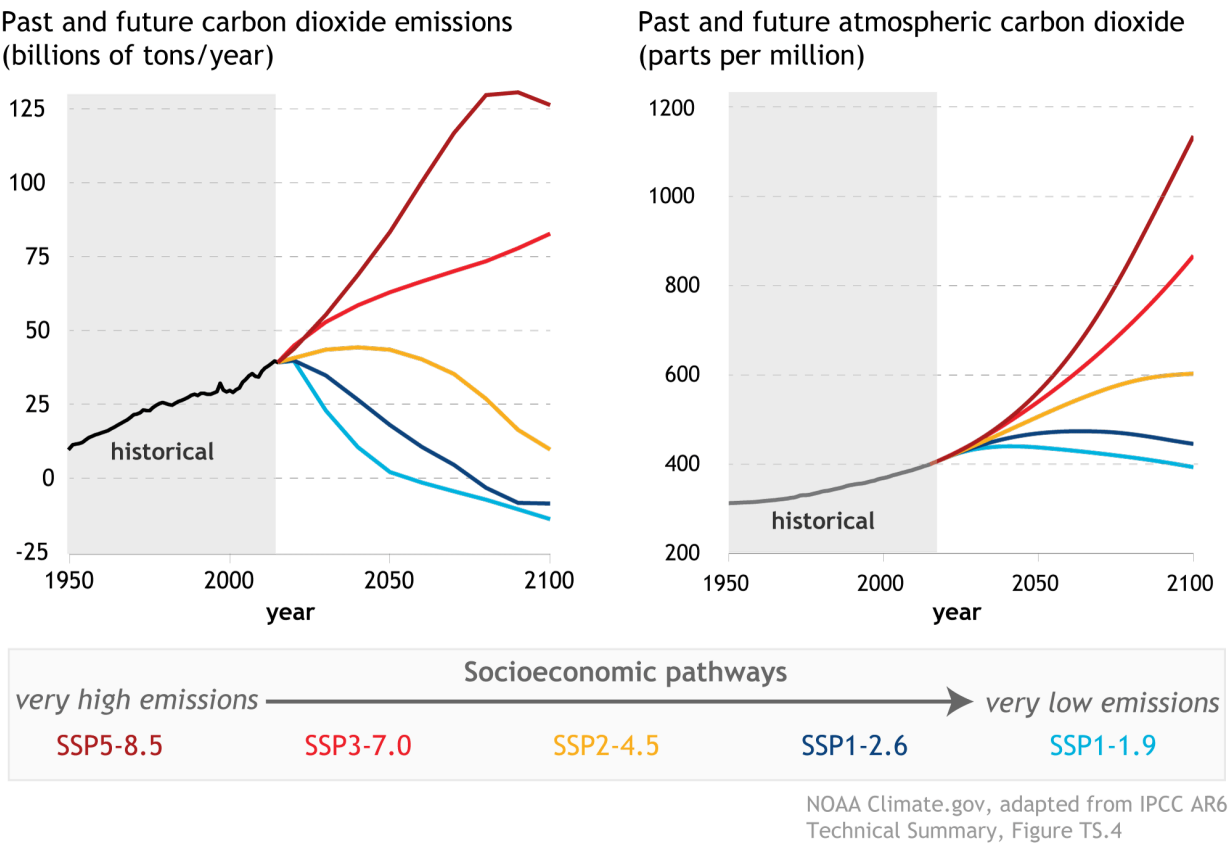

Figure 1.4: The future prediction of CO_2 emissions (left panel) and resulting atmospheric CO_2 concentrations (right panel) by 2100 [236].

1.2 Overview of carbon capture routes

The recent interest in Carbon Capture, Utilisation and Storage (CCUS) can be attributed to its potential as a solution to the emission of CO_2 via a circular economy approach where CO_2 can be effectively recycled within the industrial environment, especially where sustainable biomass is integrated into the system [18]. The CCUS process typically involves capturing CO_2 from flue gas emissions at sources such as power plants and industrial facilities, followed by CO_2 conditioning and transport for either storage or utilisation [16,19–21]. This process can be categorised into carbon capture and storage (CCS) and carbon capture and utilisation (CCU). A simplified schematic diagram of a typical CCUS process, including CO_2 separation from flue gas and the subsequent steps is shown in Figure 1.5. In CCS, CO_2 is injected into deep geological layers for long-term storage. In contrast, CCU aims to reduce CO_2 emissions by using the captured CO_2 through various chemical, physical, mineralisation and biological processes [22]. Before selecting an utilisation method, CO_2 must first be properly separated and captured from the point of emissions. This can be achieved via several methods, including absorption, adsorption, membrane separation, cryogenic separation, hydrate technology, and microbial technologies [22]. A detailed schematic representation of these capture technologies and CCU pathways is presented Figure 1.6. These illustrate how capture technologies can be integrated with downstream utilisation options for use of CO_2 as a feedstock in a circular carbon economy.

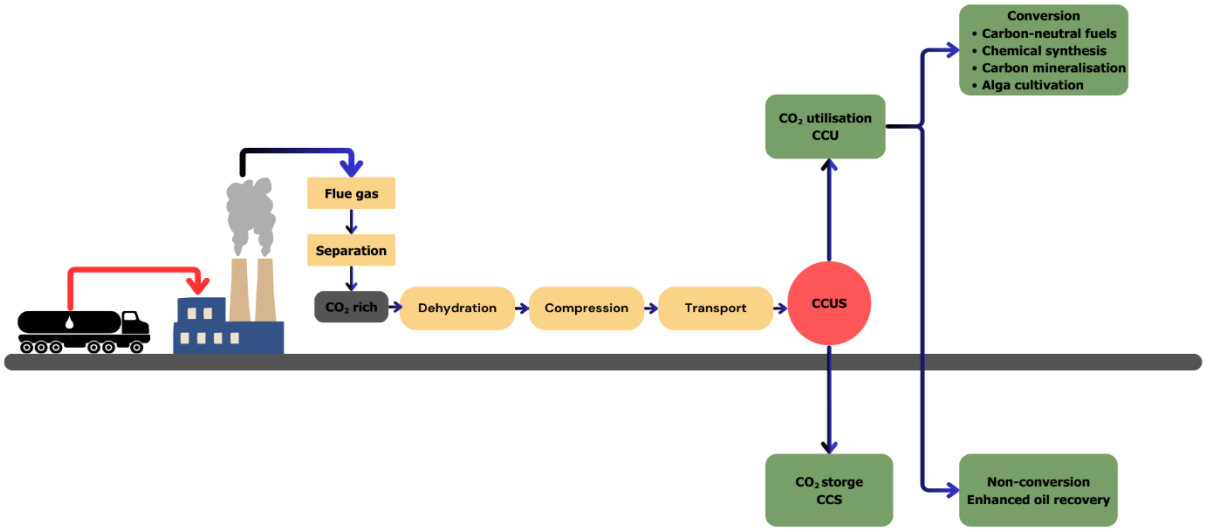

Figure 1.5: Sequences of capturing CO_2 from industrial source and relative steps for CCUS process adapted from Rowaihy et al.[17] and International Energy Forum-IEF [237].

Figure 1.6: Overview diagram of CO_2 capture and utilise pathways in CCUS [22].

CCU is considered a potential net zero technology for the long-term consequences of CCS on the environment [23]. According to the IEA [24], the utilisation of CO_2 consists of two pathways, which are conversion and non-conversion methods. The conversion approach involves utilising CO_2 as a feedstock, which is then chemically converted to value-added products. In the non-conversion approach, CO_2 can be directly used without undergoing chemical changes.

Different technologies for CO_2 conversion to fuels and chemical products have been explored by research groups. Thermochemical, electrochemical, biological and catalytic conversion methods have been reported in the literature [16,19,25–28]. All of these efforts are focused primarily on mitigating the CO_2 footprint although each method has its own limitations and strengths over the other approaches, such as production yield and energy requirement [28,29].

1.3 CCU through gasification technology

In context of reducing CO_2 emissions, one potential conversion technology route is the use of biomass gasification as a thermochemical means to convert renewable sources of carbon into valuable chemical products, e.g. reduction to carbon monoxide (CO) as a primary chemical for subsequent downstream deployment for organic chemical feedstocks [30]. In such a gasification process, CO_2 mitigation can be achieved through the reverse Boudouard reaction (Equation 1.1) by directly using CO_2 as a gasifying agent with bio-derived carbon-based material to form CO. This simple reaction produces highly pure CO, which potentially reduces the overall process cost [31]. Figure 1.7 presents a simple illustration of implanting a thermochemical gasification method to utilise CO_2 and final applications of synthesis gases (CO and hydrogen (H_2)).

$$C + CO_2 \rightleftharpoons 2CO \qquad (1.1)$$

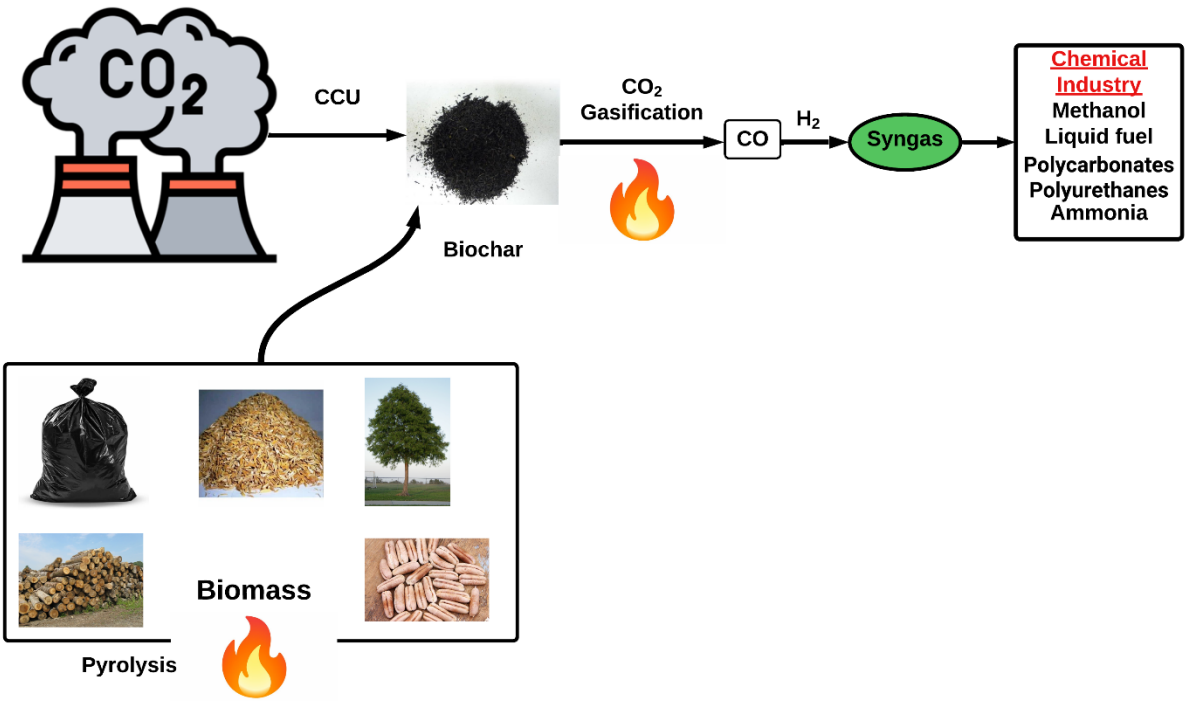

Figure 1.7: Schematic of integrating CO_2 utilisation and biomass gasification and final product applications.

The reverse Boudouard reaction is an endothermic heterogeneous reaction that requires a high temperature, typically >700°C to shift the chemical equilibrium towards CO production [32]. The equilibrium of the reaction at 1 atm is shown in Figure 1.8. Understanding the mechanism of the Boudouard reaction with inhomogeneous materials such as biochars and studying the factors that affect the reaction rate is beneficial to increase the gasification process effectiveness and hence reduce technology risks in process up-scaling. A further discussion of the reaction fundamentals and process behaviour is presented in Chapter 2.

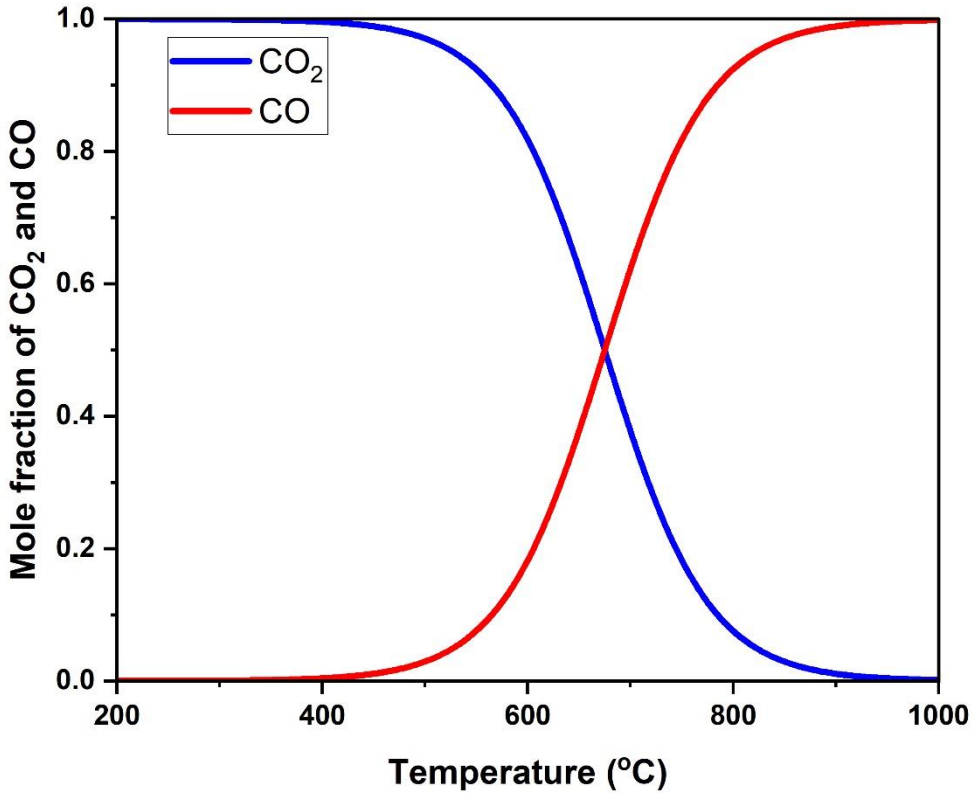

Figure 1.8: Equilibrium diagram of the reverse Boudouard reaction at atmospheric pressure [238].

1.4 Industrial circular economy

Incorporating gasification technology into industrial processes offers an opportunity to establish an industrial circular economy. This can be achieved by capturing CO_2 from flue gas exhaust and utilising it to convert bio-derived materials into CO for chemical industrial applications. The cycle continues by combining the produced CO with H_2 to generate synthesis gas which is considered as a key building block for various chemical products [33]. Syngas is a valuable feedstock for many applications as illustrated in Figure 1.9. The primary uses of syngas include synthesis of ammonia for fertiliser production, oil refining processes, and methanol production [33].

Circulating carbon within industrial operations provides a sustainable approach for reducing CO_2 emissions by converting waste carbon into valuable products instead of releasing it into the atmosphere. This strategy also increases the benefits of recycling waste materials into chemical resources for industrial applications. Moreover, integrating a gasification system within industry can effectively reduce the energy input requirements by the reverse Boudouard reaction by using the heat waste recovered from existing processes [34].

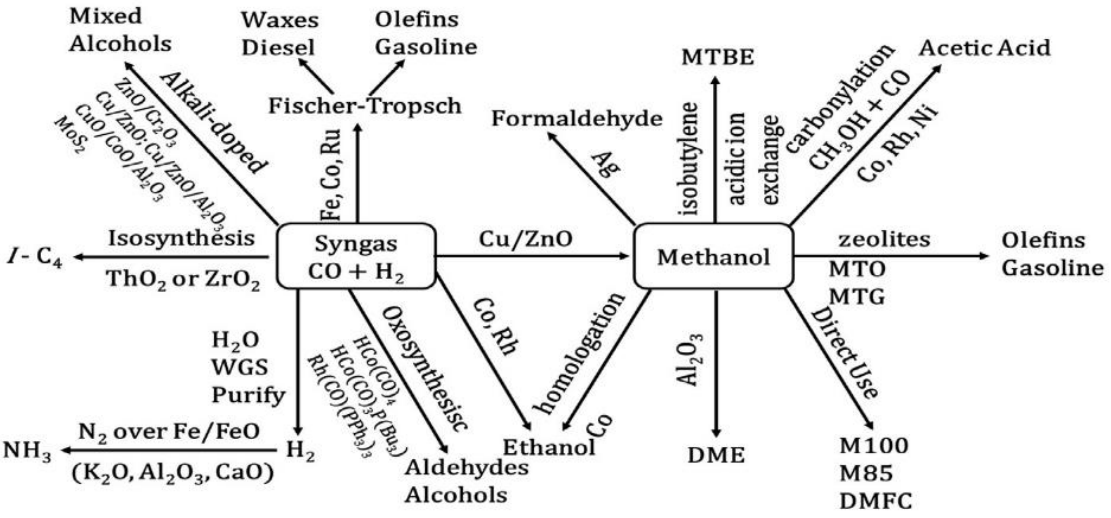

Figure 1.9: The use of syngas in industry [239] .

1.5 Motivation: Saudi Arabia's net zero CO_2 emissions target by 2060

The Kingdom of Saudi Arabia (KSA) is one of the largest twenty economies in the world (G20) and the world's largest exporter of petroleum-based fuels. Saudi Arabia plays a critical role in global energy systems and in shaping international climate decisions. As an active participant in the Paris Agreement, Saudi Arabia has committed to cooperating on international climate goals while undergoing rapid domestic development across multiple sectors. Over the past two decades, national CO_2 emissions from fossil fuel combustion have increased by 127% with a value of ~532 Mt according to IEA statistical data [35].

Figure 1.10 shows the historical emissions change since 2000 with a slight decline during the COVID-19 pandemic. In 2024, The Saudi Clean Development Mechanism Designated National Authority (Saudi DNA) released the First Biennial Transparency Report [36]. The report shows that total GHG emissions from different sectors rose from 610.2 Mt in 2019 to 650.2 Mt in 2021, with CO_2 being the dominant emitted gas. Electricity generation, road transport and desalination together accounted for about 60% of these emissions in 2021, as illustrated in Figure 1.11. Electricity alone contributed over 26% of CO_2 emissions, which shows the dominance of energy sectors and their role as a the key targets for decarbonisation in KSA.

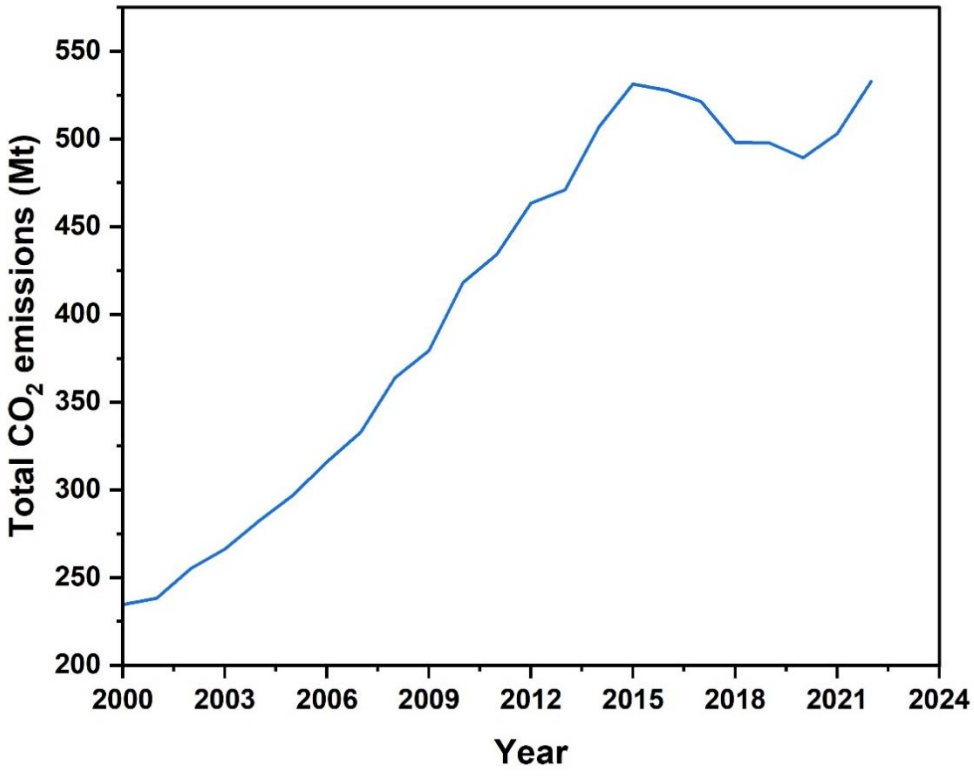

Figure 1.10: Estimation of total CO_2 emissions in KSA from fuel combustion between 2000 and 2022 based on IEA data [35].

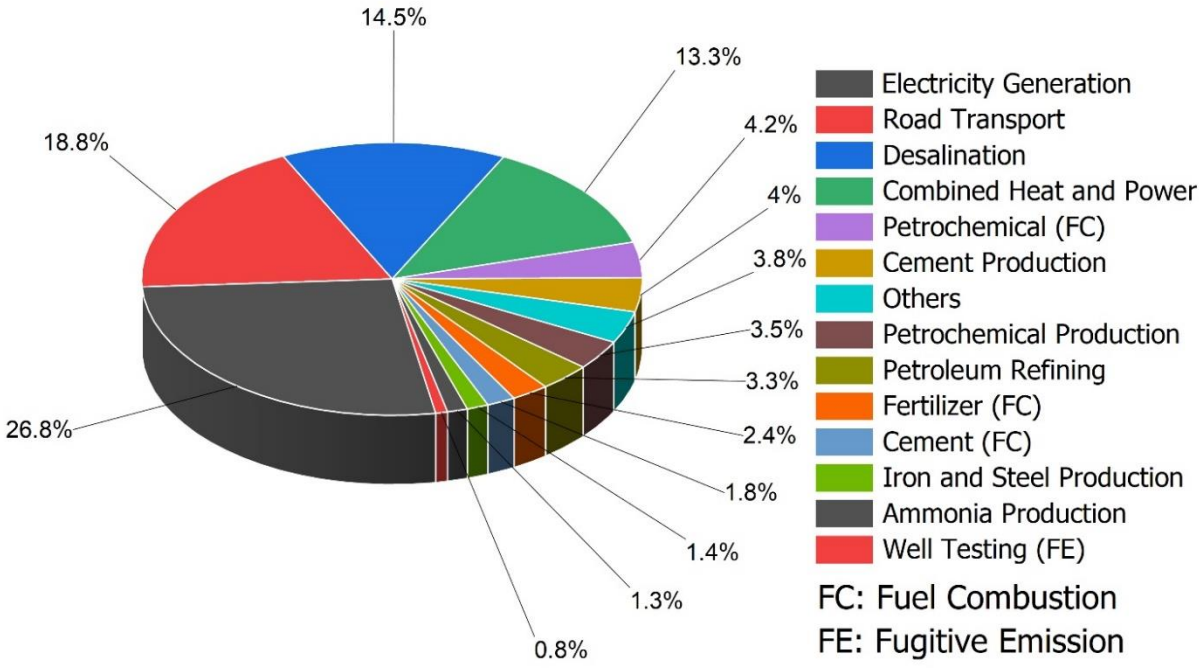

Figure 1.11: Major sources of CO_2 emissions in KSA in 2021, adapted from Saudi DNA report [36].

In response, the Kingdom has developed comprehensive strategies to mitigate CO_2 emissions and reduce environmental impact. In 2016, Crown Prince Mohammed Bin Salaman established the Saudi Vision 2030 [37]. Under this vision, key sustainability programs were introduced including the Saudi Green Initiative (SGI) and the Middle East Green Initiative (MGI) [38]. One of SGI's main objectives is to reduce carbon emissions by 278 Mt annually by 2030, aiming to achieve net zero emissions by 2060. In parallel, major industrial companies in KSA have implemented several projects using CCUS technologies to reduce the emissions. The Saudi petrochemical company (SABIC) is running a CCU unit operating since 2015 at one of its facilities [39]. Aramco is building the largest CCUS hub in the world in collaboration with SLB and Linde, based in Jubail city [40]. The project aims to capture and store up to 9 Mt of CO_2 per year and is

scheduled to begin operation by 2027. Aramco also applies CO_2 utilisation to enhance oil recovery in Uthmaniyah oil reservoir and the Ghawar oil field [17,40].

Despite these developments, research and innovation efforts in Saudi Arabia have focused primarily on CO_2 capture and storage. To date, there has been limited investigation of CO_2 utilisation through thermochemical gasification technology. No published studies in the Kingdom have addressed this pathway. This gap presents an opportunity to investigate CO_2 gasification as a viable and underexplored utilisation route that aligns with national decarbonisation goals.

Furthermore, the Kingdom generates over 31 million tonnes of biomass waste every year, including 22 million tonnes of municipal solid waste (MSW), 1.7 million tonnes of agricultural crop residues, 6.78 million tonnes of animal waste and 864 million kg of dry sewage sludge [41]. In Makkah city alone, around 2750 tonnes of MSW are disposed of daily, while this amount rises to 3000 tonnes during Ramadan and reaches 4706 tonnes per day in Hajj season [42]. These carbon-rich residues represent a valuable opportunity for thermochemical CO_2 utilisation which will support national goals of emissions reduction and waste valorisation.

1.6 Aim and objectives

This PhD aims to investigate the mechanisms associated with CO_2 utilisation via the reverse Boudouard reaction. The study focuses on the physical and chemical properties of various carbonaceous materials and their correlation with CO_2 gasification reactivity. A novel macro-thermogravimetric setup has been developed to overcome the limitation of using unfeasibly small samples in the conventional TGA (when compared with heterogeneous materials such as biomass samples). This setup will provide a precise evaluation of reactivity under conditions more representative of industrial fuels and the associated utilisation systems. Therefore, this thesis contributes to the CCUS field by

improving the understanding of how material properties influence reaction mechanisms under more practical experimental conditions.

The thesis objectives are listed below:

1. To design and test a macro-thermogravimetric system (Macro-TGA) with a top loading thermobalance system capable of measuring real-time mass change and gas production of a char sample under 100% CO_2 flow at high and uniform temperature (>700°C) distribution within the gasifier.
2. To investigate the CO_2 gasification reactivity of different biomass chars, coal char and hydrochar in isothermal and non-isothermal conditions at high temperatures (900°C-1100°C) using a standard thermogravimetric analyser.
3. To investigate the effect of exposed surface area on char reactivity under isothermal conditions in the Macro-TGA gasifier using biochar pellets of different sizes at different temperatures.
4. To assess the role of inorganic compounds in char reactivity by using a demineralisation method.
5. To evaluate the correlations between gasification reactivity and physicochemical properties of the chars as follows:
    i. Identifying ash inorganic chemical compositions using Inductively Coupled Plasma Optical Emission Spectroscopy (ICP-OES).
    ii. Determining surface area, pore size and pore volume of the chars using a N_2 physical adsorption technique.
    iii. Identifying and semi-quantifying ash mineral phases using X-ray diffraction (XRD).
    iv. Characterising surface morphologies and element distribution on the chars' surfaces using scanning electron microscopy - energy dispersive X-ray spectroscopy (SEM-EDS).
    v. Identifying the chemical functional groups on the chars' surfaces and carbon structure using X-ray photoelectron spectroscopy (XPS).

6. To compare the heat consumed during the reverse Boudouard reaction with other CCU methods.
7. To perform a kinetic modelling study of CO_2 gasification reaction under different heat treatment conditions.

1.7 Research hypothesis

Conversion of a carbon-based material via an advanced thermochemical process offers a promising route for producing chemical products. It also presents an opportunity to reduce CO_2 emissions via the reverse Boudouard reaction. It is widely accepted that material properties significantly influence the CO_2 gasification process performance. One major factor is the surface area of solid char particles. However, this PhD hypothesises that surface area is not the dominant factor controlling the CO_2 gasification of char. Instead, it is proposed that surface chemistry plays a more significant role in determining reactivity due to its influence on active site distribution and gas–solid interactions during the reaction.

1.8 Thesis structure

This PhD thesis consists of nine chapters as follows:

Chapter 1: Introduction

This chapter introduces the current status of the CO_2 emissions and their impact on climate change. It also describes different pathways of Carbon Capture, Utilisation, and Storage (CCUS) technologies. Moreover, the specific motivation related to Saudi Arabia's net zero CO_2 emissions target by 2060 is included. The research hypothesis, aim and objectives, and the overall thesis structure are also described.

Chapter 2: Literature Review

This chapter discusses the fundamental concepts of thermochemical processes including pyrolysis and gasification. It also introduces the principles of thermogravimetric analysis

(TGA) and highlights the differences between conventional TGA (Micro-TGA) apparatus and larger-scale setups (Macro-TGA), with examples from the literature. In addition, it provides a basic understanding of the physical and chemical characterisation of carbon-based chars and their roles in reverse Boudouard reactivity and gasification kinetics.

Chapter 3: Material characterisation and analytical techniques: physical and chemical properties

This chapter presents the detailed methodology of the materials characterisation and analytical techniques used in this project. A description of the pretreatment of char samples and CO_2 gasification experiments conducted using Micro-TGA can be found in this chapter. Also, the chemisorption test applied to measure both organic and inorganic active sites at low temperature is detailed.

Chapter 4: Development of a Macro-thermogravimetric reactor and experimental procedure

The development and construction of the Macro-TGA gasifier, designed specifically for this PhD project, is described in this methodology chapter. It illustrates the different subsystems integrated into the Macro-TGA setup such as the gas analysis system. Additionally, the chapter outlines the experimental procedures, and health and safety considerations related to the system's operation.

Chapter 5: Kinetic modelling of char gasification

This chapter provides a theoretical background of the kinetic models employed to evaluate the reaction of char gasification. The Volumetric Model (VM), Grain Model (GM), and Random Pore Model (RPM) are briefly described, as well as the methodology for calculating kinetic parameters, based on the conversion profiles of char samples under CO_2 gasification conditions.

Chapter 6: Mechanisms affecting char reactivity in CO_2 gasification: experimental results from Micro-TGA and physicochemical characterisation

This chapter is the first of three results chapters. It presents the results of isothermal CO_2 gasification and CO_2 chemisorption experiments conducted using the Micro-TGA. The chemical and physical properties of the char samples are analysed and correlated with their gasification reactivity and structural characteristics. In addition, the heat consumption of the reverse Boudouard reaction is quantified and compared with other CO_2 utilisation technologies.

Chapter 7: Kinetic analysis of char gasification and non-isothermal gasification results

This chapter provides a detailed kinetic analysis based on Micro-TGA conversion data of different char samples under a CO_2 atmosphere. Kinetic parameters, including activation energy, pre-exponential factor, and reaction rate constant are determined. In addition, the results of non-isothermal gasification experiments conducted at different heating rates are presented.

Chapter 8: CO_2 gasification experimental results from Macro-TGA

The experimental results of CO_2 gasification obtained from the Macro-TGA system are presented in this chapter. A comparison between Micro-TGA and Macro-TGA devices using the results of char gasification reactivity indices and kinetic analysis is performed in this chapter. This chapter shows the effect of surface area and larger samples on overall reactivity and CO yield using prepared biochar pellets at different gasification temperatures.

Chapter 9: Conclusions and Future works

This chapter summarises the main findings of the thesis and outlines potential directions for future research.

Chapter 2 Literature review

2.1 Gasification

Gasification is the process of converting carbonaceous feedstocks into valuable gaseous fuel or chemical feedstock that may be burnt to generate energy or utilised to make value-added compounds [43]. Generally, gasification takes place at temperature above >700°C in a gasifier to produce syngas (i.e. hydrogen (H_2) and carbon monoxide (CO)) in the presence of a gasifying agent such as oxygen, steam or carbon dioxide. Other gases can also be generated from this process such as methane (CH_4), and steam (H_2O). Gasification of raw biomass mainly consists of four steps, namely, drying, pyrolysis (devolatilising), combustion (oxidation) and gasification (reduction). All of these steps are consuming heat (endothermic reactions) except combustion which is exothermic process. A schematic representation of these steps is shown in Figure 2.1.

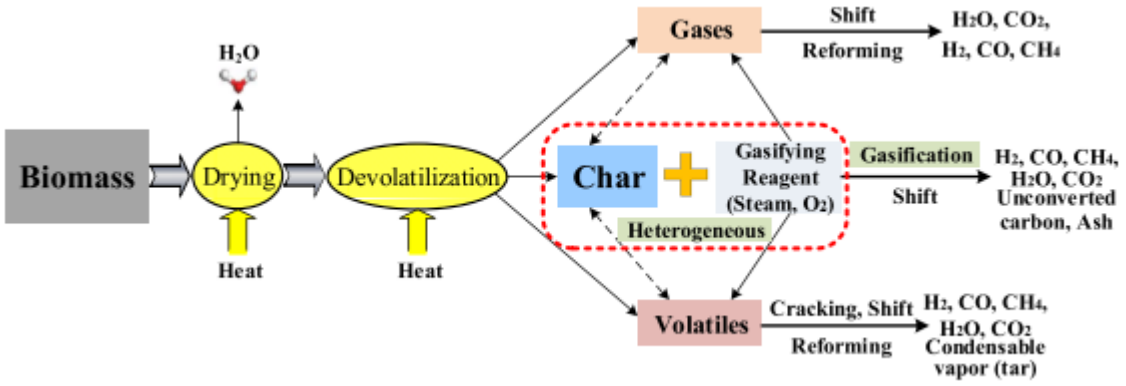

Figure 2.1: Schematic representation of the steps involved in biomass gasification [240].

2.2 Pyrolysis

Pyrolysis is the first step of all thermochemical processes because it involves chemical reactions that produce solid (char), liquid, and gaseous products without the need for oxygen [44]. It refers to the thermal decomposition of biomass by heat in the absence of oxygen. This process serves as the precursor of both combustion and gasification processes. Based on the operating conditions, pyrolysis can be categorised into three types, as shown in Figure 2.2, slow, fast and flash pyrolysis [45]. Rapid pyrolysis can be useful to obtain liquid products, whereas slow pyrolysis is more often utilised to make char [46]. In this thesis, the influence of pyrolysis conditions on char properties is not studied. However, the selection of char samples represents a range of sources and pretreatment methods such as slow pyrolysis for biomass chars, high temperature (1100°C) with short residence time for coal char and hydrothermal carbonisation for hydrochar, as discussed in Sections 3.2 and 3.3. Pyrolysis can be carried out in an inert atmosphere such as nitrogen (N_2) and argon (Ar) or under a reactive medium such as CO_2.

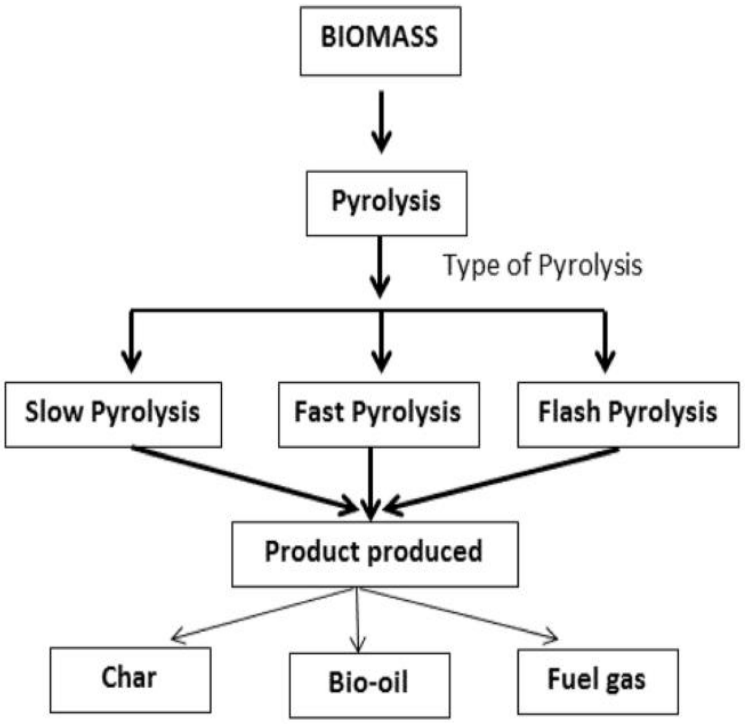

Figure 2.2: Types of pyrolysis process and their primary products [241].

2.3 Types of gasifiers

A gasifier is a chemical reactor where carbon materials are converted into produce gases such as CO, CO_2, H_2, CH_4 using gasification agents at temperatures typically ranging from 800°C to 1100°C [47]. Different gasifier configurations can be used to carry out gasification process. Based on the gas-solid interaction and gasification medium, gasifiers can be classified into three main types: fixed bed, fluidised bed and entrained bed gasifiers [48], as shown in Figure 2.3 . One of the criteria that for selecting a suitable gasifier is the type of feedstock material [49]. This is because gasifier performance is highly influenced by feed properties such as moisture content, particle size and ash composition. While different types of gasifiers are illustrated in Figure 2.3, the focus here is on fixed bed configurations as the gasifier developed in this PhD falls under this type. In the following sections, a brief discussion of fixed bed types and their features is provided.

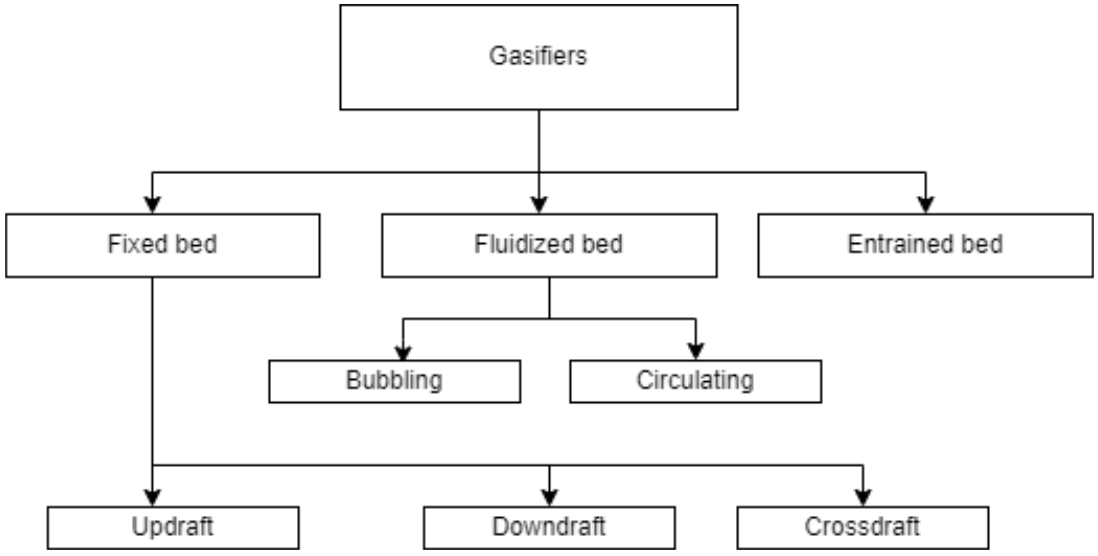

Figure 2.3: Types of gasifiers [242].

2.3.1 Fixed bed gasifier

Among all types of gasifiers, fixed bed gasifiers are considered to be the simplest type and are more suitable for small- scale applications [50]. Depending on the direction of

gasification agent movement inside the gasifier, fixed bed gasifiers are classified into three types: updraft (counter-current), downdraft (co-current) and crossdraft gasifiers [51]. Table 2.1 presents a comparison of the different types of fixed bed gasifiers characteristics.

Table 2.1: Fixed bed gasifiers characteristics [48].

Fuel (wood)	Updraft	Downdraft	Crossdraft
Moisture wet basis (%)	60	25	10–20
Dry-ash basis (%)	25	6	0.5–1.0
Ash melting temperature (°C)	>1000	>1250	-
Particle size (mm)	5–100	20–100	5–20
Application range (MW)	2–30	1–2	-
Gas exit temperature (°C)	200–400	700	1250
Tar (g/Nm^3)	30–150	0.015–3.0	0.01–0.1
Gas lower heating value (MJ/Nm^3)	5–6	4.5–5.0	4.0–4.5
Hot-gas efficiency (%)	90–95	85–90	75–90

2.3.2 Updraft fixed bed gasifier:

The updraft gasifier is the oldest and simplest kind of this type of gasifier. It is a counter-current gasifier, commonly used to convert non-volatile feedstock such as coal and charcoal [50]. In this type, the carbonaceous material is introduced from the top of the gasifier and moves down against the gasification agent which enters through the gasifier's bottom, as illustrated in Figure 2.4. Although the updraft process is more efficient thermally compared to the downdraft process, the product gas contains a very high concentration of tar [52]. The reason is that the pyrolysis zone is located above the combustion zone, thus the tar generated does not pass through the reactor's high temperature zone resulting in a greater tar concentration in the resultant gas. Relatively, updraft gasifiers can convert fuel with high moisture content more efficiently than downdraft gasifier due to upward gas movement which vaporises the moisture [49].

The main differences between updraft and downdraft fixed bed gasifiers are listed in Table 2.2. The primary aim of developing gasifier in this PhD is to investigate the effect of larger sample sizes on reaction behaviour and to accommodate various types of feed materials. It is not intended to produce high-quality syngas or minimise tar formation. Therefore, the constructed gasifier (Macro-TGA) in this PhD can be classified as an updraft fixed bed gasifier based on flow direction and fixed sample position. The design and system components are discussed in Chapter 4.

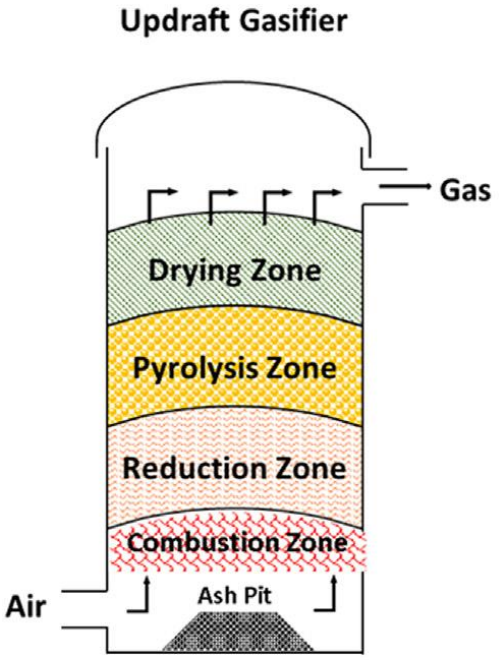

Figure 2.4: Typical schematic diagram of updraft fixed bed gasifier[242].

Table 2.2: Comparison of updraft and downdraft gasifiers [53].

Parameter[a]	Updraft gasifier	Downdraft gasifier
Carbon conversion	****	****
Thermal efficiency	*****	****
CGE[b]	*****	***
Turndown ratio	***	**
Start-up facility	*	*
Management facility	****	****
Control facility	**	**
Scale-up potential	***	*
Sized feed elasticity	****	*
Moisture feed elasticity	****	**
Ash feed elasticity	*	*
Fluffy feed elasticity	****	**
Sintering safety	*	*
Mixing	*	*
Cost safety	*****	****
Tar content	*	*****
Particulate content	*****	***
Lower heating value	*	*

a: * Poor, ** fair, *** good, **** very good, ***** excellent. b: Cold gas efficiency.

2.3.3 Downdraft fixed bed gasifier:

The downdraft is a co-current gasifier, it was developed to convert high volatile fuels into low tar gas and has therefore proven to be the most successful design for power generation [50]. In downdraft reactor, the carbonaceous material is loaded at the top while the gasifying agent is introduced at the sides above the grate and the combustible gas is blown under the grate [54], as shown in Figure 2.5. Both fuel and gas are moving downward in the same direction and exit from the reactor's bottom.

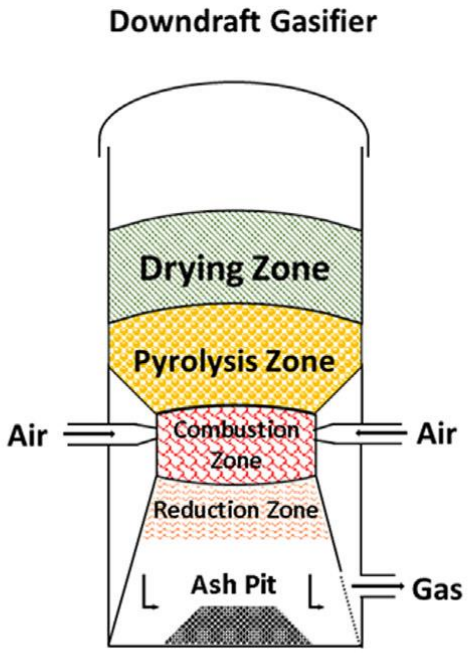

Figure 2.5: Typical schematic diagram of downdraft fixed bed gasifier [242].

2.3.4 Crossdraft fixed bed gasifier:

Typically, in crossdraft gasifier, the fuel is injected at the top of the reactor and travels downward while the gas agent enters from the side, as shown in Figure 2.6. At roughly the same level as the feedstock is supplied, the product gas exits from the top side of the reactor [55]. Crossdraft gasifiers require a shorter startup time compared to updraft and downdraft gasifiers, and another advantage is their ability to maintain a high-temperature profile [56]. When the top is open, the crossdraft reactor may work with high-moisture fuels, but it struggles with fuels that have ash content above 1% [48], therefore fuel such as charcoal is favourable [48].

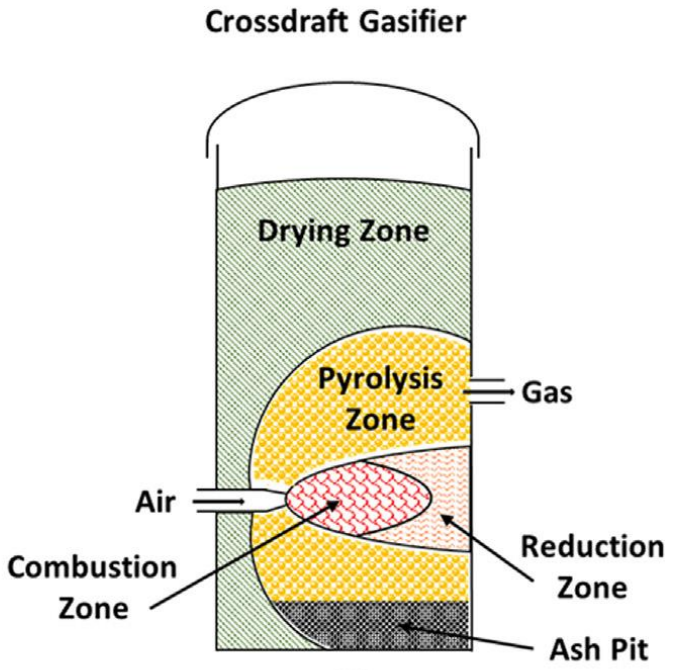

Figure 2.6: Typical schematic diagram of crossdraft fixed bed gasifier [242].

2.4 Fundamental of thermogravimetric analysis

According to the International Confederation for Thermal Analysis and Calorimetry (ICTAC) [57], thermal analysis (TA) is defined as: *"the study of the relationship between a sample property and its temperature as the sample is heated or cooled in a controlled manner."* Currently, there are a range of thermal analysis methods implemented to test materials behaviour under specific conditions, one powerful thermal analysis technique is thermogravimetric analysis or thermogravimetry which is commonly known as TGA. TGA is an analytical method used to monitor the change in the weight of a substance as a function of temperature or time while the tested sample undergoes a pre-defined temperature program and in a controlled gas flow. The weighed sample can be examined under three different types of thermogravimetry [58]:

i. Static thermogravimetry (Isothermal TGA): the sample is heated to the desired temperature and mass change is recorded as a function of time at a constant temperature.
ii. Quasistatic thermogravimetry: the sample is heated in multi-steps with the temperature held constant at each step while change in mass is recorded as a function of time.
iii. Dynamic thermogravimetry (Non-isothermal TGA): the sample is heated continuously to a final temperature using different heating rates and mass change is recorded as a function of time or temperature.

TGA analysis is conducted using thermogravimetric analyser device which is often referred as thermobalance due to its primary function. This device can be further classified into Micro-TGA and Macro-TGA according to its structural dimensions and sample capacity. Micro-TGA handles sample sizes from 1 mg to about 50 mg, while Macro-TGA fits larger samples, typically from 1 g to about 7 g [59]. A description of each system is discussed in the following sections.

2.4.1 Micro-Thermogravimetric Analyser (Micro-TGA)

Most of the thermochemical experiments, including pyrolysis, gasification and combustion reported in literature use the conventional Micro-TGA due to simplicity of use and faster results. The main drawback of micro-TG analyser is that only small sample masses in milligram can be examined which creates a gap in understanding the real behaviour of chemical reactions for larger applications. Despite this, one of Micro-TGA advantages is that heat and mass transfer limitations are insignificant compared to larger scale TGA [60]. As can be seen in Figure 2.7, the Micro-TGA apparatus consists of five main components, namely, furnace, balance, sample holder, temperature programming system and data acquisition system [61]. It is available commercially in three different setups including top loading, hang down and horizontal arrangement as shown in Figure 2.8. Part of gasification experiments in this thesis was conducted using a Micro-TGA apparatus with a horizontal sample holder (see Figure 3.27). The remaining experiments were carried out using the developed Macro-TGA which used a top-loading arrangement, where the sample is positioned inside a vertical furnace and connected to an external balance (see Figure 4.2).

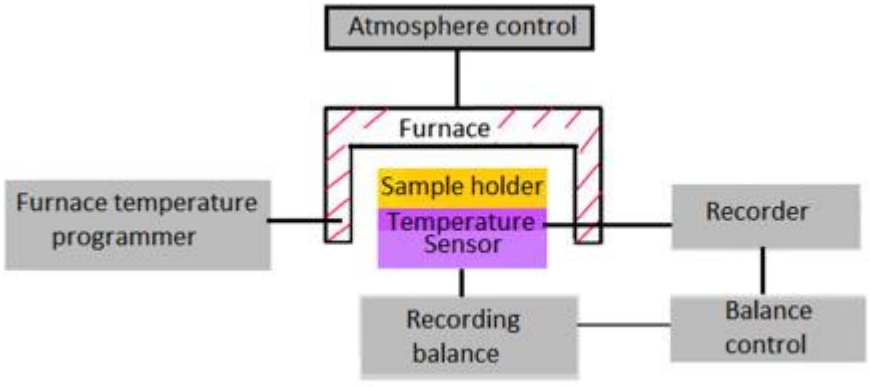

Figure 2.7: Block diagram of thermobalance component [61].

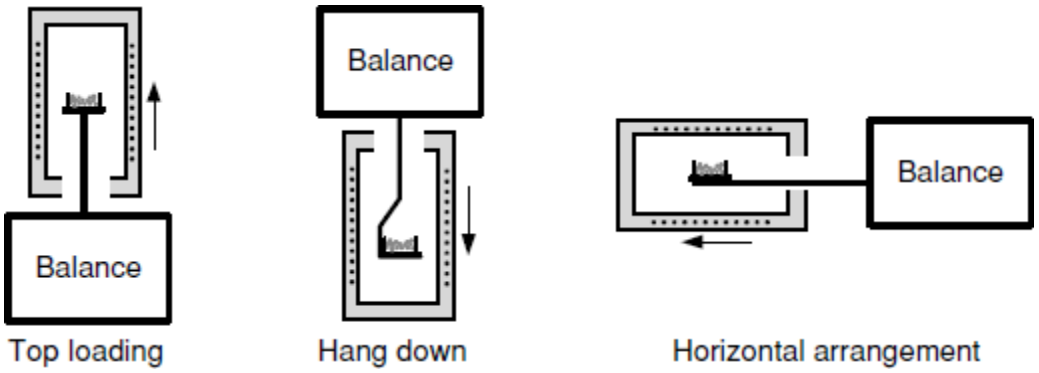

Figure 2.8: Arrangement of the sample holder and balance with respect to the furnace [243].

In addition to its primary purpose, the traditional TGA is usually equipped with some other powerful features such as measurement of differential thermal analysis (DTA) or differential scanning calorimetry (DSC). DTA is a method to measure the temperature difference between the sample and a reference material while DSC measures the difference in the heat flow absorbed or released by the sample compared to a reference material [57]. Both techniques can describe how a sample absorbs or release heat energy. However, DSC is a more precise technique to distinguish the nature of the reaction whether it is endothermic (consume heat) or exothermic (release heat).

2.4.2 Macro-Thermogravimetric Analyser (Macro-TGA)

Unlike Micro-TGA apparatus, this system is originally designed and developed to use larger sample sizes in grams and larger particle sizes in millimetre [62,63]. Macro-TGA can be considered a fixed bed reactor with performance similar to industrial-scale reactors [60]. Using gram-scale samples provides precise material characterisation through mass loss measurement, which decreases the impact of heterogeneous particle sizes and the variability of material properties across the particles [59].

Macro-TGA equipment consists of similar components as Micro-TGA and can be configured with two types of balances: suspension or compression setups. In a suspension setup, the balance is located at the top of the reactor with the sample hanging down in the chamber, whereas in a compression setup, the balance is placed underneath the reactor. The design and construction of this instrument is available commercially or can be developed in laboratories.

The Macro-TGA device has been employed in the literature to investigate thermal conversion processes including drying [64], torrefaction [65,66], pyrolysis [64,67–69], gasification [63,68,70,71] and combustion [69,72]. It has Also been used to test samples in different forms such as pulverised sample [71,73], pelletised biofuel [69,70,74] and chipped feedstocks [68,71,72].

In the context of CO_2 gasification, there are some studies implemented this kind of thermobalance system to gain insight into the reaction mechanisms and kinetic using larger particles and higher material quantities as shown in Table 2.3. As can be seen, most of these studies used suspension type balances and none of them conducting gas analysis measurement in the Macro-TGA.

Table 2.3: Overview of using Macro-TGA for CO_2 gasification from literature.

Reference	Sample	Sample mass (g)	Particle size (mm)	Temperature (°C)	CO_2 Flow rate (L/min)	Balance type
Meng et al. [75]	Biomass, vegetable food and plastics waste	0.5-1.5	0.075	1000 non-isothermal	1.36	Suspension
Zhang et al. [76]	Cellulose, xylan, lignin, starch, and pectin biomass	1.5	-	1000 non-isothermal	0.3	Suspension
Wretborn [71]	Wood and coal chars	0.1	0.25-0.3	900 isothermal	Not specified	Suspension
Cortazar et al.[63]	pine sawdust char	1	1-2	800,850,900 isothermal	0.5 (10% and 100% concentration)	Compression
Wang et al.[77]	birch wood char	20-30	-	1100 isothermal	4 (50% concentration)	Suspension
Zhang et al. [73]	Cellulose, xylan, and lignin biomass	0.5	0.25	1000 Non-isothermal	0.2	Suspension

2.4.2.1 Specifications of commercial and lab-built Macro-TGA systems

An example of commercial design of Macro-TGA is the one used in Tapasvi PhD thesis [78]. It was built and developed by Höker KFT (Hungary) as shown in Figure 2.9. This device was used for torrefaction study between 225 and 275°C with nine different heating rates allowing for torrefaction kinetics investigating. The unique feature of this device was that it can handle very large sample quantities and sizes. Consequently, Tapasvi

conducted the experiments using Norwegian birch and spruce feedstocks cubes of 10 and 40 mm sample size and with mass of 200 to 300 g. The gas inlet pipes were connected to the reactor side wall and were fed from two preheaters to reduce temperature gradients within the reactor and allow the supply of a high gas flow rate of 100 L/min. As shown in Figure 2.9, the scale was connected to the sample basket which was suspended inside the reactor. According to Tapasvi, the design of sample basket provided a uniform heat and mass transfer within the sample due to the separated layers in the basket.

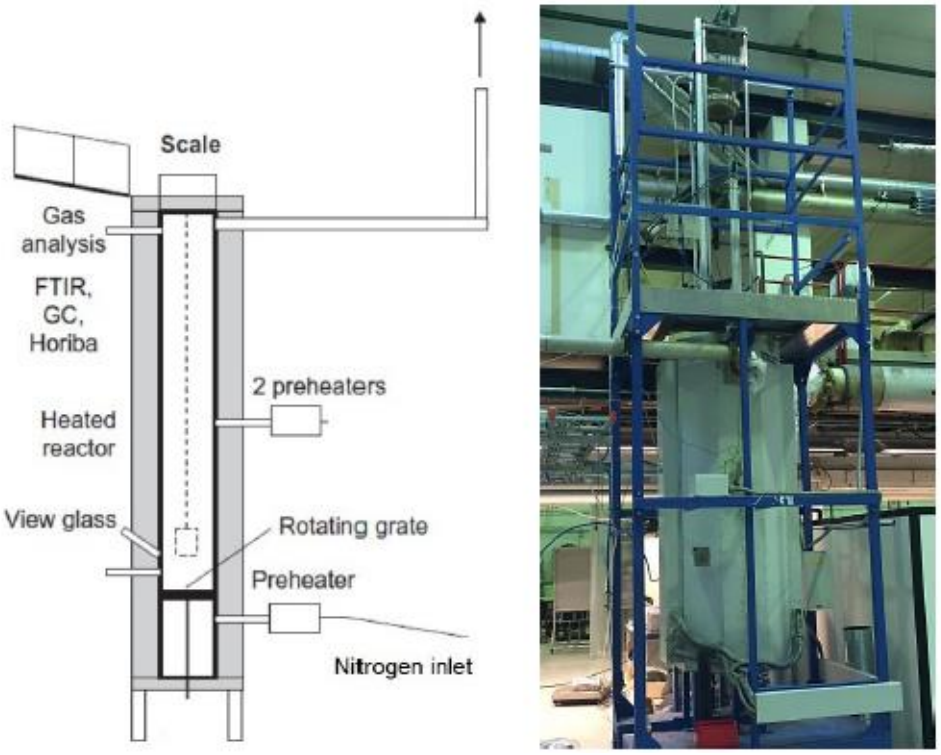

Figure 2.9: Schematic diagram (a) and photograph of torrefaction experimental Macro-TGA facility developed by Höker KFT (Hungary) [78]. Note: Dimensions were not provided in the source.

Baraket et al. [79] employed a Macro-TGA with a different design for thermal treatment of biomass ash with temperatures ranging from 200 to 500°C (see Figure 2.10). The device was developed by Nabertherm and could operate at temperatures up to 1200°C. Unlike Höker KFT apparatus, the balance (Kern type) was placed below the furnace. A porcelain crucible was used to hold the sample which was set on a flat ceramic surface supported by a large diameter ceramic rod. This design provides effective method for placing and removing the sample from the rectangular furnace compared to the previous Macro-TGA. However, the cylindrical furnace ensures a better temperature distribution around the sample [80]. The authors used 15 g of biomass mixture ash in their experiment but did not specify the maximum capacity of the system or whether it could be fed with other gases.

Figure 2.10: Macro-TGA system with high temperature furnace developed by Nabertherm [79].

Others Macro-TGA devices have been developed within laboratories. One such device was DANTE, it was designed and constructed by Balme and his co-workers [80]. The authors provided detailed information on the DANTE configuration and illustrated their design with a schematic drawing and a photograph of the system, as shown in Figure 2.11. DANTE was able to analyse samples up to 90 g with ability to detect mass losses up to 30 g. Heat was supplied to the system by a vertical cylindrical furnace and sample mass was monitored using a 5 kg strain gauge scale, with the sample suspended into the reaction zone via a 1 m ceramic rod. A thermocouple was fitted inside the rod for continuous measurement of sample temperature. The main challenge of the system was the viscosity effect caused by the pressure drop when gas flowed through the insulating unit. This introduced errors in the mass reading that increased with gas flow rate. To address this, DANTE developers measured the viscous force and applied a calibration curve for correction. The research group demonstrated that their Macro-TGA system produced results comparable to those obtained from commercial thermogravimetric analysers.

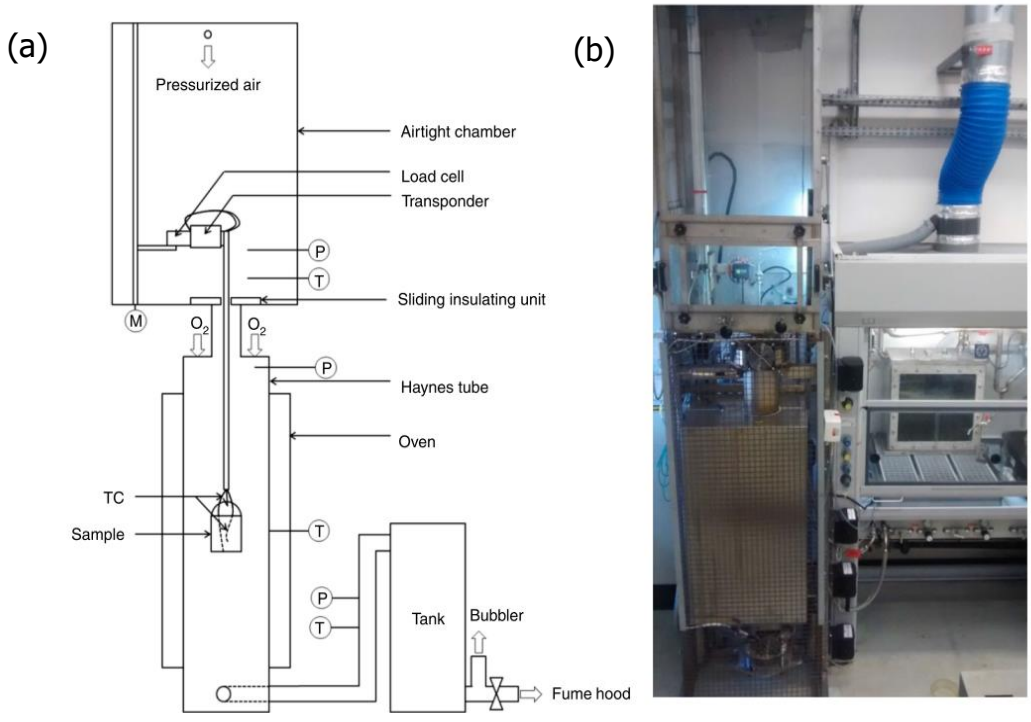

Figure 2.11: Schematic drawing (a) and photograph (b) of DANTE macro-TGA [80].

Another self-built Macro-TGA is shown in Figure 2.12. Cortazar et al. [63] primarily developed the thermobalance to investigate CO_2 gasification kinetics. Gasification experiments were conducted using 1 g of pine sawdust char with particle size of 1-2 mm at temperatures ranging from 800 to 900°C in CO_2 medium varying between 10-100%. The novelty of this Macro-TGA setup lay in the char bed which consisted of a fine stainless-steel mesh (< 90 µm) to hold the sample. The char bed was supported by two layers of quartz wool: one piece was placed under the mesh and the other above the char sample to prevent char particles from escaping. According to Cortazar et al., this design allowed CO_2 to flow directly through the char bed thus enhancing the gas-solid contact and reducing external mass transfer limitations. Additionally, an electronic scale (type Kern Plus PLS420-3F) was modified by adding a metal plate of 50 mm diameter to secure the bottom of the quartz tube reactor. The reactor itself had two gas inlet holes sealed using a rubber ring. This configuration enabled more accurate mass loss data in real-time measurement for kinetic study as emphasised by the authors. The reactor setup, particularly the gas flow direction, sample holder arrangement and overall purpose, is similar to the Macro-TGA developed in this thesis.

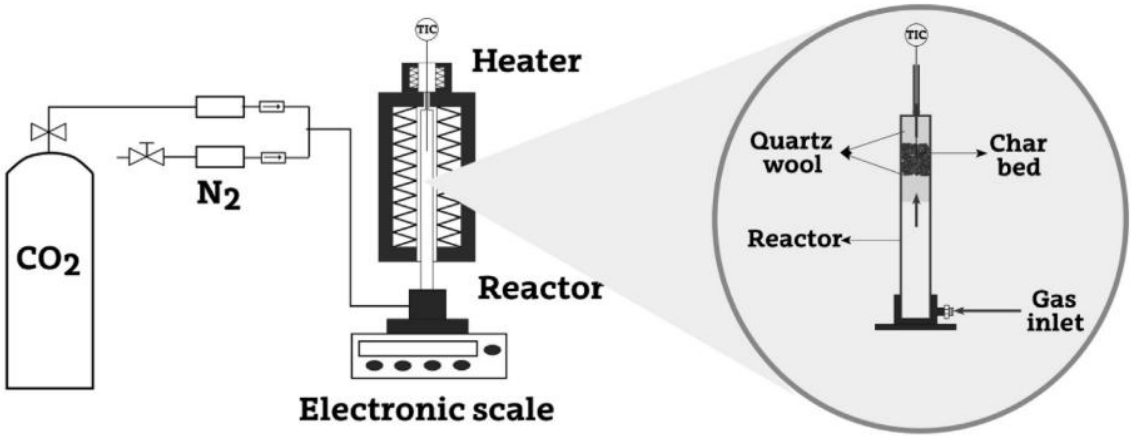

Figure 2.12: Macro-TGA setup used to study CO_2 gasification kinetics of pine wood char [63].

2.5 Gasification reactions

In the gasification process of carbonaceous materials, several reactions occur to produce the final gas composition. These chemical reactions involving carbon, carbon monoxide, carbon dioxide, hydrogen, steam and methane are the most important during the gasification of solid carbon, whether in the form of raw feedstocks or char [81]. Table 2.4 shows the main gasification reactions of the fuel occurring in the different zones inside the gasifier. There are a number of steps involved in heterogeneous reactions [82]. These steps include gaseous diffusion, adsorption and desorption processes on the solid surface, and the chemical reaction itself. The reaction rate is controlled by one or a combination of these steps, referred to as the rate-limiting step. The process steps are listed below and a visualisation of the CO_2 gasification mechanism is shown in Figure 2.13 below:

1. Diffusion of the reactant gases from bulk gas phase to the solid surface.
2. Adsorption of the reactant gases on the solid surfaces.
3. Diffusion of the reactant gases from the adsorption site to the reaction site based on the reaction mechanism.
4. Chemical reaction of the adsorbed gases and solid surface occurs at the reaction site.
5. Diffusion of the product gases from the reaction site to the desorption site based on the reaction mechanism.
6. Desorption of the product gases from the solid surface.
7. Diffusion and fluid flow transport the product gases into the bulk gas.

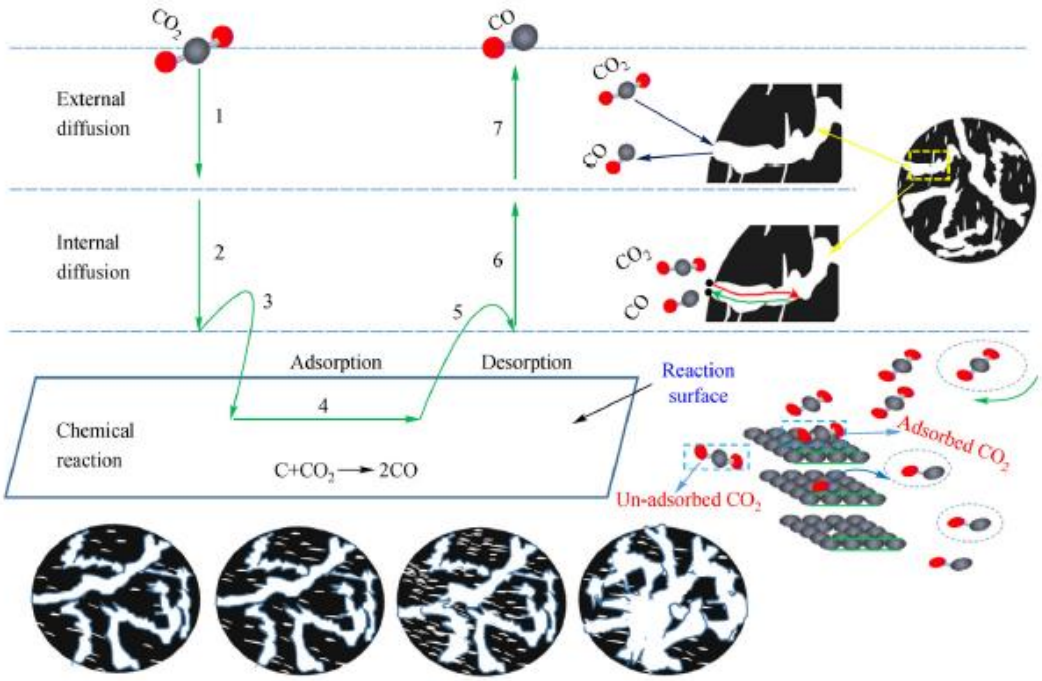

Figure 2.13: Schematic illustration of the heterogeneous solid-gas reaction mechanism within char porous structure during CO_2 gasification of char [244].

2.5.1 The reverse Boudouard reaction

All the work presented in this PhD is based on implementing this reaction to utilise CO_2 via the gasification process. As illustrated in the introduction chapter, the endothermic nature of this reaction is the main challenge; therefore, this PhD provides a comprehensive investigation of the reverse Boudouard reaction. Ergun [83] proposed the oxygen-exchange mechanism, which has been widely used to describe the mechanism of CO_2 gasification of the char, this mechanism consists of three steps as follows:

- First step: in this step, carbon dioxide is dissociated at a free carbon active site C_f, which releases carbon monoxide and forms carbon – oxygen complex C(O) as shown in the following equation:

$$C_f + CO_2 \xrightarrow{k_1} C(O) + CO \qquad (2.1)$$

- Second step: as illustrated in Equation 2.2, the carbon–oxygen complex reacts with carbon monoxide since it is reversible reaction and forming carbon dioxide and a new carbon active site.

$$C(O) + CO \overset{k_2}{\rightarrow} C_f + CO_2 \qquad (2.2)$$

- Third step: in this final step, the carbon- oxygen complex produces a new molecule of carbon monoxide, as shown in the following equation:

$$C(O) \overset{k_3}{\rightarrow} CO \qquad (2.3)$$

Where k_1, k_2 and k_3 represent the Arrhenius rate constants, C_f is a carbon active site and C(O) is a carbon–oxygen complex.

Table 2.4: Main gasification reactions.

Number	Reaction	Reaction name	Heat of reaction at 25°C (kJ/mol)	Reference
R1	Biomass → Char+ Tar + H_2O + CO +CO_2+ CH_4+H_2+ O_2	Biomass devolatilisation	>0	[84]
R2	$C + ½\ O_2 \rightarrow CO$	Carbon partial oxidation	-110.4	[43]
R3	$CO + ½\ O_2 \rightarrow CO_2$	Carbon monoxide oxidation	-284	
R4	$C + O_2 \rightarrow CO_2$	Carbon oxidation	-394	
R5	$H_2 + ½\ O_2 \rightarrow H_2O$	Hydrogen oxidation	-242	
R6	$CH_4 + 2O_2 \rightarrow CO_2 + 2H_2O$	Methane oxidation	-803	
R7	$C + H_2O \leftrightarrow CO + H_2$	Water-gas reaction	+131	
R8	$C + CO_2 \leftrightarrow 2CO$	Reverse Boudouard	+172	
R9	$C + 2H_2 \leftrightarrow CH_4$	Hydrogasification	-74.8	
R10	$CO_2 + CH_4 \leftrightarrow 2H_2 + 2CO$	Dry reforming	+247	
R11	$CO_2 + 4H_2 \leftrightarrow CH_4 + 2H_2O$	Methanation	-165	
R12	$CO + 3H_2 \leftrightarrow CH_4 + H_2O$	Methanation	-206	
R13	$CO + H_2O \leftrightarrow CO_2 + H_2$	Water-gas shift	-41.2	
R14	$CH_4 + H_2O \leftrightarrow CO + 3H_2$	Steam methane reforming	+206	
R15	$CH_4 + ½\ O_2 \leftrightarrow CO + 2H_2$	Partial oxidation of methane	-36	

2.6 CO_2 gasification reactivity of char

The reactivity concept in context of carbon materials refers to how easily carbon can be gasified or combusted [85]. Marsh et al. [85] summarised the reasons for investigating carbonaceous material reactivity in four categories as illustrated in Figure 2.14. In the gasification process, the properties of the carbon materials play a great role in explaining the overall performance of the thermochemical conversion systems. A huge number of studies have been aimed at finding parameters that dominate the reaction, Table 2.5 shows a summary of these parameters from literature. These include crystalline structure, surface area, particle size, morphology, ash mineral content and chemisorption. In the following sections, the factors affecting char reactivity are discussed.

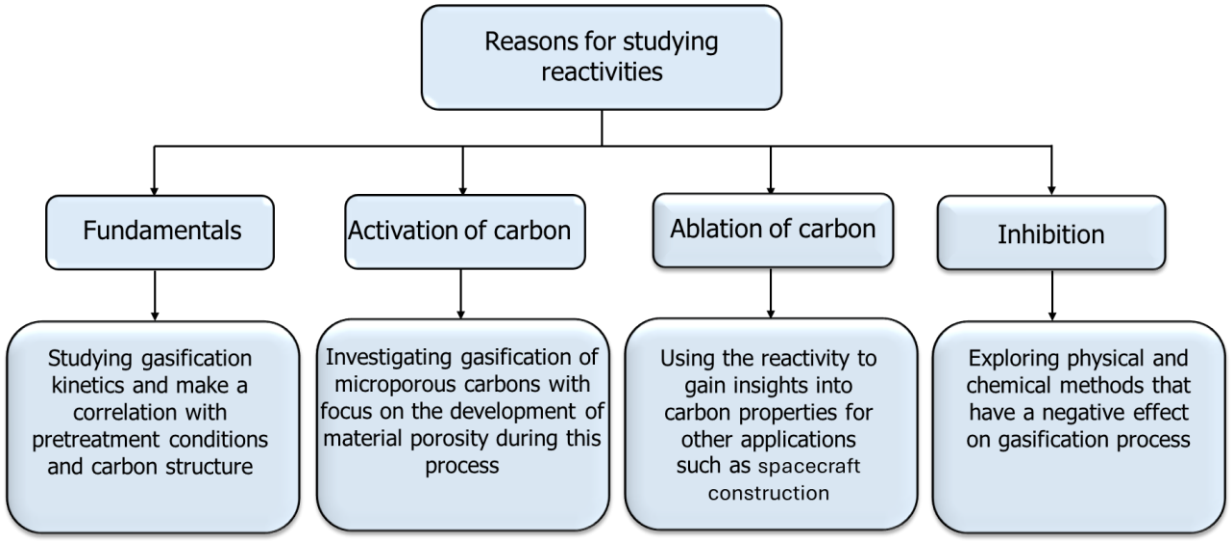

Figure 2.14: Reasons for studying carbonaceous materials reactivities [85].

Table 2.5: Char physical and chemical properties and their impact on CO_2 gasification from literature.

Reference	Char type	Key physical properties	Key chemical properties	Relative reactivity	Dominate factor and remarks
Huo et al. [86]	Biomass, petroleum coke and coal chars	Crystalline structure, surface area	Ash mineral content, Alkali index	Biomass >coke and coal	Biomass is more reactive due to less ordered crystalline structure
Jing et al.[87]	Xiangyuan bituminous, Yangcheng anthracite (fine chars from fluidized-bed gasifier and their corresponding coal chars from pyrolysed process)	Surface area, morphology	Catalytic alkali and alkaline earth metals (AAEMs)	Fine chars better than coal chars from pyrolysed process	Catalytic effect of alkali and alkaline earth metals (AAEMs) but inhibited by the enrichment of the ash layer in a higher carbon conversion range or the ash melting at a higher temperature
Jing et al. [88]	Different coal rank chars	Surface area	Alkali index, carbon crystalline structure and chemisorption	Decreases with increasing coal rank	Total and strong chemisorption (related to inorganic components)
Lv et al. [89]	Coal char	Surface area	Aromatic condensation degree, alkali and alkaline earth metals (AAEMs)	Correlates with specific surface area	Specific surface area and degree of aromatic condensation after removing AAEMs from coal char demineralisation becomes the dominant factor
Phounglamcheik et al. [90]	Pine bark, forest residue, corncob chars	Surface area	Inorganic content, Carbon structure	Highly influenced by K content	Ash inorganic content (especially potassium)
Tong et al. [91]	Pine sawdust chars	Pore structure, surface area	Active sites	Decreases with increasing pyrolysis temperature	Chemical contact as increasing pyrolysis temperature enhances porosity and diffusion path but reduces active sites

Table 2.5 (continued): Char physical and chemical properties and their impact on CO_2 gasification from literature.

Reference	Char type	Key physical properties	Key chemical properties	Relative reactivity	Dominate factor and remarks
Wang et al. [92]	Biomass chars, anthracite char	Particle size porosity and specific surface	Ash mineral content, Alkali index, carbon structure	Biomass chars > anthracite char	Carbon structure amorphous carbon (positive effect) graphite carbon(crystalline) (negative effect)
Xu et al. [93]	Corn straw char	Pore structures	Carbon structure ordering	Increases with temperature	Amorphous carbon, gasification temperature
Huang et al. [94]	Fir char	Crystalline structure, morphology	Metal catalysts (K, Na, Ca, Mg, Fe)	Improved with Catalysts addition: K>Na > Ca> Fe >Mg	-
Pacioni et al. [95]	Apple pomace, spent coffee grounds and sawdust chars	Morphology	Lignocellulosic components (Cellulose, Hemicellulose and Lignin) and ash composition	Apple pomace char is the most reactive char	Ash mineral content (high potassium) the inorganic component

2.7 Influence of char physical and chemical properties

2.7.1 Particle size

Particle size is significant during the gasification process because of its impact on mass and heat transfer [96]. The smaller the particles, the larger the surface area and the faster the heat transfer. Yin et al. [97] investigated the effect of biomass particle size on the gasification performance in a downdraft fixed bed gasifier, they found H_2 and CO contents increased with decreasing particle size. Also, the low heating value of the gas slightly decreased with increasing particle size. Xiao and co-workers [98] observed during a study of the effect of municipal solid waste (MSW) particle size in fixed bed pyrolysis and gasification that decreasing particle size produced more syngas and less tar and char. However, at temperatures between 800°C to 900°C, particle size had no effect on the reaction mechanism and only affected reaction intensity. According to Kirubakaran et al. as cited in Inayat et al. [99] a smaller biomass particle size enhanced heat transfer and increased the surface area during the gasification process, which led to high syngas production. Mani et al. [100] studied the influence of particle size (<60, 250, 638 and 925 μm) on wheat straw char gasification with CO_2. It was concluded that the char reactivity increased as particle size decreased. The results showed that 80% of the char was converted with fine powder particles (<60 μm), whereas under the same conditions at 800°C, the lowest conversion of 47% was achieved at large size particle.

In another investigation conducted by Hernández et al. [101], the gasification performance of different types of biomass (agricultural, forestry and industrial wastes) in an entrained flow gasifier was studied. The results showed that reducing biomass particle size improved gasification reactivity. According to them, to guarantee that chemical kinetics was the rate-controlling mechanism and that the heat was evenly distributed throughout the particle, sufficiently small particles were needed.

At temperatures ranging from 800 to 950°C, Gómez-Barea et al. [102] performed CO_2 gasification experiments of wood matter and found that increasing particle size had two

limitations on CO_2 gasification. The first was linked to diffusional resistances, a physical limitation resulting from temperature or CO_2 concentration gradients inside the char particles. The second was related to an inhibition effect, a chemical limitation resulting from the increased CO yield as the gasification reaction proceeded.

2.7.2 Char porosity and surface area

Among these features, pore structure and surface area of the char are considered two of its most crucial factors, due to the association of these characteristics with the available active sites within the solid particle, hence improving char reactivity [103]. However, there is no definitive agreement among studies about the impact of the specific surface area (SSA), pore size and pore volume on char gasification reactivity [104,105]. Generally speaking, porosity is a dimensionless quantity that refers to the empty spaces within the material, and it can be described as the ratio of the total pore volume to the volume of the particle or agglomerate [106]. According to the International Union of Pure and Applied Chemistry (IUPAC) [107], pores can be classified into three main groups (as shown in Figure 2.15) according to their size as follows:

i. Macropores denote pores with widths > 50 nm.
ii. Mesopores denote pores with widths between 2 and 50 nm.
iii. Micropores denote pores with widths < 2 nm.

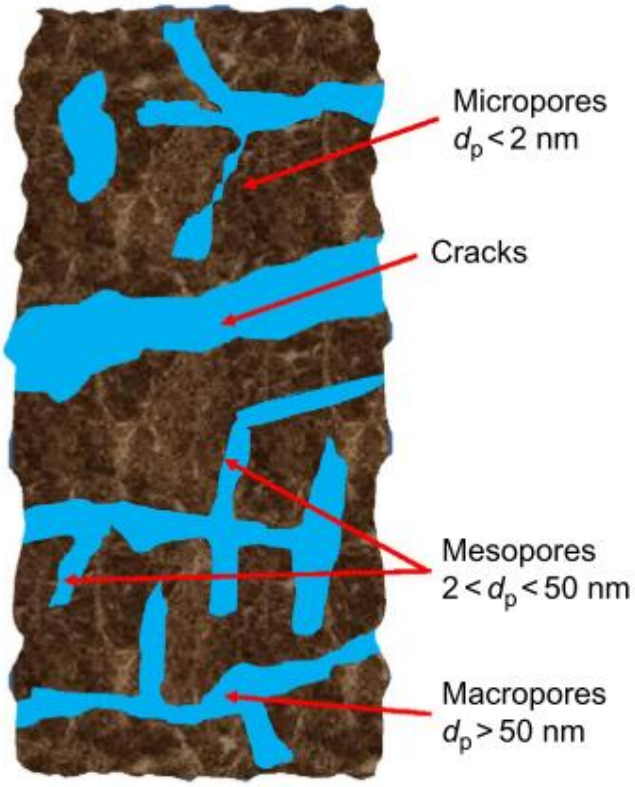

Figure 2.15: Schematic of porosity structure of coal, d_p denotes the pore diameter [82].

It has been reported that the reaction rate at a given temperature is influenced by the magnitude and accessibility of surface area for solid-gas reaction on the inside surfaces of the char particles [108]. Rollinson et al. [109] examined the char gasification reactivity of seven different types of biomass and observed that the reactivity increased as the specific surface area of the biomass increased. In the study of gasification reactivity of four types of coal conducted by Zou and coworkers [110], the specific surface area of demineralised coal char significantly increased with carbon conversion, resulting in a significant increase in the gasification reactivity. However, at high conversion, the specific surface areas of both raw char and HCl-wash char decreased. According to Roncancio et al. [96], there are several factors, such as active sites, char source, and mineral composition, that influence the specific surface area. Table 2.6 summarises the relationship between biomass and coal chars physical structure features and their reactivity from catalytic and non-catalytic CO_2 gasification studies. This table presents a

comparison of the effects of two main factors on char reactivity, namely, surface area and catalytic addition. It includes both non-catalytic chars and catalytic chars where metals such as Ni, Ca and K were added. A closer look at the reactivity order reveals that it does not follow surface area trends. For example, activated carbon (AC) with a surface area of 1055 m^2/g exhibited lower reactivity than coal char (KD), which had a much lower surface area of 314 m^2/g. However, after catalyst addition, the reactivity of both chars significantly increased, and AC became more reactive than KD. This suggests that catalytic minerals have a stronger influence on CO_2 gasification reactivity than surface area. Even when comparing non-catalysed chars with varying surface areas, the effect of this physical property was negligible. Gupta et al. [111] found that Eucalyptus char, which had the lowest surface area, was more reactive than Jackfruit char, which had the highest. In this PhD, it was therefore important to investigate the role of both structural and chemical properties in the reverse Boudouard reaction.

Table 2.6: Correlation between char physical properties and isothermal CO_2 gasification reactivity reported in literature.

Char type	Catalyst addition	S_{BET} (m^2/g)	Pore volume (cm^3/g)	Temperature (°C)	Reactivity* (min^{-1})	Gasification reactivity order of char	Reference
Sawdust char (SW)**	Non-catalytic	391.17	9.74	700,750 and 800	Does not reach 50% of conversion	SW-char < SW_{KCe}-char < SW_{KFe} -char < SW_{KNi}-char< SW_{KCo} -char	Jiao et al.[112]
	5%K-5%Ni	39.67	0.158		0.007, 0.020 and 0.071		
	5%K-5%Fe	43.19	0.199		0.006, 0.018 and 0.058		
	5%K-5%Co	35.71	0.087		0.012,0.032 and 0.095		
	5%K-5%Ce	45.92	0.323		0.005,0.017 and 0.058		
Low rank coal char (KD)	Non-catalytic	314	0.11	850	0.023	AC-char < KD-char < KD_{Ca}-char < AC_K-char	Zang et al.[113]
	2.5%Ca	308	0.11		0.050		
Coal based activated carbon char (AC)	Non-catalytic	1055	0.63		0.002		
	2.5%K	1043	0.62		0.107		
Jackfruit char	Non-catalytic	80.5	-	800	-	Jackfruit char< Mango char< Raintree char< Eucalyptus char***	Gupta et al.[111]
Mango char		37.4	-		-		
Raintree char		2.8	-		-		
Eucalyptus char		1.9	-		-		

Table 2.6 (continued): Correlation between char physical properties and isothermal CO_2 gasification reactivity reported in literature.

Char type	Catalyst addition	SBET (m^2/g)	Pore volume (cm3/g)	Temperature (°C)	Reactivity* (min^{-1})	Gasification reactivity order of char	Reference
Peanut shell char (PS)	Non-catalytic	22.56	0.0252	850,900,950 and 1000	0.035, 0.106, 0.2 and 0.349	PSD-char < BS-char < RL-char < WS-char < MC-char < PS-char	Wang et al.[114]
Maize cob char (MC)		4.31	0.0097		0.036, 0.086, 0.16 and 0.231		
Wheat straw char (WS)		29.56	0.0342		0.031, 0.076, 0.151 and 0.259		
Rice lemma char (RL)		9.62	0.0182		0.026, 0.067, 0.14 and 0.212		
Pine sawdust char (PSD)		56.38	0.0485		0.019, 0.033, 0.062 and 0.11		
Bamboo sawdust char (BS)		31.16	0.0241		0.019, 0.041, 0.096 and 0.163		
Charcoal char (CC)	Non-catalytic	14.31	0.0054	977,1077 and 1177	0.05, 0.054 and 0.095	CB-char < TC-char < CB	Htet et al.[115]
Thermal coal char (TC)		22.1	0.0167		0.036, 0.049 and 0.069		
Carbon black (CB)		9.89	0.0307		0.035, 0.046 and 0.052		

* Recalculated reactivity index values, ** Reactivity measured based on 99% of char conversion and on 50% for the other chars.*** Reactivity was evaluated based on conversion versus time curves.

2.7.3 Catalytic effect of ash mineral content

Biomass is composed of three main organic components: hemicellulose (15-40 wt.%), cellulose (25-50 wt.%), and lignin (10-40 wt.%), as well as extractives (0-15 wt.%) and trace quantities of inorganic mineral species [116]. These mineral compounds consist mostly of alkali (e.g. K and Na) and alkaline earth metals (e.g. Ca and Mg), collectively known as AAEMs, as well as other transition metals (e.g. Al, Fe, Si). The mineral species play an important role in CO_2 gasification of carbonaceous materials. Hence, the mineral content in the feedstock is considered to have a catalytic effect on the reaction rate [117]. In the study conducted by Li et al. [117], they found that alkali and alkaline earth metals were the dominant factor in increasing the gasification reactivity of the coal char prepared from co-pyrolysis at 600 and 900°C. They separated coal char from various biochar–coal char mixtures to evaluate reactivity and structure and concluded that AAEMs had a significant influence on char reactivity when compared to microcrystalline structural parameters. Recently, Li et al. [118], also observed the effect of AAEMs on their investigation of the reactivity of separated coal char from the biomass and coal chars blending during co-gasification which led them to propose a relational equation to predict char reactivity as shown in the following equation:

$$R_{0.5} = 0.07164AI - 0.9432N + 5.7514 \quad (2.4)$$

Where $R_{0.5}, AI$, N represent the reactivity index in min^{-1}, alkali index and the stacking layer number, respectively. The alkali index AI can be calculated using Equation 2.6. The stacking layer number N , which represents the number of stacked graphene like carbon, layers is evaluated from the XRD parameters, the stacking height L_c and interlayer spacing d_{002} using following expression:

$$N = \frac{L_c}{d_{002}} + 1 \quad (2.5)$$

However, the formation of alkali silicates due to the reaction between alkali metals and SiO_2 may cause agglomeration issues, which can affect gasifier operation [119]. To investigate the influence of mineral matter in the ash on char reactivity, the alkali index was established by Sakawa et al. [120]. It is defined as the ratio of the mass fractions of AAEM compounds to the acid compounds in the ash multiplied by the ash content in the carbon source. It can be measured using the following formula [121]:

$$Alkali\ Index\ (AI) = Ash\ (\%) \times \frac{Fe_2O_3 + CaO\ + K_2O\ +\ MgO\ +\ Na_2O}{Al_2O_3 + P_2O_5 + SiO_2} \quad (2.6)$$

Researchers used the leaching method to isolate the effect of inorganic elements on CO_2 gasification reactivity. This method, also known as demineralisation, aims to remove specific catalytic elements such as potassium (K) and calcium (Ca) from biochars to evaluate their role in the gasification process. For example, diluted acetic acid leaching was used on different biomass samples by Phounglamcheik et al. [90]. The results indicated that K content significantly decreased leading to a substantial decrease in gasification reactivity. In another study, Ca and K were removed from spruce wood using acid leaching and then reintroduced into the washed sample with different concentrations using ion-exchange [122]. They found that the reaction rate increased proportionally with the concentrations of Ca and K.

2.7.4 Active sites-CO_2 chemisorption

In the gasification of chars, active sites are considered to be a rate-determining property [96]. Carbon active sites are related to the edge carbon atoms, the carbon atoms bonded to heteroatoms and nascent sites attached to aromatic clusters which are chemically

unstable [123]. Obviously, the mechanism of CO_2 gasification of char as mentioned in Section 2.5.3, indicates that the number of carbon active sites is an important factor for char reactivity. There is no common approach for determining the number of active sites. Several studies have indicated that CO_2 chemisorption is a characteristic indicator of the active sites present in the char.

Molina et al. [124] carried out CO_2 chemisorption experiments at 300°C using chars produced from fresh coal, demineralised coal, and K, Fe-loaded coal. They found that strong CO_2 chemisorption (C_{str}) of demineralised coal does not exist, and the total CO_2 chemisorption is almost similar to the weak CO_2 chemisorption (C_{wea}) for the same char sample. As a result, they concluded that C_{str} is related to the presence of catalytic active sites (inorganic matter) and C_{wea} associated with the carbon active sites (organic components) of the char. In another similar investigation undertaken by Xu et al. [123], the CO_2 chemisorption measurements were obtained by Micro-TGA for coal chars which were prepared from fast and slow pyrolysis processes. Their results show that C_{str} and C_{wea} decreased at high pyrolysis temperature and slower heating due to the reduction of active mineral matter in the chars. Additionally, they also found that the char reactivity correlates better with CO_2 chemisorption characteristics than with surface area. In this thesis, CO_2 chemisorption analysis was adopted to reveal any correlation between char surface chemistry and gasification reactivity.

2.8 Influence of operation conditions and char pretreatment

2.8.1 Char pretreatment

Another important factor affecting CO_2 gasification reactivity is char thermal history, which vary depending on pretreatment conditions. Biomass and coal chars can be produced from thermal conversion processes such as pyrolysis, hydrothermal carbonisation and torrefaction. These treatment methods alter the physical structure and chemical composition of the remaining carbonaceous char. Therefore, describing the

variation in gasification reactivity based on char properties is complex as these properties depend on the char production conditions [125]. Influence of pyrolysis and hydrothermal are discussed in the following sections.

2.8.1.1 Pyrolysis conditions

Char gasification reactivity is commonly linked to pyrolysis conditions used to convert raw carbon materials into chars such as temperature, heating rate and holding time. Increasing pyrolysis temperatures generate char with a more stable and graphitised carbon structure compared to those obtained at lower temperatures, which reduces gasification reactivity in CO_2 [126]. Similarly, longer residence time during pyrolysis was found to have a negative impact on gasification reactivity [127]. This is because extending pyrolysis time, especially at high temperatures (as shown in Figure 2.16) allows for the formation of a more graphitic carbon structure which is less reactive [128]. Also, slow heating rate at atmospheric pressure typically yields more reactive char than char produced at high pressure conditions [77]. There are many studies in the literature investigating CO_2 gasification reactivity to assess heating rate influence. Under non-isothermal conditions, increasing the heating rate positively affects char reactivity [129–131]. However, Liu et al. [132] found that carbon conversion in isothermal gasification at 950°C was not affected when heating rate exceeded 50°C/min. Biochar produced from pyrolysis under different gaseous flow has been also investigated in literature. Tian et al. [129] prepared Miscanthus chars in a tube furnace under different gas atmospheres including N_2, He and CO_2 at temperatures ranging from 600°C to 1000°C. The proximate analysis showed that chars produced under N_2 had a significantly higher carbon content whereas CO_2-chars exhibited lower carbon content at 1000°C. N_2-chars yield were higher than that of CO_2 due to the decomposition of oxygen-containing functionals groups which leads to the formation of stable aromatic ring compounds. They found that gasification reactivity of He-chars was higher than that of both N_2 and CO_2-chars. According to the authors, the higher value of K content led to this reactivity variation. In addition, the

specific surface area was the dominant factor influencing the gasification reactivity for CO2-chars. Pyrolysis conditions strongly influence gasification reactivity. Therefore, in this work, a standardised pyrolysis step was applied before introducing CO_2 to ensure a consistent baseline for reactivity comparison. Also, conducting isothermal and non-isothermal gasification allowed to produce chars with different structural properties.

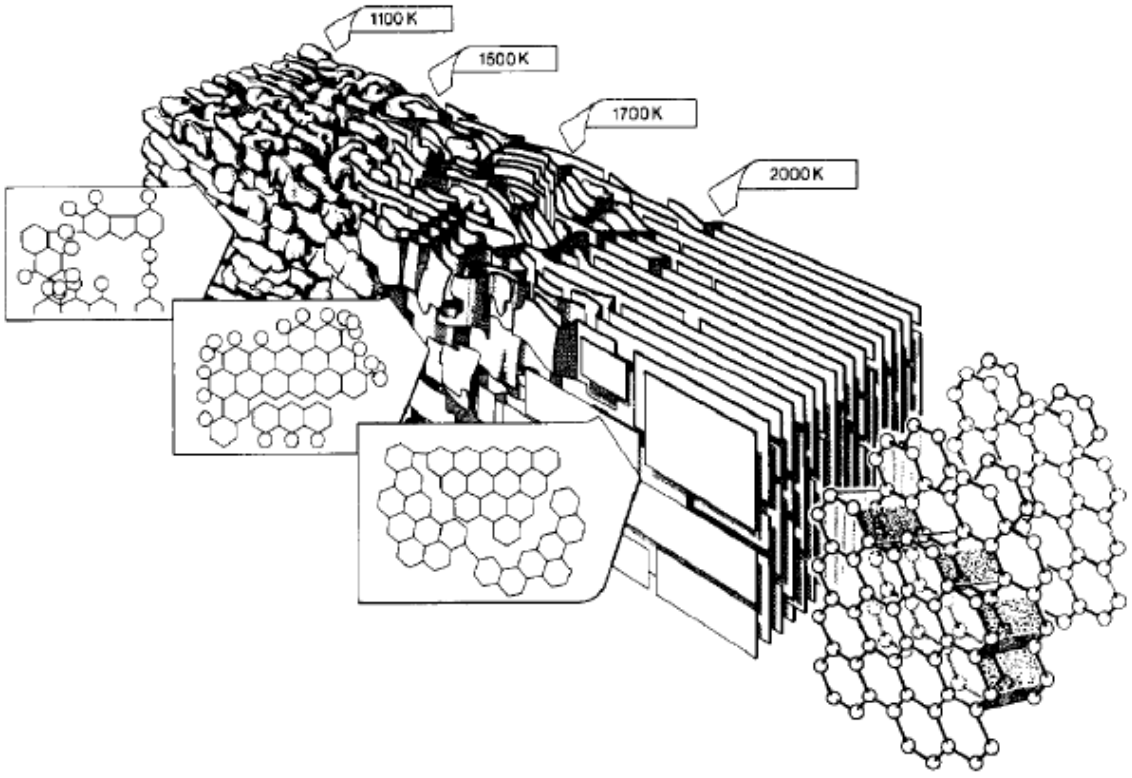

Figure 2.16: Schematic of carbon structure transformation from amorphous carbon to more organised form (crystalline graphite structure) due to thermal treatment [245].

2.8.1.2 Hydrothermal carbonisation

One attractive method to improve biofuel features is hydrothermal carbonisation (HTC) or wet torrefaction process [133]. It is a thermochemical conversion technology in which wet biomass feedstocks are converted to a solid product, known as hydrochar, at typical temperatures ranging between 150 and 300°C [134] in a pressurised water conditions [135]. Figure 2.17 presents an overview of HTC process and hydrochar utilising for different applications. Higher HTC temperatures result in a reduction of hydrochar performance in CO_2 gasification. This phenomenon is attributed to different changes in hydrochar parameters as reported in the literature. In a study carried out by Yuliansyah et al. [136], the influence of HTC on CO_2 gasification reactivity of blended corn cob and coconut shell was investigated at temperatures ranging from 200°C to 270°C. They related the decrease in gasification reactivity to the reduction in volatile matter, moisture content, and potassium content of the hydrochars as carbonization temperatures increased. Ulbrich et al. [137] noted that CO_2 gasification reactivity of brewers' spent grains hydrochars decreased with increasing HTC temperature and residence time ranged between 180-280°C and 0.5-12 h, respectively. According to their analysis, the lower hydrochar reactivity was attributed to higher HTC reaction severity, which led to the formation of more fixed carbon in the hydrochar. It has also been reported that increasing HTC temperature can enhance microcrystalline carbon structures formation and consequently reduces CO_2 gasification reactivity [138]. In contrast to these studies, Lahijani et al. [133] demonstrated that rubber seed shell-derived hydrochar produced at 240°C was more reactive than those obtained at lower carbonisation temperatures (160°C and 200°C).

Limited research studies have considered utilising hydrochar as a potential fuel for gasification process. This PhD thesis will investigate the use of hydrochar material and compare it with pyrolytic chars under CO_2 gasification tests.

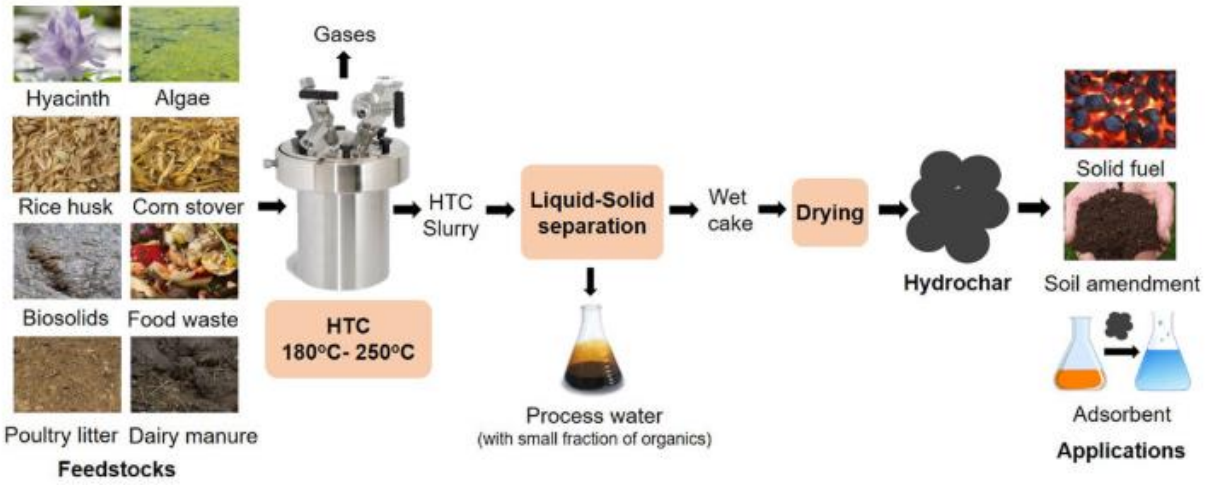

Figure 2.17: Diagram showing HTC process of biomass waste and hydrochar utilisation [246].

2.8.2 Gasification temperature

In the process of char conversion into synthesis gas, char gasification is considered to be the slowest step [105]. The most important parameter that influences the gasification reactivity of char and governs reaction rate is gasification temperature [139,140]. Gasification reactions involve physical and chemical steps as shown in Section 2.5, only the interaction between CO_2 and char surface relates to the chemistry of the reverse Boudouard reaction [105]. Char gasification temperature has a notable impact on the rate of the reaction and its controlling mechanism as illustrated in Arrhenius plot in Figure 2.18. The Arrhenius plot can be divided into three regimes to elucidate the effects of mass transport phenomena on both reactant gases and product gases to highlight the limitations imposed by diffusion processes [141]. In this plot, the slope which represents the relationship between logarithm of the reaction rate and the inverse of the reaction

temperature determines kinetic parameters and hence the transition between the three regimes.

McEnaney [141], Tremel [125] and Bikane [142] fundamentally explained temperature effect on the reaction mechanism under each kinetic regime. In the chemical reaction zone (Regime I), at low temperatures, reactant gas concentration is distributed uniformly within char particle similar to bulk gas concentration. Typically, the reaction is slow and considered as the rate-limiting step with char surface chemistry controls the overall reaction rate. Most of the kinetic studies conducted under Regime I conditions because the apparent reaction rate is the same as the intrinsic reactivity [139]. The reaction rate proportionally increases as the temperature rises, this leads to a transition from Regime I to pore diffusion control, denoted as Regime II. The concentration of reactant gas gradually decreases within char particle until it reaches zero at the centre. This happens because the rate of gas supplied through the char particle becomes insufficient as the reaction rate increases and inhibiting effect of the desorbed product gas [141]. With additional temperature increases, the reaction rate is controlled by the diffusion of the reactant gas from the bulk gas phase to the external char particle surface. Known as external mass transfer (Regime III), the reactant gas does not reach the inner particle surfaces, and the reaction rapidly occurs on the outer surface of the particle where its concentration is zero. An effective way to overcome the external mass transfer limitations is increasing the reactant gas flow rate [143,144].

In Arrhenius plot, the reaction rate can be affected by two mechanisms due to the transition between the regimes [125]. For CO_2 gasification of char, temperature ranges of each regime vary in literature and primarily depend on char properties and experimental conditions [139]. A common approach to identify transitions between regimes involves conducting gasification tests at different temperatures. Hence, temperature significantly accelerates the reaction in Regime I but this influence diminishes as the reaction moves to other regimes [145]. Shaofeng et al. [146] suggested that CO_2-char reaction is chemically controlled at temperature lower than 1150°C while pore diffusion becomes the dominant mechanism above this temperature.

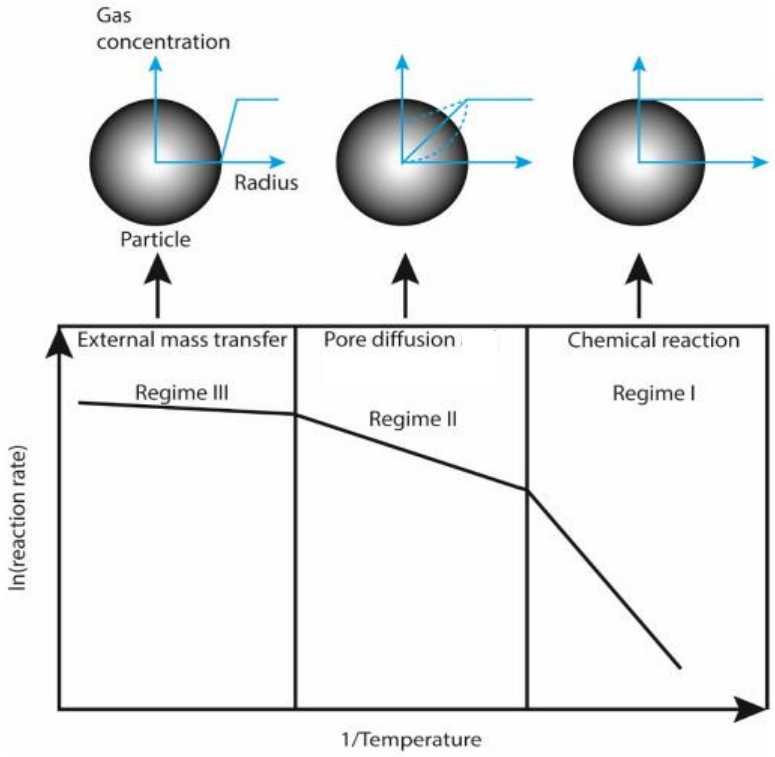

Figure 2.18: An illustration of three reaction zones in gasification process [142].

Table 2.7 provides a summary of some kinetic works and at which regime the reactions occurred. As shown, most studies reported that at temperatures below 950°C the reaction was chemically controlled, while increasing temperature beyond 1000°C often shifted the reaction to pore diffusion or mixed regimes. However, this trend is not consistent and depends on char properties; for example, Sean Connolly et al. [143] observed external mass transfer limitations even at temperatures below 815°C. Obviously, temperature has a clear role in keeping the reaction under chemical control regime by conducting the gasification under low temperature. However, this is not the case in the industrial process where the process undergoes diffusional constraints [141], further work should be conducted to optimise the process at high temperatures (>850°C).

Table 2.7: Variation of kinetic regimes of CO_2 gasification of char from literature.

Reference	Sample	Particle size (μm)	Temperature (°C)	Apparatus*	Kinetic regime
Kajitani et al.[147]	Bituminous coal chars	43.9-44.1	1100-1200	PDTF	Chemical reaction
Shahabuddin et al. [139]	Bituminous coal char	20–38	800-1100	Micro-TGA	Chemical reaction
Yuan et al.[148]	Rice straw, chinar leaves and pine sawdust chars	56-180	850-950	Macro-TGA	Chemical reaction
Yuan et al. [148]	Rice straw, chinar leaves and pine sawdust chars	56-180	950-1050	Macro-TGA	Pore diffusion
Tanner et al. [145]	Brown coal chars	38-106	650-900	Micro-TGA	Chemical reaction
Tanner et al. [145]	Brown coal chars	38-106	1000-1100	Micro-TGA	Pore diffusion
Htet et al.[115]	Charcoal, thermal coal char and carbon black	63-90	1250-1450	Micro-TGA	Mixed control regime (chemical and pore diffusion)
Sean Connolly et al. [143]	black liquor char	N/A	675-815	Fixed bed	External mass transfer

* PDTF is pressurised drop tube furnace.

On the other hand, gasification temperature has an impact on both the composition of the produced gas and its heating value [149]. A recent study by Ofuani et al. [150] found that elevating the gasification temperature from 700°C to 900°C significantly increased the production of carbon monoxide. For instance, when injecting the reactor with a 5L/min gas mixture containing 15% of CO_2 to gasifiy Kingsford biochar, the CO concentrations after 5 minutes were 3.2%, 10%, and 19.3% at 700°C, 800°C and 900°C, respectively. Further increasing the inlet CO_2 concentration to 30% at these temperatures increased the CO yields to 4.6%, 17.2%, and 26%, as depicted in Figure 2.19.

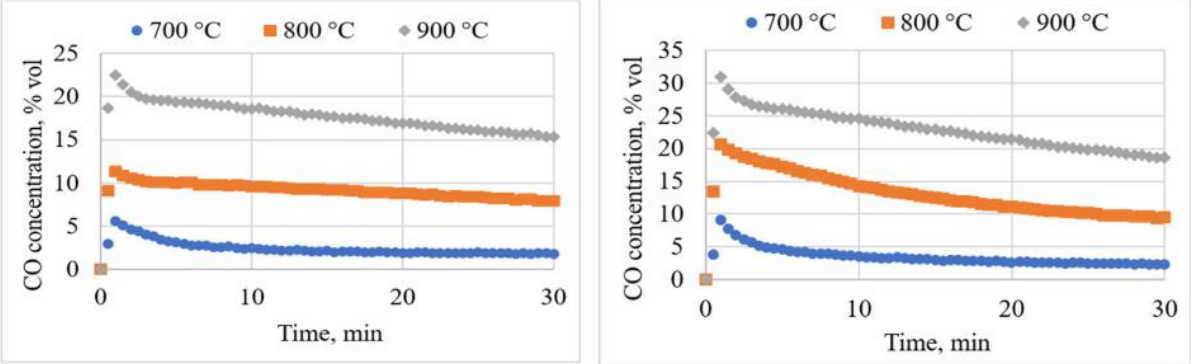

Figure 2.19: Influence of gasification temperature on CO yield using different CO_2 concentration (a) 15% CO_2 (b) 30% CO_2 [150].

2.9 Chapter summary

This chapter has explored the existing literature on thermochemical gasification technology for converting carbonaceous materials into value-added products using CO_2 as the gasifying agent. It briefly described the main gasification steps, the pyrolysis process for char production and the homogenous and heterogeneous reactions involved in gasification. Different types of fixed bed gasifiers were examined for their features and operational characteristics.

The fundamentals of thermogravimetric analysis were discussed and its use in studying different thermochemical processes was highlighted. It was found that the main drawback of the conventional Micro-TGA is that only small sample sizes can be used. To address this, different Macro-TGA configurations whether self-built or commercially designed were reviewed. Macro-TGA is representative of industrial processes and offers real examination of industrial conditions at high temperature and larger mass sizes.

In the context of the reverse Boudouard reactivity, several factors influencing CO_2 gasification reactivity were identified. These include material properties such as particle size, porosity and surface area, ash mineral composition and surface-active sites. The reviewed works showed that the reaction is also affected by the pretreatment conditions

at which the char was produced and reaction temperature. The reverse Boudouard reaction can occur under one of three kinetic regimes, with the chemical reaction-controlled regime (Regime I) being favourable at lower temperatures, while the diffusion-controlled regime (Regime II) is most common in industrial processes

The conclusions from the existing literature in this field suggest a lack of clarity regarding the role of surface area on enhancing the reaction and whether the char surface chemistry is controlling the process. To address this, this study will investigate the role of char physical and chemical properties in CO_2 gasification reactivity. This will be conducted using different analytical techniques to reveal the potential correlation with the reactivity. It will also study the impact of char surface area on the reaction performance by developing and using a novel Macro-TGA.

Chapter 3 Material characterisation and analytical techniques: physical and chemical properties

3.1 Introduction

This chapter details the material samples used in this thesis as well as the analytical techniques of physical and chemical property characterisation. Char samples were prepared and treated in accordance with British Standards to provide a solid base of materials characterisation. A robust approach was used to identify char sample physical and chemical properties, although there were some limitations associated with obtaining the materials and the availability of the analytical instruments in Cardiff University. The following sections illustrate the pretreatment of char samples including drying, particle size classification, proximate and ultimate analysis, carbon and sulphur analysis and a demineralisation process. This chapter also explains the methodology used to characterise physical and chemical properties of biomass char, hydrochar and coal char samples using a variety of laboratory techniques to measure properties including mineral content, porosity, microcrystalline structure, morphology, surface elements and surface functional groups. These were characterised by X-ray Fluorescence (XRF), Inductively coupled plasma optical emission spectroscopy (ICP-OES) analysis, nitrogen adsorption analysis, X-ray diffraction (XRD), Scanning electron microscopy coupled with energy dispersive spectroscopy (SEM-EDS) and X-ray photoelectron spectroscopy (XPS). Furthermore, Thermogravimetric analysis (TGA) was used to study the gasification reactivity of char samples under a CO_2 atmosphere. The CO_2 chemisorption measurements of the char samples were also examined to measure both organic and inorganic active sites using the TGA.

3.2 Material selection

In order to achieve a beneficial comparison to gain a comprehensive understanding of both carbonaceous materials and the thermochemical processes examined in this thesis, char samples were selected from a variety of production methods in order to make a balanced comparison. In this study, a range of commercially supplied carbonaceous materials with different properties were chosen for the experiments, these include biochars, coal char and hydrothermally carbonised char (hydrochar). Four were biomass chars, two from recovered wood and two from wastewater sludge, both biochar types were produced through pyrolysis. Because these were commercially supplied samples the specific pyrolysis conditions were subject to confidentiality. The coal char was made using a drop tube furnace (DTF) at 1100°C at a residence time of 35 ms as discussed in the following section. Hydrochar was produced from high plastic content anaerobic digestion (AD) fibre in a hydrothermal carbonisation plant [151]. In the hydrothermal carbonisation process (HTC), the solid residue from digested food waste was subjected to high temperature in an aqueous environment at 200°C to produce the hydrochar. The char samples were labelled as BC1 and BC2 for wood chars; BC3 and BC4 for sewage sludge chars; CC for coal char and HC for hydrochar.

3.3 Charing coal

In this study, coal char was produced using a drop tube furnace (DTF) made at Severn Thermal Solution, Dursley, Gloucester. Figure 3.2 shows a schematic diagram of the drop tube furnace used in this experiment, whereas Figure 3.1 presents a photograph of the same furnace. Prior to the use of the DTF, the furnace temperature was elevated to the desired temperature of 1100°C. After preheating, 10 g of the dried pulverised coal sample was weighed to the nearest 0.1 g. Consequently, the sample was introduced to the top of DTF via the vibrating sample feeder using a funnel at feeding rate of 30 g/h. The charged coal sample was then carried along the DTF reactor by air flow of 20 L/min in

Laminar flow. The produced coal char was then collected in a sample collector located at the bottom of the DTF. The exhaust flow was then sent through the filter, which effectively gathered a combination of tar and fine particles, prior to being transmitted to the DTF exhaust via the laboratory extraction system. The DTF operation and coal char production were carried out by Dr Julian Steer.

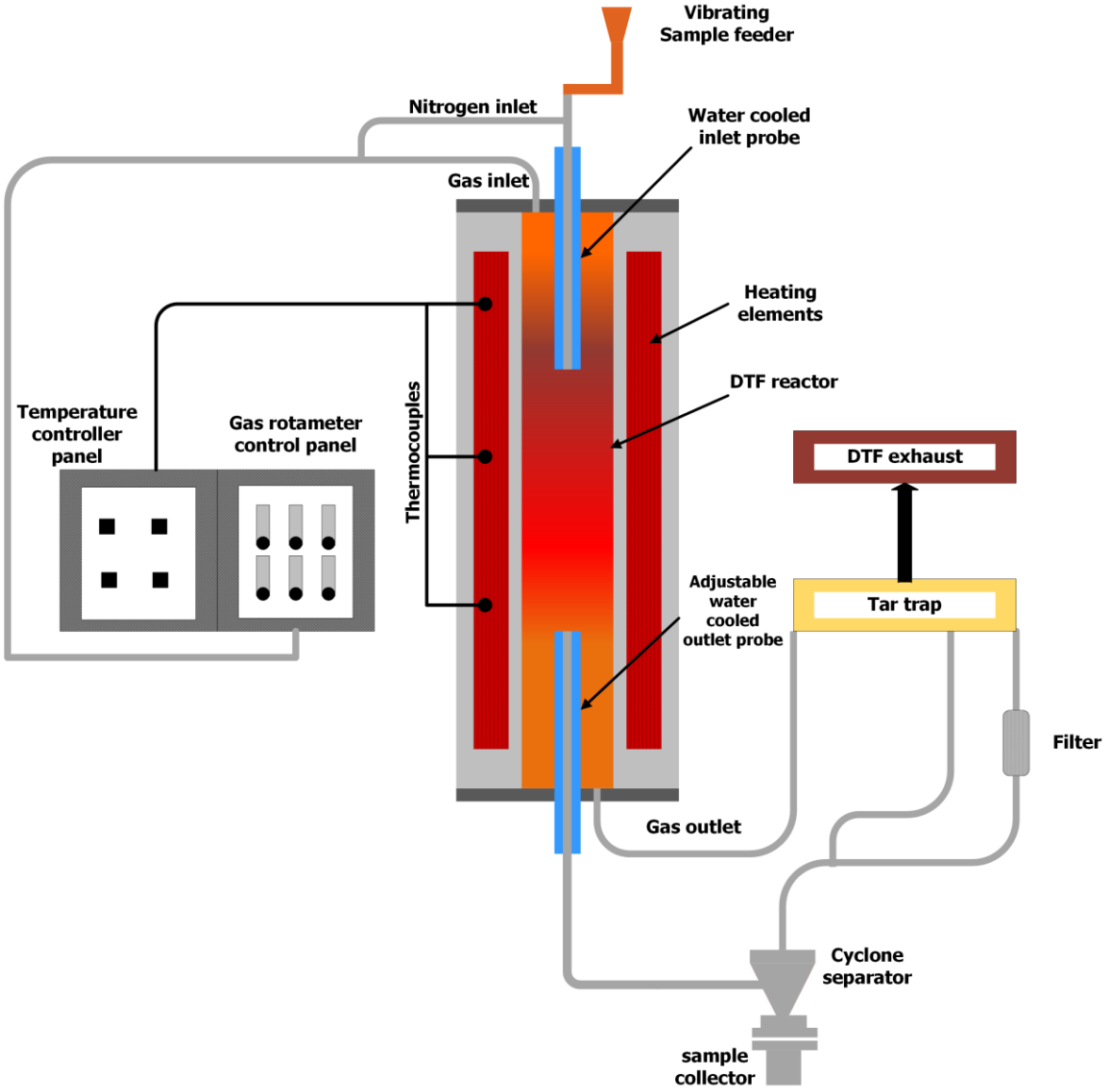

Figure 3.1: Drop tube furnace (DTF) in Cardiff University School of engineering.

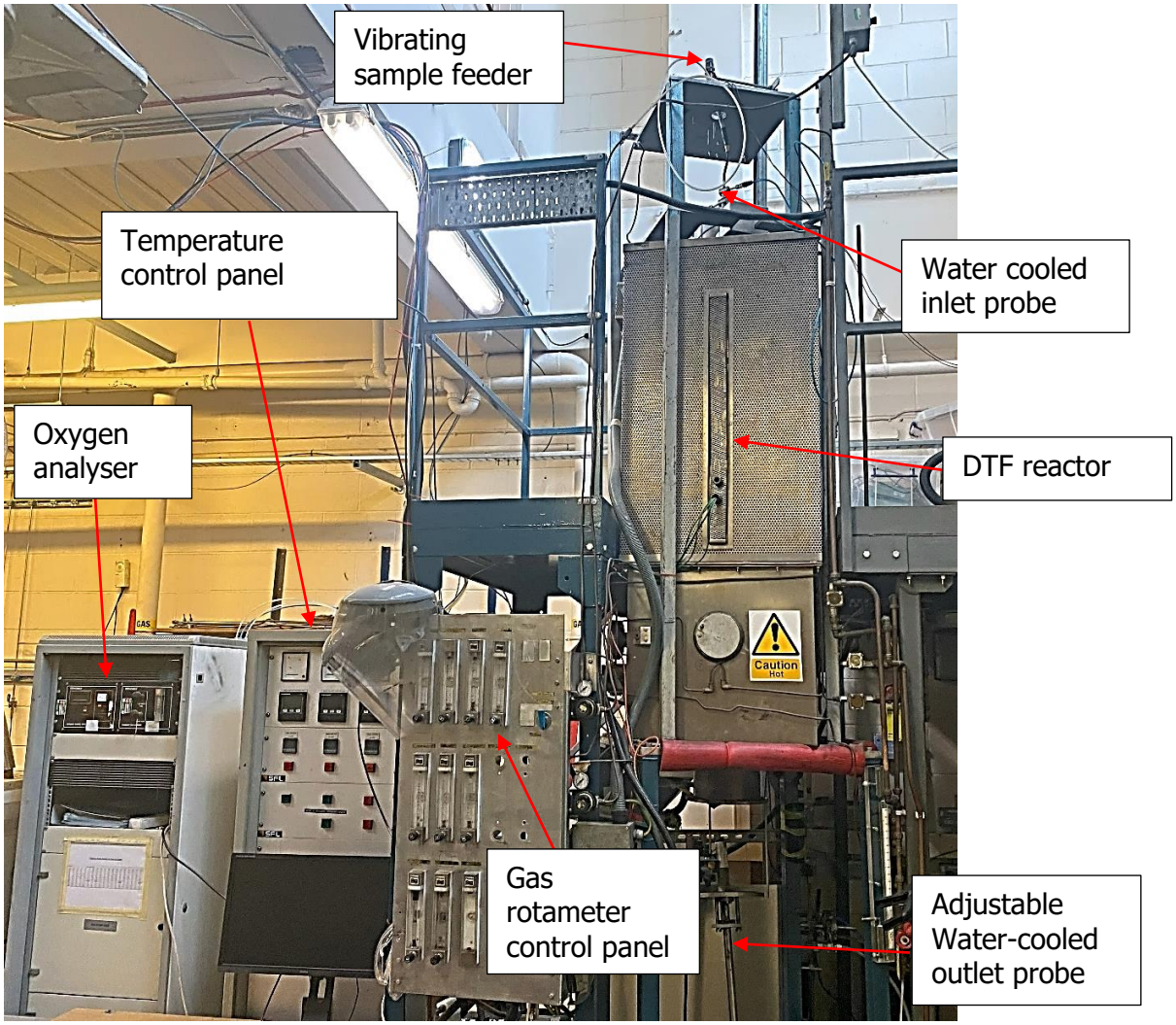

Figure 3.2: Schematic diagram of the drop tube furnace.

3.4 Char sample characterisation approach

Figure 3.3 illustrates the approach taken in this thesis to investigate char sample properties to enhance insight into the behaviour of the materials and investigate potential

correlations to the measured CO_2 gasification performance.

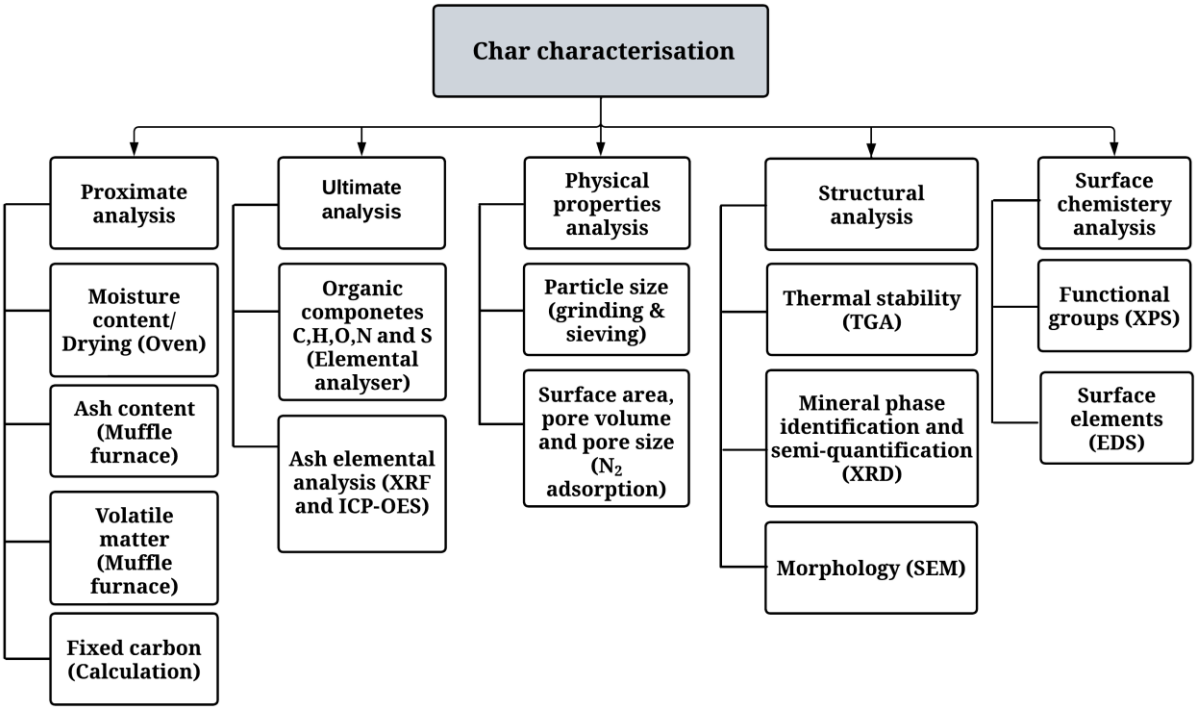

Figure 3.3: Simplified flowchart showing methodology of biochar, hydrochar and coal char characterisation in this study.

3.5 Char sample pretreatment

3.5.1 Char sample drying

All char samples were fully air-dried prior to any testing in this thesis. The drying procedure of char samples was carried out based on BS ISO 11722-2013 [152]. The moisture removal from the samples was performed using a Heraeus T6060 oven, as shown in Figure 3.4.

The drying method was as follows:

1. The drying oven was switched on and set to the desired temperature (105°C).

2. 100 g of 'as received' char was weighed to the nearest 0.1 g and evenly distributed in a clean dry watch glass dish (100 mm diameter) using a plastic scoop.
3. The loaded dish was placed inside the preheated oven for one hour and dried to a constant weight.
4. After complete drying, the sample was taken out from the oven and stored in labelled resealable polythene bag in a desiccator to be used for further analysis.

Figure 3.4: Drying oven, Heraeus T6060 oven.

3.5.2 Particle size classification (grinding and sieving)

The main purpose of standardising the particle size of char samples was to eliminate the influence of particle size variation among the samples, which could affect the precision of

the comparison in different tests throughout this thesis. The correlation between char particle size and CO_2 gasification reactivity was well established in the literature, so this relationship will not be investigated in the present work. However, Boudouard reaction rate was reported to be chemically controlled for particle sizes <650 μm [1], therefore particle specification of 100% less than 250 μm was chosen.

The dried char samples (as discussed in the previous section) were classified according to the standard dry sieving protocol BS ISO 1953:2015 [2].

A TEMA bowl mill was used to grind the samples, as shown in Figure 3.5. The following procedures were undertaken to obtain the desired particle size specification:

1. The dry char sample was loaded into the bowl and the rotating disc was placed on the top of the sample. The bowl was covered by the lid and it was then fitted into TEMA bowl mill's rotator.
2. The TEMA bowl mill was switched on once the safety lid was closed.
3. The sample was ground for 10 seconds before being removed from the milling machine.
4. The TEMA bowl mill was switched off and the pulverised sample was dispersed into a standard sieve with a mesh size of 250 μm. This sieve was equipped with a top lid and a bottom collecting dish.
5. The sieve was then put into an automated shaker machine, as shown in Figure 3.6, and ground particles were left to pass through the mesh for 20 seconds.
6. The Sieve was removed from the shaker machine and the unpassed particles were returned into the TEMA bowl mill for another grinding and sieving cycle. The desired pulverised size specification (100%< size 250 μm) was achieved by repeating this procedure as required.

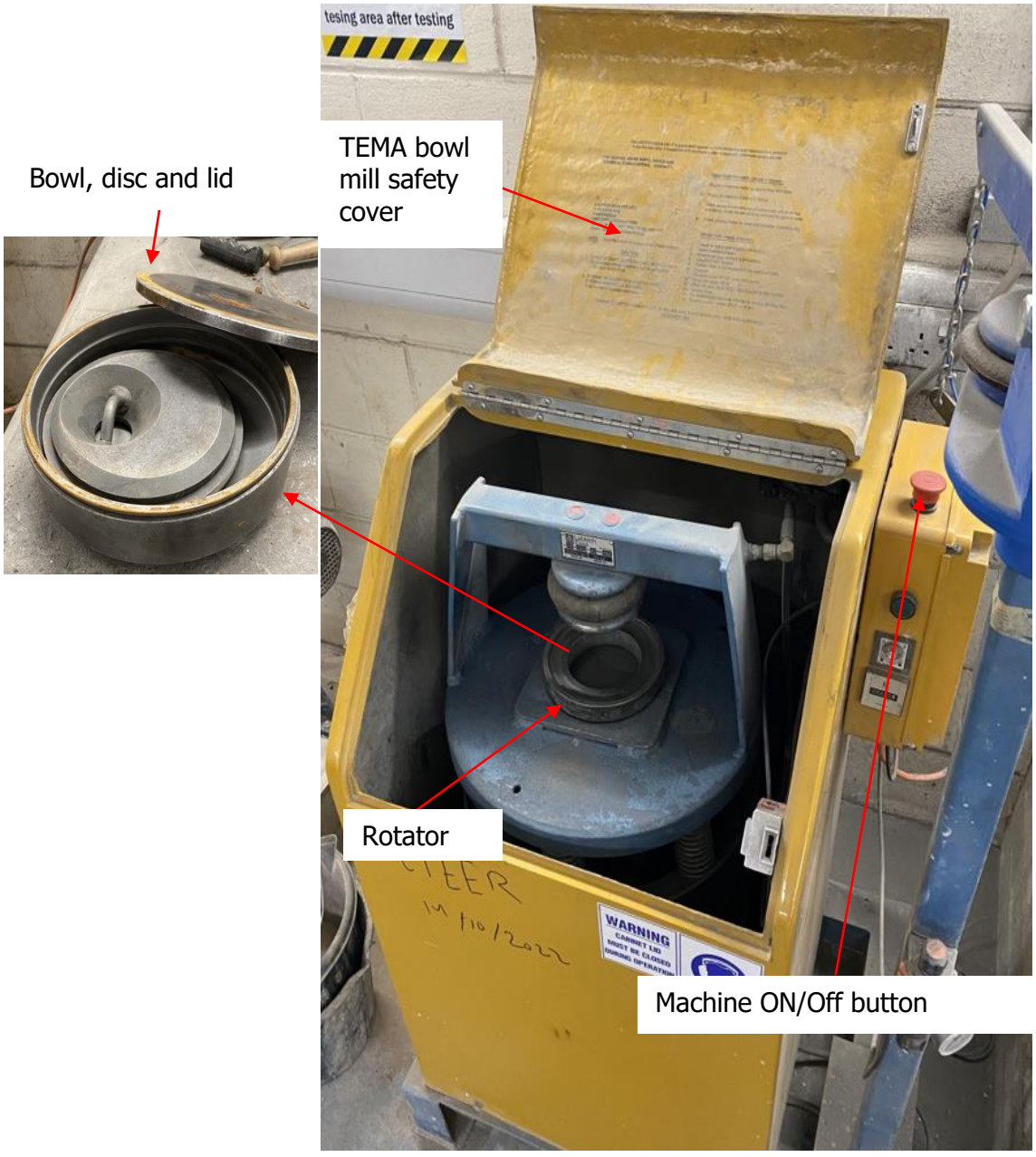

Figure 3.5: Grinding machine, TEMA bowl mill.

Figure 3.6: Automated shacking machine.

3.5.3 Pelletisation of char sample

The aim of producing pellets is to obtain samples with different surface areas to use in the constructed gasifier (described in Chapter 4). One biochar sample (BC1) was selected for the pelleting process. Approximately 50 g of ground and sieved char was mixed with corn flour binder and water at 15% and 20% (w/w), respectively. The mixture was stirred thoroughly to ensure uniform binder and moisture distribution. Two stainless-steel pressing dies with inner diameters of 12 mm and 16 mm were manufactured in the school's mechanical workshop to produce the pellets, as shown in Figure 3.7 (b). In each

run, the die was filled with a biochar mixture to the top, manually compressed using the top pressing rod, and refilled until it was full. A Clarke Strong-Arm hydraulic press machine with 15 tonne compression force was used to compact the wet mixture, as shown in Figure 3.7 (a). The die was placed on the pressing bed, and the pump handle was moved down until the maximum load was reached. The pressure was held for 10-15 seconds to reduce voids between mixture particles. After that, the handle was released and secured to remove the die safely, and the cylindrical pellet was gently ejected.

The pellets and remaining mixture were oven-dried at 105°C for 24 hours to remove the moisture completely. Then, they were stored in labelled resealable storage bottles in a

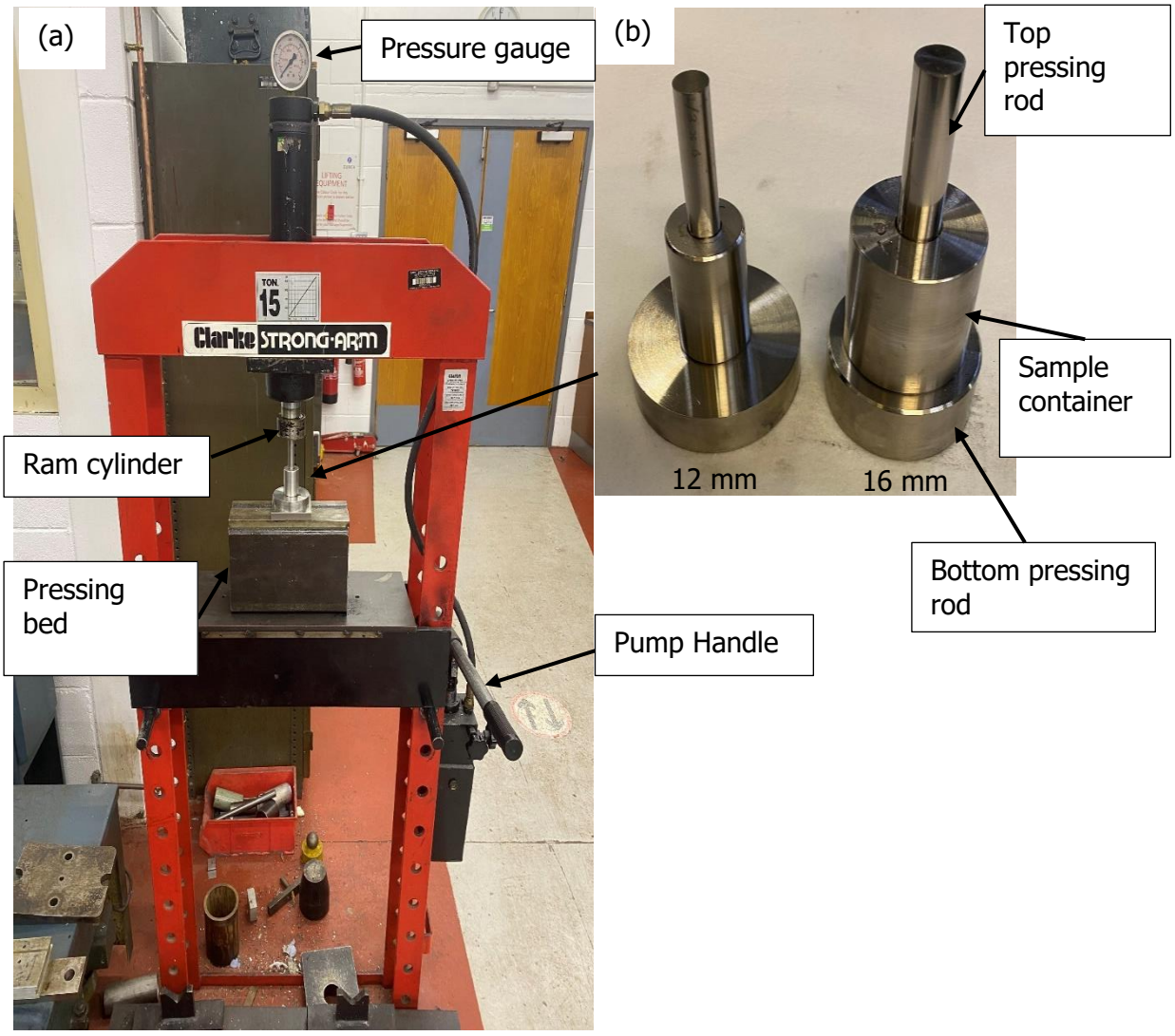

Figure 3.7: Pelletisation process system: (a) 15 tonne hydraulic press machine and (b) pellet pressing dies.

desiccator to be used for Macro-TGA gasification experiments. The samples were labelled as Mixture P for mixture powder, Pellet A for 12 mm diameter and Pellet B for 16 mm diameter. Figure 3.8 shows the dried mixture and the resulting pellet samples.

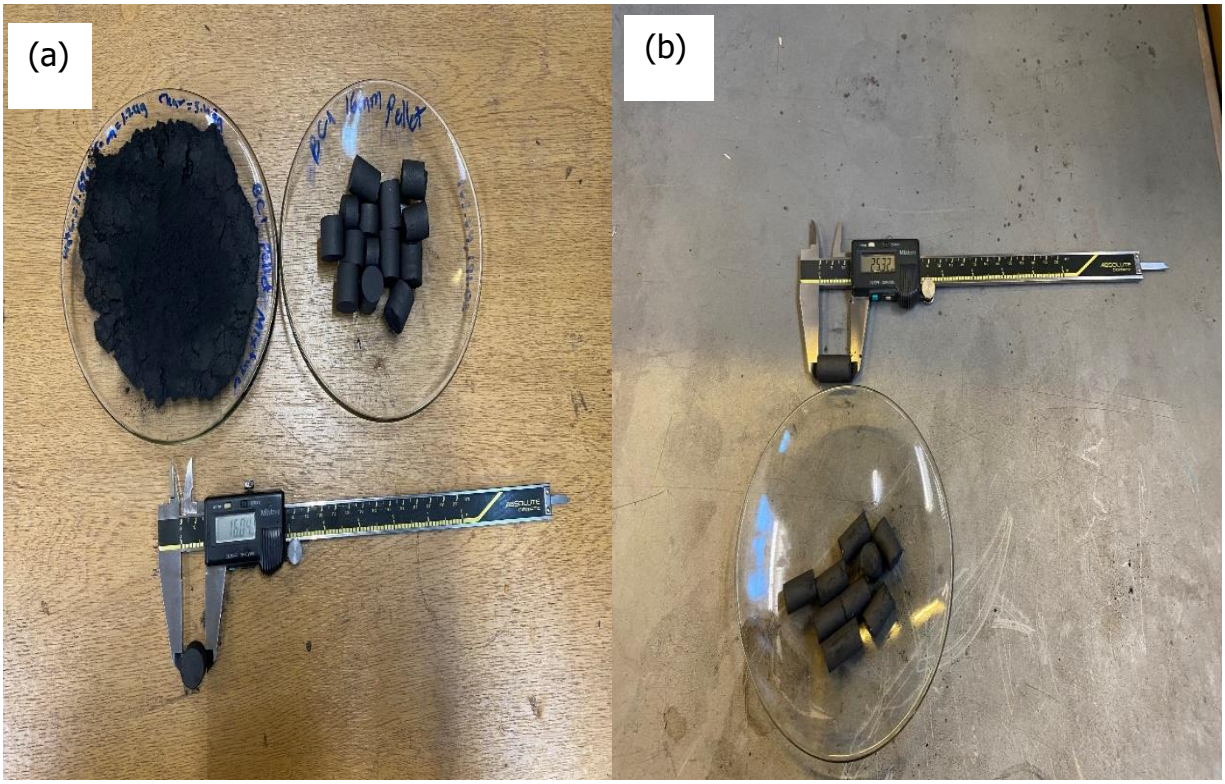

Figure 3.8: (a) Mixture P and Pellet B and (b) Pellet A samples.

3.5.4 Proximate analysis

Understanding the behaviour of carbon-based fuel materials fundamentally serves as the foundation for conducting research on thermochemical conversion processes. One of the widely used methods is proximate analysis. Proximate analysis is a method of determining the behaviour of a fuel based on four main categories of substances contained within it. These compounds consist of moisture content (MC), ash content (Ash), volatile matter (VM) and fixed carbon (FC). In this thesis, moisture content was eliminated prior to

testing (as seen in Section 3.5.1), therefore the proximate analysis results are presented on dry basis. The following methodologies were applied to measure ash and volatile matter according to British standards.

3.5.4.1 Ash content

Ash content refers to the inorganic residue that remains after a solid-gas reaction is completed at a sufficient temperature. This content is typically expressed as a percentage of the mass fraction of the inorganic components in the fuel. The determination of ash content was conducted based on the standard BS EN ISO 18122:2015 [153].

Prior to the measurement, three empty clean porcelain dishes were placed into a Carbolite Muffle furnace, as shown in Figure 3.9, at 550°C ± 10°C for no less than an hour before being removed to avoid the existence of volatile matter in the dishes. After that, the dishes were taken out from the furnace and placed on heat-resistant surface to cool down for 10 minutes before being transferred to a desiccator to reach the ambient temperature. Once the dishes had cooled, the mass of the empty dishes was taken to the nearest 0.1 mg. Each dish was then loaded evenly with 1 g of dried char sample, and the mass of both dish and sample was taken to the nearest 0.1 mg. Subsequently, the loaded dishes were placed in a cold furnace and the temperature program was initiated as follows:

1. The sample was heated in air to 250°C at a heating rate of 4.5-7.5°C/min for 50 minutes.
2. The furnace temperature was held at 250°C for an hour to remove volatile matter before the combustion.
3. The furnace temperature was increased to 550°C at a heating rate of 10°C/min over 30 minutes.
4. To achieve complete combustion, the furnace temperature was maintained at 550°C for two hours.

Following the completion of the heating procedure, the dishes were removed from the furnace and left to cool for 10 minutes on a heat-resistant surface before being placed in a desiccator. This was done to prevent moisture absorption from the surrounding environment. When the temperature of the dishes with the test samples reached the ambient temperature, the mass was measured. To ensure repeatability, the test was performed at least three times, and the mean was calculated. Ash content on a dry basis can be measured by using the following equation:

$$Ash\ content\ (\%) = \frac{m_2 - m_0}{m_1 - m_0} \times 100 \qquad (3.1)$$

Where:

m_0 is the mass of the empty dish, m_1 is the mass of the test sample and the dish before test and m_2 is the mass of the residue material and the dish after test.

The above procedures were performed to measure ash content of both biomass char and hydrochar samples, whereas ash content measurement for coal char sample was carried out in TGA as described in Section 3.14.1.

Figure 3.9: Muffle furnace, Carbolite furnace used for volatile matters and ash content measurement.

3.5.4.2 Volatile matter content

According to the standard method BS EN ISO 18123:2015 [154], the volatile matter represents the mass loss of carbonaceous material when a sample is heated in the absence of oxygen under standard conditions. In order to ensure consistent results, measurement of the volatile matter content was repeated in quadruplicate. Therefore, a multiple stand holding four empty fused silica crucibles and the corresponding lids were heated using the above Muffle furnace at 900°C and kept for 7 minutes. This step is to take away any absorbed species on the crucibles' walls. After removal from the furnace, the crucibles were left to cool to room temperature before being put into a desiccator. Once the empty crucibles and lids had cooled, they were then weighed to the nearest 0.1

mg and the mass was recorded. Then 1 g of the dried sample was placed and spread inside each crucible and the mass of the covered crucible was measured to the nearest 0.1 mg. Similar to previous cleaning procedure, the filled crucibles were loaded into the holding stand and inserted again in the furnace at 900°C for 7 minutes. Once the heating period passed, the four crucibles were placed on a heat-resistant surface to cool down for 10 minutes before being moved to a desiccator. Finally, the total mass of remaining solid sample and the crucible with the lid was taken to the nearest 0.1 mg. The volatile matter percentage on dry basis was taken as the mean value of the four repeats and measured using following equation:

$$Volatile\ matter\ (\%) = \frac{m_1 - m_2}{m_1 - m_0} \times 100 \qquad (3.2)$$

Where: m_0 is the mass of the empty crucible and lid, m_1 is the mass of the filled crucible and lid before heating and m_2 is the mass of the residual sample, crucible and lid after the test.

3.5.4.3 Fixed carbon content

Fixed carbon content is the solid residue that remains in the char sample after the devolatilization process, where all moisture and volatile matter are excluded. This carbon is not pure carbon but it is a mixture of several species such as carbon, hydrogen, oxygen, nitrogen, and sulphur[155]. The amount of fixed carbon in char samples was determined by subtracting the sum of ash content and volatile matter from 100% as shown in following equation:

$$Fixed\ carbon\ \% = 100 - (Ash\ content\% + Volatile\ matter\ \%) \qquad (3.3)$$

3.5.5 Ultimate analysis

The organic elemental composition measurement of the fuel is an essential factor in the designing of thermochemical conversion systems [156]. Ultimate analysis is a common method utilised to present these elements namely, carbon, hydrogen, nitrogen, sulphur, and oxygen. This analysis was carried out using Thermosientifc FlashSmart Organic elemental analyser (OEA), CHNS/O in Cardiff University School of Engineering CLEER Lab as shown in Figure 3.10. The uncertainty of the analyser depends on the sample size and type according to the manufacturer's technical report [157]. The relative standard deviation of elemental analysis should be <3% for results to be considered reliable [158]. The analysis was carried out by Dr Julain Herbet and was repeated in duplicate with the error reported as standard deviation.

Figure 3.10: Thermosientifc FlashSmart Organic elemental analyser (OEA), CHNS/O for Ultimate analysis.

3.6 Carbon and sulphur analysis

The measurement of carbon and sulphur content in the char samples was performed using the LECO SC-144DR carbon and sulphur analyser shown in Figure 3.11. The sample was burnt in the furnace at 1350°C in an oxygen-rich environment to ensure complete combustion of the sample. Sulphur and carbon were then reacted with oxygen to produce CO_2 and SO_2. The analyser then measured the CO_2 and SO_2 produced by comparing the quantity of measured gas to the inputted sample mass, such that a total sulphur value can be produced. The instrument was regularly calibrated with standards supplied by LECO and checked prior to the commencing of any work. Results were taken from the mean value of a minimum of three repeats. Error values were calculated by using the standard deviations of these results. According to the manufacturer's application note, standard deviations were found to range from ±0.13% to ±0.60% for C and from ±0.0007% to ±0.007% for S for coal, coke and graphite samples [159].

The LECO SC-144DR was run in the following procedures:

1. The instrument was prepared for the experiment by initiating the oxygen supply and heating up the combustion furnace to 1350°C.
2. A nickel boat liner was placed onto a four-figure balance, which was then zeroed. A sample of 100 to 300 mg was loaded into the boat. The mass of the sample depends on the sample properties - for instance, a sample with high carbon content was about 0.1 mg.
3. The loaded nickel boat liner was transferred to a ceramic combustion boat and positioned on a tray to be inserted into the tube furnace. The SC-144DR software was luanched and the mass of the sample was entered into the software. Once the software reading became stable and displayed a prompt, the sample was pushed inside the furnace to begin the experiment.
4. The concentration of the combustion products was then measured using an infrared (IR) detection system, and data was recorded in the software. Carbon and sulphur were logged in the SC-144DR software.

5. The experiment was completed when no further changes occurred to the analysis of carbon and sulphur on the software.
6. The ceramic boat was then removed from the furnace and allowed to cool.

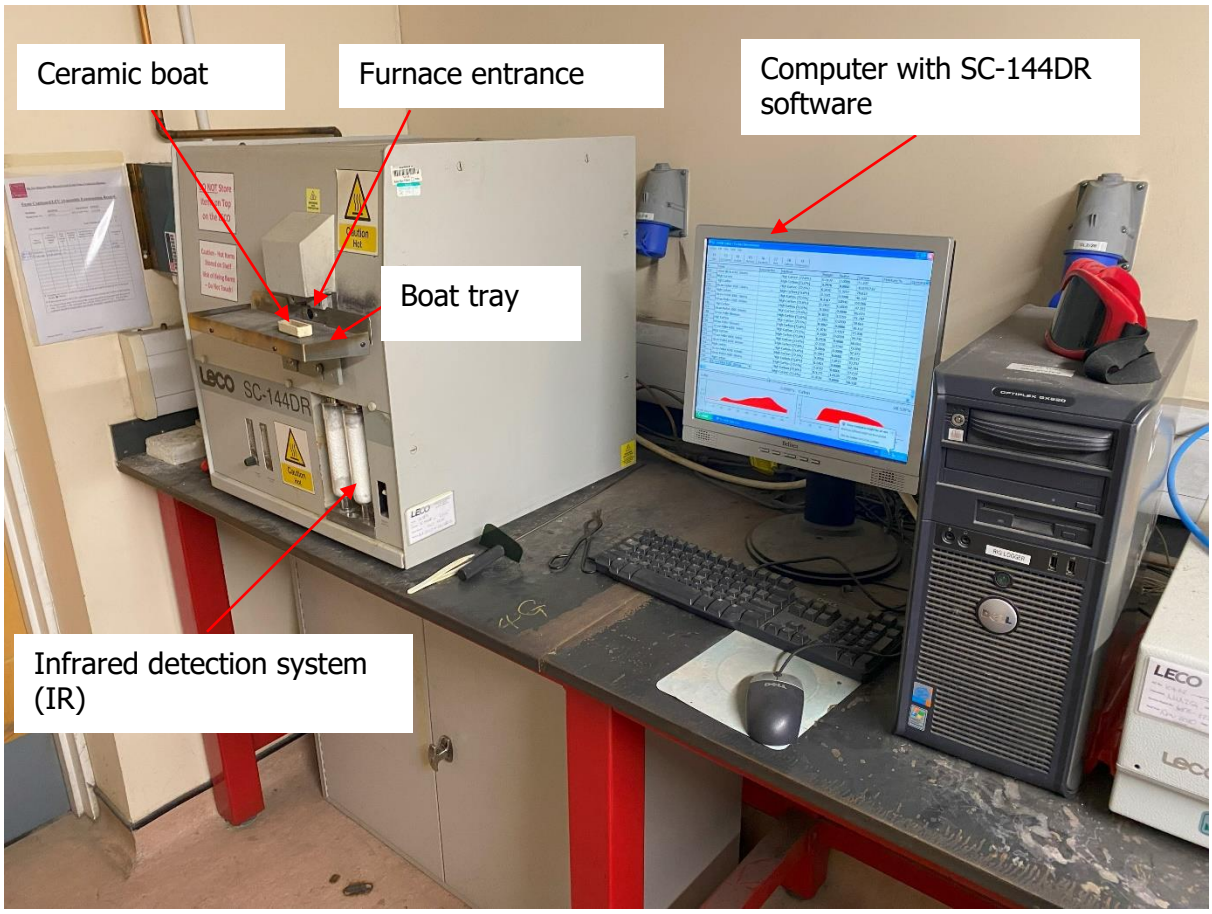

Figure 3.11: LECO SC-144DR carbon and sulphur analyser.

3.7 Demineralisation treatment of char sample

A demineralisation process with hydrochloric acid (5 wt.% HCl) solution was carried out following a washing method from literature [160]. Dried and sieved samples of both BC1 and HC were chosen for demineralisation treatment due to their higher reactivity compared to the other chars in this work. In this process, 12.5 g each of BC1 and HC

were added to 125 ml of the prepared washing solutions in flasks, shaken manually, and left for 24 hours at room temperature to dissolve completely. The mixtures were then washed with deionised water and subjected to vacuum filtration to separate the solid char particles from the solutions. Figure 3.12 shows the vacuum filtration setup. Finally, the washed samples were dried in the oven at 105°C for an additional 24 hours and were denoted BC1HCl and HCHCl.

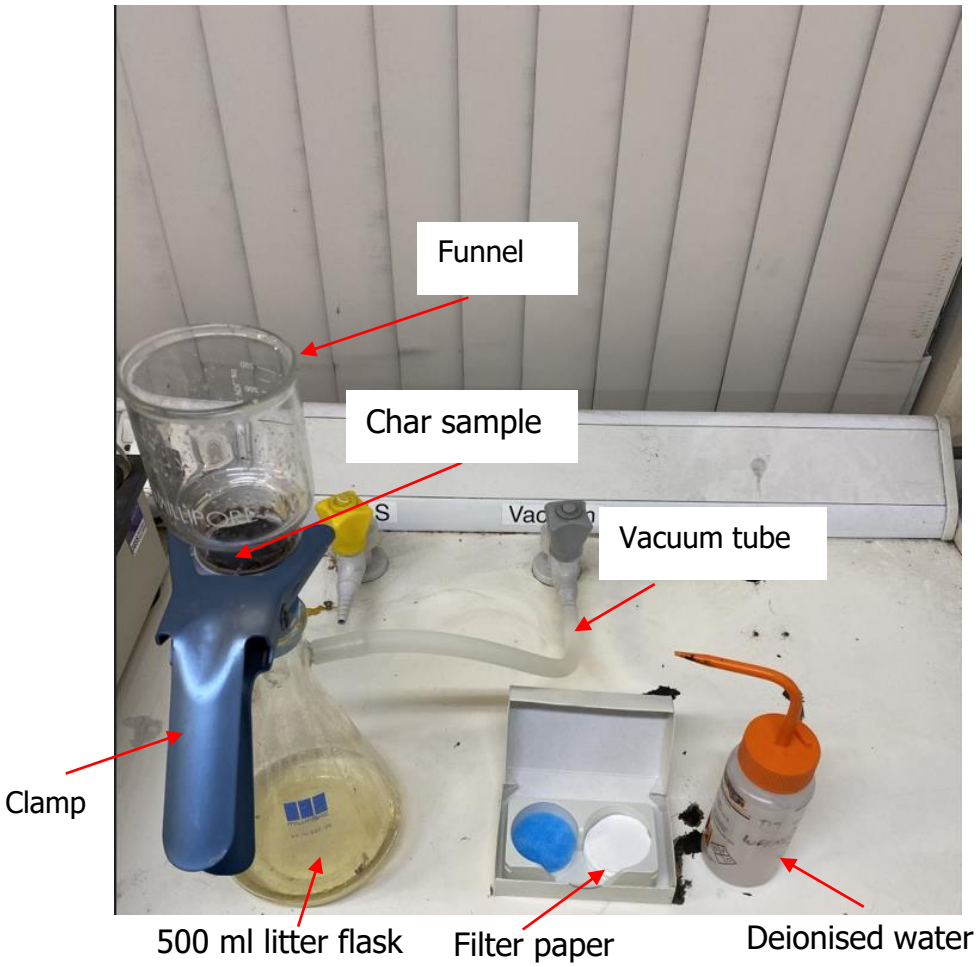

Figure 3.12: Filtration apparatus system.

3.8 X-ray fluorescence (XRF)

The purpose of carrying out this analysis was to obtain sufficient information about which elements are present in the samples prior to subjecting them to the Inductively Coupled Plasma Optical Emission Spectroscopy (ICP-OES). The advantage of this approach lies in non-destructive nature of XRF analysis and quick testing. However, the XRF is not able to detect elements lighter than magnesium. The elemental compositions of powdered dry samples were assessed using an Innov-X Systems, model Olympus X5000 series X-ray fluorescence (XRF) analyser with a repeatability of 0.0015 wt.% under standard conditions [161] (as illustrated in Figure 3.13). To commence the XRF experiment, the Mining Plus mode was selected to conduct the test. Subsequently, a 316 stainless steel sample was utilised to calibrate the instrument. Upon completing the calibration process, a new thin-film sample support was attached to a clean sample holder. Thereafter, approximately 1 g of the sample powder was evenly distributed into the holder using a spatula, ensuring a minimum thickness of 3 mm. The sample holder was then placed into the instrument and the lid was closed. An automated analysis took place, and a set of results were produced and stored in the device.

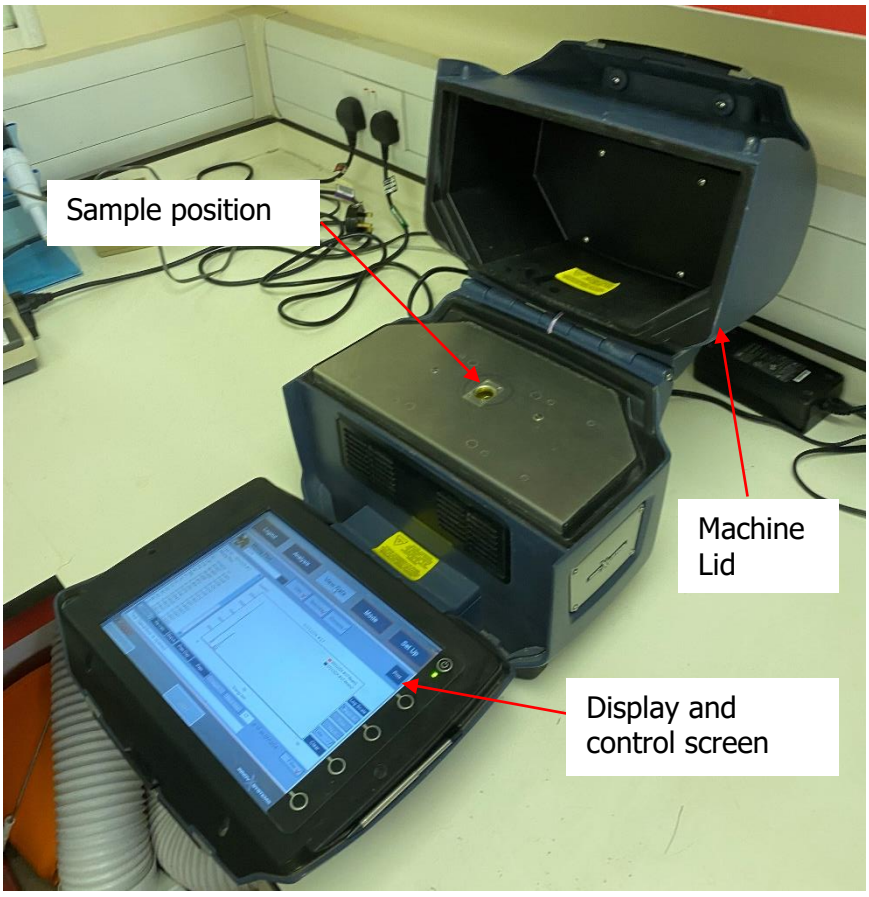

Figure 3.13: X-ray fluorescence (XRF) analyser, Innov-X Systems, model Olympus X5000 series.

3.9 Inductively coupled plasma optical emission spectroscopy (ICP-OES)

Inductively coupled plasma optical emission spectroscopy (ICP-OES) is an analytical technique extensively used to measure and identify elements in the tested sample. ICP-OES offers a high level of accuracy for analysing the elemental composition of different materials [162]. However, this multi-elemental technique requires a pre- treatment of the sample such as digestion [163]. The Perkin Elmer Optima 2100 DV ICP-OES (as shown in Figure 3.14) was used to analyse the chemical compositions of the ash powders. Elemental analysis by ICP-OES can achieve precision as low as 0.2%, though concentration uncertainties are often 10% or higher [164].

Following is a description of the elemental compositions analysis method that was conducted by the operator in the CLEER lab at Cardiff University School of Engineering via ICP-OES:

1. Approximately 100 mg of a dry ash sample was weighed to the nearest mg using an analytical balance and added into a digestion vessel (exact weight was recorded).
2. 2 ml of reagent grade hydrofluoric acid (HF) at a concentration of 48-51% was added to the weighed sample and left to soak for 24 hours.
3. A combination of 3 ml of 37% reagent grade hydrochloric acid (HCl) and 3 ml of 70% reagent grade nitric acid (HNO_3) was added into the digestion vessel, and the assembled vessel was added to the sample holder rotor.
4. The rotor was placed in an Ethos Easy microwave, and the sample was digested for 20 minutes at 180°C.
5. On completion, the vessel was opened in a fume cupboard and 12ml of 4% boric acid (H_3BO_3) was added to neutralise HF, and previous step was repeated.
6. Once microwave digestion was completed, the vessel was opened in a fume cupboard and contents were poured into a glass beaker The vessel was rinsed with deionised water and the rinse was added to the beaker.
7. The contents of beaker were then poured into 50 ml volumetric flask and made up to volume with deionised water.
8. The digested sample was transferred into a suitable container and analysed using a Perkin Elmer Optima 2100 DV ICP-OES instrument.
9. The ICP machine was calibrated prior to each test campaign using a 28-element calibration solution with a concentration of 100 mg/l.
10. The solution was diluted down to 10 mg/l and 1 mg/l to perform the calibration, and the calibration curves created during this process were used to determine the concentration of the elements in the tested ash samples.

11. The subsequent results were expressed as mg/kg and were divided by 10,000 to be expressed as mass%.

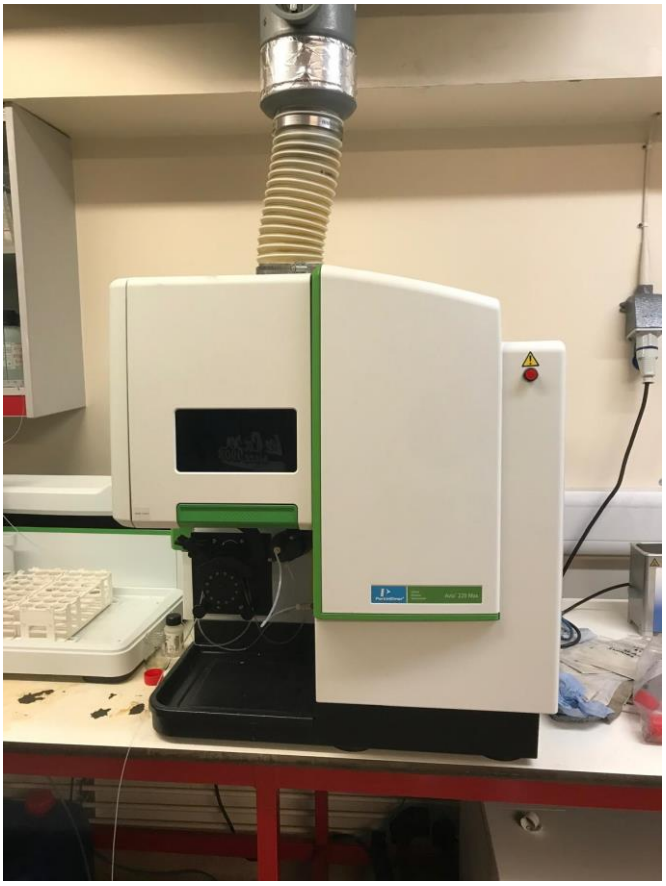

Figure 3.14: Inductively Coupled Plasma Optical Emission Spectroscopy (ICP-OES), Perkin Elmer Optima 2100 DV ICP-OES.

3.10 Gas physical adsorption technique

3.10.1 Instrument method

Physical structural features of the char samples were identified using the gas physical adsorption method. N_2 at boiling temperature is commonly employed as an adsorbate gas to prevent any reaction with adsorbent surface [165].

N_2 adsorption analysis at -196°C was carried out in a Quantachrome Quadrasorb EVO Surface Area & Pore Size Analyser, shown in Figure 3.15, to measure surface areas, pore volumes, pore size distribution and average pore diameters of the samples. It should be mentioned that there is a possibility of a 20% inaccuracy in the surface area measurement using N_2 adsorption because of its sensitivity to surface chemistry [106].

The gas adsorption analysis were conducted according to BS ISO 9277:2022 [166], BS ISO 23604:2022 [167], and BS ISO 15901-2:2022 [168]. Prior to the measurements, 0.2-0.5 g of dried, classified char samples (as mentioned in Section 3.5.2) were loaded in a glass container and degassed in a vacuum at 250°C for 24 hours. The degassing process was carried out using a Quantachrome FloVac-Six-Port Vacuum and Flow Degasser, as shown in Figure 3.16. This step was essential to ensure that the sample surface was free from contaminants. Once degassed, the sample was allowed to cool to room temperature.

Figure 3.15: Quadrasorb EVO Surface Area & Pore Size Analyser.

The cooled, degassed sample was then transferred into the analyser, where it was submerged in liquid nitrogen to achieve the required temperature for analysis.

The experiment was set up and controlled using the Windows® based QUADRAWin software. This procedure was carefully followed to ensure accuracy and repeatability of the results. The entire process, including the setup and operation of the equipment, was conducted at the Translational Research Hub (TRH) at Cardiff University by Dr Greg Shaw.

The N_2 adsorption isotherm data were analysed using three methods. The Brunauer-Emmett-Teller (BET) model [169] was used to determine the total surface area, S_{BET}, while the t-plot method [170] was applied to the adsorption branch to estimate the micropore surface area and micropore volume, S_{Micro} and V_{Micro}. The Barrett-Joyner-Halenda (BJH) desorption method [171] was used to determine pore size distribution and average pore size diameter, D_p. The total pore volume, $V_{Total,}$ was calculated based on the amount of N_2 adsorbed at a relative pressure of P/P_0= 0.938-0.956.

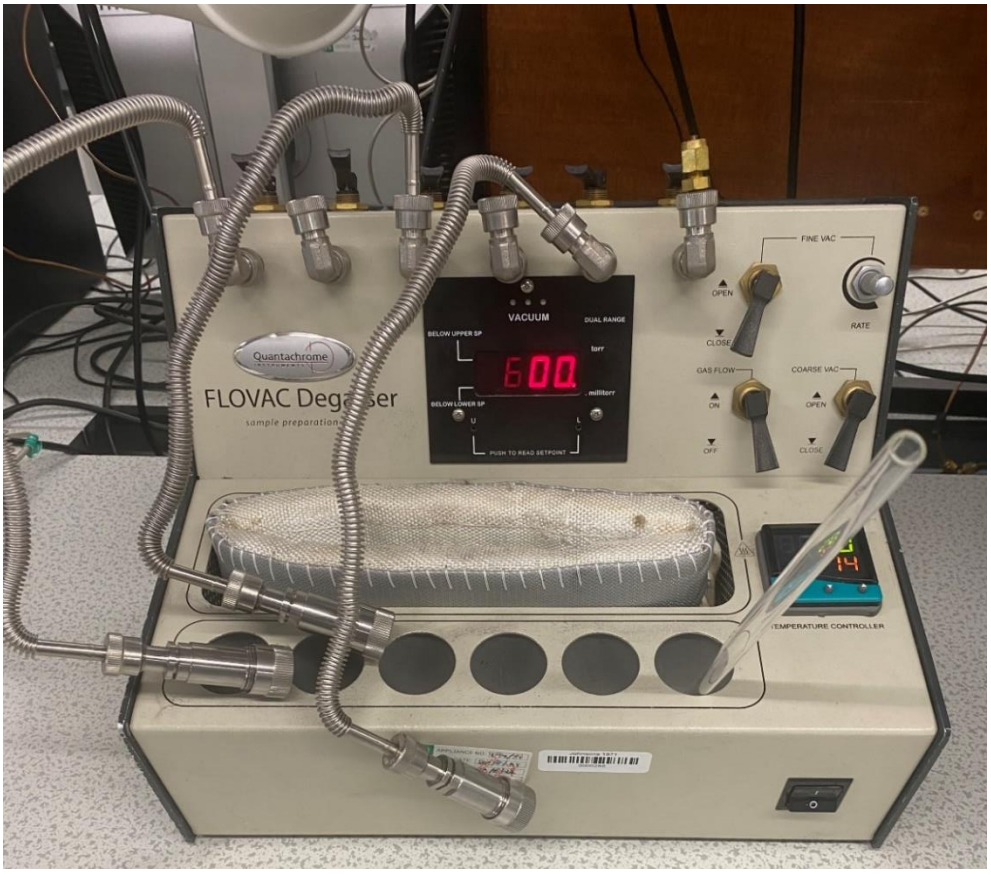

Figure 3.16: Quantachrome FloVac-Six-Port, Vacuum and flow Degasser.

3.10.2 An example of N_2 physisorption analysis calculation

In this example calculation, the data reports of biochar sample (BC1) were used to illustrate how N_2 isotherms were returned.

Brunauer-Emmett-Teller (BET):

The BET equation (Equation 3.4) was implemented at relative pressures range of 0.005 to 0.263 from the desorption isotherm curve shown in Figure 3.17.

$$W = \frac{W_m c \left(\frac{p}{p_0}\right)}{\left[1 - \left(\frac{p}{p_0}\right)\right]\left[1 + (c-1)\left(\frac{p}{p_0}\right)\right]} \tag{3.4}$$

Where, p_0 is the saturation pressure of the inert gas (N_2), p is the equilibrium pressure of the N_2 with the sample surface, $\frac{p}{p_0}$ is the relative pressure and c is dimensionless constant. W is the volume of adsorbate introduced to the sample and W_m is the monolayer volume of the N_2 adsorbed onto the sample's surface when a full unimolecular layer was formed at standard temperature and pressure (STP) in cm^3/g.

A linear regression was performed using the BET linear form (Equation 3.5) to plot $\frac{p}{p_0}$ on x-axis against $\frac{p}{W(p_0-p)}$ in y-axis to construct a straight line as shown in Figure 3.18.

$$\frac{p}{\mathrm{W}(p_0 - p)} = \frac{1}{W_m c} + \frac{c-1}{W_m c}\left(\frac{p}{p_0}\right) \tag{3.5}$$

Consequently, the unknown monolayer capacity W_m and BET constant c can be calculated using the slope and intercept values obtained from the multi-point BET linear plot as following [169]:

$$W_m = \frac{1}{slope + intercept} = \frac{c-1}{c_m} \tag{3.6}$$

$$c = 1 + \frac{\text{slope}}{intercept} \tag{3.7}$$

Once these parameters are determined, the BET surface area (total surface area m^2/g) can be obtained through the following formula:

$$S_{BET} = \frac{W_m N_{av} A_m}{M} \tag{3.8}$$

Where N_{av}, A_m and M are Avogadro's number (6.02×10^{23} molecules/mol), the cross-sectional area of N_2 which equals 0.162 nm^2 and the molecular weight of N_2 is 28.02 g/mol, respectively.

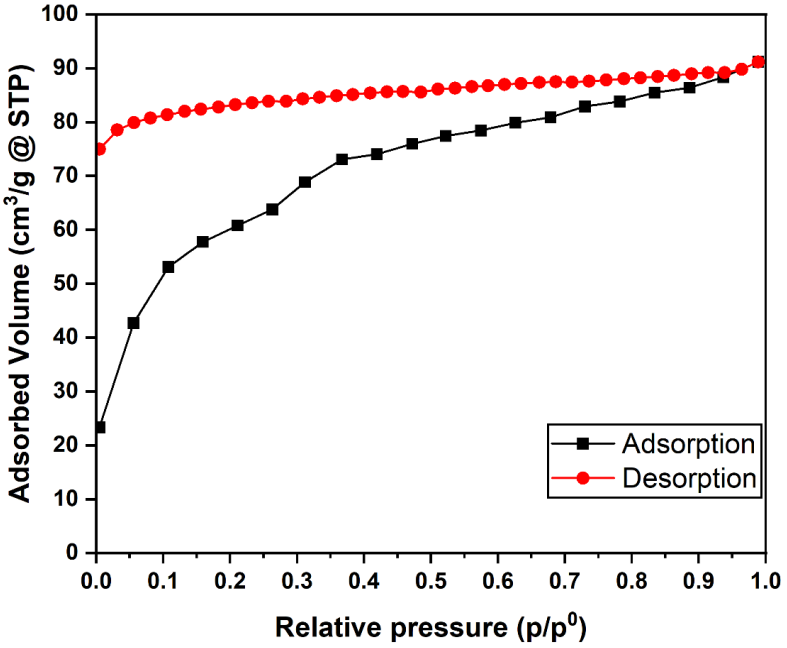

Figure 3.17: N_2 adsorption and desorption isotherm curves of BC1.

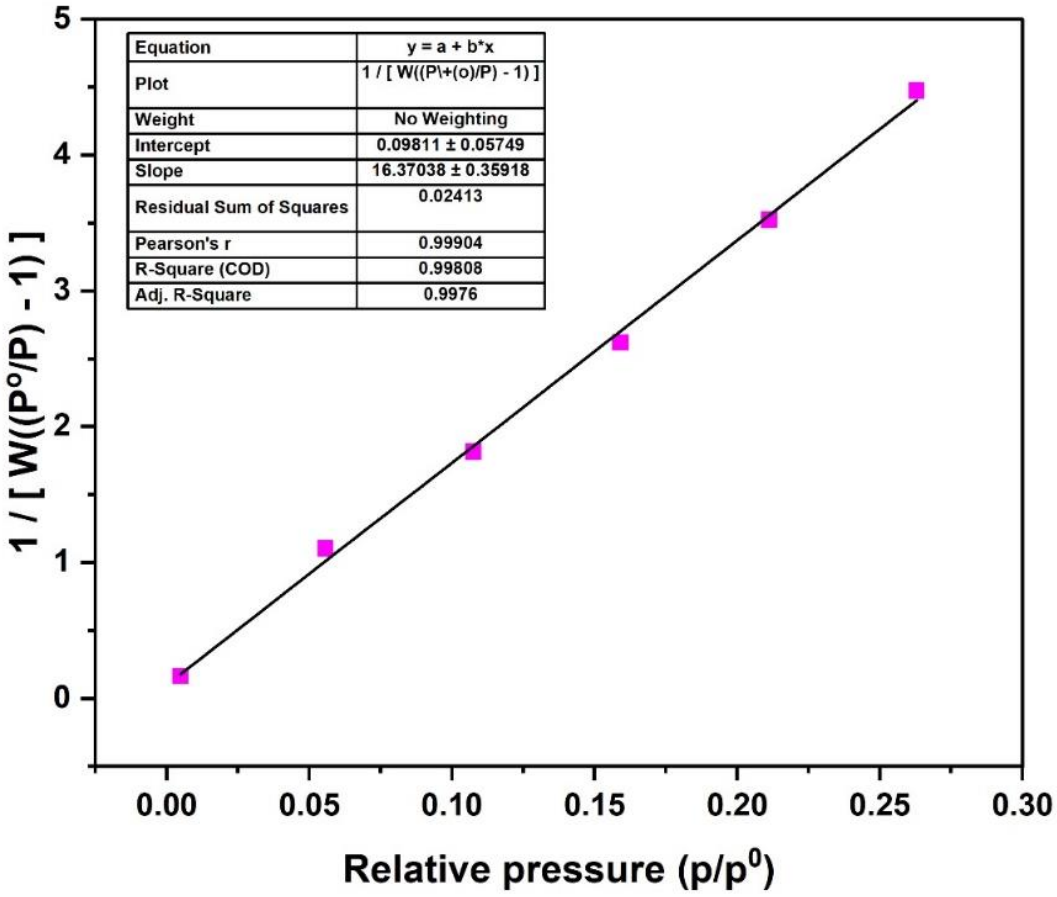

Figure 3.18: Multi-Point BET linear plot of BC1 sample.

t-plot:

The statistical thickness of the adsorbed N_2 layer on the surface of the solid sample (t) (the de Boer method) can be calculated using Harkins and Jura equation [172] from the isotherm data within the relative pressure range of 0.17 to 0.45, as follows:

$$t = \sqrt{\frac{13.99}{0.034 - log\frac{p}{p_0}}} \qquad (3.9)$$

Where t is the statistical thickness of the adsorbed N_2 layer, expressed in Angstroms (Å). Similar to BET analysis, a linear regression was performed to generate the t-plot by plotting t versus the adsorbed volume of N_2 (cm^3/g) at STP, as shown in Figure 3.19. This enables the measurement of external surface area $S_{external}$ (m^2/g) and micropore volume V_{micro} (cm^3/g) by using the slope and intercept obtained from this plot through the following formulas:

$$S_{external} = Slope \times 15.468 \tag{3.10}$$

$$V_{micro} = Intercept \times 0.0015468 \tag{3.11}$$

The micropore surface area S_{micro} can be then determined by subtracting the $S_{external}$ From S_{BET}. This calculation isolates the contribution of micropores to the overall surface area, providing insights into the porous structure of the material:

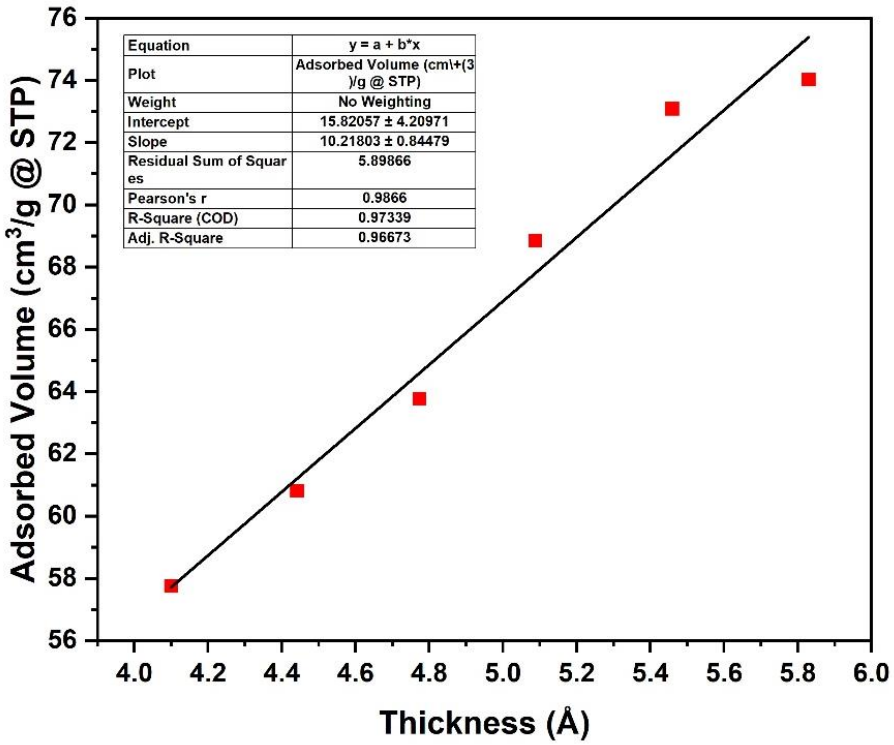

Figure 3.19: t-plot curve of BC1 sample.

$$S_{micro} = S_{BET} - S_{external} \tag{3.12}$$

Barrett-Joyner-Halenda (BJH):

Pore size distribution, as shown in Figure 3.20, and average pore diameter (D_p) were evaluated using the BJH method. This method applies the modified Kelvin equation to relate relative pressure to pore radius as illustrated in the following equation:

$$n\left(\frac{p}{p_0}\right) = \frac{-2\gamma V_m}{rRT} \tag{3.13}$$

Where γ is the surface tension of liquid N_2 (8.9×10^{-3} N/m), V_m is the molar volume of liquid N_2 (3.47×10^{-5} m³/mol), r is the pore radius (m), R is the gas constant (8.314 J/mol·K) and T is the absolute temperature (77 K).

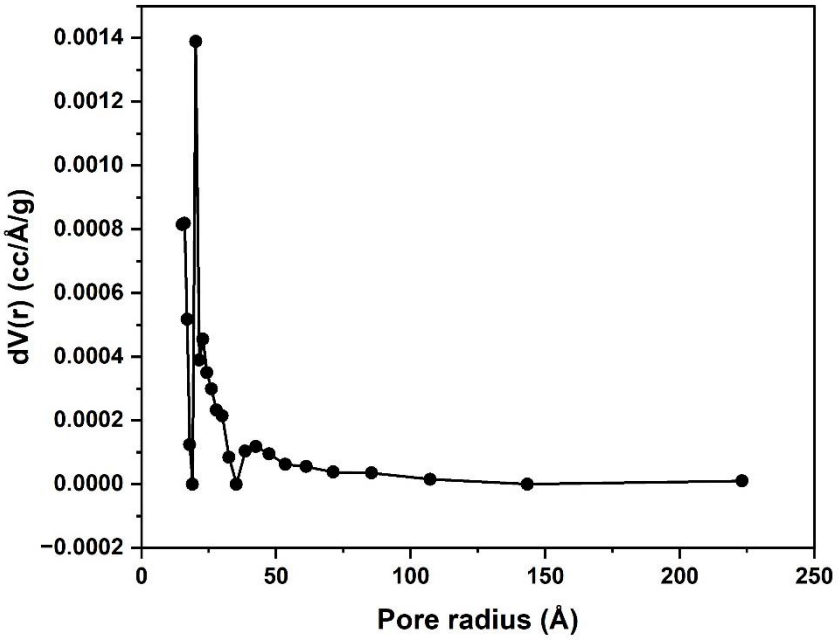

Figure 3.20: BJH pore size distribution of BC1 sample.

3.11 X-ray diffraction (XRD)

3.11.1 Crystalline mineral components identification method

Mineral phase identification of the ash residues from the char samples was carried out using X-ray diffraction (XRD) on a Siemens D5000 diffractometer, as illustrated in Figure 3.21. The diffraction was collected from 10° to 80° 2 theta at a scan speed of 0.02 degrees per second using copper radiation (Cu Kα) at 35 kV and 40 mA. The sample was prepared for the test by placing and distributing the sample evenly into an XRD sample holder using a glass slide. Once the sample holder was filled and physically pressed to the top of its centred square hole, it was then inserted inside the designated position within the Siemens-Diffractometer goniometer and securely positioned. The machine door was then closed and the XRD cooling system (chiller unit) was turned on before powering the XRD instrument. The diffraction range, scanning speed, and power were entered into the controlling platform (DIFFRAC plus XRD Commander), and the experiment was launched. After the completion of the run, data obtained from XRD was saved and analysed by Panalytical X'Pert HighScore Plus software using the reference patterns database from the Crystallography Open Database (COD) [16]. It was reported that the repeatability of the XRD technique was 15% [173].

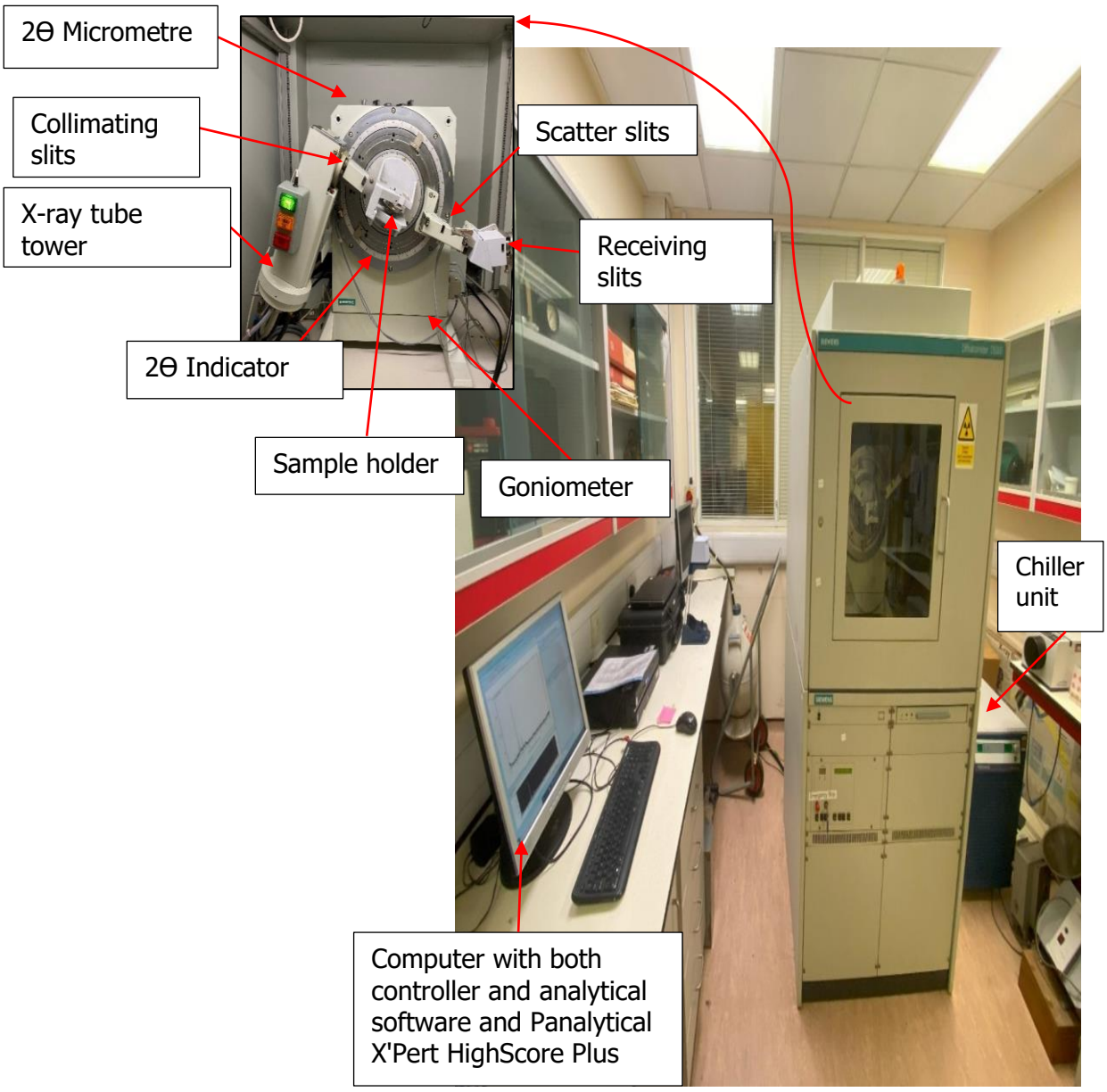

Figure 3.21: X-ray diffraction (XRD), Siemens-Diffractometer/D5000.

3.11.2 Semi-quantification of mineral composition method

The mineral composition present in the ashes of char samples was semi- quantified by adopting a simple method that recently implemented Julian Herbert in a PhD thesis [173]. According to Herbert, the uncertainty of this semi-quantitative method was estimated to be within ±10%. This method is not a definitive quantification of the ash components; however, it was chosen owing to its simplicity and availability of pattern reference databases in the School of Engineering. More accurate quantification can be achieved using the Rietveld refinement method [174]. However, this method requires access to commercial crystallographic databases such as PDF-5+ [175], which provide complete crystal structure data. It also involves creating a mathematical model of diffraction patterns to fit the experimental diffractogram of each mineral phase [176]. Therefore, a semi-quantitative method based on peak area integration was adopted in this PhD.

In the reference method [173], mineral quantities were estimated by manually calculating the area under each mineral's main peak using peak height (intensity) and full width at half maximum (FWHM), with a baseline set at y=0, as shown in Figure 3.22. In contrast, this study used numerical integration in Origin software to calculate the areas under crystalline peaks with the baseline adjusted to capture start and end of the peak. This approach ensures more robust and reliable measurements of the areas under the crystalline peaks.

The first step of semi-quantification method was identifying the main peak for each mineral using the peak list in the reference patterns. When a peak was matched a single mineral, it was considered a 100% peak and used for area calculation. For overlapping peaks, a lower intensity but 100% peak was used instead. The sum of the calculated areas was taken as 100% and each mineral was expressed as a percentage of this total in the ash samples. An example of X-ray diffraction patterns with crystalline peak identification and a custom baseline is shown in Figure 3.23.

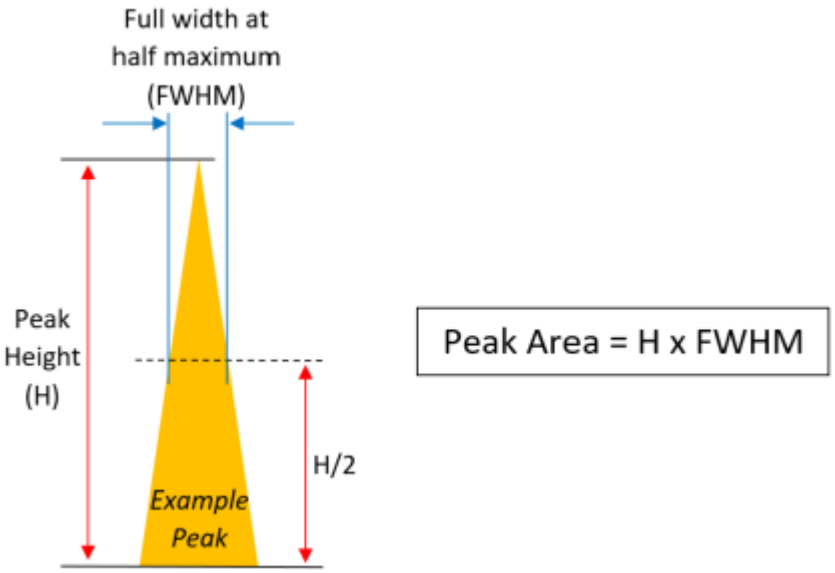

Figure 3.22: Crystalline peak area calculation using FWHM [173].

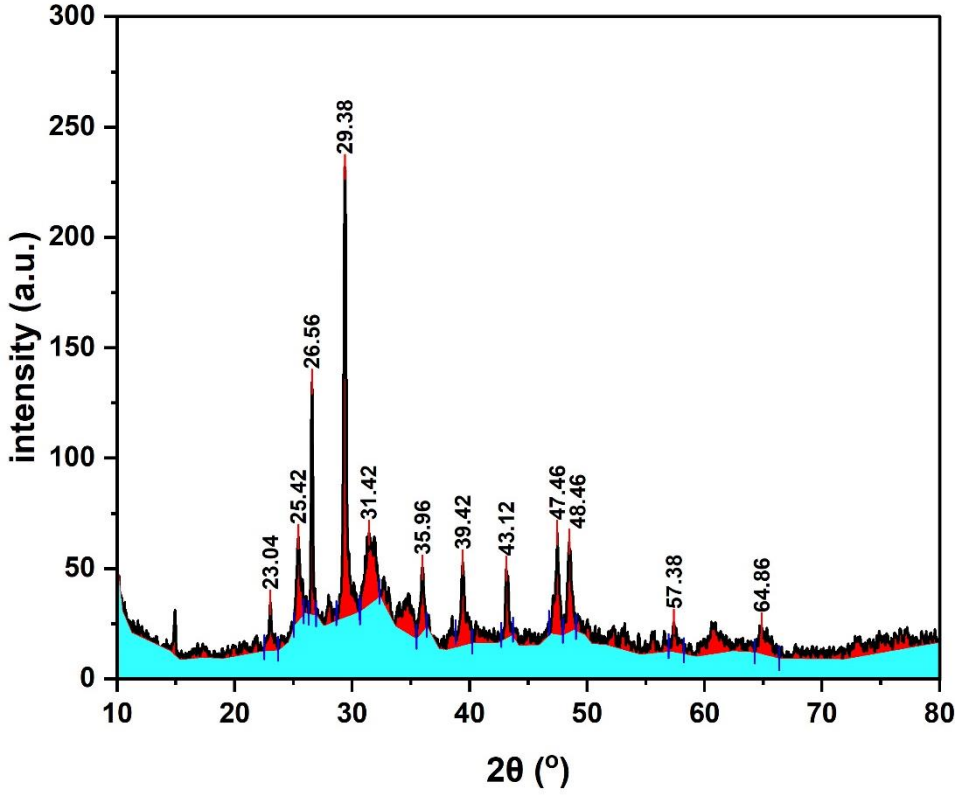

Figure 3.23: X-ray diffraction patterns of ash produced from HC sample showing crystal peaks position (2θ) and crystals area (red), amorphous area (blue).

3.12 Scanning electron microscopy coupled with energy dispersive spectroscopy (SEM-EDS)

The morphology and distribution of elements on the surfaces of the chars were observed by Scanning electron microscopy coupled with energy dispersive spectroscopy (SEM-EDS), which included SEM. This included a Zeiss Sigma HD field emission gun SEM, 20 kV beam energy, ~1.5 nA beam current using a 60 µm diameter final aperture. Figure 3.24 shows an image of the Zeiss SIGMA HD VP Field Emission Scanning Electron Microscopy system used in this work. Typically, EDS has an analytical accuracy of about ±2% but it can achieve precision better than ±1% for major elements [177]. For chemical analysis, dry powder samples were mounted on aluminium SEM stubs using carbon adhesive tabs, coated with a 15 nm thick layer of carbon prior to being loaded in the SEM. The application of carbon coating was to improve the electrical conductivity of the char samples and preventing charging effects that lead to distortion of the SEM images.

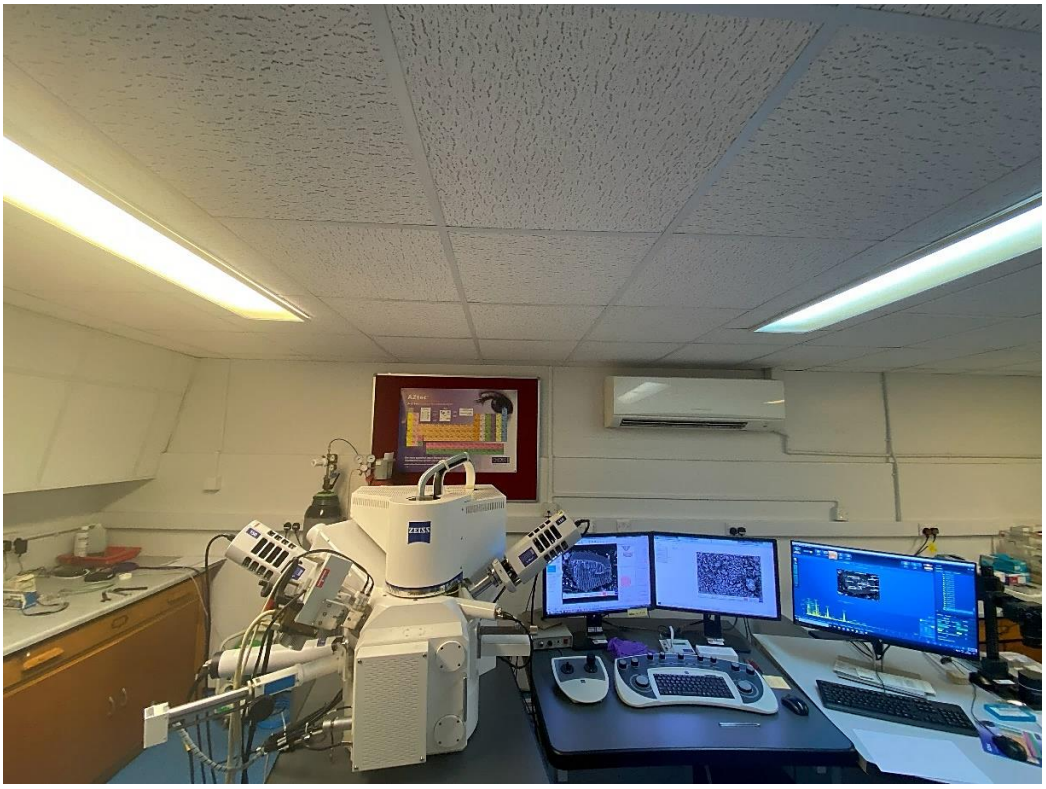

Figure 3.24: Zeiss SIGMA HD VP Field Emission Scanning Electron Microscopy system used for SEM-EDS analysis.

The coating was conducted using an Agar Turbo Carbon Coater, shown in Figure 3.25. Two 150 mm^2 Oxford Instruments X-Max silicon drift detectors were used for semi-quantitative Energy Dispersive Spectroscopy (EDS) analysis. Backscattered electron images and EDS spectra were acquired and processed using Oxford Instruments Aztec software. EDS results were quantified using factory standards and data was normalised to 100 wt.%. It should be noted that char samples used in this analysis were selected from the sieving procedure described in Section 3.5.2 and their particles size were 150µm for imaging quality purposes. The analysis was performed by Dr Duncan Muir at Cardiff University's School of Chemistry.

Figure 3.25: Agar Turbo Carbon Coater.

3.13 X-ray photoelectron spectroscopy (XPS)

X-ray photoelectron spectroscopy (XPS) was performed using a Kratos Axis Ultra DLD system with a monochromatic Al Kα X- source operating at 144 W (12 mA x 12 kV), as shown in Figure 3.26. Data was collected with pass energies of 160 eV for survey spectra, and 40 eV for the high-resolution scans with step sizes of 1 eV and 0.1 eV respectively. The system was operated in the Hybrid mode, which uses a combination of magnetic immersion and electrostatic lenses for high sensitivity and acquired using a slot aperture which gives an analysis area of ca. 300 $\times$ 700 μm^2. As samples were electronically isolated form the spectrometer, a magnetically confined charge compensation system was used to minimise charging of the sample surface, and all spectra were taken with a 90° take-off angle. A base pressure of ca. 5×10^{-9} Torr was maintained during collection of the spectra. Data was analysed using CasaXPS (v2.3.26) [178], after calibration to the lowest energy C 1 s peak taken to be 284.5 eV. Analysis was performed using a Shirley background to account for electron scattering and using modified Wagner sensitivity factors as supplied by the manufacturer. This surface chemistry technique can produce a relative error of 10% in repeated analyses and may differ from actual values by 20% [179]. The XPS analysis was conducted by Dr David Morgan at Cardiff University's School of Chemistry.

Figure 3.26: X-ray photoelectron spectroscopy (XPS), Kratos Axis Ultra DLD system.

3.14 Thermogravimetric analysis (TGA)

The principle of thermogravimetric analysis is based on monitoring the changes in the mass of a sample over time as it is heated in isothermal or non-isothermal conditions. Thermochemical processes including gasification, combustion and pyrolysis are possible tests that can be carried out using TGA. This technique provides sufficient information about the material behaviour when subjected to different gaseous atmospheres. Moreover, TGA is a powerful technique in the evaluation of kinetic parameters, thus enhancing the understanding of the material thermal stability and the chemical reactions. The following sections discuss the analysis conducted using the Mettler Toledo TGA-DSC 3+, shown in Figure 3.27, in this thesis. This device has a weighing resolution of 0.0001 mg with an accuracy of 0.005% [180].

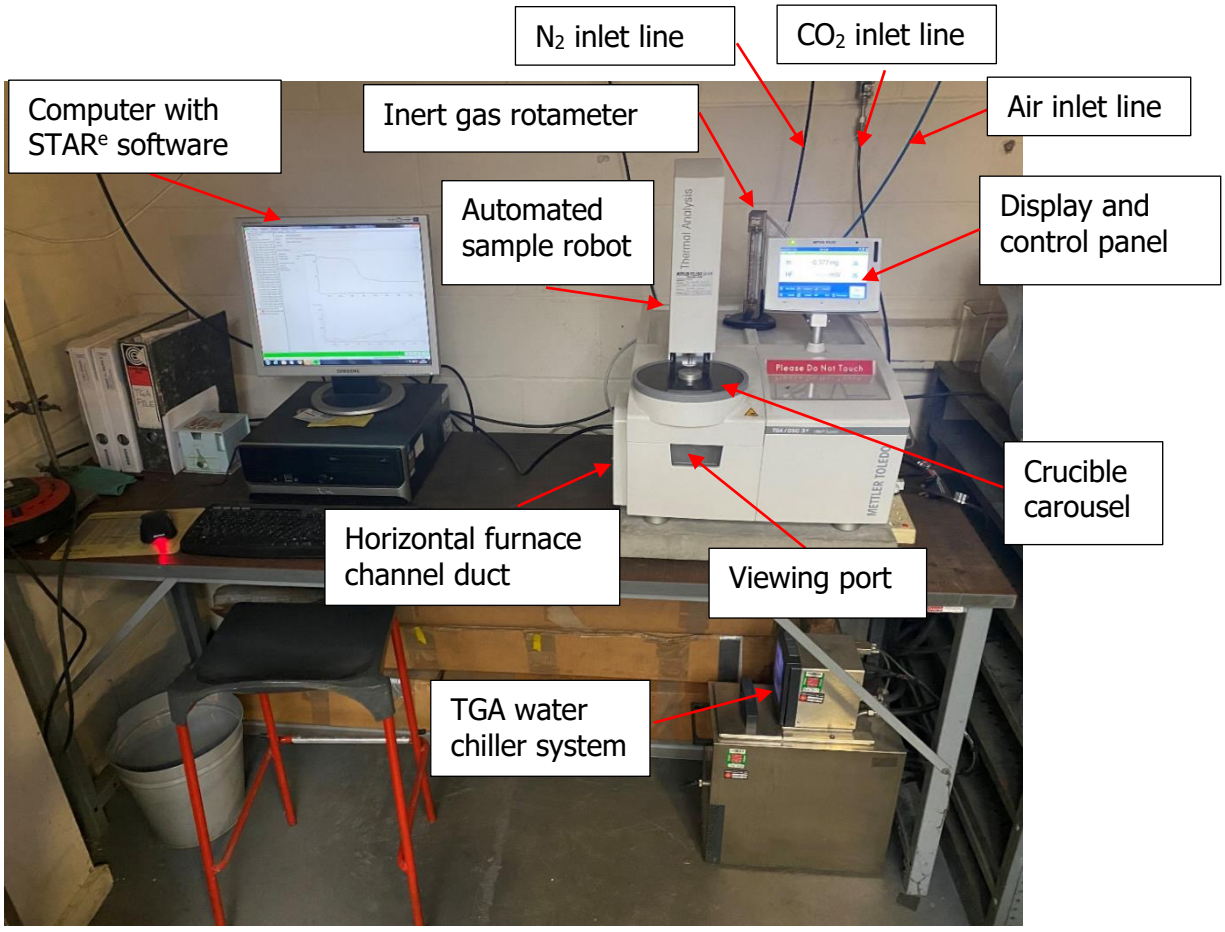

Figure 3.27: Thermogravimetric analysis system, Mettler-Toledo TGA/DSC 3^+.

3.14.1 Proximate analysis using TGA

The amount of coal char produced in DTF (Section 3.3) and the demineralised chars (Section 3.7) was limited at the start of this PhD project. To overcome this limitation, TGA was employed to measure ash content and volatile matter. The proximate analysis method used in the TGA is described in the following steps:

For ash content:

1. The sample was heated from 30°C to 500°C at a heating rate of 30°C/min in air flow of 100 ml/min.
2. The sample was held at 500°C for 10 minutes, then ramped to 815°C at 30°C/min.
3. The sample was held at 815°C for 90 minutes.

For volatile matter:

1. The sample was heated from 30°C to 900°C at a heating rate of 100°C/min in N_2 flow of 100 ml/min.
2. The sample was held at 900°C for 7 minutes in N_2 flow of 100 ml/min.

The mass loss data were then analysed using Equation 3.1 and Equation 3.2 to determine the ash content and volatile matter of the sample, respectively. Three runs were performed, and the results were reported as the mean of these runs.

3.14.2 Isothermal and non-isothermal CO_2 gasification tests

One of the most commonly used methods to investigate the isothermal CO_2 gasification and kinetics of chars is thermogravimetric analysis (TGA). In this study, gasification experiments were carried out in the Mettler-Toledo TGA/DSC 3^+ STAR®, analysing 15 mg of the char sample in an alumina crucible. The isothermal gasification experiments were conducted at three selected temperatures 900°C, 950°C and 1000°C. In each run, the sample was heated to 900°C in 100 ml/ min of N_2 flow at a heating rate of 20°C /min and held at that temperature for 7 minutes to remove the volatile matter before switching

to the CO_2 flow. This holding period and temperature was chosen based on the standard volatile matter content method to generate a 'fixed carbon' produced in repeatable conditions as a consistent baseline for CO_2 gasification comparisons. The sample was then heated to the target gasification temperature and N_2 was replaced by CO_2 with a flow rate of 60 ml/min. The final temperature was held constant until the conversion was completed. This work presents a comparison of the gasification reaction, via the reverse Boudouard reaction, of the 'fixed carbon' portion of the different samples. In the current work, the pyrolysis data have been excluded from TGA results, and just the CO_2 gasification stage is presented. A typical TGA curve of the complete experimental method is provided in Figure 3.28, showing pyrolysis and reverse Boudourd gasification phases as well as initial mass considered for the calculation of CO_2 reactivity. To ensure reliability, each test was performed twice, except BC4 which was repeated three times at 1000°C. Errors were reported as standard deviations of these repeats. Figure 3.29 is an example of TGA profiles & temperature programme of CO_2 isothermal gasification test.

The experimental conversion (X_{exp}) of the gasification was obtained using following equation:

$$X_{exp} = \frac{m_i - m_t}{m_i - m_f} \tag{3.14}$$

where m_i represents the post pyrolysis mass after N_2 switched to CO_2, m_t is the measured mass at time t and m_f is the final mass remaining after complete gasification. Gasification reactivity at different temperatures was evaluated using the reactivity index $R_{0.5}$ (s^{-1}) as proposed by Takayuki et al. [181], expressed by following equation:

$$R_{0.5} = \frac{0.5}{t_{0.5}} \tag{3.15}$$

where $t_{0.5}$ denotes the time in seconds required to convert 50% of the sample. Consequently, chars with a shorter $t_{0.5}$ gasification time are more reactive than those with longer $t_{0.5}$ gasification times [182].

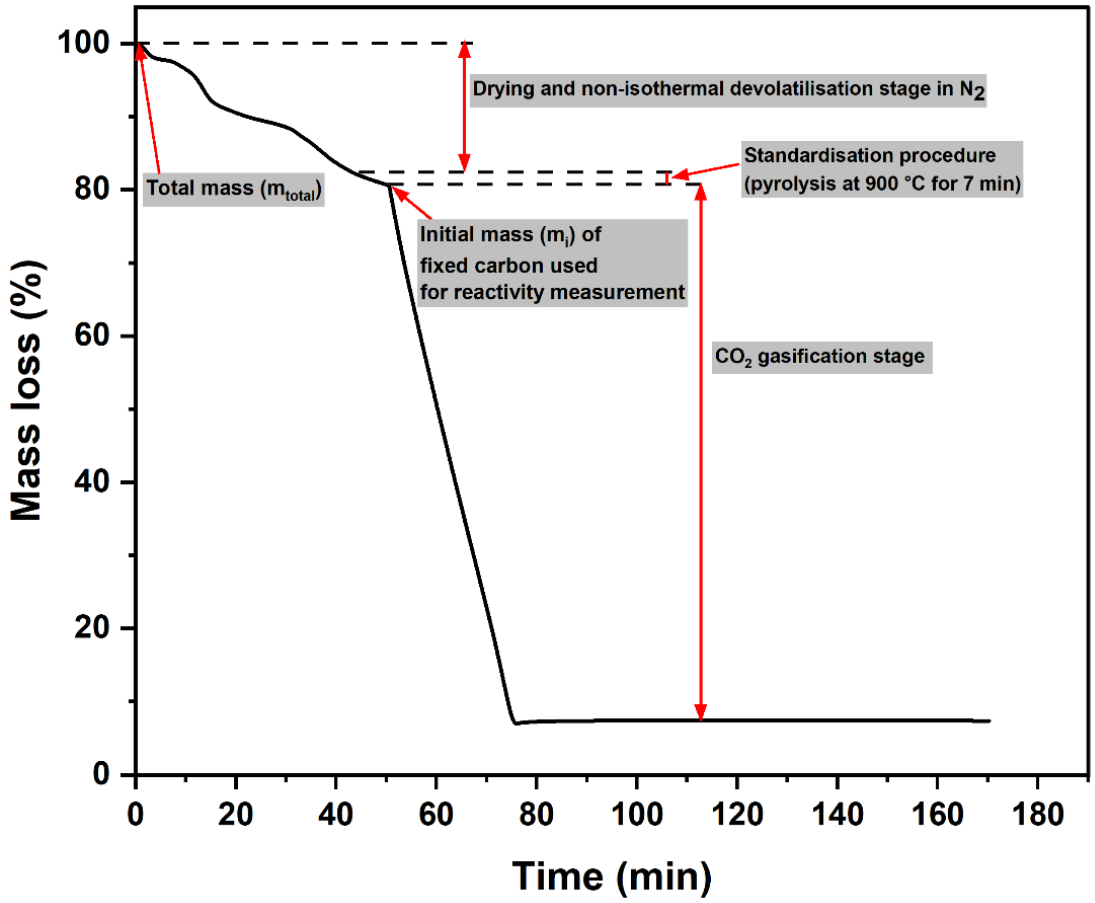

Figure 3.28: Typical TGA curve for isothermal CO_2 gasification test.

The non-isothermal gasification was carried out under the same CO_2 flow rate using same amount of char mass as in the isothermal tests. In this experiment, the char sample was heated from room temperature to 1100°C at three heating rates of 5, 10 and 15°C/min, respectively. The evaluation of gasification reactivity in non-isothermal conditions is further discussed in Section 7.3. The Mettler-Toledo TGA/DSC 3^+ STAR® will be referred to as 'Micro-TGA' in some of the following chapters to distinguish it from the Macro-TGA.

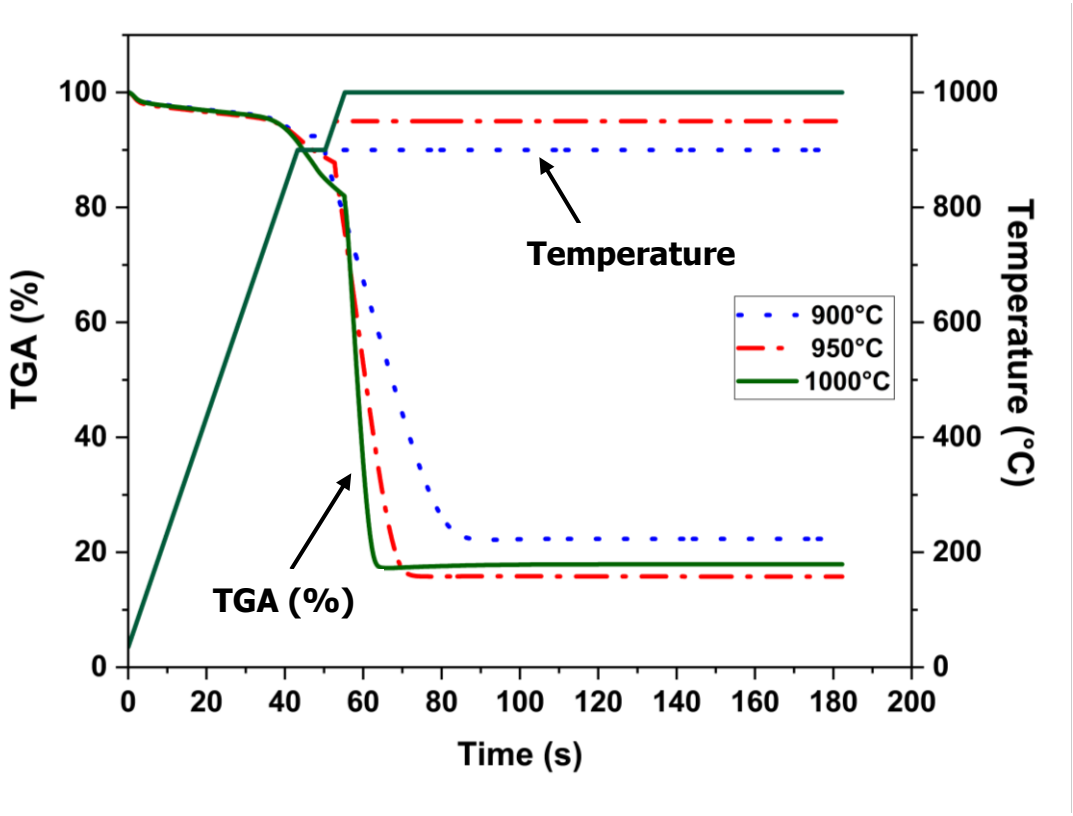

Figure 3.29: Example of TGA profiles and temperature programme of isothermal CO_2 gasification test.

3.14.3 CO_2 chemisorption

Chemical adsorption of CO_2 is used to measure the availability of active sites for CO_2 to combine with the surface of a material. The combination of gas phase CO_2 with the solid sample is essential to the char gasification reactivity [123]. In this work, measurement of CO_2 chemisorption was conducted in the TGA apparatus by following the method described in the literature [88,123]. In each chemisorption test, a platinum crucible was filled with about 40-50 mg of char. Under a N_2 atmosphere, the sample was heated to 850°C with a heating rate of 30°C/min, and the temperature was held for 30 min to

prepare the char surface for the adsorption process. The char sample was subsequently cooled to 300°C at 10°C/min. At that temperature, the sample was held for an additional 30 minutes, and the temperature remained constant until the end of the test. N_2 was then replaced with CO_2, the CO_2 chemisorption proceeded, and the change in the sample weight as a function of time was recorded. In order to eliminate any remaining weakly chemisorbed CO_2 molecules, the gas was switched back to N_2 after 30 minutes of adsorption, and the sample was degassed for another 30 minutes. Throughout the experiment, a constant flow rate of 100 ml/min was employed for the flow of both N_2 and CO_2. The chemisorption experiment was blank corrected by subtracting a blank curve recorded of an empty crucible. Chemisorption temperature programme is presented in Figure 3.30. Standard deviation was used to assess the repeatability of chemisorption measurements. The test was performed in quadruplicate for BC1, BC2, BC4 and HC; in triplicate for BC3; and in duplicate for CC, BC1HCl and HCHCl.

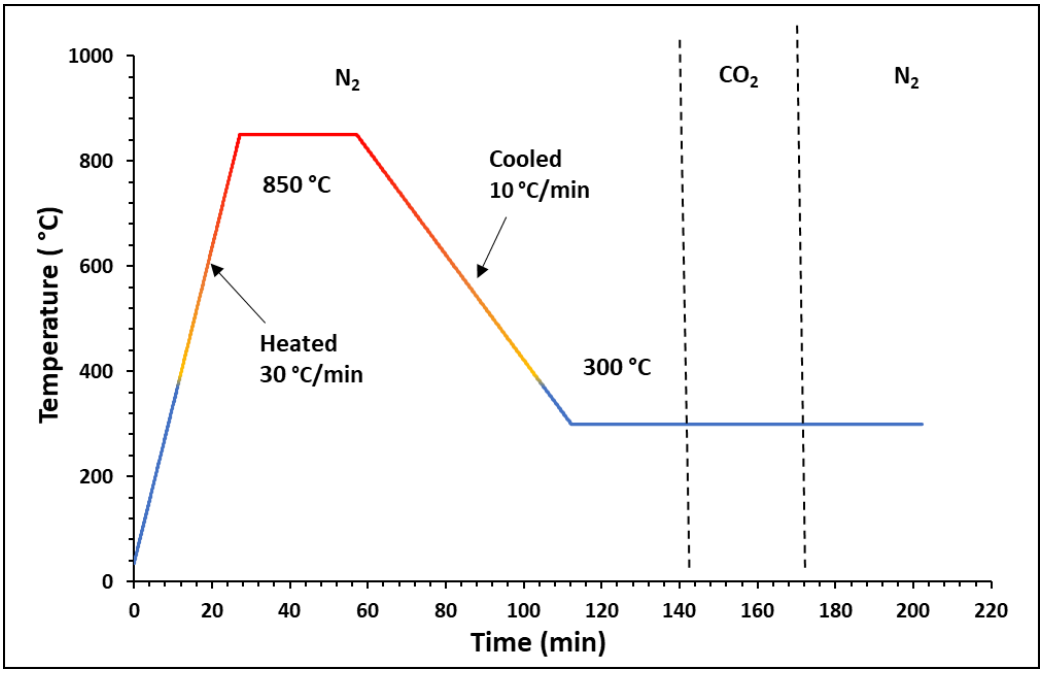

Figure 3.30: temperature programme of chemisorption test.

3.15 Experimental error analysis:

The complexity and the variation of data sets obtained from various examinations carried out in this research were evaluated using statistical analysis. It was crucial to assure the repeatability of the current work, hence, the standard deviation (SD) was used to assess the experimental error, as defined in the following expression:

$$SD = \sqrt{\frac{\sum_i^n (x_i - \bar{x})^2}{n-1}} \tag{3.16}$$

Where x_i represents each individual value from the sample, $\bar{x}$ is the sample mean, and n is the size of the sample.

3.16 Chapter summary

Six char samples were initially prepared and characterised to understand their physical and chemical properties using a variety of analytical techniques. All the characterisation experiments of the char samples were carried out in Cardiff University. The following table summarises the methods and techniques that were used in this chapter and their corresponding determined parameters. It also outlines the limitations of each test.

Table 3.1: Summary of analytical techniques methodology and limitations.

Material/Method/analytical technique	Measured properties/purpose	Limitation	Action
Char samples selection	Different properties under different conditions	Suppliers offer large quantities of requested materials-limited storage space	Available sample was used to understand reverse Boudouard reaction until additional samples were received
Drop tube furnace (DTF)	Production of coal char sample	Small amount was produced at start of this PhD/no enough sample	Proximate analysis in TGA
Ultimate analysis	CHNOS elements	-	-
Carbon and Sulphur analysis	C and S contents	-	-
Demineralisation treatment	Removing inorganic components	-	Proximate analysis in TGA
XRF	Determine which elements should be measure in ICP-OES	-	-
ICP-OES	Elemental composition	-	-
Gas physical adsorption technique	Surface areas, pore volumes, pore sizes distribution and average pore diameters of the samples	-	-
XRD	Mineral phases identification and semi-quantification of mineral composition	Siemens-Diffractometer/D5000 failure	-
SEM-EDS	Morphology and distribution of elements on the surfaces of the chars	-	-
XPS	Surface chemistry parameters	-	-
TGA	Ash content measurement, CO_2 gasification, CO_2 chemisorption	Mettler Toledo TGA-DSC 3+ damage	-

Chapter 4 Development of a Macro-thermogravimetric reactor and experimental procedure

4.1 Introduction

The development and construction of a macro-thermogravimetric reactor (Macro-TGA) are detailed in this chapter. The Macro-TGA was designed and configured specifically for this thesis to study the influence of a larger char sample with a higher surface area on the behaviour of reverse Boudouard reaction. The aim of studying such large samples was to investigate the impact of more realistic fuel particles, rather than relying on small samples of finely ground fuel. This device is a scaled-up version of the conventional TGA and was constructed in the combustion lab in the school of engineering at Cardiff University. The CO_2 gasification reactivity was investigated, and the mass loss of char samples was monitored in real-time using a precise analytical balance with 0.01 g accuracy. The product gas from the gasification system was analysed to validate the thermal balance data. In this thesis, the Macro-TGA was built based on the practical considerations and to meets the lab's safety and operational requirements.

4.2 Design and construction considerations of the Macro-TGA

In this study, the fundamental idea of constructing a Macro-TGA apparatus relies on establishing a thermobalance system capable of precisely measuring the changes in char sample mass during CO_2 gasification. This system is an important approach to investigating the mechanisms of the reverse Boudouard reactivity using a larger sample mass. In the current work, Macro-TGA development is driven by practical and specification requirements. These requirements focused on optimizing the reaction environment and ensuring ease of setup adjustment. The following criteria were considered before constructing the reactor:

1. The gasification system must be built to maintain a steady state conditions during the operation to ensure the constancy.
2. The Macro-TGA is designed to gasify a char sample weighing up to 10 g whether in pellet or powder form.
3. The sample container must be in a fixed position inside the reactor and made of a material that can resist temperatures over 700°C.
4. The sample container must provide the maximum surface area exposed to the CO_2 gas.
5. The setup of the Macro-TGA must give access for loading and removal of the char sample.
6. The height of the sample container and the length of the reactor are established based on the dimensions of the available furnace and product gas sampling accessibility configuration.
7. The thermobalance system must be designed as a top-loading type to minimise the sample holder movement caused by gas flow and furnace expansion.
8. The heating system must provide the temperature range of interest for the reverse Boudouard reaction >700°C.

9. The mass loss of the char sample due must be monitored and recorded in real time using an analytical balance with a precise resolution integrated with a data acquisition system.
10. A slight positive pressure must be maintained within the Macro-TGA to prevent air accessing the system, as this will influence the reverse Boudouard reaction.
11. The temperature inside the Macro-TGA must be continuously monitored.
12. The analytical balance reading must be protected from the high temperature (>700°C) of furnace and its temperature monitored by a thermocouple.
13. The product gas from the reactor must be cooled, cleaned of hydrocarbon condensate and its composition measured.
14. The system must meet the standard health, safety and operational regulations in the laboratory.

4.3 Macro-TGA system components

The Macro-TGA system was developed in accordance with the specifications discussed above. It consists of five main components including gasifier, gas delivery system, heating system, cooling and tar cleaning system, product gas analysis system. A photograph of the experimental rig is shown in Figure 4.1 and a schematic diagram of the system components is illustrated in Figure 4.2. The experimental apparatus construction is discussed in detail in the following sections.

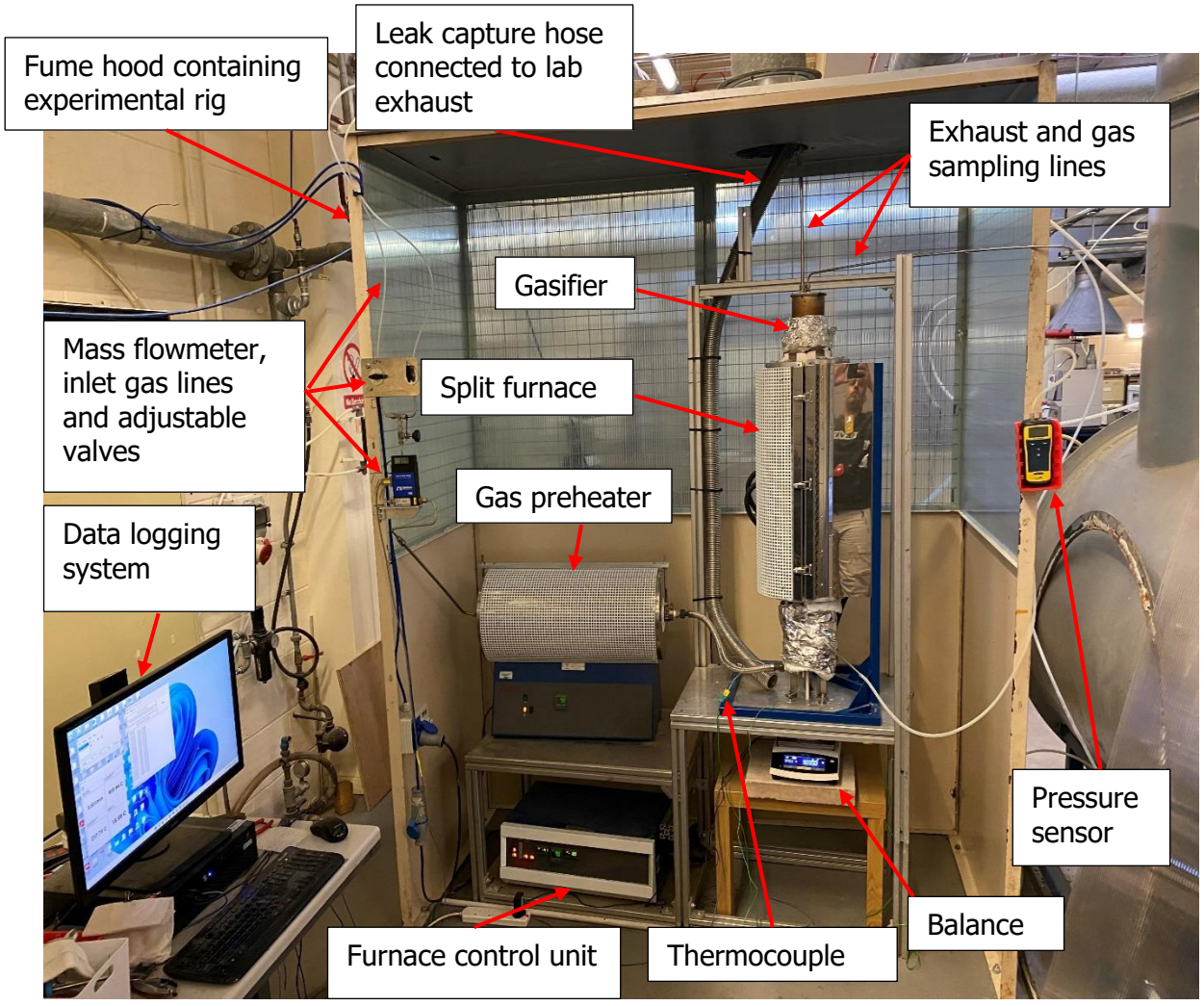

Figure 4.1: Macro-TGA experimental rig setup for CO_2 gasification test.

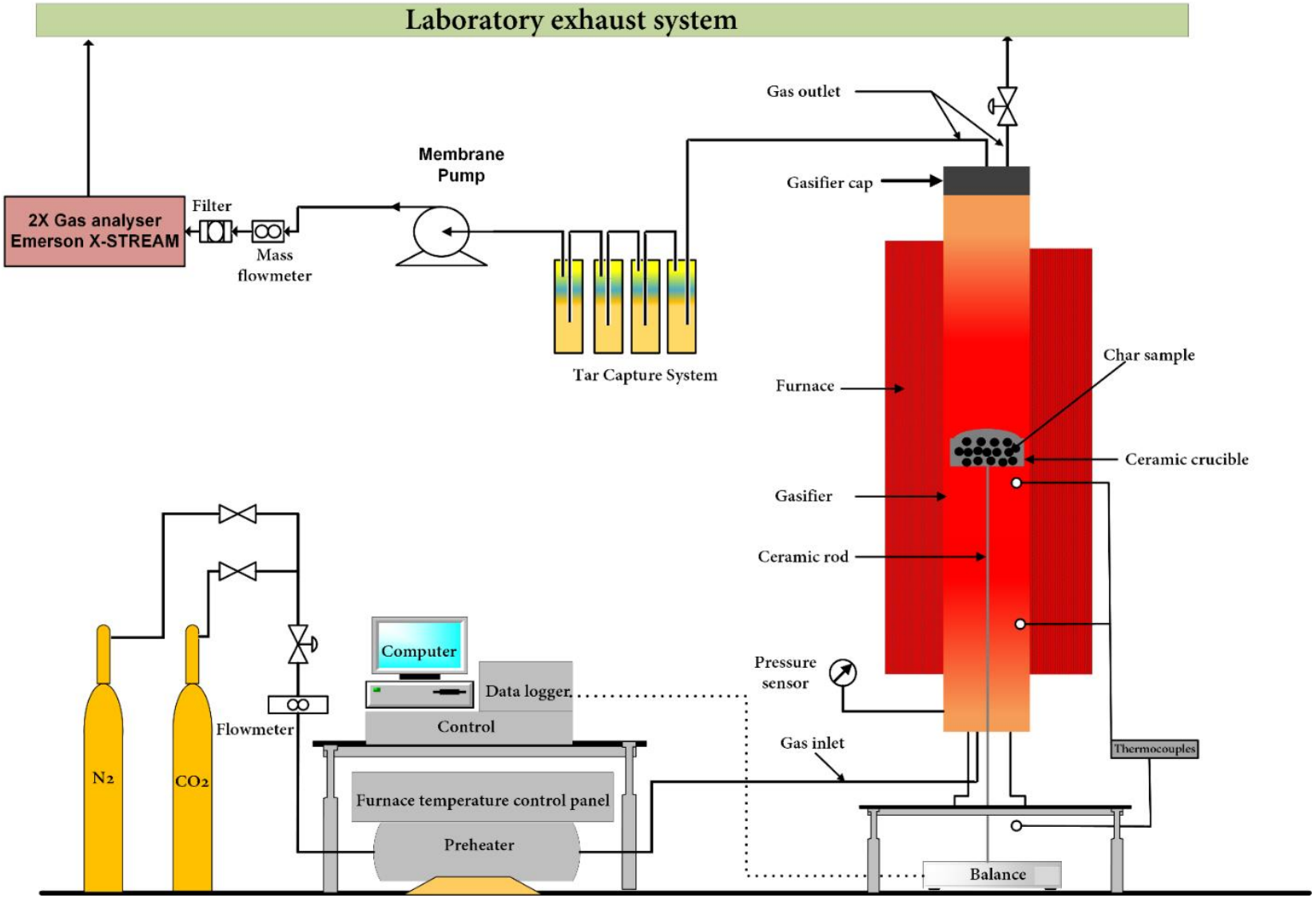

Figure 4.2: Schematic diagram of the Macro-TGA.

4.3.1 Thermobalance development

4.3.1.1 Vertical tube gasifier

The gasifier consists of four main components, upper tube, bottom tube, gasifier cap and sample container (ceramic crucible and ceramic rod). The gasifier setup is visualised in a 3D model drawing in Figure 4.3 (a) and the internal components with the position of the sample container in the gasifier are illustrated in Figure 4.3 (b). It was made of a stainless-steel 304-cylinder with a length of 1000 mm, 77.92 mm inner diameter and 88.9 mm outer diameter. The size of the reactor was selected in accordance with the available furnace height in the laboratory and to provide the maximum allowance for the sample container size.

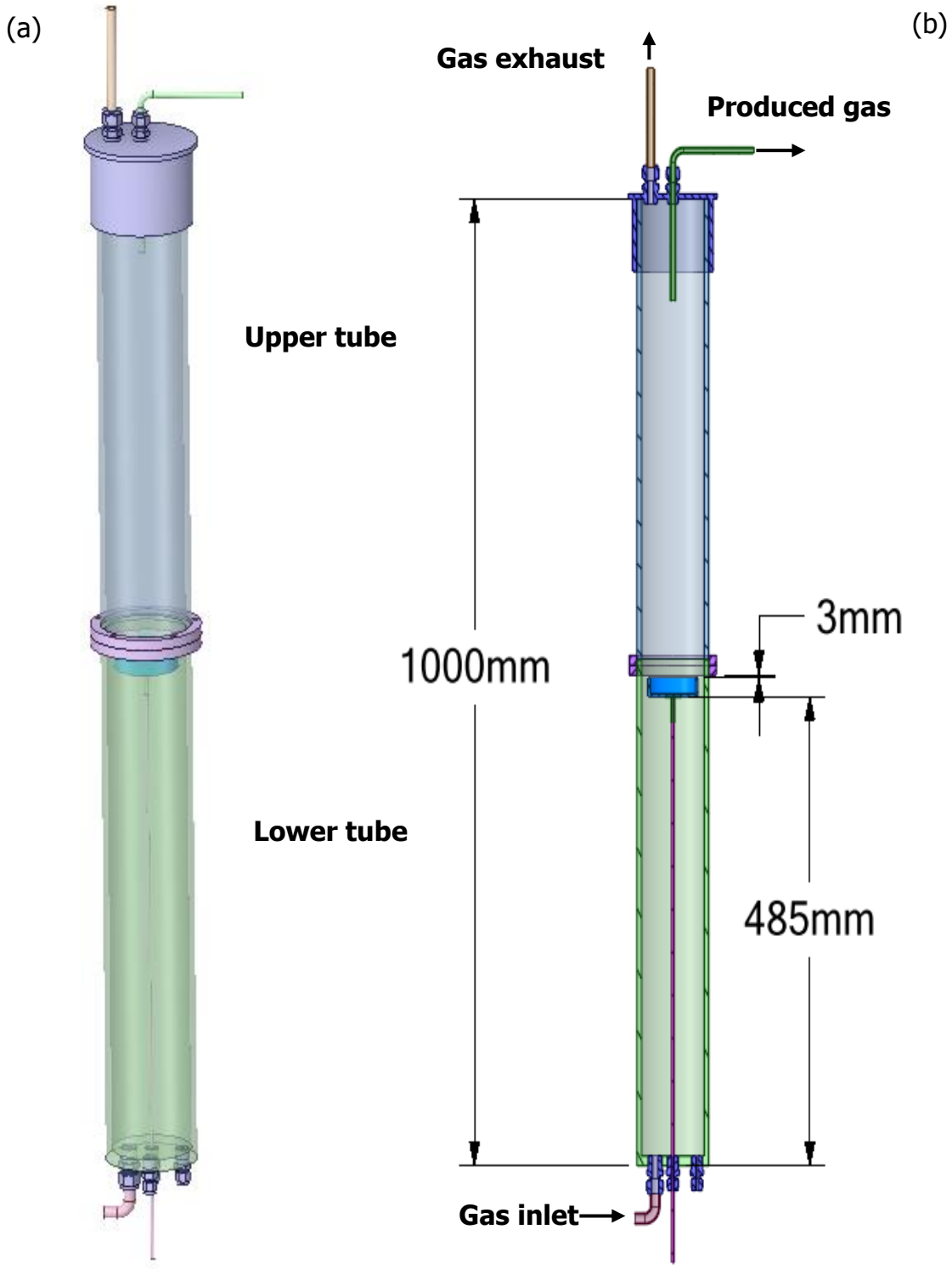

Figure 4.3: 3D model of the gasifier (a) and a cross-section view showing internal components with the position of the sample container in the gasifier (b).

Additionally, the upper and lower tubes were attached to each other by two custom stainless-steel flanges, each with an outer diameter of 108 mm and a thickness of 10 mm. The flange on the top tube was welded 6 mm from the tube's mouth, whilst the flange on the bottom tube was welded 6 mm below the mouth. This configuration enabled the upper tube to rest securely above the lower tube, ensuring a sound connection and sufficiently gastight seal. Figure 4.4 shows the detailed dimensions of both gasifier tubes. On the top of the gasifier, a 90-mm-inner diameter cap was made to close the system for gas sampling on top of the gasifier, but it was slightly loose for safety purposes (i.e. to prevent overpressure in case of ignition of the product CO in the tube). The sampling pipe was positioned in the middle of the gasifier cap and projected down inside the gasifier by 100 mm. The exhaust line was equipped with a control valve to control the gas stream, as shown in Figure 4.5. This is to guarantee a slight positive pressure to prevent the air from entering the system so the reaction will not involve any combustion. This was further adjusted by increasing the carrier gas flow.

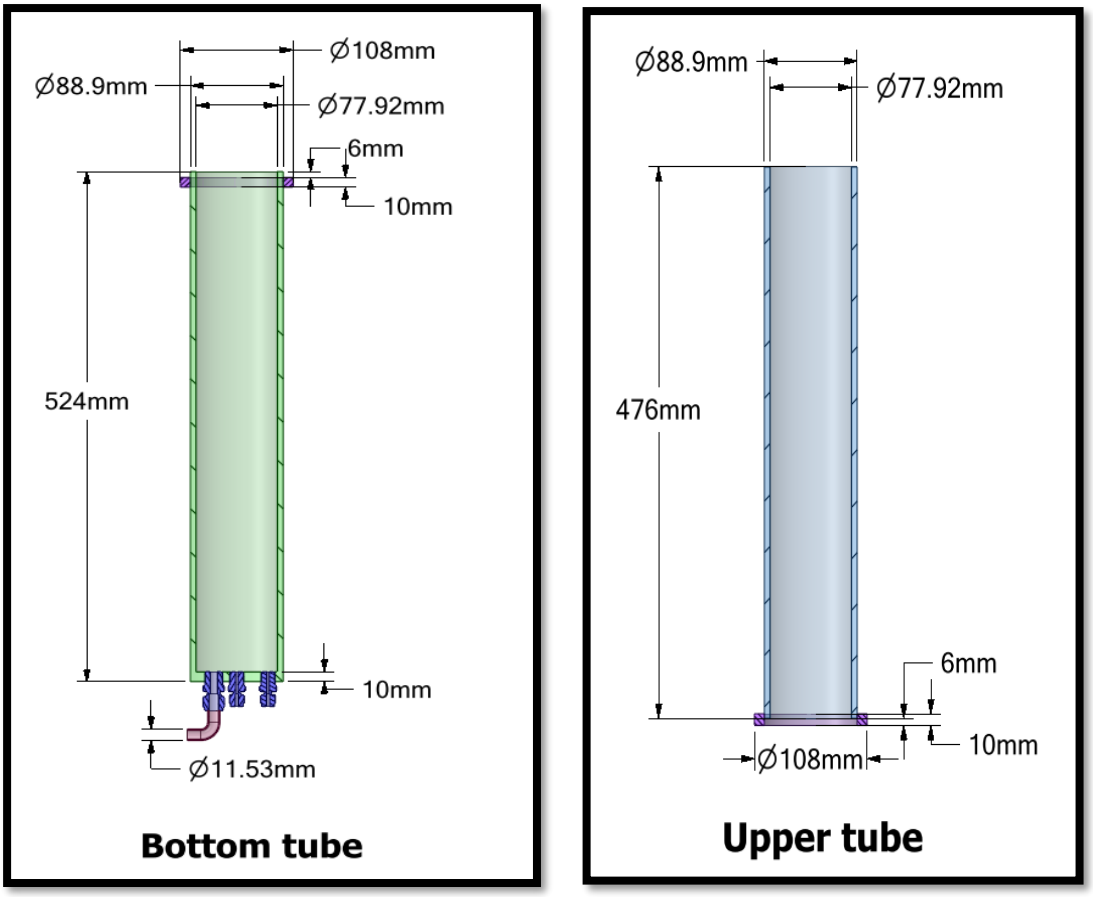

Figure 4.4: Detailed dimensions of the gasifier (bottom and upper tubes).

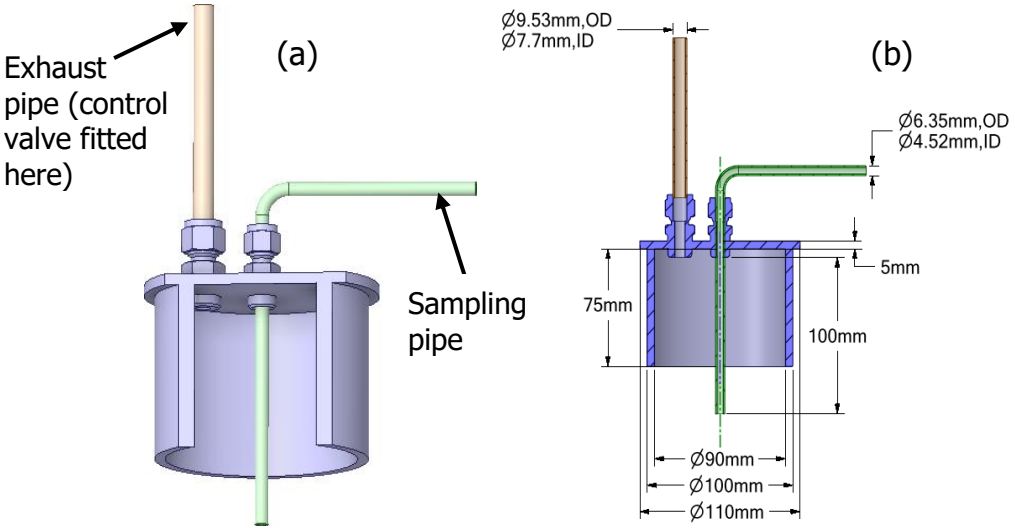

Figure 4.5: The gasifier cap showing exhaust and gas sampling pipes (a) with detailed dimensions (b).

4.3.1.2 Fixed bed sample container

Two fixed bed holder setups were developed to assess the stability of the mass measurement during CO_2 gasification experiments. Figure 4.6 shows photographs of the two setups. The aim was to identify which configuration provided more stable and reliable mass readings during the reaction.

In the first setup, the fixed-bed holder system of the char sample was made of a 99.8% alumina material by 4-visa and Almath suppliers. The container system consisted of a crucible, 3 mm rod and bush, this is shown in Figure 4.7 (a) and (b). These ceramic parts were specifically made for this project and are suitable for high-temperature applications of up to 1750°C, making them excellent for the gasification experiments. A 56.4 mm inner diameter of the crucible was selected to increase the surface area for the reverse Boudouard reaction which was deemed suitable to investigate the influence of this physical property on the reaction mechanism. The crucible was placed onto the ceramic rod by the bush and glued using an alumina ceramic adhesive (Resbond® 940HT) stable up to 1540°C [183]. The design itself was made to provide convenient crucible loading and unloading of the char sample.

The same crucible and adhesive were used in the second setup, but the ceramic rod was replaced with a 12 mm diameter rod and supported by a stainless-steel block. The crucible was directly attached to the top of the rod and the rod was fixed securely into the block to improve mechanical stability. A detailed evaluation of how the rod diameter influences the stability of the Macro-TGA balance system and selectin of the suitable setup is presented in Chapter 8.

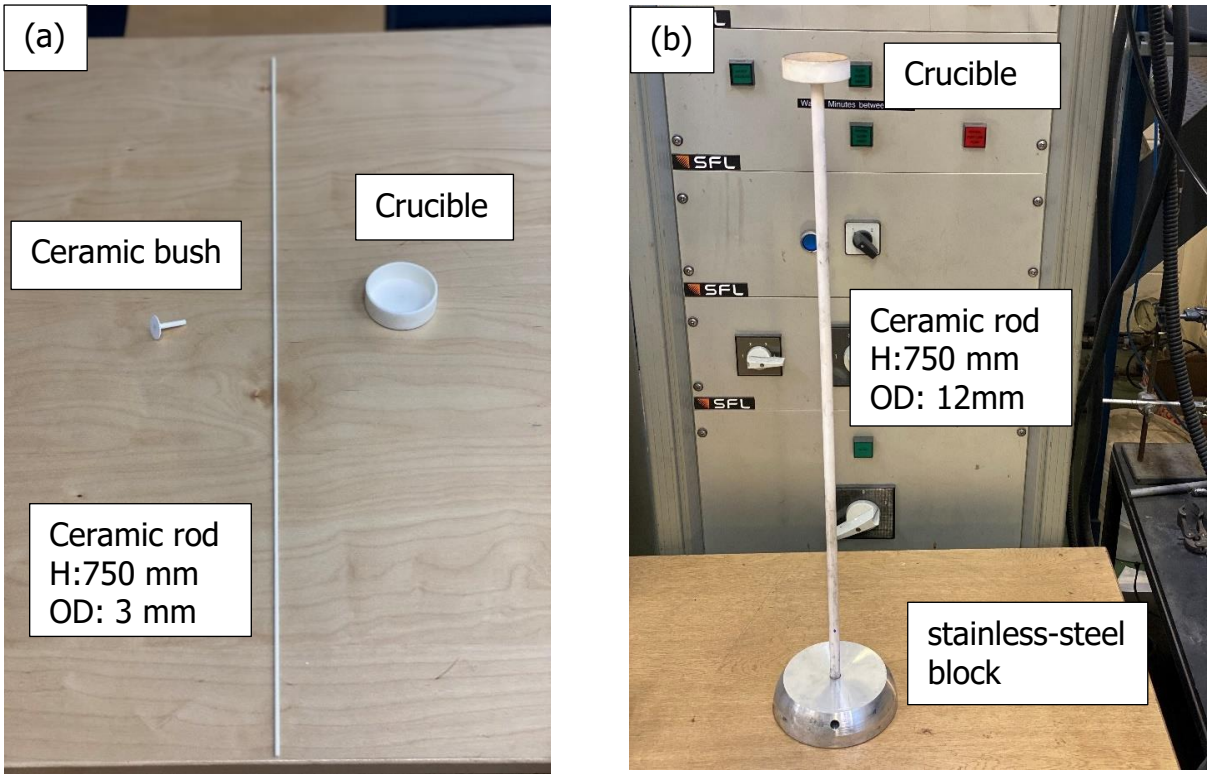

Figure 4.6: Fixed bed setup using 3 mm ceramic rod (a) and 12 mm ceramic rod (b).

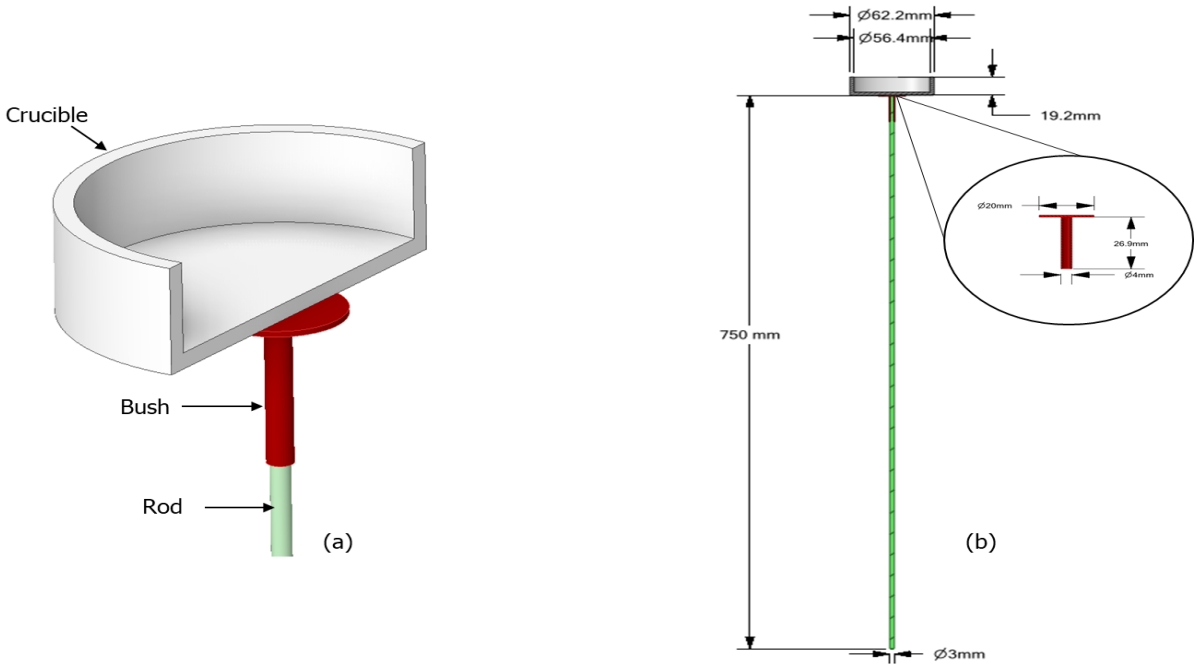

Figure 4.7:Char sample container of the Macro-TGA using 3 mm rod: crucible, bush and rod; setup (a) and detailed dimensions (b).

4.3.2 Gas flow dynamic in the gasifier

The desorption of the producer gas in the solid-gas reaction plays a critical role in determining the gasification reaction rate. In the reverse Boudouard reaction, carbon monoxide can build up within the porous structure of the char sample causing nonuniform CO_2 gasification [1]. Such a phenomenon can occur when the transportation of carbon monoxide from the reaction site to the bulk gas phase is hindered by an ineffective CO_2 flow profile in the gasifier. This can lead to accumulation of the carbon monoxide above the crucible, thus occupying the active reaction sites on the char surface and inhibiting further reaction. Therefore, maintaining optimal conditions of CO_2 flow within the gasifier is crucial in this work to ensure a smooth transportation of the product gas. This can be achieved by keeping the Macro-TGA in a laminar environment during the gasification process, which can be observed by maintaining a Reynolds number below 2000. Figure 4.8 is a representation of the gas input flow throughout the system.

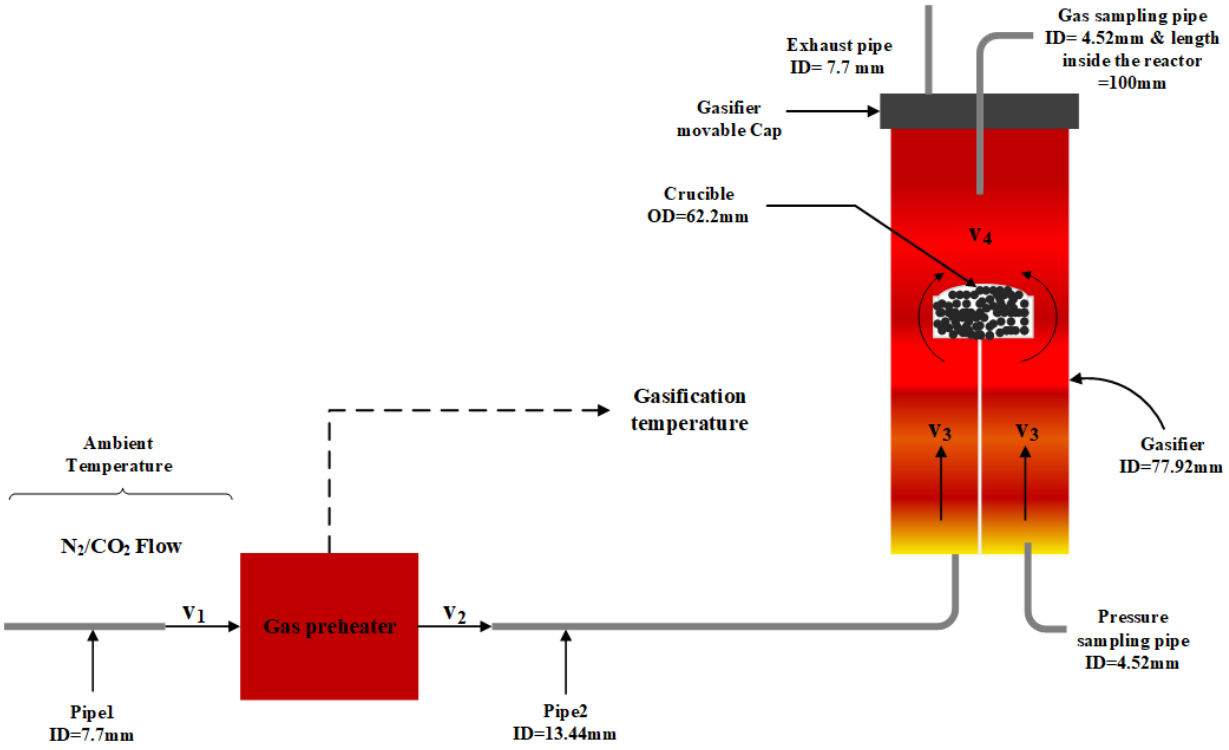

Figure 4.8: Schematic diagram of the gas input velocities through the Macro-TGA.

The Reynolds number can be calculated using Equation 4.8, based on CO_2 velocity profile above the crucible (v_4) and gasification temperature. The velocities of CO_2 in the system depend on the selected CO_2 volumetric flow rate that is required to completely convert the char sample and produce carbon monoxide. The CO_2 flow rate can be estimated by determining the theoretical yield from the reverse Boudouard reaction based on the moles of CO_2 needed to convert 5 g of the char sample as well as using the reaction time profile obtained from the Micro-TGA experiments, as presented in Chapter 6.

The following equations were used to determine the CO_2 velocities in the system thus measuring the flow type above the crucible.

CO_2 velocity in the cold condition at pipe 1 can be calculated using the following equation:

$$v_1 = \frac{Q_1}{A_{pipe_1}} \tag{4.1}$$

Where Q_1 is the CO_2 volumetric flow rate at pipe1 in m^3/s and A_{pipe_1} is the cross-section area of pipe 1 in m^2.

To determine the cross-section area of a pipe, the following equation can be used:

$$A = \frac{\pi}{4} d^2 \tag{4.2}$$

Where d is the diameter of the pipe in m. The gas exits the preheater at the gasification temperature which will change its density, but the mass flow rate will remain constant and can be used to measure the new CO_2 volumetric flow rate as follows:

$$\dot{m}_1 = \dot{m}_2 = \dot{Q}_2 * \rho_2 \quad (4.3)$$

Where $m_{\dot{1}}$ and $m_{\dot{2}}$ are the CO_2 mass flow rate in kg/s and ρ_2 is CO_2 density at the gasification temperature in kg/m^3. Using the $Q_{\dot{2}}$ value in the following equation to determine the velocity:

$$v_2 = \frac{Q_{\cdot 2}}{A_{pipe_2}} \quad (4.4)$$

Where A_{pipe_2} is the cross-section area of pipe 2 in m^2. The velocities inside the gasifier, v_3 and v_4, can be calculated using the continuity equation as follows:

$$A_{pipe_2} v_2 = A_{gasifier} v_3 \quad (4.5)$$

$$A_{gasifier} v_3 = A_n v_4 \quad (4.6)$$

Where $A_{gasifier}$ and A_n is the cross-section area of the gasifier and the narrow area between the crucible wall and the gasifier wall, respectively. A_n can be found using the following equation:

$$A_n = A_{gasifier} - A_{crucible} \quad (4.7)$$

Once the velocities are calculated, the Reynolds number can be estimated to characterise both the overall gasifier flow and the local flow above the crucible using the following equation:

$$Re = \frac{\rho_2 * v * D}{\mu} \tag{4.8}$$

Where μ is the CO_2 dynamic viscosity in kg/m.s. The values of D and v depend on the flow region: for the overall gasifier flow, D is the inner diameter of the gasifier and $v = v_3$ (inlet velocity); for the local flow above the crucible, D is the hydraulic diameter of the annulus and $v = v_4$ (velocity around the crucible). The dynamic viscosity was calculated according to Sutherland's Law:

$$\mu = \mu_{ref} \left(\frac{T}{T_{ref}}\right)^{1.5} \frac{T_{ref} + S}{T + S} \tag{4.9}$$

where T is the gasification temperature in Kelvin. μ_{ref}, T_{ref} and S are the reference viscosity (1.37×10^{-5} kg/m.s), reference temperature (273K) and the Sutherland Constant for the CO_2 (222K), respectively [184].

The calculation was based on the assumption that changing the flow direction in the bottom of the reactor will cause a slight turbulent flow in this area, but it was neglected since the gasifier length smoothes-out the gas flow once it reaches the top of the crucible. The results indicated that the crucible is in laminar flow and can be seen in Table 4.1.

Table 4.1: CO_2 flow dynamics and calculated Reynolds number at the top of the crucible in the Macro-TGA at gasification temperature of 1000 °C.

CO_2 flow rate (L/min)	Gasification temperature 1000 °C						
	v_1 (m/s)	v_2 (m/s)	v_3 (m/s)	v_4 (m/s)	$Re_{crucible}$	$Re_{overall}$	Flow regime
1	0.36	0.52	0.02	0.04	5.97	10.74	Laminar
2	0.72	1.04	0.03	0.09	11.91	21.47	Laminar
3	1.07	1.56	0.05	0.13	17.91	32.21	Laminar
4	1.43	2.08	0.06	0.17	23.88	42.95	Laminar
5	1.79	2.50	0.08	0.21	29.85	53.69	Laminar

4.3.3 Carbon dioxide and Nitrogen delivery system

Two compressed gas cylinders were used to supply a continuous stream of carbon dioxide and nitrogen to the gasification rig. The cylinders were fitted with regulator valves and the maximum outlet pressure was set to 0.5 bar to meet safety operation requirements. The gases were delivered to the system via a flexible PVC pipeline with two isolation valves placed upstream of the mass flowmeter to control the gas flow input to the system along with a control valve to adjust the gas flow rate. The mass flowmeter was an Omega-FMA1818A model which offers a flow range of 0.0 to 5.0 standard litters per minute (slm). The mass flowmeter was manufacturer calibrated using dry nitrogen gas at 21.1°C with a deviation within ±0.13% of the reading. It was necessary to perform a calibration correction when switching the gas between N_2 and CO_2 as recommended in the user manual [185]. The calibration conversion is based on thermophysical properties of both gases, which are determined using Equation 4.10 and then used in Equation 4.11 to calculate the correction factor. The actual volumetric flow of CO_2 can then be measured using Equation 4.12. In this thesis, the correction factor K value of CO_2 relative to N_2 was 0.7382 [185].

$$K_{gas} = \frac{1}{d \times C_p} \tag{4.10}$$

$$K = \frac{\dot{Q}_{CO_2}}{\dot{Q}_{N_2}} = \frac{K_{CO_2}}{K_{N_2}} \tag{4.11}$$

$$\dot{Q}_{CO_2} = \dot{Q}_{N_2} \times \mathrm{K} \tag{4.12}$$

Where d is the gas density at STP (1.964 g/L for CO_2 and 1.25 g/L for N_2) and C_p is coefficient of specific heat at STP (0.2016 cal/g.K for CO_2 and 0.2485 cal/g.K for N_2) [186]. K_{CO_2} and $K_{N_2}$are factors of CO_2 and N_2, respectively. $\dot{Q}_{CO_2}$, $\dot{Q}_{N_2}$ and K are mass flow rate of CO_2 and N_2 in L/min and the correction factor of CO_2 relative to the reference gas (N_2), respectively.

During the initial system testing, a flow rate of 3.5 L/min N_2 was selected to maintain a slight positive pressure before reaching the required the desired gasification temperature. For the gasification experiments, CO_2 was adjusted to 2.58 L/min on the flow meter equivalent to an actual flow rate of 1.91 L/min.

4.3.4 Sample mass measurement

The mass changes during the gas-solid reaction were measured in real-time to provide sufficient information about the kinetics and the reactivity of the reverse Boudouard reaction. An analytical top-loading balance, model BCE2202-1S from Sartorius, was used to continuously measure and monitor the mass of the char sample throughout gasification tests. The digital balance had a maximum capacity of 2200 g with an accuracy of 0.01 g. The balance was placed underneath the gasifier and protected from the heat transferred from the gasifier by a metal shelf, while a calibrated thermocouple was installed near to the balance surface to ensure that it operated within its operating temperature. The end of the ceramic rod was placed on the balance and then re-zeroed before running the system. The data were logged via the Smartiux Simple Data Logger (SDL) software [187]. Figure 4.9 is a screenshot of the SDL window. This open access software was developed to record and save the data from balances. The mass changes were recorded every 1 second and then saved to a CSV Microsoft excel file for further analysis.

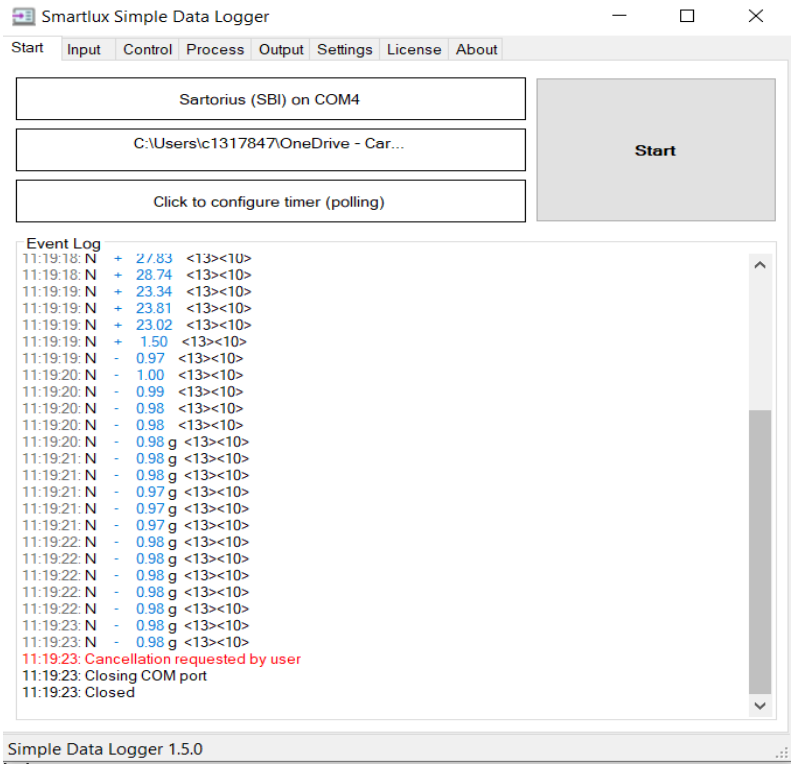

Figure 4.9: A screenshot of the Smartiux Simple Data Logger (SDL) interface window.

4.3.5 Pressure and temperature measurement

Th only reaction to study in this thesis is the reverse Boudouard reaction and occurrence of combustion will negatively produce other gases. Therefore, the Macro-TGA was kept running under a slight positive pressure. To monitor the system pressure, a portable digital pressure meter, model: Digitron PM-20, was connected via a pipe with an inner diameter of 4.52 mm to monitor the pressure. The temperatures in the Macro-TGA were monitored using three calibrated type-K thermocouples. Two of these were installed inside the gasifier at the bottom of the crucible and at the bottom of the gasifier. The last one was attached to the nearest surface of the balance as mentioned in Section 4.3.4. An Omega multiple-channel data acquisition system, model OM-DAQ-USB-2401, was used to receive the signals from the thermocouples. These signals were then converted using Omega DAQ central software, as shown in Figure 4.10. Upon completion of the experiment, the data file was saved and exported to Microsoft Excel for further analysis.

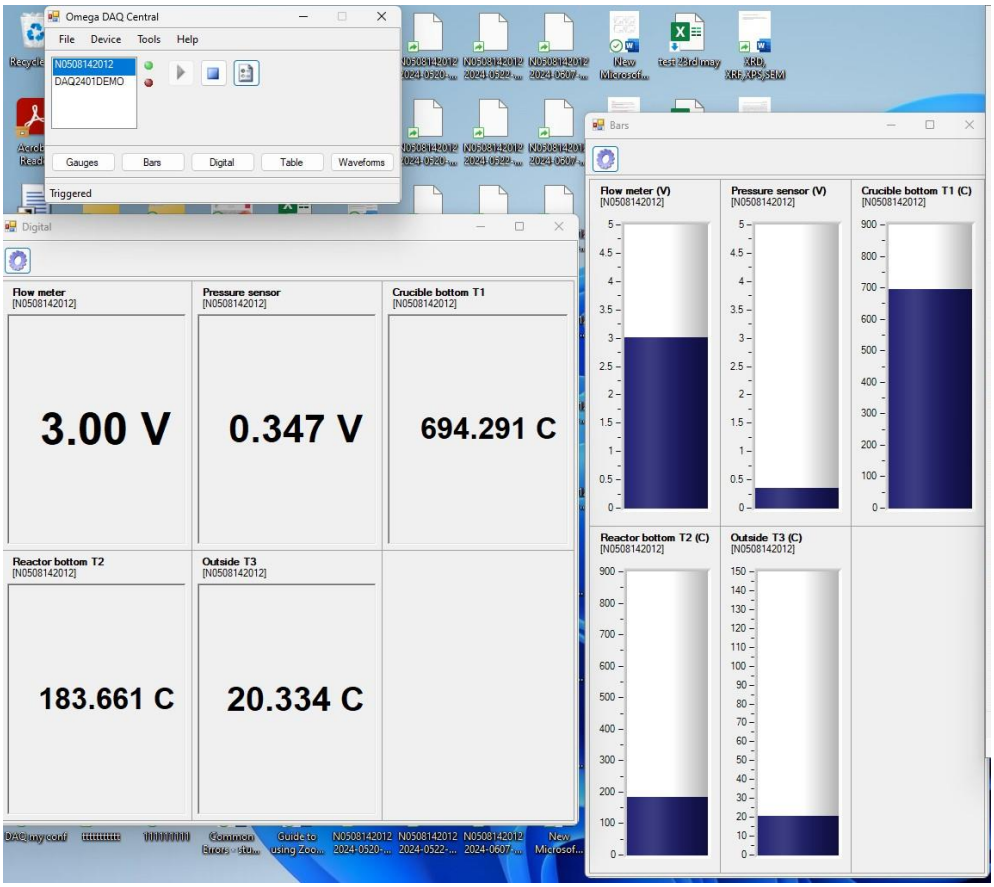

Figure 4.10: A screenshot of Omega data logger system.

4.3.6 Heating system

4.3.6.1 Gasifier heating furnace

An external heating source was used to reach the desired gasification temperatures inside the chamber. The gasifier was heated using a Lenton 3-zone split vertical tube furnace (model number PSC 12/100/600). This electrical furnace included 8 heating elements arranged in parallel: 4 pairs in parallel each pair consisted of 2 in series, with a maximum operating temperature of 1200°C, as shown in Figure 4.11. The furnace was designed to achieve an extended uniform heating zone and was suitable for the current work as it does not have a direct physical contact with the Sartorius mass balance, thereby preventing errors in the mass readings.

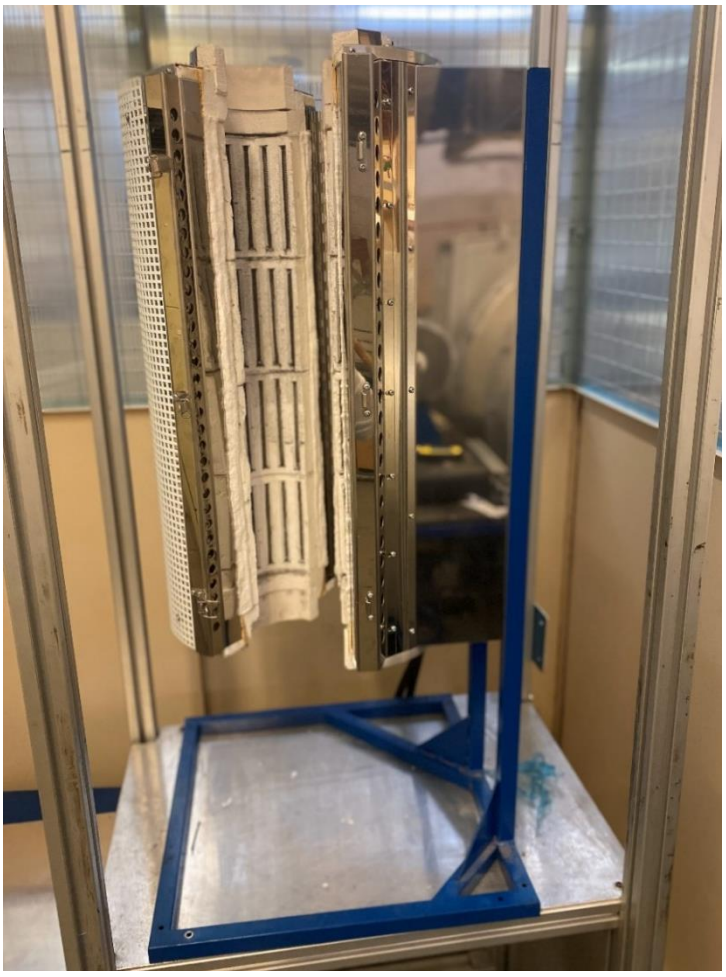

Figure 4.11: Lenton 3-zone split vertical furnace.

4.3.6.2 Gas preheater

A horizontal tube furnace gas preheater unit, a Lenton model number LTF 12/100/940 was used to preheat CO_2 and N_2 before entering the gasifier. This was essential to avoid heat loss within the gasifier that may occur due to the temperature difference between gasification gas agent and gasifier walls. When CO_2 and N_2 are supplied to the gasifier they passed through the preheater which consisted of a tube filled with Impervious Alumina Porcelain (IAP) beads. The beads transfer the heat from the horizontal furnace and the gas. Figure 4.12 shows the gas preheater used in this project.

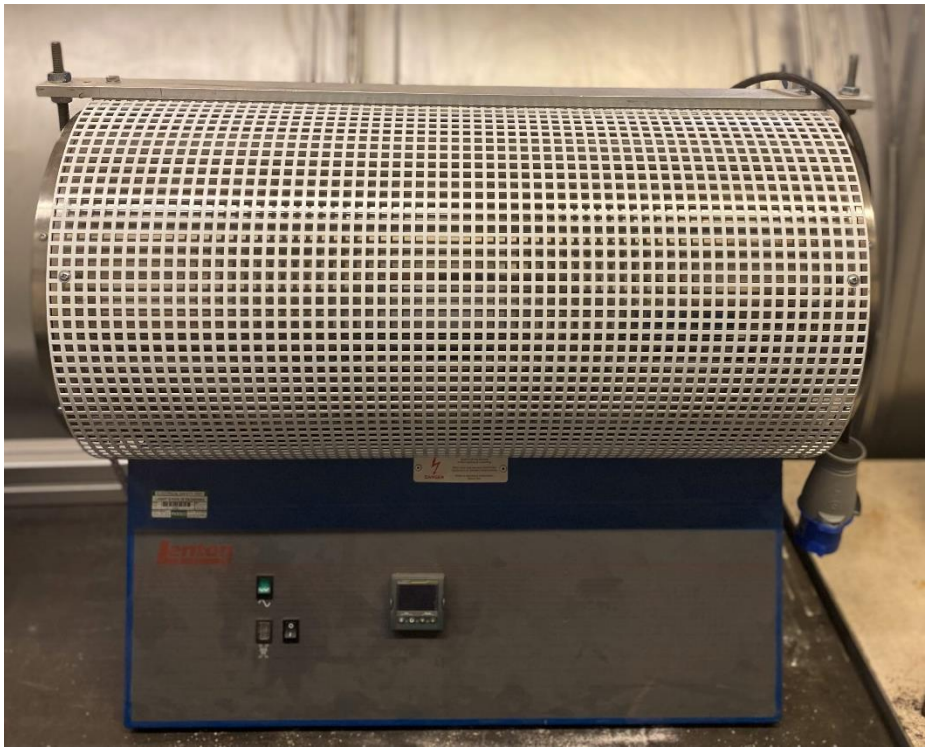

Figure 4.12: A horizontal tube furnace gas preheater unit from Lenton.

4.3.7 Cooling and Tar cleaning system

Four 90 ml glass bottles were placed and secured in a stainless-steel tray filled with water and ice to clean the gas produced from the reactor. Three of them were filled to 90% capacity with liquid isopropanol to dissolve the tar particles. Silica gel crystal grains were used to fill the fourth bottle to capture any solvent carry-over from the first three bottles. A membrane pump was used to suck the producer gas from the reactor and send it to the gas analyser through the tar capture unit. Furthermore, for more cleaning, an empty bottle with similar size to the previous was fitted before the gas analyser This process was set to protect the gas analyser from potential contaminants in the product gas. A bypass condenser was attached to cool the gas. The cooling system consisted of stainless-steel heat exchanger with water as the coolant. A schematic drawing of the tar capture unit is shown in the Figure 4.13 which describes the physical unit as shown in Figure 4.14.

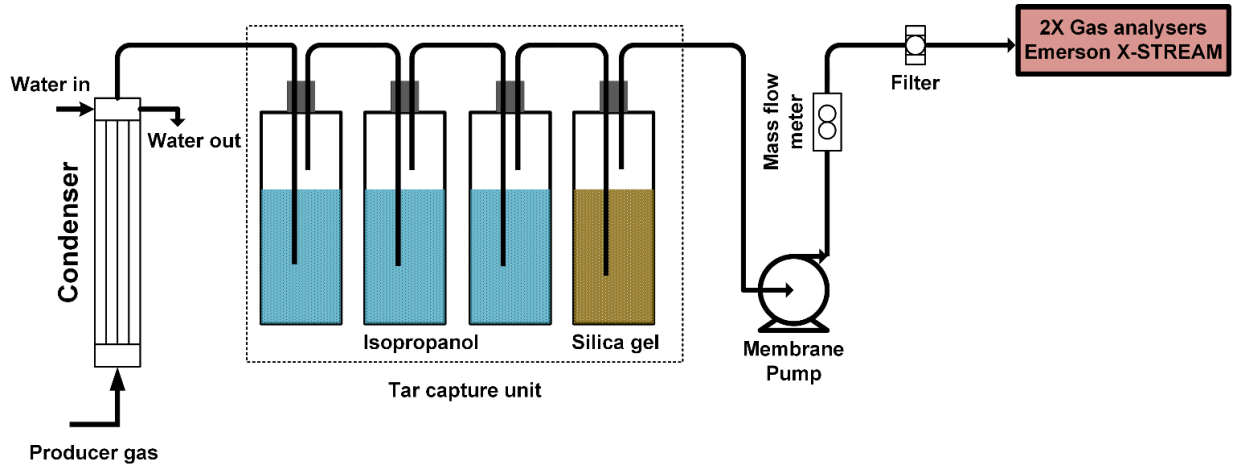

Figure 4.13: Schematic of cooling system and the tar capture unit.

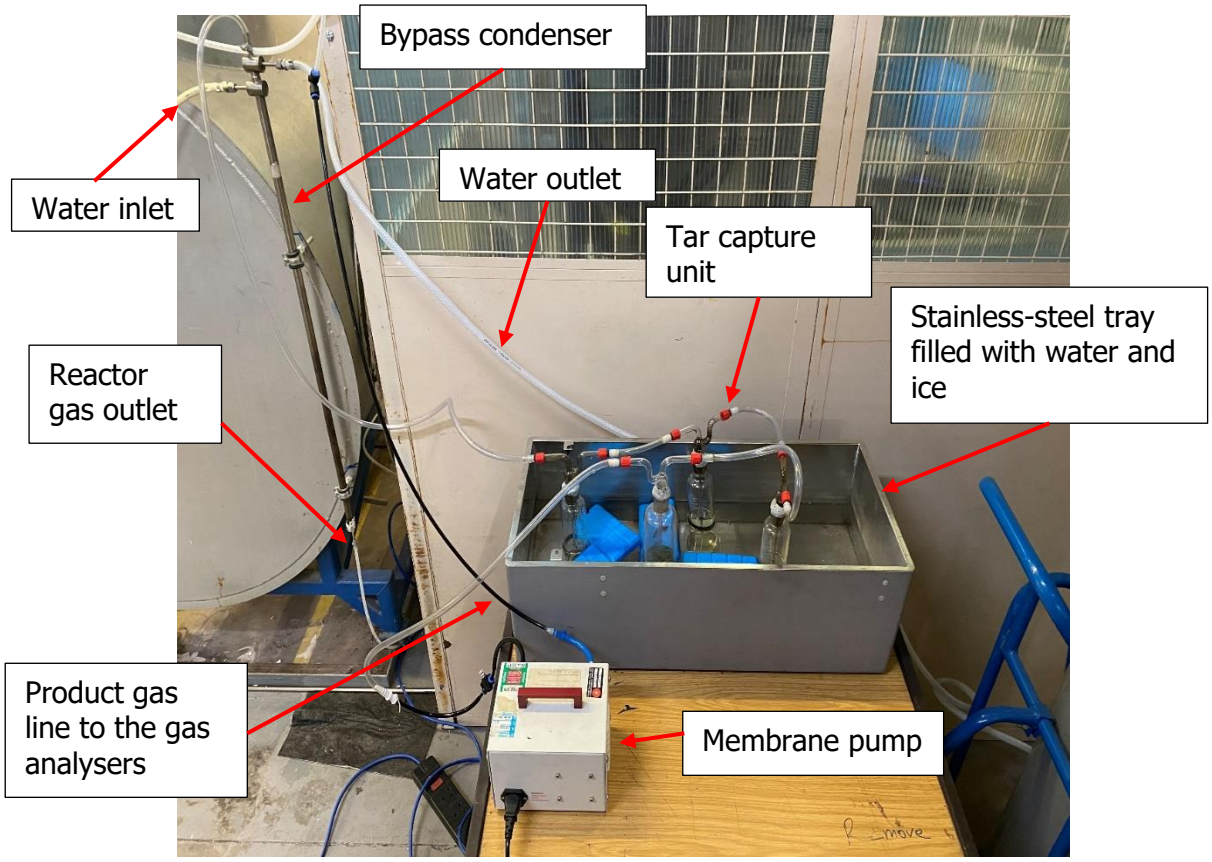

Figure 4.14: Labelled photograph of the cooling system and the tar capture unit.

4.3.8 Gas analysis

The gas produced from the gasifier underwent gas composition analysis using two Emersion X-Stream gas analysers, model numbers XEA04303555317 and XEA04303555319. These gas analysers are labelled as gas analyser 1 and gas analyser 2, respectively, as shown in Figure 4.15. The gas analysers were configured to detect and measure the gas concentrations in volume percent (vol%) of CO, CO_2, CH_4, H_2 and O_2. However, during the initial testing the CO_2 channel was significantly fluctuating, for that gas analyser 1 was employed to measure CO_2 concentration for comprehensive gas analysis. The devices were connected in series as shown in the diagram in Figure 4.16.

In addition, a rotameter was used to adjust the flow rate of the product gas within the range of 0 to 1 L/min before being directed to the analysers inlets. Both Emerson analysers were equipped with X-Stream XE software to record and visually monitor gas concentrations over time.

In this thesis, it was crucial to obtain precision readings of the reverse Boudouard reaction product gas through the gas analysers as this will be used to validate mass changes of the char samples. Therefore, two step calibrations for the gas analysers were performed prior to commencing the experiments. At the beginning, N_2 was purged through the product gas line in order to eliminate existing gas residues and reset the gas analyser channels to zero. Then, gas analysers were exposed to a span calibration, which is a process involving applying a known concentrations of gas mixture to the corresponding gas sensors. The span gas concentrations comprised CH_4 (5%), CO_2 (15%), H_2 (15%) and CO (15%).

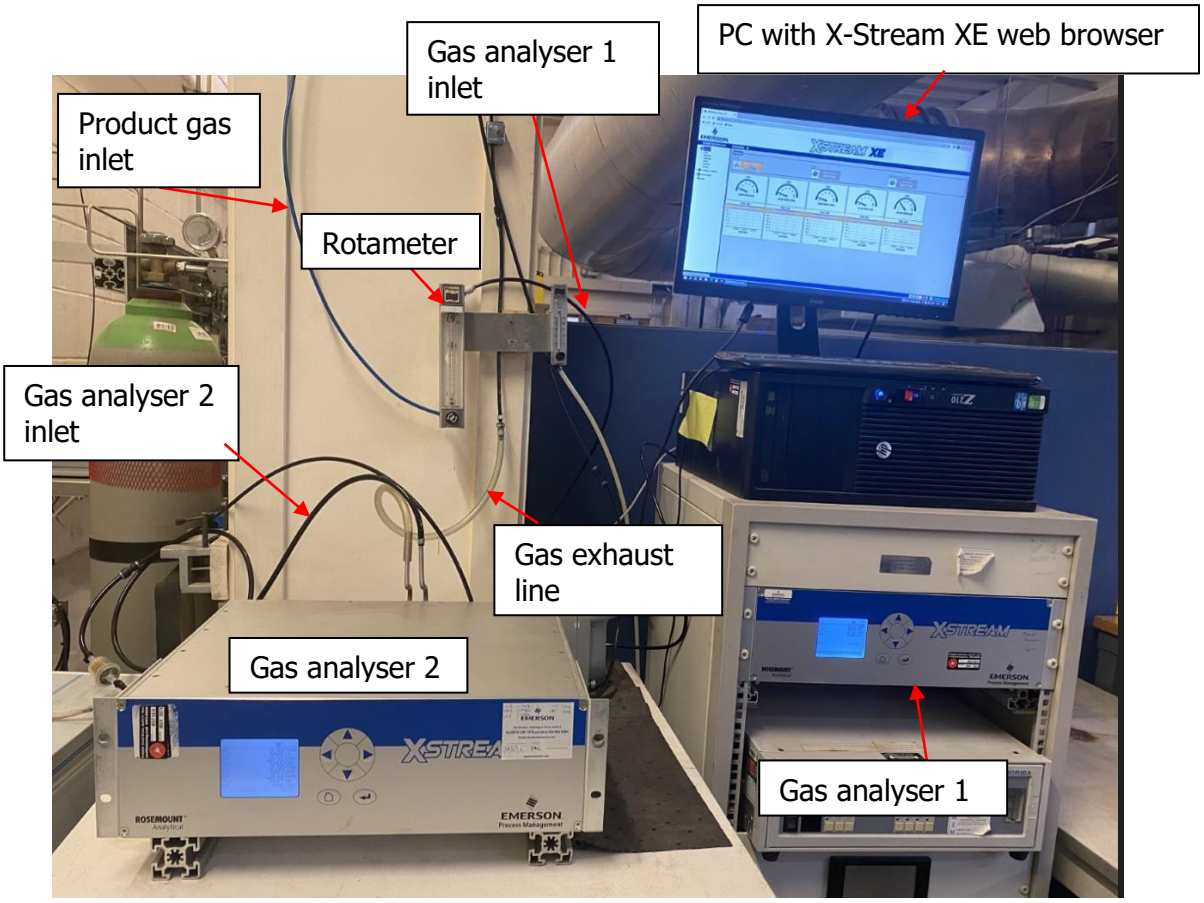

Figure 4.15: Emerson X-Stream gas analysers.

Once the experiment was finished, the recorded volumetric percentage of the detected gases was saved and stored in text files for subsequent analysis.

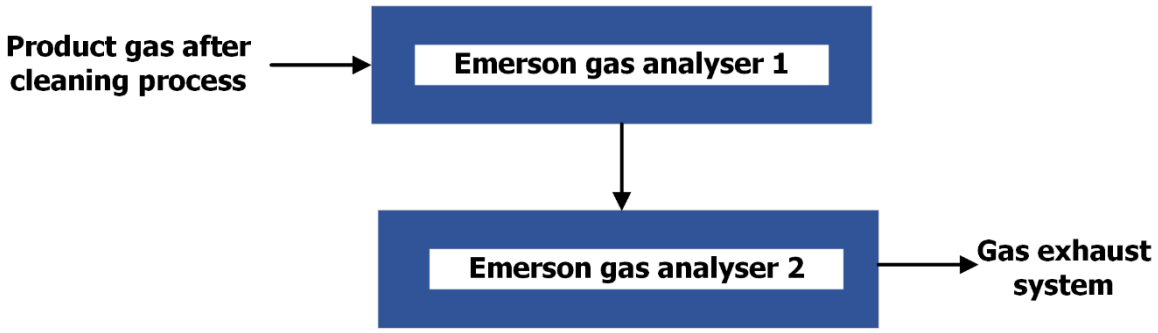

Figure 4.16: Series connection diagram of Emersion X-Stream gas analysers.

4.4 CO_2 gasification Experimental procedures in the Macro-TGA

The Macro-TGA experimental rig procedures were undertaken to establish a carefully controlled environment for robust repeatable tests and to ensure laboratory users safety. The procedures were as follows:

1. In all cases the lab extraction system must be on all the time and a personal gas safety monitor should be worn during the tests.
2. Open the cold vertical split furnace and remove the gasifier cap and the upper tube of the reactor carefully to prevent the ceramic rod and crucible from being damaged. Then, remove the crucible to add the char sample material.
3. Place 5 g of the pulverised dried sample (see Section 3.5.2) or pellets (see Section 3.5.3) onto the crucible and spread it evenly.
4. Return the crucible inside the gasifier by placing it above the ceramic rod.
5. Once the crucible is placed in position, close the upper tube part and cover it with the gasifier cap.

6. Close the furnace door and turn on both N_2 and CO_2 cylinders to 0.5 bar.
7. Ensure all pipework is connected and sealed properly before any runs.
8. Prepare the tar trap system by filling the assigned bottles with both isopropanol and silica gel as explained in Section 4.3.7.
9. Activate the gas preheater (900°C) and the split furnace to the desired gasification temperature.
10. Turn on the mass flowmeter and let it warm up for 15 min to stabilise the reading.
11. Purge the system at 3.5 L/min N_2 until no further change was observed in the mass, then switch N_2 off to introduce CO_2 at a corrected flow rate of 1.91 L/min to the system (as shown in Section 4.3.3).
12. Record both readings of the char sample mass and the product gas using the balance and the gas analysers.
13. The experiment should run until no more mass changes are observed and the product gas remains constant.
14. Switch off CO_2 and purge N_2 into the system to cool down the system and remove any existing gases from the lines.
15. Switch off the temperature control panel and allow the system to completely cool down.

4.5 Health and Safety considerations

A health and safety assessment were carried out prior to the Macro-TGA system's operation. The assessment included a Risk assessment (RA) and a Control of Substances Hazardous to Health (COSHH) assessment forms of the potential hazards and the control measures following the School of Engineering guidance documents. Table 4.2 summarises the activities that were determined as potential hazards associated with the gasification rig operation, along with the control measures were undertaken. The full documents are in the Appendix A.

Table 4.2: Potential hazards associated with the gasification rig operation and the control measures.

Work Activity	Hazard	Control Measures
High temperature surfaces: pipes, furnace, preheater	Burns	Thermal gloves will be worn when handling hot materials
Using electrical equipment	Electric shock	All electrical equipment will be PAT tested
Gas cylinders	Explosion	Cylinders will be used in accordance with cylinder regulations
Moving around testing area	Trips/slips	Working area will be maintained tidy, any trip hazards will be identified and removed
	Production of carbon dioxide, carbon monoxide, hydrogen and hydrocarbon, risk of asphyxiation, poison or fire	Ensure area is well ventilated during experimentation by turning the extraction on, personal gas monitor to be worn (CO detector), lab gas monitor, masks to be worn
	Carbon Dioxide, Nitrogen	Stored in pressurised cylinder, used in accordance with cylinder regulations
	Isopropanol	Stored in suitable labelled container, gloves to be worn

4.6 Chapter Summary

In this methodology chapter, a detailed description of the development of the Macro-TGA that was built in the combustion lab at the School of Engineering at Cardiff University. The aim of scaling-up the conventional TGA was to investigate the CO_2 gasification reactivity of a larger char sample with a high surface area, simulating real industrial conditions. It was used to test the hypothesis of this PhD study by comparing the reverse Boudourd mechanisms in different conditions. The experimental results obtained using the Macro-TGA are presented and discussed in Chapter 8.

Chapter 5 Kinetic modelling of char gasification

5.1 Introduction

This chapter describes kinetic analysis of CO_2 gasification of different chars using three kinetic models, namely, the Volumetric model (VM), the Grain model (GM) and the Random pore model (RPM). The theoretical background of each model was briefly discussed to understand their fundamental assumptions. Furthermore, this chapter explains the calculation procedures to determine reaction rate constant, activation energy and pre-exponential factor from the models at different thermal conditions.

5.2 Kinetic Models

The gasification reaction rate of char is often used to describe the universal gasification reaction of carbonaceous material as a function of conversion, temperature and pressure using the following equation [96]:

$$\frac{dX}{dt} = k\left(T, P_{CO_2}\right) f(X) \tag{5.1}$$

Where k is the apparent gasification reaction rate constant, which is dependent on the reaction temperature (T) and CO_2 partial pressure $\left(P_{CO_2}\right)$, and $f(X)$ is a conversion function that indicates the reaction model being employed for the gasification process. The Arrhenius equation can be used to define the reaction rate constant k under the assumption that the partial pressure of CO_2 remains constant while the reaction proceeds and is only influenced by temperature, which is given by:

$$k = A_0 e^{-E/RT} \quad (5.2)$$

Where A_0, E and R are the pre-exponential factor, activation energy and universal gas constant, respectively.

Understanding kinetics is crucial for CO_2 gasification operations, as it offers valuable information about the rate and mechanisms of reactions, thus enabling for the improvement of operating conditions and reactor design to achieve higher conversion or thermal efficiency [188,189]. The following sections briefly describe the fundamentals of the commonly used kinetic models for CO_2 gasification [190–193].

5.2.1 Volumetric model

The volumetric model (VM) [194], also referred to as the homogeneous model is based on the assumption that the interaction between the solid particle and the reactant gas occurs uniformly throughout all active sites within the char particle, whether located externally or internally [115]. Consequently, the reaction rate is proposed to decrease linearly with carbon conversion [195]. This model takes into account that although particle density fluctuates during char gasification, particle size remains constant [139]. A simple graphical representation of the conversion profile and char particle based on the VM assumption is shown in Figure 5.1 (a). The reaction rate equation of the VM is written as:

$$\frac{dX}{dt} = k_{VM}(1 - X) \quad (5.3)$$

5.2.2 Grain model

The grain model or the shrinking core model was proposed by Sezekely and Evans [196]. According to the GM, char structure consists of numerous numbers of spherical or cylindrical particles, and the reaction takes place at the outer surface of these particles as shown in Figure 5.1 (b). As the reaction progresses, the char particles shrink in size and only the ash layer remains. Assuming that the particles have a spherical shape, the GM is expressed by the following equation:

$$\frac{dX}{dt} = k_{GM}(1 - X)^{2/3} \tag{5.4}$$

5.2.3 Random pore model

The main consideration of the random pore model (Figure 5.1(c)) is the overlapping of pore structure, which reduces the available surface area for the reaction [197,198]. The overall reaction rate is expressed as:

$$\frac{dX}{dt} = k_{RPM}(1 - X)\sqrt{1 - \psi ln(1 - X)} \tag{5.5}$$

RPM accounts for pore growth at the initial stages of char conversion and the merging of collapsing pores as the reaction proceeds, consequently enabling it to predict the reaction rate peak [96]. As shown in Equation 5.5, the RPM consists of two parameters, namely, the gasification reaction rate constant k_{RPM} and ψ, which is a dimensionless parameter related to initial pore structure of the char.

There are three different methods to measure this structural parameter. The first method uses the following equation [198]:

$$\psi = \frac{4\pi L_0(1-\varepsilon_0)}{S_0^2} \tag{5.6}$$

Where L_0, ε_0 and S_0 are pore length, material porosity and initial surface area, respectively. The second method is based on the experimental char conversion by differentiating Equation 5.5 [191], as follows:

$$\psi = \frac{2}{2\ln(1-X_{max})+1} \tag{5.7}$$

In this PhD investigation, ψ, was used as a fitting parameter and the value of ψ at each gasification temperature was obtained by a nonlinear fitting method by maximising the coefficient of determination (R^2) as the objective function using the following equation:

$$R^2 = 1 - \frac{\sum_{i=1}^{N}(X_{exp,i} - X_{model,i})^2}{\sum_{i=1}^{N}(X_{exp,i} - \bar{X}_{exp,i})^2} \tag{5.8}$$

Where $X_{exp,i}$, $X_{model,i}$, $\bar{X}_{exp,i}$ and N represent experimental conversion data, conversion values calculated by the models, average of experimental conversion data and the total number of experimental conversion data points, respectively.

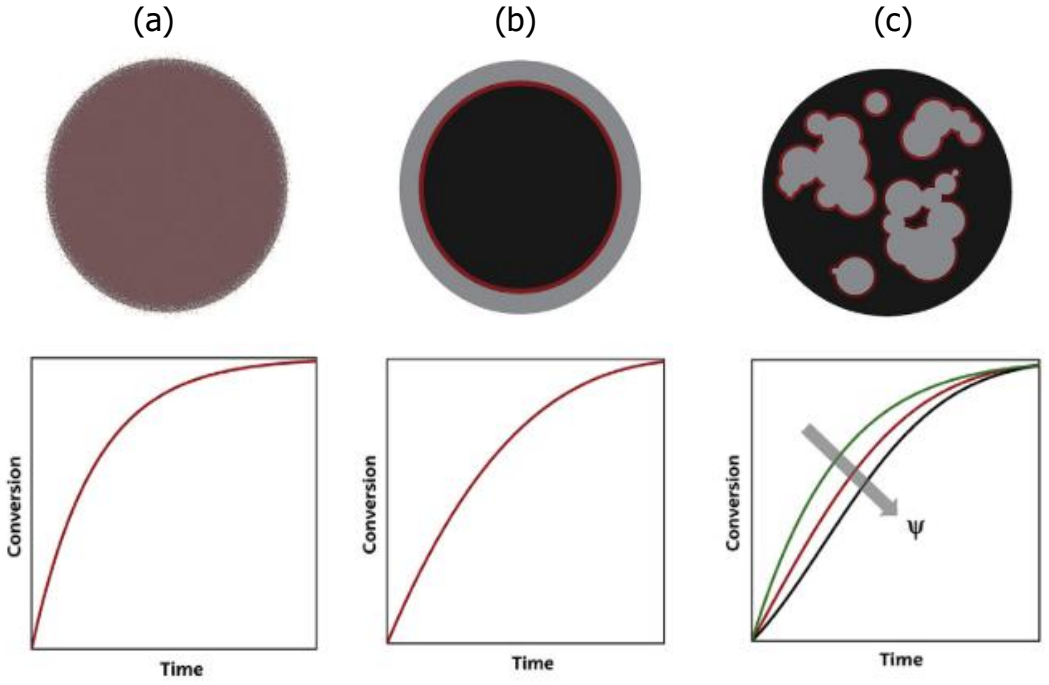

Figure 5.1: An illustration of the chemical reaction on char particles' surfaces (marked in red) and the conversion profiles vs. time based on the model's assumption: (a) Volumetric model, (b) Grain model and (c) Random pore model [195].

5.3 Kinetic model fitting and evaluation

The application of VM, GM and RPM in CO_2 gasification under both isothermal and non-isothermal conditions allows assessment of the effect of thermal treatment on the kinetic parameters. It also helps determine whether the reaction follows the same mechanism by identifying the best fit model for each condition.

5.3.1 Isothermal gasification kinetics

The apparent gasification reaction rate constants for the three models (k_{VM}, k_{GM} and k_{RPM}) can be determined using experimental conversion data from 0 to 0.9 collected from

Micro-TGA and Macro-TGA in CO_2 isothermal conditions as the slopes of the linearised forms of Equations 5.3, 5.4 and 5.5 for VM, GM and RPM, respectively[114], as follows:

$$-\ln(1-X) = k_{VM}t \tag{5.9}$$

$$3[1-(1-X)^{1/3}] = k_{GM}t \tag{5.10}$$

$$\left(\frac{2}{\psi}\right)\left[\sqrt{1-\psi ln(1-X)}-1\right] = k_{RPM}t \tag{5.11}$$

Based on the Arrhenius expression, Equation 5.2, the values of the activation energy E and the pre-exponential factor A_0 for the three models were calculated by taking the natural logarithm of both sides of Equation 5.2 as shown in following equation and plotting (lnk) vs. ($1/T$) as the slope and intercept:

$$lnk = lnA_0 - \frac{E}{RT} \tag{5.12}$$

Activation energy and pre-exponential factor values were obtained for each model and implemented into Equation 5.2 to re-calculate (k_{VM}, k_{GM} and k_{RPM}). The new values of the apparent rate constants were then employed to predict conversion values of char samples from each kinetic model (X_{VM}, X_{GM} and X_{RPM}) by using the following equations:

$$X_{VM} = 1 - exp(-k_{VM}t) \tag{5.13}$$

$$X_{GM} = 1-(1-k_{GM}t/3)^3 \tag{5.14}$$

$$X_{RPM} = 1 - exp(-k_{RPM}t(1 + k_{RPM}t\psi/4) \quad (5.15)$$

The experimental conversion results were compared with that predicted from the kinetic models. The following equation was used to calculate the deviation $DEF(X)(\%)$ between the experimental and predicted data [114]:

$$DEV(X)(\%) = 100 \times \frac{\sqrt{(\sum_{i=1}^{N}(X_{exp,i} - X_{model,i})^2/N)}}{\max(X)\ exp} \quad (5.16)$$

Here $\max(X)\ exp$ is the maximum conversion of the experiment and N is the total number experimental conversion data points. Figure 5.2 illustrates the calculation procedure that was used to find the kinetic parameters obtained by the VM, GM and RPM models.

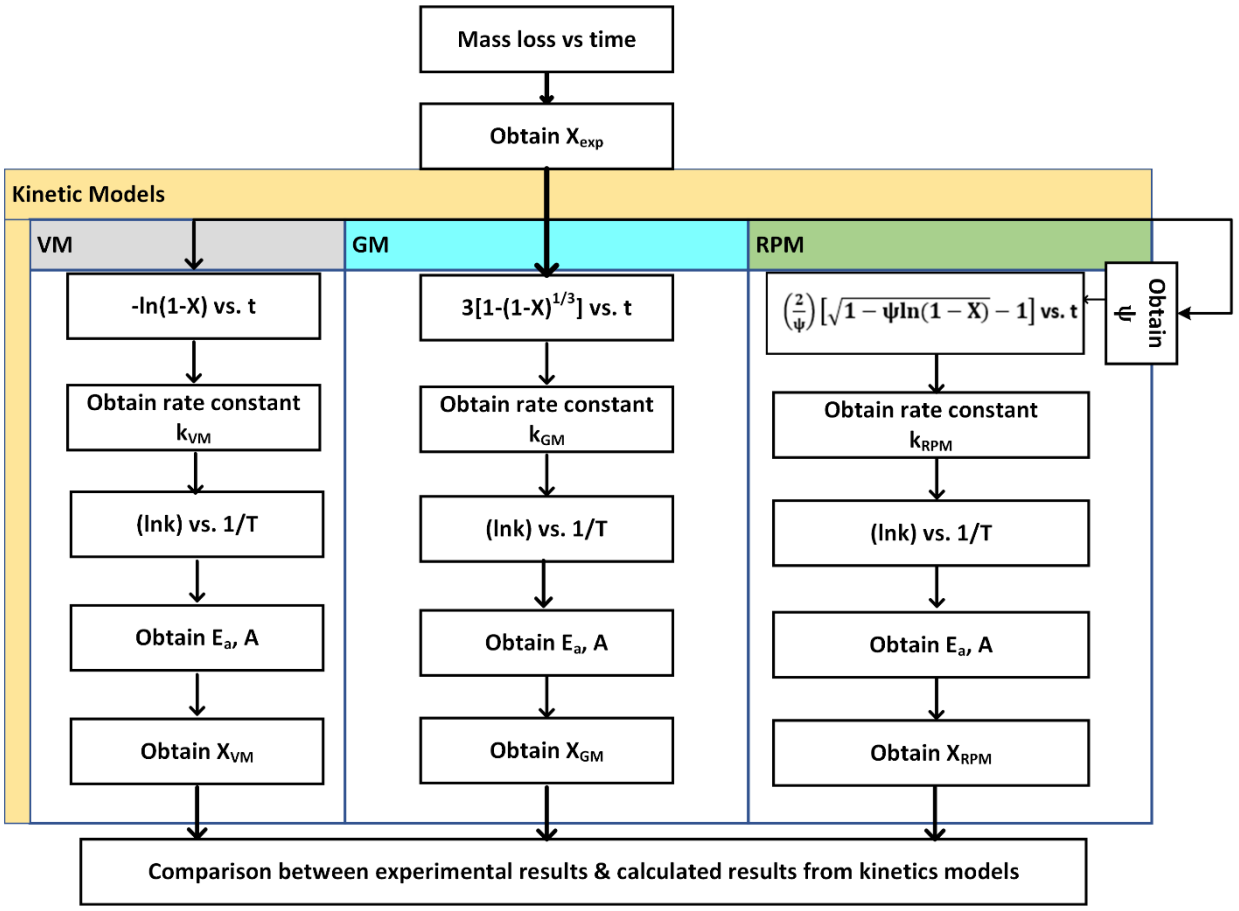

Figure 5.2: Flowchart procedures to determine the kinetic parameters.

5.3.2 Non-isothermal gasification kinetics

For non-isothermal CO_2 gasification, the three models (VM, GM and RPM) were also employed to describe the reaction after adjusting them by considering the dynamic temperature effect. In this part, Arrhenius (Equation 5.2), model Equations 5.3-5.5 and experimental reaction rate $\frac{dX}{dt}$ were used to calculate the kinetic parameters (E, A_0 and ψ) by the nonlinear fitting method. The objective function, given in Equation 5.8, can be written as follows:

$$R^2 = 1 - \frac{\sum_{i=1}^{N}\left(\left(\frac{dX}{dt}\right)_{exp,i} - \left(\frac{dX}{dt}\right)_{model,i}\right)^2}{\sum_{i=1}^{N}\left(\left(\frac{dX}{dt}\right)_{exp,i} - \overline{\left(\frac{dX}{dt}\right)_{exp,i}}\right)^2} \quad (5.17)$$

Where $\left(\frac{dX}{dt}\right)_{exp,i}$, $\left(\frac{dX}{dt}\right)_{model,i}$, $\overline{\left(\frac{dX}{dt}\right)_{exp,i}}$ and N are experimental reaction rate, reaction rate calculated by the models, the average of experimental reaction rate and the total number of experimental reaction rate data points, respectively. To further examine these models' ability to fit the experimental results, conversion (X) was calculated by integrating kinetic model Equations 5.3-5.4 and substituting the obtained kinetic parameters from the previous step.

Under non-isothermal gasification conditions, the char samples are heated at a constant heating rate to the final temperature. This results in a dynamic change in temperature T over time t, which can be described using the following formula:

$$T = T_0 + \beta . t \quad (5.18)$$

Where T_0 is the initial temperature before the heating programme begins and β is the heating rate (5,10 and 15°C/min). Based on temperature and time relationship, the integrated forms of the kinetic expressions can be written as follows [199]:

$$X_{VM} = 1 - exp\left(-\frac{A_0 R T^2}{\beta E} . exp\left(\frac{-E}{RT}\right)\right) \quad (5.19)$$

$$X_{GM} = 1 - \left(1 - \frac{A_0 R T^2}{3\beta E} . exp\left(\frac{-E}{RT}\right)\right)^3 \quad (5.20)$$

$$X_{RPM} = 1 - exp\left(-\left(\frac{A_0 RT^2}{\beta E}.exp\left(\frac{-E}{RT}\right)\right).\left(1 + \frac{A_0.\psi}{4}.\frac{RT^2}{\beta E}.exp\left(\frac{-E}{RT}\right)\right)\right) \quad (5.21)$$

Similar to the procedure used to estimate the relative error under isothermal gasification conditions, Equation 5.16 can be adapted to determine the relative error in non-isothermal gasification, as follows:

$$DEV(dx/dt)(\%) = 100 \times \frac{\sqrt{(\sum_{i=1}^{N}\left((dx/dt)_{exp,i} - (dx/dt)_{modle,i}\right)^2/N)}}{\max(dx/dt)\,exp} \quad (5.22)$$

Here $\max(dx/dt)\,exp$ is the maximum reaction rate of non-isothermal gasification experiment.

5.4 Chapter summary

This chapter presents the methods of measuring the char gasification kinetic parameters using three known kinetic models (VM, GM, RPM). These models have been used widely to describe char gasification in CO_2 atmospheres in isothermal and non-isothermal conditions. They were selected in this thesis due to their different assumptions related to solid particle consumption and reaction progression. The outcomes of using these kinetic models are discussed in Chapters 7 and 8.

Chapter 6 Mechanisms affecting char reactivity in CO_2 gasification: experimental results from Micro-TGA and physicochemical characterisation

6.1 Introduction

The main purpose of this chapter was to investigate the critical mechanisms affecting char reactivity in CO_2 gasification. This chapter investigates the influence of physical and chemical properties of biochar, hydrochar and coal char samples during CO_2 gasification using a variety of laboratory techniques to measure properties including mineral content, porosity, microcrystalline structure, morphology, surface elements and surface functional groups.

Furthermore, CO_2-chemisorption measurements of the char samples were examined to measure both organic and inorganic active sites using thermogravimetric analysis. The CO_2-chemisorption method at low temperatures (300°C) was implemented to quantify the amount of CO_2 adsorbed/desorbed within the char's surface and to identify its role in char reactivity. Finaly, heat consumption by the reverse Boudouard reaction was measured using TGA/DSC under isothermal conditions to understand performance of this reaction compared to other carbon capture technologies.

6.2 Isothermal gasification reactivities

For this approach to be considered as a means to produce carbon monoxide as a chemical intermediate to utilise carbon dioxide, the char reaction needs to take place at the lowest temperature and for the shortest time, to minimise the overall energy input for the reaction.

The six chars' reactivities were measured at three different temperatures to compare the effect of this parameter on the reactivity at 900°C, 950°C and 1000°C, as shown in Figure 6.1. It is clear that all the biomass chars are significantly more reactive than the coal char sample at all gasification temperatures, particularly at the lowest temperature. The hydrochar (HC) reactivity was higher than the others, with reactivity values of 3.19×10^{-3}, 5.03×10^{-3} and 6.54×10^{-3} s^{-1} at temperatures of 900°C, 950°C and 1000°C, respectively. The reactivity values of HC were around 4 times higher than the most reactive biochar in this study, namely, BC1. Research carried out by Lanhijani and co-workers [133] also found that hydrothermal carbonisation (HTC) treatment of biomass enhanced the CO_2 gasification reactivity of the char produced. In comparison to the hydrochar, the results

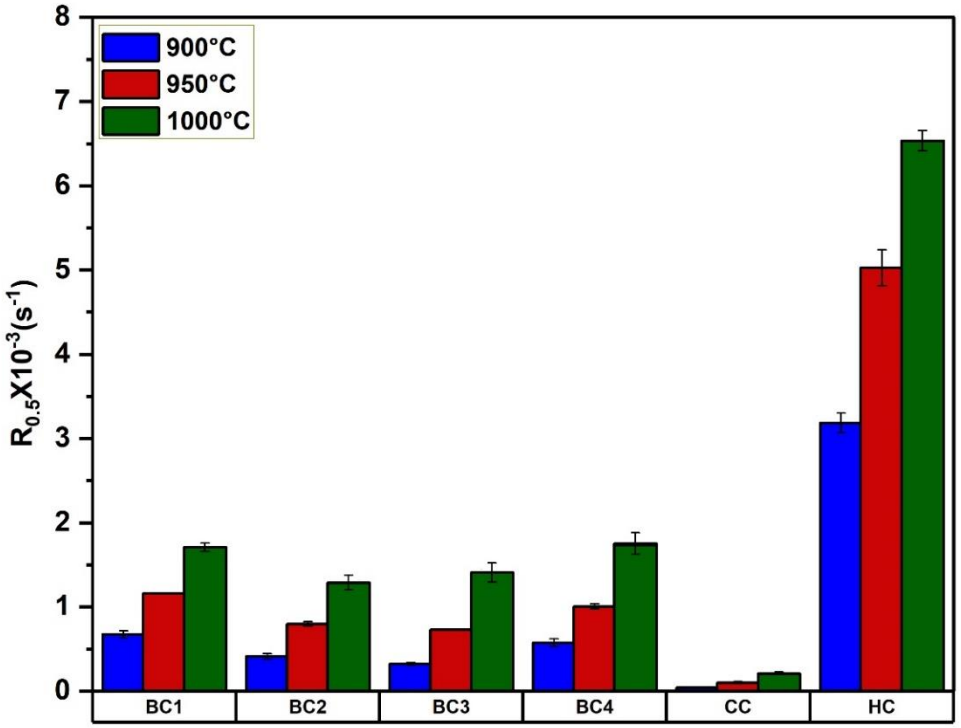

Figure 6.1: CO_2 gasification reactivities of chars at different temperatures.

in Figure 6.1, show a narrower difference in the reactivities of the other samples derived from woody biomass and pyrolysed sewage sludge.

To measure the effect of varying masses of fixed carbon remaining after the N_2 pyrolysis; TGA curves were run using different total sample masses (m_{total}) to determine the role of the varying fixed carbon mass left post pyrolysis on the final reactivity. The influence of variations in the fixed carbon on chars' reactivity was also examined using a smaller sample size. In this test, 5 mg of the fixed carbon was tested using the same TGA gasification conditions. The number of repeats at 900°C, 950°C and 1000°C, respectively, were BC1 (2, 2, 3), BC2 (3, 3, 3), BC3 (3, 2, 2), BC4 (2, 3, 3), CC (3, 2, 2) and HC (3, 3, 2). The results in Figure 6.2 show consistent reactivity trends, suggesting that the relative reactivities were a reflection of the intrinsic properties of the char samples and were not significantly affected by the fixed carbon mass.

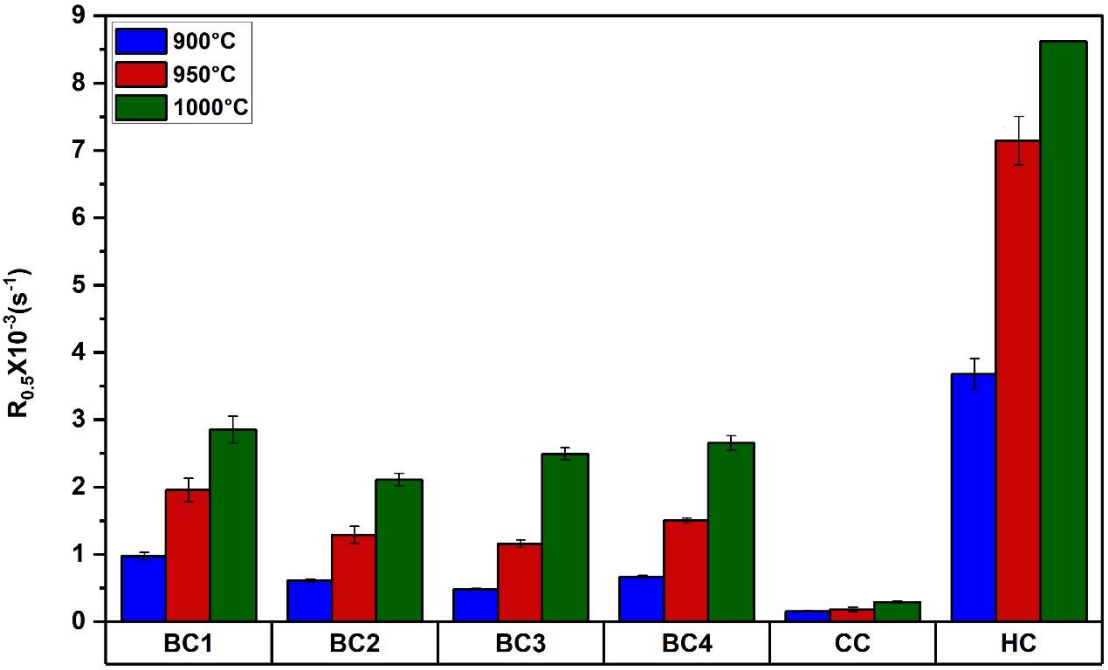

Figure 6.2: CO_2 gasification reactivities of chars at different temperatures with sample mass of 5 mg.

The results indicate that the gasification reactivity is significantly influenced by the reaction temperature and as expected the reactivity of all the chars exhibit an upward trend as the temperature is elevated from 900°C to 1000°C.

The catalytic effect associated with the components contained in the ash has been widely researched, as discussed in Section 2.7.3. In the context of this approach, the catalytic effect of the mineral components on CO_2 gasification reactivity has been compared between the most reactive chars by acid leaching using hydrochloric acid. The effect of removing minerals from the two chars, BC1 and HC, is shown in Figure 6.3; in both cases the reactivities were reduced.

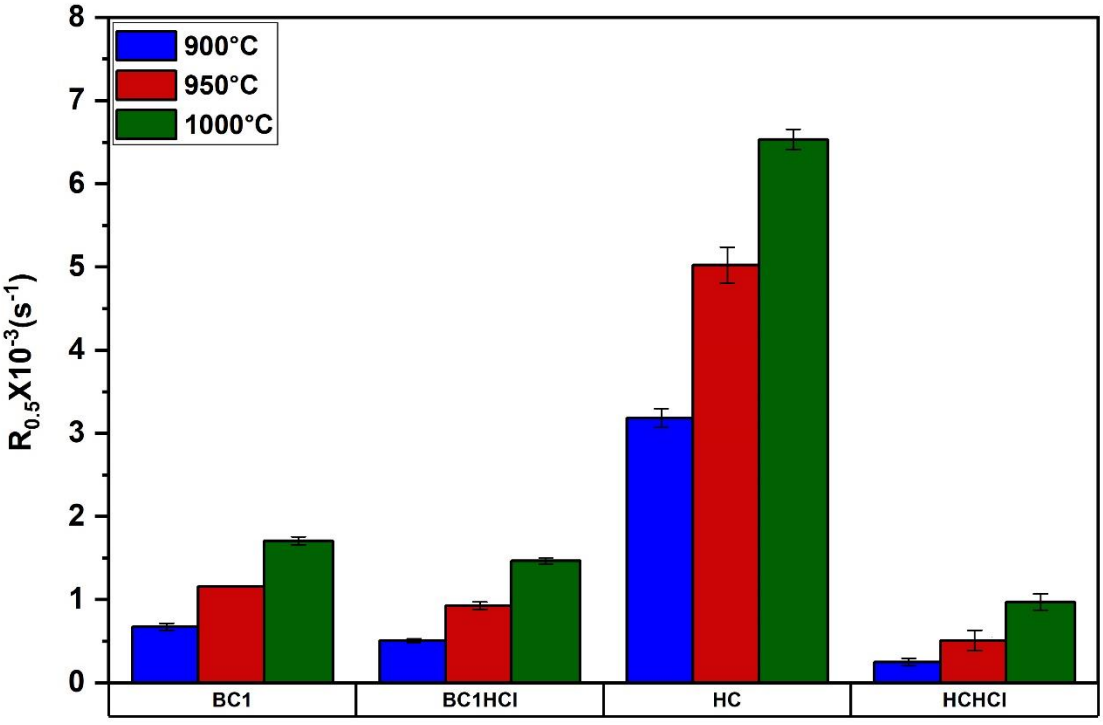

Figure 6.3: Comparison of raw biochar and hydrochar reactivities before and after acid treatment.

The reactivity of BC1 was reduced by up to 27%, while the reactivity of HC was reduced by up to 92%. The large reactivity reduction for the hydrochar demonstrates the importance of the role of the ash components in determining subsequent reactivity. In comparison, the mechanism by which the ash is working in BC1 does not dominate the reactivity to the same extent as HC. Further, the effectiveness of acid washing on the

char samples was examined using a paired difference t-test to evaluate if a significant difference occurred between the reactivity of non-demineralised samples and reactivity of the demineralised sample. The results confirmed that the reduction significantly occurred with a p-value of <0.05 for all the gasification temperature range (as shown in Table 6.1).

Table 6.1: Paired t-test parameters for non-demineralised and demineralised char samples at different gasification temperatures.

Char sample groups	Gasification temperature (^{O}C)	t-value	p-value
BC1 & BC1HCl	900	21.69	0.0293
	950	13.12	0.0484
	1000	52.52	0.0121
HC & HCHCl	900	51.80	0.0123
	950	137.64	0.0046
	1000	719.22	0.0009

The TGA conversion profiles and DTG rate of change profiles illustrate the clear difference of the gasification reactivity of BC1 and HC before and after the washing process, as shown in Figure 6.4. The biochar sample, BC1 (Figure 6.4 (a)), achieved complete conversion between 10 to 25 minutes depending on the temperature, whereas it took between 13 to 36 minutes for the demineralised sample, Figure 6.4 (b), to complete the reaction. As shown in Figure 6.4 (c, d), the impact of acid washing on the hydrochar was stronger than biochar. The DTG curve of HC shows maximum weight losses of 16 to 27.5%/min for the unwashed, but only 0.9 to 4.5%/min for the washed sample. Although raw char from HC was more reactive than BC1, the demineralised sample of the latter char showed better reactivity than HCHCl. This suggests that the dominant factor of HC reactivity is the presence of the minerals and their catalytic effect. However, when considering the selection of chars for the CO_2 utilisation reaction using the reverse

Boudouard reaction, even after acid washing the two biobased chars were significantly more reactive than coal char.

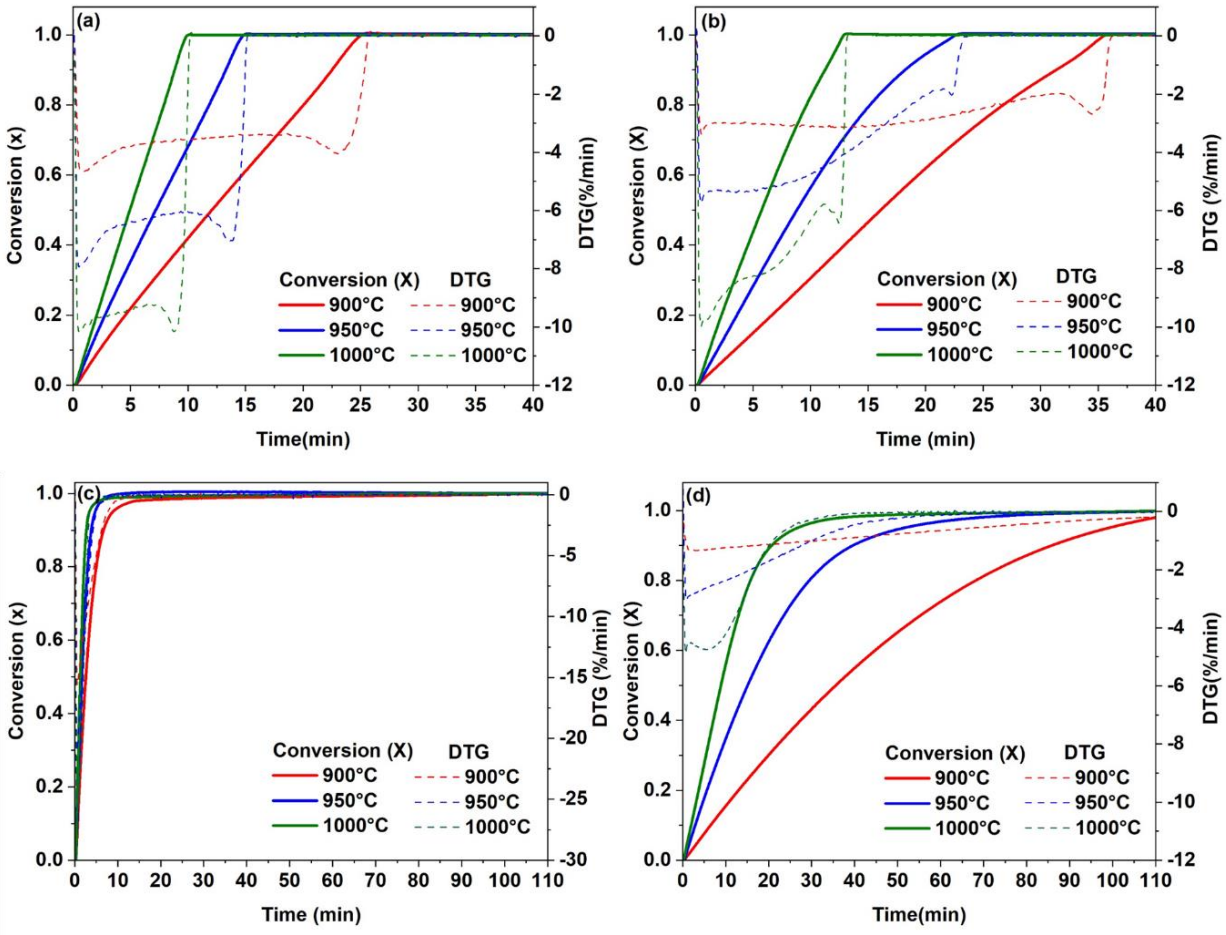

Figure 6.4: Carbon conversion profiles and DTG curves of the isothermal gasification step for raw chars and their demineralised chars: (a) BC1, (b) BC1HCl; (c) HC, (d) HCHCl.

6.3 Influence of physical and chemical properties on char reactivity

In the context of the CO_2 gasification reactivity, many researchers have studied factors related to physical structure / chemical properties of char and operational conditions. Specifically for porosity and surface area, the catalytic effect of alkali and alkaline earth metals and transition metals, and the availability of active sites. The variability in CO_2

gasification reactivity of carbonaceous materials was the focus in these studies to determine the likely strongest factors.

6.3.1 Porosity and surface area

In this work, N_2 adsorption at -196°C was employed to investigate the physical properties of the char samples, owing to its affordability and availability. However, it should be noted that access of the smallest micropores is limited due to the diffusional limitation of this probe. Alternatively, applying CO_2 at 0°C for analysis of the ultra-micropores can be effective, particularly for porous solids without polar surface groups, as suggested by IUPAC [106].

There are different theoretical physical adsorption isotherm models which can be used to interpret the experimental adsorption data such as Langmuir, BET, DFT, DR, etc. However, these models cannot provide an absolute value for the specific surface area [200]. According to Al-Ghout et al. [201], choosing the optimum physisorption isotherm model relies on three key criteria, which are;

- The goodness of fitting of the experimental data.
- The model function should be thermodynamically realistic.
- The utility of the model: it should allow calculation of capacity and concentration using the main function and its inverse.

A recently published study [202], used gas adsorption technique to implement BET specific surface area tests using N_2 and CO_2 physisorption on wood char, the results were 593 and 676 m^2/g respectively. This demonstrated that while N_2 may underestimate the contribution from very narrow pores [203], the overall impact on surface area determination can be minimal, especially for larger pores and when using it for just comparison purposes.

The N_2 adsorption-desorption isotherm profiles of biochars, hydrochar and coal char are illustrated in Figure 6.5. As shown in the figures, the physisorption isotherms for all chars

belong to type II according to IUPAC [106]. Micropores (>2nm) are filled by N_2 molecules at low P/P^0 and isotherm profiles indicate different levels of microporosity. Biochars demonstrate higher micropore structures compared to HC and CC, this is supported by their high fraction of S_{Micro}/S_{BET} with values of (25.25 to 54.26%), as shown in Table 6.2. In particular, BC4 has the highest microporosity of 54.26% as evidenced by its high adsorption volume at low P/P_0 in Figure 6.5(d). The desorption branches are not matching adsorption branches at low P/P^0, which is more pronounced for woody biochars (BC1 and BC2) and coal char (CC) as shown in Figure 6.5 (a), (b) and (e)). This phenomenon is attributed to the presence of very restricted tiny pores rather than capillary condensation [114,204]. In Figure 6.5 (f), the HC sample shows a weak adsorption at low relative pressure indicating a macroporous structure. The higher adsorption volume of biochar samples at higher P/P^0 suggests the presence of more pores available for N_2 to fill which means higher porosity compared to HC and CC. Appendix B provides the complete dataset of the N_2 physical adsorption analysis of the samples, including Multi-Point BET linear plots, t-plot curves and BJH Pore size distribution.

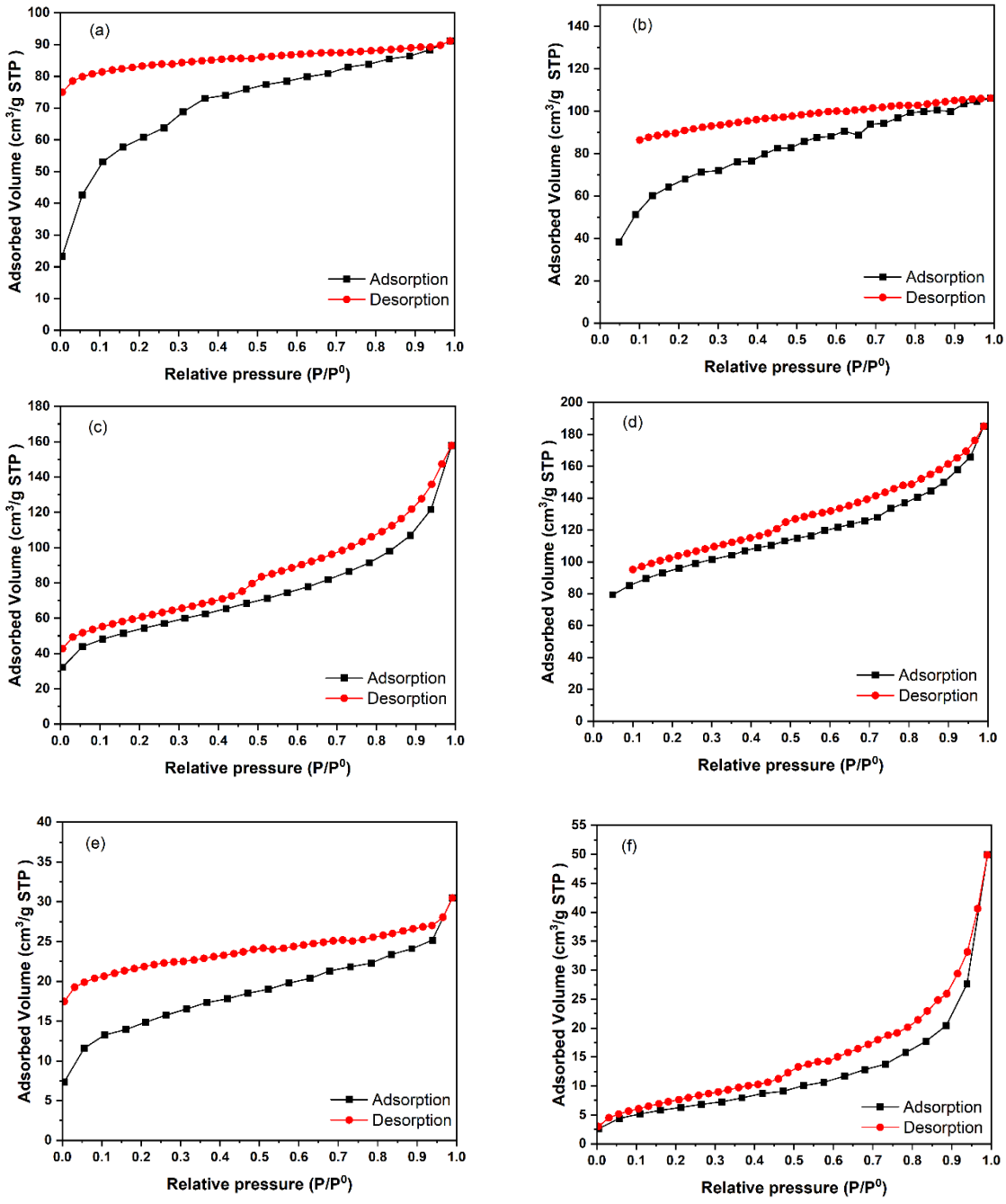

Figure 6.5: N_2 adsorption-desorption isotherm curves obtained at -196°C of (a) BC1, (b) BC2, (c) BC3, (d) BC4, (e) CC and (f) HC.

The relationship between porosity and reactivity for gas-solid reactions where surface area and mass transfer play such a well-documented role has been widely researched. However, the reactivity of hydrochar was not explained by BET surface area as it had the lowest for all chars, with an S_{BET} of 22.27m^2/g.

For the surface area and isotherm parameters of the chars shown in Table 6.2, the biomass char samples displayed a variation in structural features. Biomass-derived chars BC1-BC4 had the highest BET, micropore surface areas, and pore volumes compared to hydrochar and the coal char, which showed significantly lower porosity characteristics.

Table 6.2: N_2 adsorption isotherm parameters.

Sample	S_{BET} (m^2/g)	S_{Micro} (m^2/g)	S_{Micro}/S_{BET} (%)	V_{Micro} (m^3/g)	V_{Total} (cm^3/g)	Avg. pore, D_p (nm)
BC1	211.50	53.41	25.25	0.02	0.14	2.58
BC2	261.74	120.76	46.14	0.04	0.16	2.47
BC3	185.53	63.23	34.08	0.03	0.19	4.06
BC4	319.98	173.62	54.26	0.08	0.23	2.88
CC	51.24	15.66	30.56	0.01	0.04	3.04
HC	22.27	ND	ND	ND	0.04	6.87

*ND: Not Detected.

The physical structure differences measured using BET can also be seen in the SEM images in Figure 6.7(a, b, c, d). All biomass chars BC1-BC4 exhibit the cellular structure characteristic of bioderived materials, whereas both the hydrochar and the coal char exhibit closed structures, seen in Figure 6.7(e, f) which is also consistent with the higher pore diameter of 6.87 nm. Coal char has a solid smoothed surface with some cracks and fewer pores.

Figure 6.6 shows the relationship between BET surface areas and chars reactivities at different gasification temperatures. The figure highlights a linear relationship between surface area and reactivity for the set of chars BC1-BC4, and the coal char. However, the very high reactivity of the hydrochar, combined with the importance of the mineral ash

components, flag it as an outlier. It shows no correlation with its porosity. In comparison, these results suggest that porosity is an important factor to describe biochar and coal char reactivity.

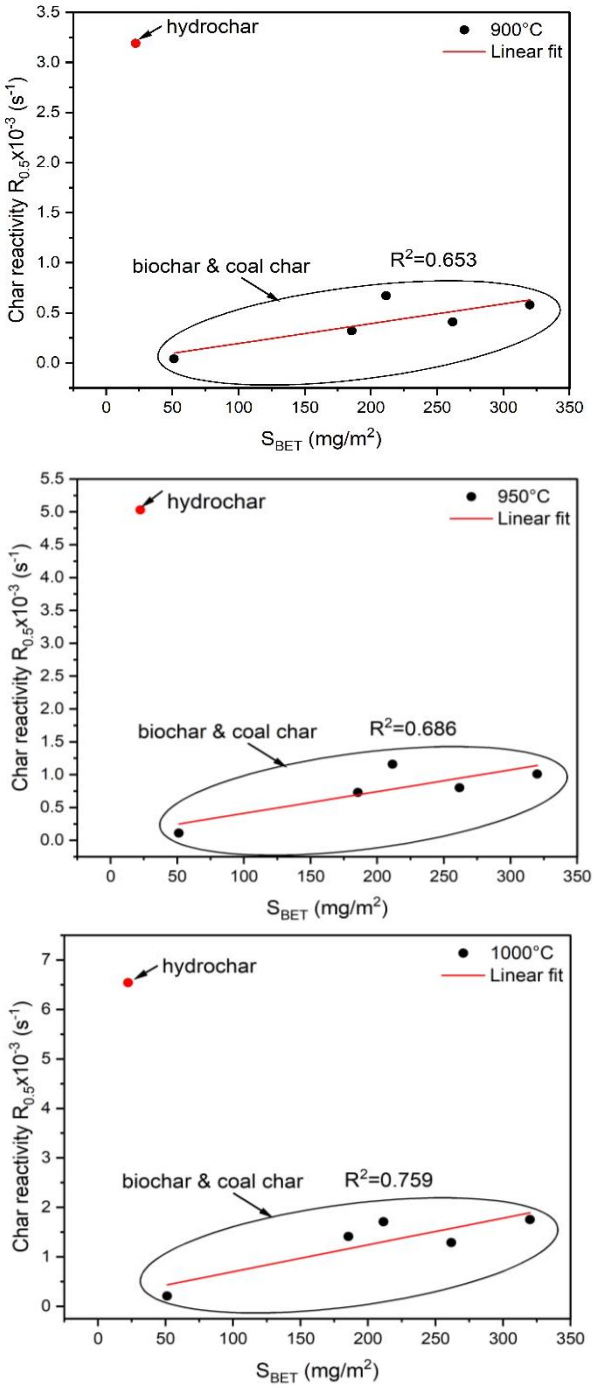

Figure 6.6: Correlation between S_{BET} and gasification reactivity.

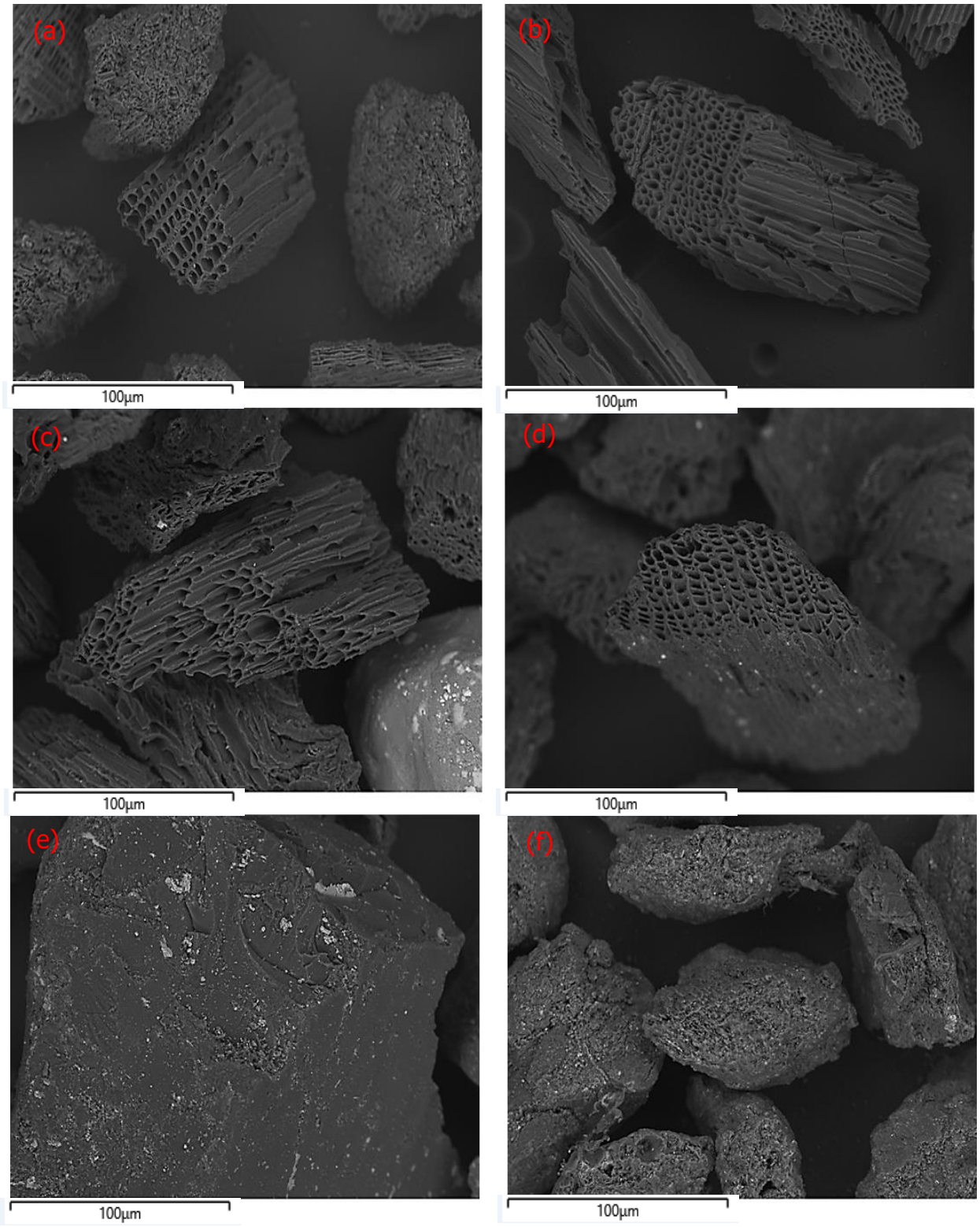

Figure 6.7: SEM morphology images of char samples taken: (a) BC1, (b) BC2, (C) BC3, (d) BC4, (e) CC and (f) HC.

6.3.2 Ash mineral content and composition

It is well understood that the presence of metal compounds in the ash can have a catalytic effect on the sample reactivity by promoting electron transfer which facilitates the surface combination of CO_2 with the carbon contained in the sample. The sample demineralisations shown in Figure 6.3 for BC1 and HC, demonstrate the particular importance of the ash to the reactivity of the hydrochar after the demineralisation. However, the results indicate that for the CO_2 gasification reaction the importance of the ash content and composition varies depending on the sample. As shown in Table 6.3, the biochar samples BC1-BC4 vary in ash between 2.6 - 37.0% but the reactivities do not show any significant variation. The coal char sample CC contains 17.6% ash but is much less reactive than BC1 or BC2, which have ash contents of 4.7 and 2.6% accordingly. The hydrochar sample HC has an ash content of 21.2% but has much higher reactivity than any of the chars, including BC3 with 37.0% ash. However, when demineralised its reactivity falls accordingly.

Table 6.3: Proximate and ultimate analysis of char samples.

Sample	Proximate analysis (wt.%, d)			Ultimate analysis (wt.%, d, daf)				
	V	A	FC[a]	C	H	O[a]	N	S
BC1	17.6	4.7	77.7	81.7	2.3	14.1	1.9	0.02
BC2	12.6	2.6	84.8	85.2	2.6	10.9	1.3	0.03
BC3	4.5	37.0	58.5	55.9	0.5	41.5	1.5	0.54
BC4	10.0	21.0	69.0	68.5	0.9	28.4	2.0	0.17
CC	18.3	17.6	64.1	76.0	2.6	18.2	3.0	0.26
HC	56.7	21.2	22.1	47.7	4.8	45.4	1.7	0.45
BC1HCl	17.1	2.8	80.1	84.1	2.2	13.8	0.01	ND
HCHCl	66.0	3.5	30.5	56.3	5.4	35.2	2.6	0.60

FC, fixed carbon; V, volatile matter; A, ash content; d, dry basis; daf, dry ash free basis; [a] by difference. Values are given as averages and errors are reported as standard deviations in Appendix C. ND: Not detected.

A closer examination of the compositions shows a wide variation in components which is difficult to assign trends to, see normalised figures in Table 6.4. The catalytic effect of calcium oxide (CaO) on gasification has been well documented and is present at high levels in the hydrochar, BC3 and BC4. However, BC1 and BC2 have a much lower CaO content (35.55 & 47.13%) but are much more reactive than the coal char sample CC which has 10.96% CaO.

What is clear about the coal is the presence of acidic oxides in its ash, based on aluminium and silicon and consequently the base/acid ratio is very low for the coal compared to the other chars. The ratio between the CaO and the sum of Al_2O_3 and SiO_2 is 0.18 for coal compared with 5.92 for the hydrochar. The basicity could play a role in charge transfer which would have an effect on the mechanism of surface interactions. In comparison, a more acidic environment could influence a counter-acting mechanism. The catalytic and inhibition effect of the ash minerals on gasification performance were evaluated using alkali index. This tool is a simple measurement of the ratio of the basic oxides and the acidic oxides as shown in Equation 2.6.

Alkali index values for the char samples are shown in Table 6.4. The results revealed that BC1 and HC samples have a high alkali index (62.17 & 55.14%) and the highest reactivities. However, the alkali index values of sewage sludge derived chars BC3 and BC4 are higher than HC but their reactivity is much lower. This is contrary to the expected relationship between alkali index and char reactivity, suggesting that other properties are playing a role.

The acid demineralisation treatment shows a corresponding reduction of the AI values by more than 50% for BC1HCl and HCHCl identifying the importance of ash components on the reactivity. However, even though the AI value for HCHCl was reduced from 55.1 to 3.03, the reactivity is still higher than the coal (CC) with an AI value of 10.9. In this study, the data implies that the alkali index alone will not explain the differences in the reactivity.

Table 6.4: ICP ash composition analysis of char samples (wt.%, dry basis).

Sample	Fe_2O_3	CaO	MnO	ZnO	Al_2O_3	NiO	K_2O	MgO	Na_2O	P_2O_5	SiO_2	AI
BC1	38.84	35.55	2.52	0.13	1.36	0.01	9.84	5.30	0.97	2.48	3.00	62.17
BC2	15.01	47.13	2.05	0.33	0.72	0.01	19.84	7.27	0.19	4.55	2.90	28.45
BC3	22.57	28.64	0.72	0.47	12.45	0.03	3.53	4.91	1.70	22.85	2.14	60.64
BC4	8.02	51.16	0.75	2.21	15.16	0.04	5.40	6.08	6.43	2.64	2.11	81.30
CC	16.76	10.96	0.19	0.07	53.82	0.04	5.89	3.66	0.89	1.09	6.63	10.91
HC	10.75	55.93	0.24	0.18	8.02	0.01	1.02	3.66	0.55	18.21	1.43	55.14
BC1HCl	44.52	31.61	3.10	0.16	1.99	0.02	3.35	7.70	0.40	3.38	3.77	26.83
HCHCl	34.61	5.20	0.12	0.24	23.25	0.15	2.35	3.55	0.44	7.31	22.78	3.03

To further investigate elemental composition and the distribution on the chars' surfaces, five areas were chosen on each char surface to establish the distributions of the elements present on the surface, see Figure 6.8. The heavier metal elements back-scatter electrons which show-up as light areas distributed through the sample against the darker background of carbon.

Particles of the biochar samples BC1- BC4 exhibit visible open pores corresponding to a cellular structure (see Figure 6.7 and Figure 6.8). The distribution of the ash shows some variation between samples, where BC1, 2 & 3 indicate more isolated distribution where the ash seems to be localised rather than evenly distributed. In comparison, the hydrochar's finely speckled surface suggests a wider distribution on the surface, but it is not strongly visible considering it has a 21.2% ash content which would suggest it is distributed through the sample rather than on the surface.

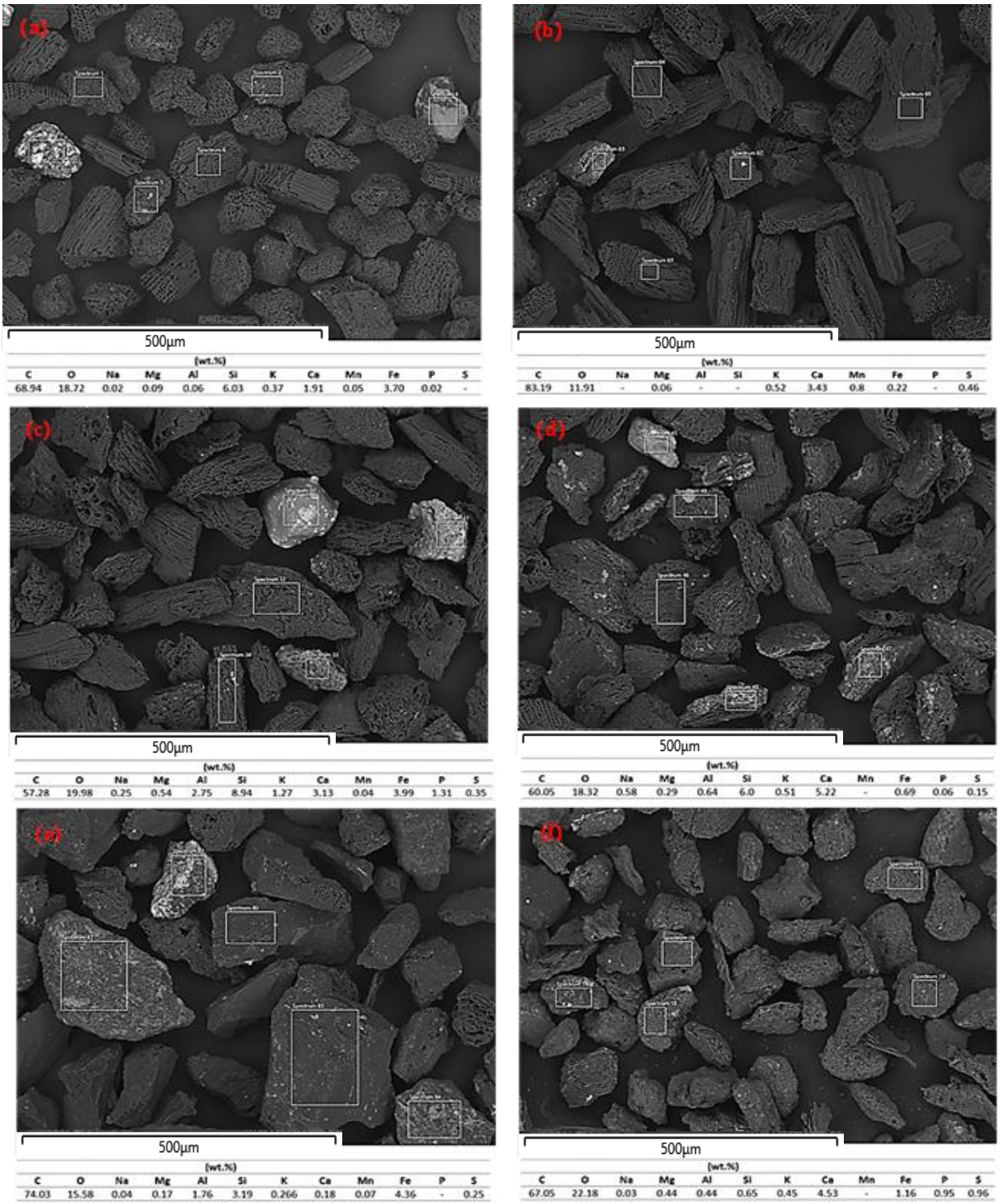

Figure 6.8: Backscattered EDS analysis of semi-quantitative and elements distribution on char surfaces taken in back-scattered mode: (a) BC1, (b) BC2, (C) BC3, (d) BC4, (e) CC and (f) HC.

The X-ray diffraction patterns of BC1 and the hydrochar HC, before and after acid washing, are shown in Figure 6.9 with quantification in Table 6.5. More crystalline phases of biochar BC1 are visible after acid washing and the BC1HCl diffractogram patterns are more detailed. This phenomenon is due to leaching of the of carbonate minerals that are often effectively dissolved in hydrochloric acid HCl [205], leading to appearance of hidden minerals [206].

The main crystalline components identified in the XRD for the hydrochar (HC) sample are dominated by calcite ($CaCO_3$), with smaller quantities of kaolinite ($Al_2Si_2O_5(OH)_4$), illite ($(K, H_3O)Al_2Si_3AlO_{10}(OH)_2$) and quartz ($SiO_2$). However, after the demineralisation, the hydrochar (HCHCl) is dominated by quartz and an associated significant reduction in reactivity. In comparison, after demineralisation of the BC1 the XRD indicates there is still a significant range of crystalline mineral components, and the reactivity was less affected than demineralisation of the hydrochar.

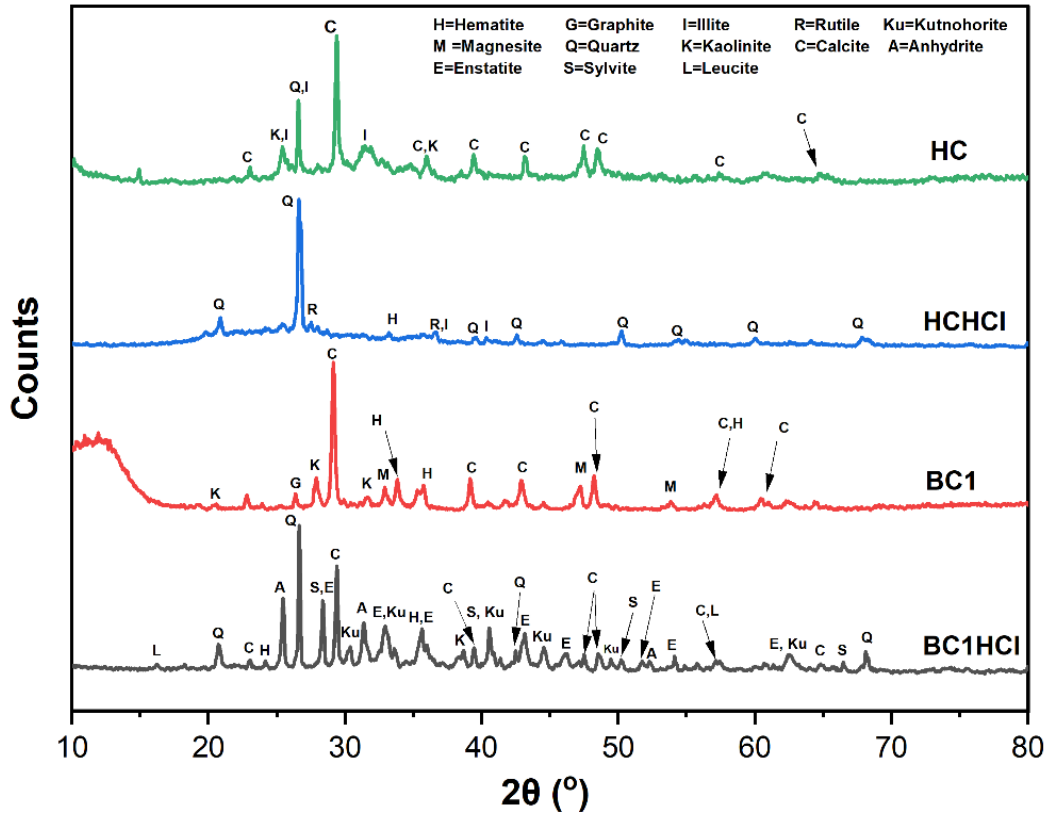

Figure 6.9: XRD patterns of BC1, HC and their demineralised chars BC1HCl, HCHCl.

Table 6.5: Semi-quantification of the crystalline phases of the biochar and hydrochar samples and their demineralised chars obtained from XRD analysis of the ash (absolute wt.% of dried sample).

Mineral	BC1	BC1HCl	HC	HCHCl
Calcite	2.9	0.3	11.0	ND
Graphite	0.3	ND	ND	ND
Hematite	0.7	0.2	0.0	0.2
Illite	ND	ND	3.1	0.2
Kaolinite	0.3	0.2	3.8	ND
Magnesite	0.5	ND	ND	ND
Quartz	ND	0.5	2.9	3.2
Sylvite	ND	0.4	ND	ND
Leucite	ND	0.1	ND	ND
Rutile	ND	ND	ND	0.1
Enstatite	ND	0.6	ND	ND
Anhydrite	ND	0.3	ND	ND
Kutnohorite	ND	0.1	ND	ND

*ND: Not Detected.

6.3.3 Characterisation of surface chemistry and CO_2 chemisorption

The XPS analyses of the samples shown in Table 6.6 were used to give an insight into the chemical groups present on the surface, and to help explain the differences in reactivity with a view to understanding factors that might influence CO_2 reactivity. Considering the relationship between the ash content and the reactivity of the hydrochar, as demonstrated by the demineralisation, the surface functionality of the hydrochar is expected to play a dominant role on the gas-solid gasification reactivity.

In comparison to the other tests used, XPS is a powerful surface analysis technique which gives a more detailed description of the area dominated by gas-solid interactions, i.e. at

the surface. XRD and SEM-EDS analyses only identify the crystalline phases and ICP is a bulk analysis technique.

The hydrochar sample (HC) had the highest surface concentrations of calcium and iron, both of which are known to catalyse gasification reactions [207]. BC3 & BC4 also both had high concentrations of calcium while BC1 & BC2 had potassium on the sample surface, which has also been identified as an important gasification catalyst.

Table 6.6: Surface atomic concentrations for each carbon sample.

Sample	Elemental at%										
	Al 2p	C 1s	Ca 2p	Cl 2p	Fe 2p	Co 2p	N 1s	Na 1s	O 1s	S 2p	K 2p
BC1	ND	75.47	0.21	ND	ND	ND	0.35	0.14	23.24	ND	0.59
BC2	ND	91.22	0.43	0.07	ND	ND	0.42	ND	7.55	ND	0.31
BC3	0.37	90.59	0.86	0.18	0.28	ND	0.42	0.19	6.76	0.35	ND
BC4	0.13	91.90	0.93	0.54	ND	0.04	0.57	0.22	5.51	0.16	ND
CC	1.40	83.35	0.20	ND	0.12	0.08	1.66	ND	12.84	0.35	ND
HC	1.01	67.64	1.85	ND	0.50	ND	3.45	ND	25.11	0.44	ND
BC1HCl	ND	75.25	ND	ND	ND	ND	3.69	ND	22.26	0.41	ND
HCHCl	ND	73	ND	ND	ND	ND	4.13	ND	21.14	0.32	ND

*ND: Not Detected.

An often-overlooked parameter to gasification reactivity is the form of carbon present on the surface. The XPS can be used to determine the sp^2/sp^3 carbon hybridisation bonding using the X-ray excited carbon Auger (C_{KLL}) spectra. This was first carried out by Lascovich and Scalione and quoted as the D-parameter derived from the differential of the carbon Auger signal [208] (Table 6.7). The technique involves a linear approximation for the parameter ranging from diamond-like (100% in the sp^3 configuration) where D=14 eV; to graphitic-like carbon at 23 eV where the carbons are 100% in their sp^2 configuration.

Other researchers have shown associations between the more structurally ordered graphitic sp^2 type bonding and lower reactivity as associated with aromatic ring structures compared to the less structurally ordered sp^3 type bonding. This is consistent for the hydrochar sample in Table 6.7 which has a low sp^2 content and a higher gasification reactivity, but less obvious with the other biochars which vary from 0 to 94% sp^2 bonding, but exhibit less variability in the reactivity compared to each other. The D-parameters indicate that hybridised bonding of BC1 and HC remains predominantly sp^3 after acid washing, showing no evidence of a significant change in the type of carbon.

Table 6.7:XPS Carbon Auger (CKLL) D-parameter and sp hybridised bonding.

Sample	D-Parameter	$\%sp^2$	$\%sp^3$
BC1	14	0	100
BC2	18	44	56
BC3	22	94	6
BC4	22	89	11
CC	18	44	56
HC	15	12	88
BC1HCl	15	10	90
HCHCl	14	3	97

Analysis of the carbon, C(1s) and oxygen, O(1s) core-levels (Figure 6.10), reveal significant differences in the surface functionalities of the chars. Where significant oxygen functionality exists (HC, BC1 and CC), the materials exhibit some carbonyl containing functionalities, as evidenced by peaks above *ca*. 287 eV and pi-pi* signal in the corresponding O(1s) peak (typically this is observed above *ca*. 534 eV).

The spectra for HC and BC1 contain ether and alcohol (C-O-C/C-OH) moieties (*ca*. 286 eV and 532 eV for C(1s) and O(1s) respectively). A deeper understanding of the O(1s) peaks is complicated by the presence of other inorganic elements, such as sulphur and

calcium, all of which are in their oxidic and/or hydroxide forms and have binding energies similar to those bound to carbon.

The wider C(1s) peak asymmetry indicates more types of functional surface bonding which could play a role in facilitating chemisorption of CO_2 onto the surface. This is greatest for the most reactive hydrochar and the BC1; both show peaks with binding energies around 287.5 eV corresponding to carbonyl groups (C=O) and 288.5 eV corresponding to carboxyl (typically acid groups) and ester groups (from the formation of acid and alcohol reactions). The different type of carbon-oxygen bonding sets up dipole moments with asymmetric electron distribution that could play an important role in facilitating the CO_2 combination on the surface.

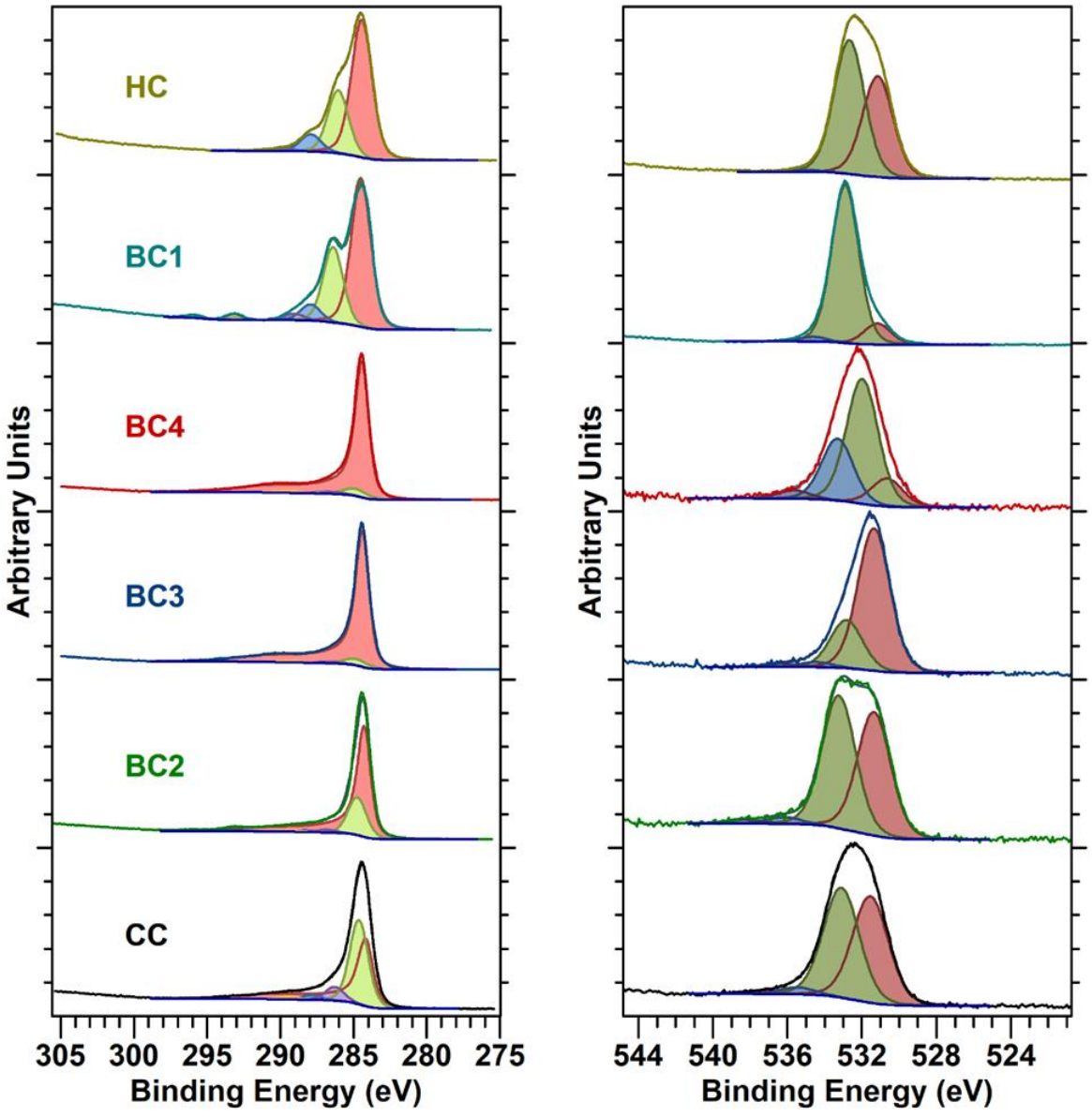

Figure 6.10: C(1s) (left) and O(1s) (right) core-level spectra for each material studied.

Several studies have been carried out to establish a connection between the chemical adsorption of CO_2 molecules on the char surface and the reactivity of char gasification [88,112,124]. Continuing from the XPS surface analysis, the CO_2 chemisorption of char samples is discussed in this section. As shown in Figure 6.11, the chemisorption is split into two parameters based on the characterisation of the chemisorption as weak and strong, denoted in the figure as C_{wea} and C_{str} and has been related to the organic and inorganic components of the char [123,124].

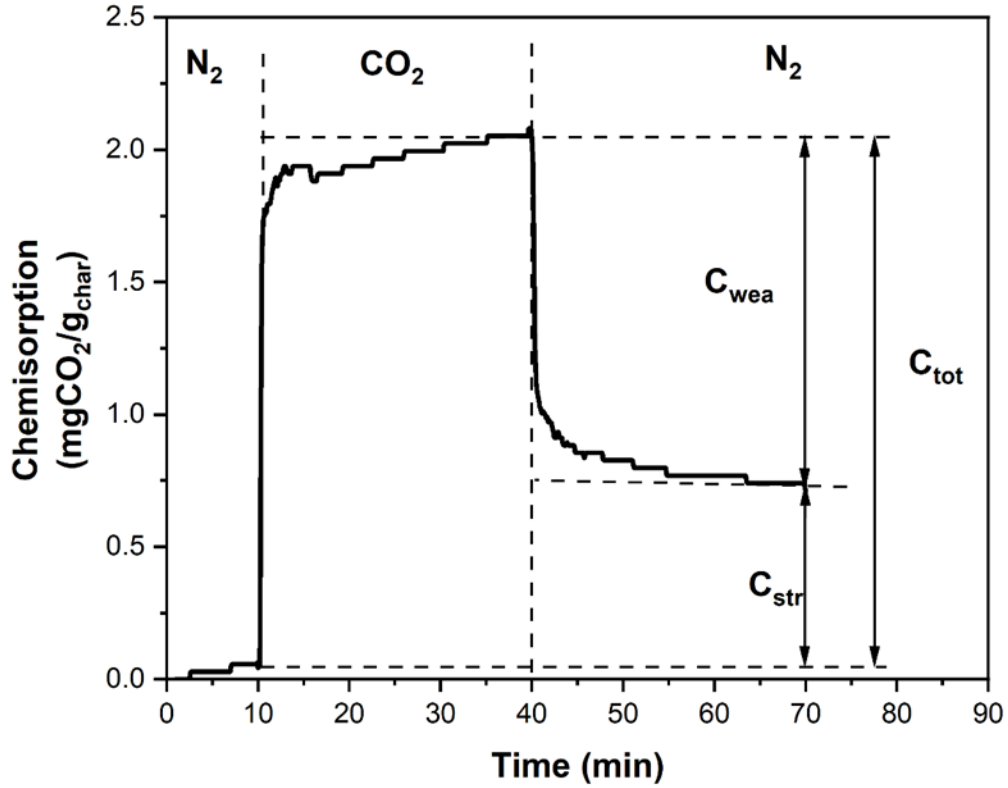

Figure 6.11: An example of CO_2 chemisorption of BC4.

CO_2 chemisorption capacities of char samples are shown in Figure 6.12. The hydrothermal char (HC) had the highest C_{str} value of 13.60 mg of CO_2/g of char which corresponds to its high reactivity. This amount of CO_2 chemisorbed on HC was expected as one of the advantages of such char is its adsorption capability [209–211], which is greater than biochars [212–214]. The C_{str} values of woody biochars, BC1 and BC2, were 4.37 and 3.32

mg of CO_2/g of char respectively while the sewage sludge chars, BC3 and B4, had comparable C_{str} values to the coal but lower C_{wea}.

The C_{wea} has been linked to reversible interactions with organic active sites and other researchers have questioned if the weak interaction is a predictor of char gasification reactivity [113,124]. For this study coal char, CC, has the highest capacity of C_{wea} of 7.73 mg of CO_2/g but a much smaller C_{str} and a correspondingly lower reactivity.

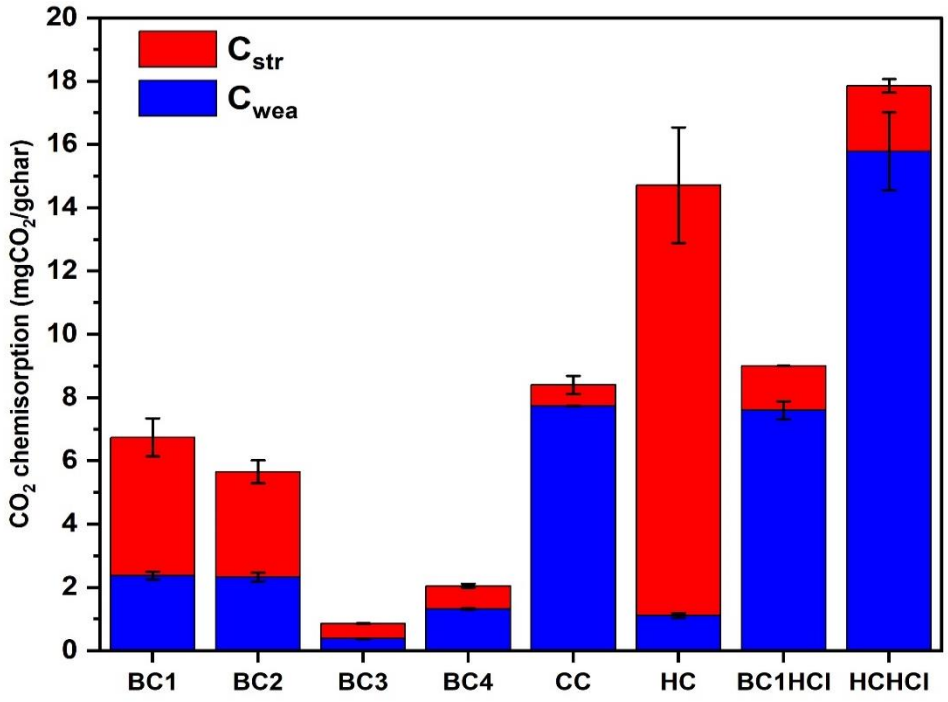

Figure 6.12: Strong and weak CO_2 chemisorption (C_{str}, C_{wea}) for char samples at 300°C.

After demineralisation, both BC1HCl and HCHCl show a significant reduction in strong chemisorption capacities replaced by a corresponding increase in weak chemisorption. As shown in Figure 6.12, the amount of irreversible CO_2 strong chemisorption (C_{str}) of BC1 and HC decreased by 68% and 85% respectively. The demineralisation of the chars appears to reduce the strength of CO_2 chemisorption with a corresponding reduction in reactivity, suggesting that the ash minerals play a direct role in the mechanism of CO_2 surface reactions.

A closer look at the relationship between the reactivity of chars and C_{str} is shown in Figure 6.13. The high values of R^2 of 0.924, 0.919, and 0.890, indicate a strong linear correlation between C_{str} and chars reactivity in the temperature range studied, and a similar positive correlation was recently reported by other investigations [215].

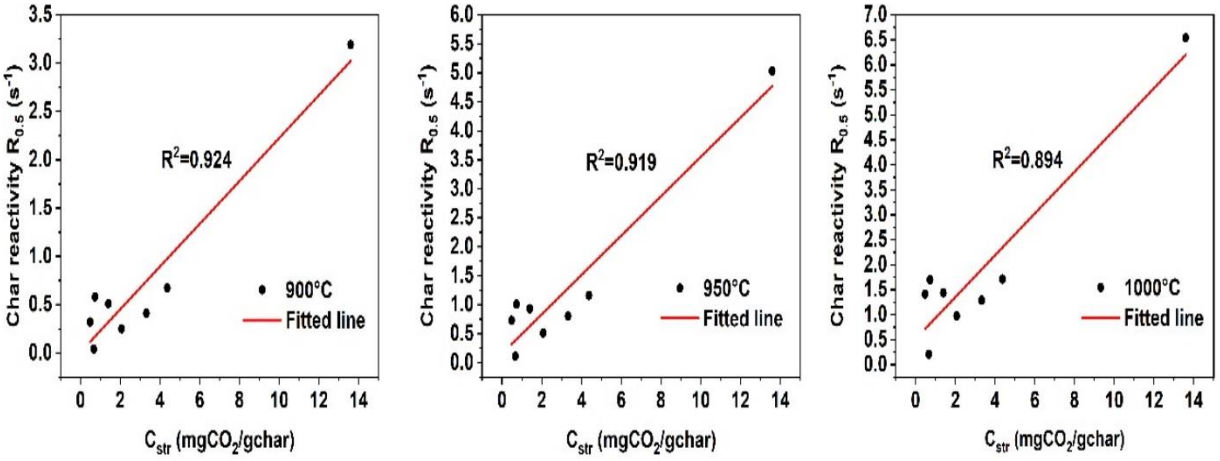

Figure 6.13: Correlations of the strong CO_2 chemisorption (C_{str}) with gasification reactivities at 900°C, 950°C, and 1000°C.

6.4 Heat energy consumption by the reverse Boudouard reaction

Mitigating CO_2 from flue gases in industrial applications can be expensive due to the high energy demands required to sustain the capture plant. Examining the use of CO_2 gasification of bio-based materials as a potential CCU method can provide an important insight to further explore its economic viability. In this PhD, the TGA/DSC was used to estimate the heat consumed to react CO_2 by the reverse Boudouard reaction. In the calculation, endothermic heat absorption was measured for the complete conversion of the char (post pyrolysis). Total heat absorbed to utilise CO_2 can be determined from the integrated heat flow over time, as expressed by the following equation:

$$Total\ Heat\ Consumed\ (J) = \int_{t_0}^{t_{end}} Heat\ flow\ (W)\ dt \qquad (6.1)$$

The integration was performed over reaction times from t_0 to t_{end} which denote the time in minutes from when CO_2 was introduced and the time at the end of CO_2 gasification step. To normalise the total heat consumed per mass of CO_2, from the reaction stoichiometry one mole of carbon react with one mole of CO_2 thus the following relationship can be used:

$$m_{CO_2} = m_{C_{converted}} \times \frac{M_{CO_2}}{M_C} \qquad (6.2)$$

Where m_{CO_2}, M_{CO_2} and M_C are mass of CO_2 utilised, the molar mass of CO_2 and the molar mass of carbon, respectively. $m_{C_{converted}}$ denotes the mass of total carbon converted and can be determined by subtracting the final mass remaining after complete gasification (m_f) from the post pyrolysis mass after N_2 is switched to CO_2 (m_i) as illustrated in Figure 3.28, which is expressed using the following equation:

$$m_{C_{converted}} = m_i - m_f \quad (6.3)$$

The total endothermic heat requirements to utilising CO_2 via the gasification process at different temperatures are shown in Table 6.8. The results clearly demonstrate a correlation between material reactivities, and their heat demands during the reaction. As shown, a superior performance of biochars (BC1, BC2, BC3 and BC4) and hydrochar (HC) samples is seen when compared to coal char (CC) as they consume less energy over the temperatures studied. In particular, the heat requirement of CC is 3 times higher than the most reactive sample (HC) at 900°C. This energy demand increases to more than 4 times and 6 times at 950°C and 1000°C respectively. It is suggested that the lower reactivity of CC leads to insufficient CO_2 utilisation and thus material reactivity to determine its suitability for CCU. Conversely, HC demonstrates superior performance with values of 1.93-2.82 MJ/kgCO_2 which align well with its reactivity. The results also show that heat requirements increase as gasification temperature increases, which reflects the endothermic nature of the reverse Boudouard reaction.

Table 6.8: Total Heat consumption by the reverse Boudouard reaction at different temperatures.

Temperature (°C)	900	950	1000
	Energy consumption (MJ/kgCO_2)		
BC1	2.34±0.08	2.65±0.11	3.20±0.09
BC2	2.52±0.24	2.74±0.13	2.78±0.14
BC3	2.64±0.12	4.65±1.11	3.79±0.66
BC4	3.27±0.16	3.62±0.52	3.00±0.08
CC	5.85±1.02	10.82±0.33	18.55±1.05
HC	1.93±0.16	2.53±0.08	2.82±0.06

Table 6.9 presents energy requirements for capturing CO_2 using different methods. In comparison to other carbon capture techniques, the reverse Boudouard reaction shows a good performance using hydrochar and biochars with values of 1.93 to 4.65 MJ/kgCO_2. Although these figures were determined under laboratory conditions using a pure CO_2 flow, but they provide valuable insights into the reaction efficiency in terms of energy cost per mass of CO_2. However, further work is strongly recommended to achieve fair comparison between those methods.

Table 6.9: Energy requirements for different CO_2 capture technologies.

CO_2 capture method	Energy consumption (MJ/kgCO_2)	reference
Chemical absorption	4-6	[216]
Adsorption beds	2-3	[216]
Membrane separation	0.5-6	[216]
Cryogenic Separation	0.74-2.6	[217]
Swing Adsorption (TSA, VPSA, ETSA and VSA)	1.9-5.64	[218]

6.5 Chapter summary

In this chapter, char samples were reacted with CO_2 at 900°C-1000°C to examine their reactivities during gasification using TGA and detailed surface analysis techniques. A demineralisation treatment was performed to investigate the ash composition influence on chars' reactivity. A CO_2 chemisorption method was used to evaluate char surface adsorption and desorption capacities. Finaly, heat energy consumption by the reverse Boudouard reaction was determined using TGA to investigate its viability as a potential CCU method and compared to other CO_2 capture technologies. The following conclusions were therefore drawn:

1. Biochars have much better CO_2 gasification reactivity compared to coal char and are strong candidates for consideration in a carbon utilisation reaction to produce carbon monoxide for the synthesis of platform chemicals. The shorter reactivity time at lower temperatures will result in lower energy requirements to carry out the carbon utilisation reaction compared to other materials.
2. XPS gave a valuable insight into the type of functional chemical groups associated with the highest reactivity chars. The hydrochar and the BC1 surfaces both showed a wide range of functional chemical groups such as carbonyl, ester and carboxyl groups. It was less clear however, what role the sp^2/sp^3 bonding played for all the chars; although the highest reactivity chars did correspond with lower sp^2 bonding in agreement with other literature findings.
3. The reduction in the ash content by demineralisation of the chars reduces the strong CO_2 chemisorption and also relates to the rate of reaction. The results suggest minerals play a role in the mechanism by which CO_2 combines with carbon on the surface of the chars but there is some variation on its importance depending on the sample.
4. According to physicochemical properties of chars there is more than one parameter controlling CO_2 gasification reactivity of chars at high temperature. While the pore structure of chars is indeed a significant characteristic, it appears that porosity alone does not exert the primary influence on gasification reactivity. This conclusion is supported by the findings of analytical techniques, which indicate that the types of inorganic elements present and their distribution on the surface may be more closely associated with the observed variations in reactivity.
5. The impact of demineralisation treatment on hydrochar was stronger than biochar, suggesting that the dominant factor of HC reactivity is the presence of the minerals and their catalytic effect.
6. The CO_2 chemisorption procedure can be used as an evaluation tool to predict different char reactivities, i.e. gasification reactivity is well correlated with CO_2 strong chemisorption C_{str}.

7. Heat requirement per unit mass of CO_2 confirm that biomass materials have more visible benefits than coal on the efficiency of CO_2 utilisation via the reverse Boudouard reaction. This indicates that the reactivity of carbonaceous material determines their suitability for CCU applications.

Chapter 7 Kinetic analysis of char gasification and non-isothermal gasification results

7.1 Introduction

Kinetic analysis of the reverse Boudouard reaction is an important aspect of understanding the reaction mechanisms at different conditions. In this chapter, the results of kinetic model applications are discussed, and the variation of kinetic parameters is evaluated. In addition, the reactivity and performance of biochars, hydrochar and coal char were examined under non-isothermal CO_2 gasification at different heating rates.

7.2 Kinetic analyses of isothermal CO_2 gasification

Isothermal CO_2 gasification experiments were conducted in the Micro-TGA at 900°C, 950°C and 1000°C for each char sample to obtain conversion data over time as discussed in Section 3.14.2. The following analysis of the reaction kinetics has been carried out to better understand the dominant mechanisms of the gasification reactions and determine the kinetic parameters in relation to the previous findings using linearised forms of the VM, GM and RPM (Equations 5.9-5.11), which were plotted against conversion time at 900°C to 1000°C as shown in Figure 7.1 and Figure 7.2. The reaction rate constants obtained from these models are presented in Figure 7.3.

The reaction rate constants , k_{VM}, k_{GM} and k_{RPM}, which represent the apparent rate constants obtained from the linearised forms of the volume model (VM), grain model (GM) and random pore model (RPM), respectively, were determined by obtaining the slopes of the corresponding linear plots (see Section 5.3). Meanwhile, the structural parameter, ψ, values in the RPM model were estimated using the optimum fitting, which was achieved by maximising the coefficient of determination R^2 (Equation 5.8). These values remained constant across varying gasification temperatures due to their association with the initial pore structure of the chars [114].

As shown in Figure 7.3, the reaction rate constant values significantly increased as the gasification temperature increased from 900°C to 1000°C for all the kinetic methods. These results indicate that the gasification temperature is the most important factor controlling the reaction rate over the conditions studied and is with agreement with results found in the literature [129].

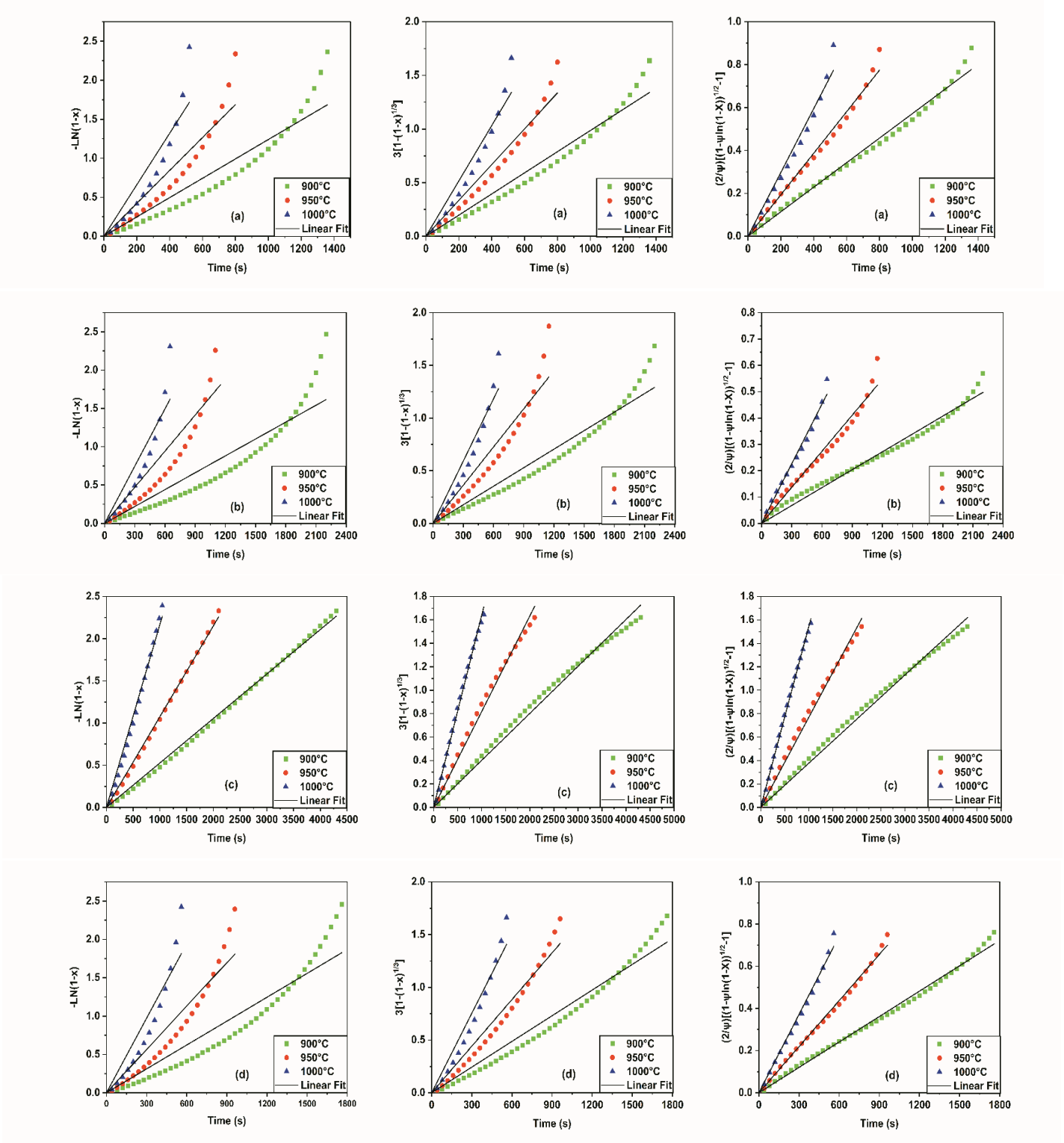

Figure 7.1: Linearisation of the VM, GM and RPM models:(a) BC1, (b) BC2, (c) BC3 and (d) BC4.

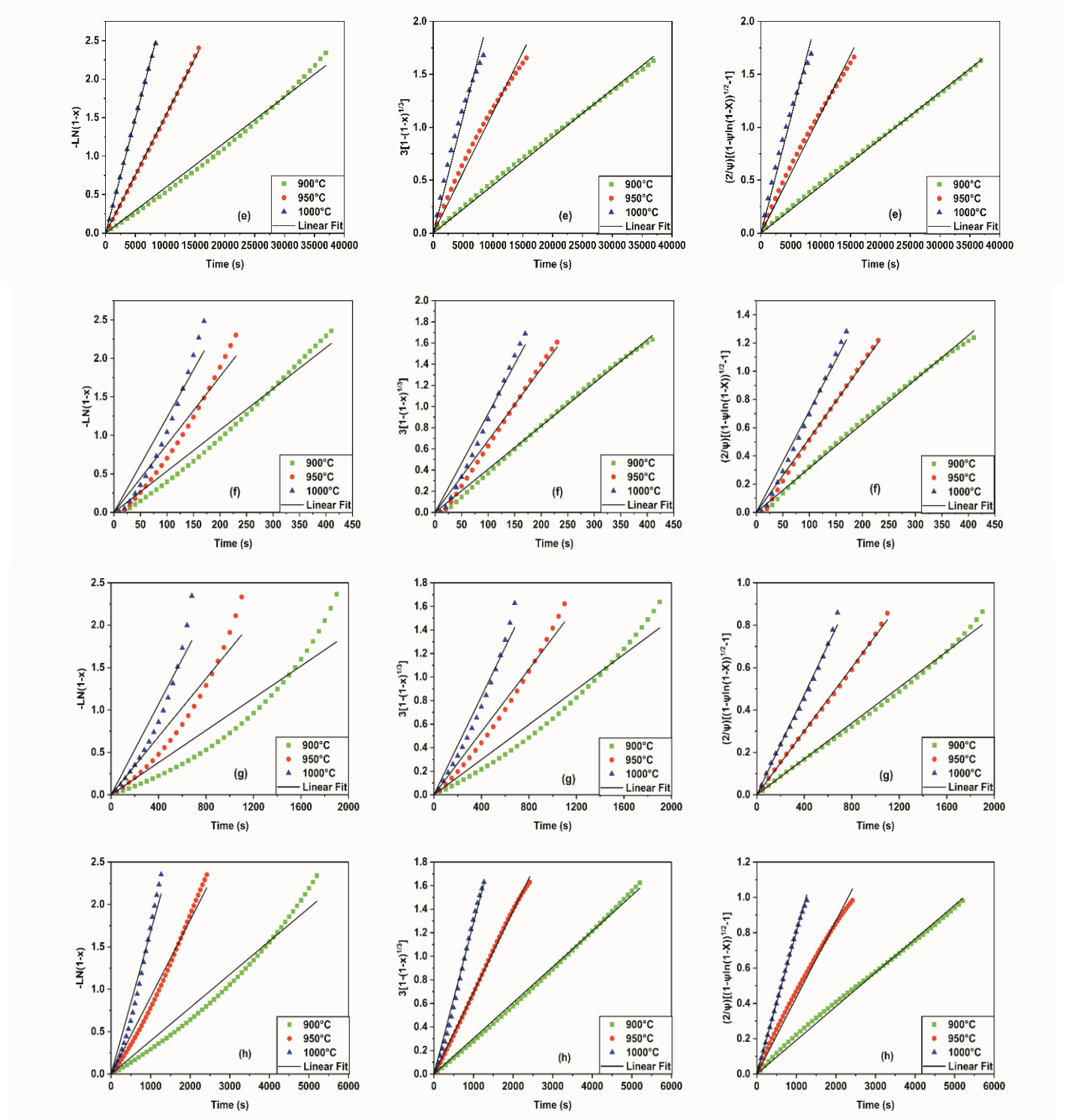

Figure 7.2: Linearisation of the VM, GM and RPM models:(e) CC, (f) HC, (g) BC1HCl and (d) HCHCl.

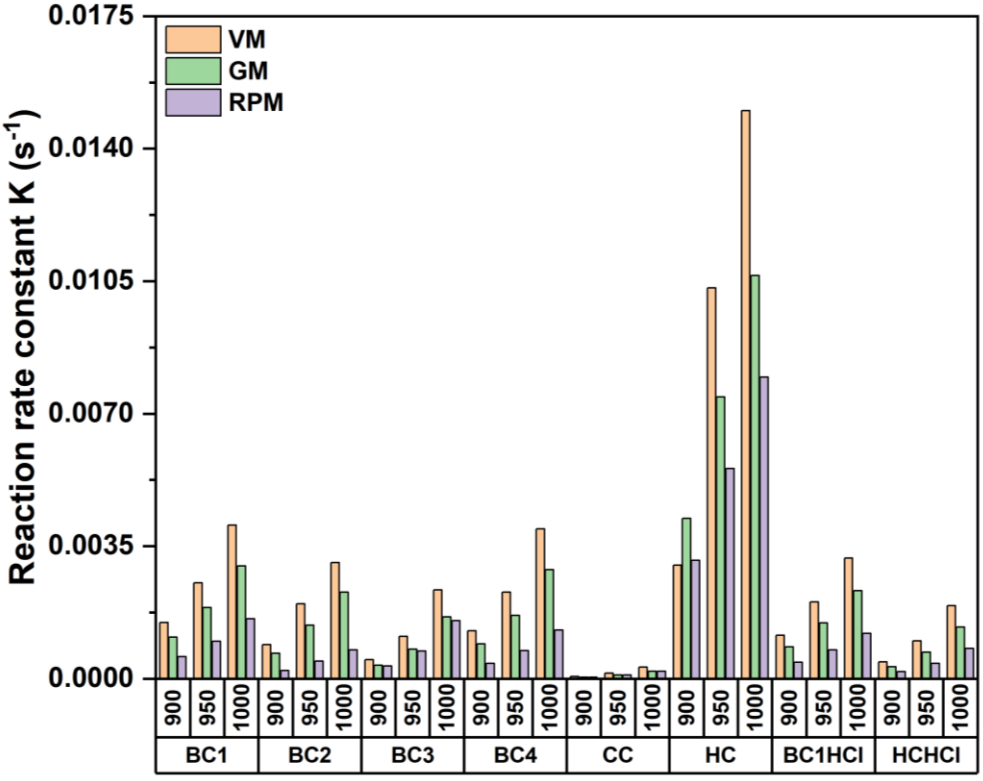

Figure 7.3: Reaction rate constants obtained from VM, GM and RPM.

The calculated reaction constants from VM, GM and RPM were used to generate Arrhenius curves by plotting (lnk) vs. $(1/T)$ to determine the kinetic parameters, activation energy E and the pre-exponential factor A_0. According to Figure 7.4, a good linear relationship is observed between (lnk) and $(1/T)$ for the chars at the gasification temperatures studied, which indicates that the process is likely governed by the chemical reaction [114]. However, the linearity of Arrhenius plot is not conclusive for the chemical reaction regime as the pore diffusion regime can exhibit similar trends at high gasification temperatures. Therefore, additional data points would be required for precise assessment. This could be attained by extending the range of the gasification temperature, specifically toward lower temperatures, to observe the change in the reaction controlling mechanism (see Section 2.8.2). Unfortunately, this was not feasible at this stage of the PhD due to the breakdown of the Mettler-Toledo TGA/DSC 3+ during this experimental work.

Fitting the calculated conversion to the experimental conversion data was carried out in MATLAB and can be found in Appendix D. The fitting curves at different temperatures were obtained by fitting the experimental results of CO_2 gasification to the kinetic models, as shown in Figure 7.5 and Figure 7.6. The RPM model provides the most optimal fit for gasification data of the biomass chars and hydrochar under investigation at all temperatures studied. This finding is consistent with the existing literature [114,115,219–221].

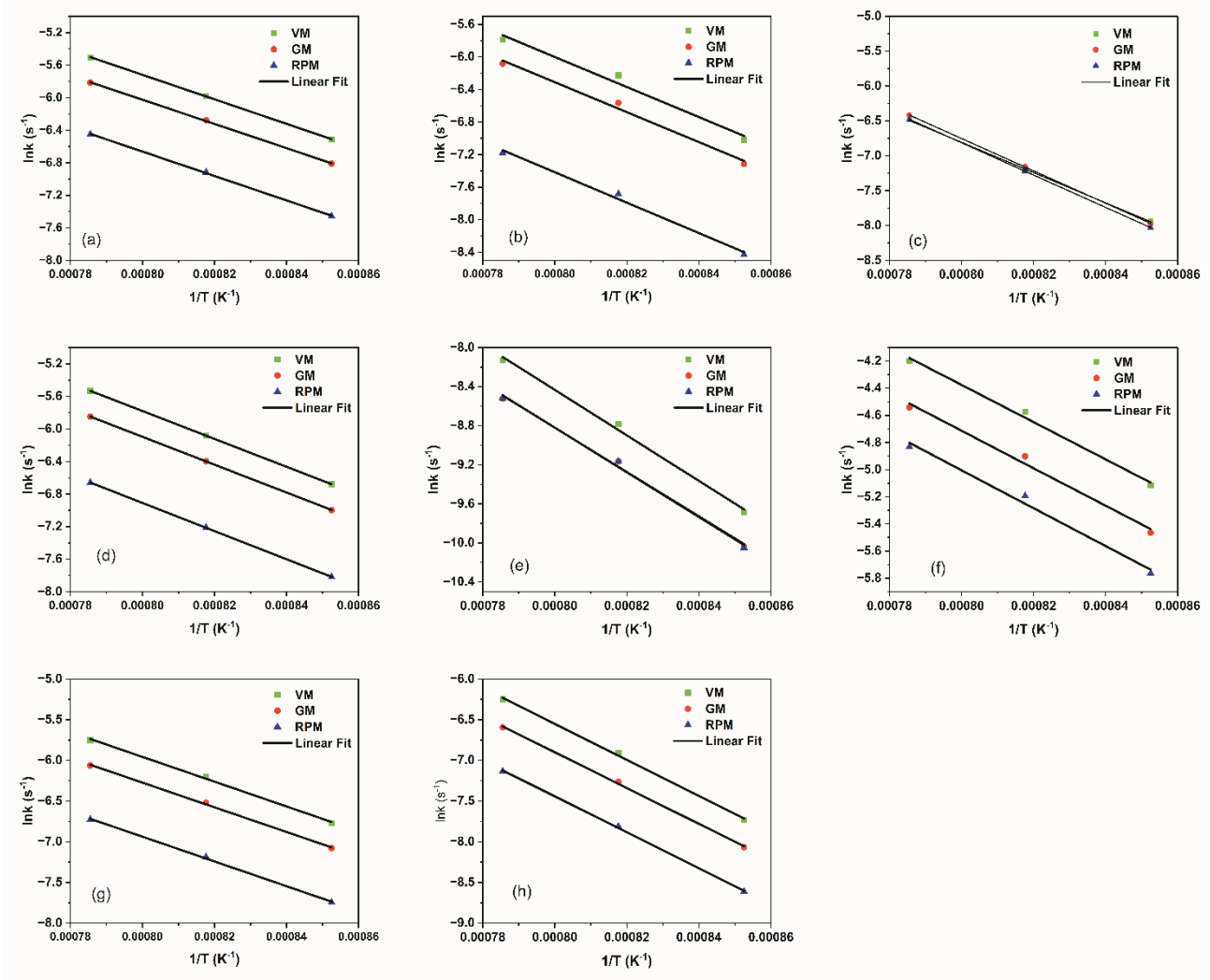

Figure 7.4: Arrhenius plots of different chars obtained by the VM, GM and RPM models:(a) BC1, (b) BC2, (c) BC3, (d) BC4, (e) CC, (f) HC, (g) BC1HCl and (h) HCHCl.

The effect of demineralisation on the hydrochar (HCHCl at 900°C and 950°C) was a change from the best fit of the random pore model to the grain model instead, whilst maintaining similar kinetic parameters, suggesting a change in the reaction mechanism of HC with the loss of catalytic ash components. The kinetic parameters of HC were measurably changed after demineralisation with significant increases in activation energies for HC from 116.2 to 183.0 kJ/mol whereas BC1 was much less affected ranging from 124.9 to 126.5 kJ/mol as shown in Table 7.1.

In this study, the activation energy values obtained from the kinetic models are 114 to 193.6 kJ/mol. These values fell within the activation energy values reported in the literature as shown in Table 7.2. Although the activation energy of HC is slightly lower, this may be attributed to the hydrothermal treatment applied to this sample. The advanced surface analysis using XPS identified increased chemical surface functionality for the HC and BC1 samples. This was indicated by wide asymmetric carbon peaks, and the predominately sp^3 allotropic forms of carbon and correspondingly lower activation energies. The range of techniques used to analyse and compare the samples used in this study, including demineralisation, illustrating the potential contribution of other reaction mechanisms on the activation energy.

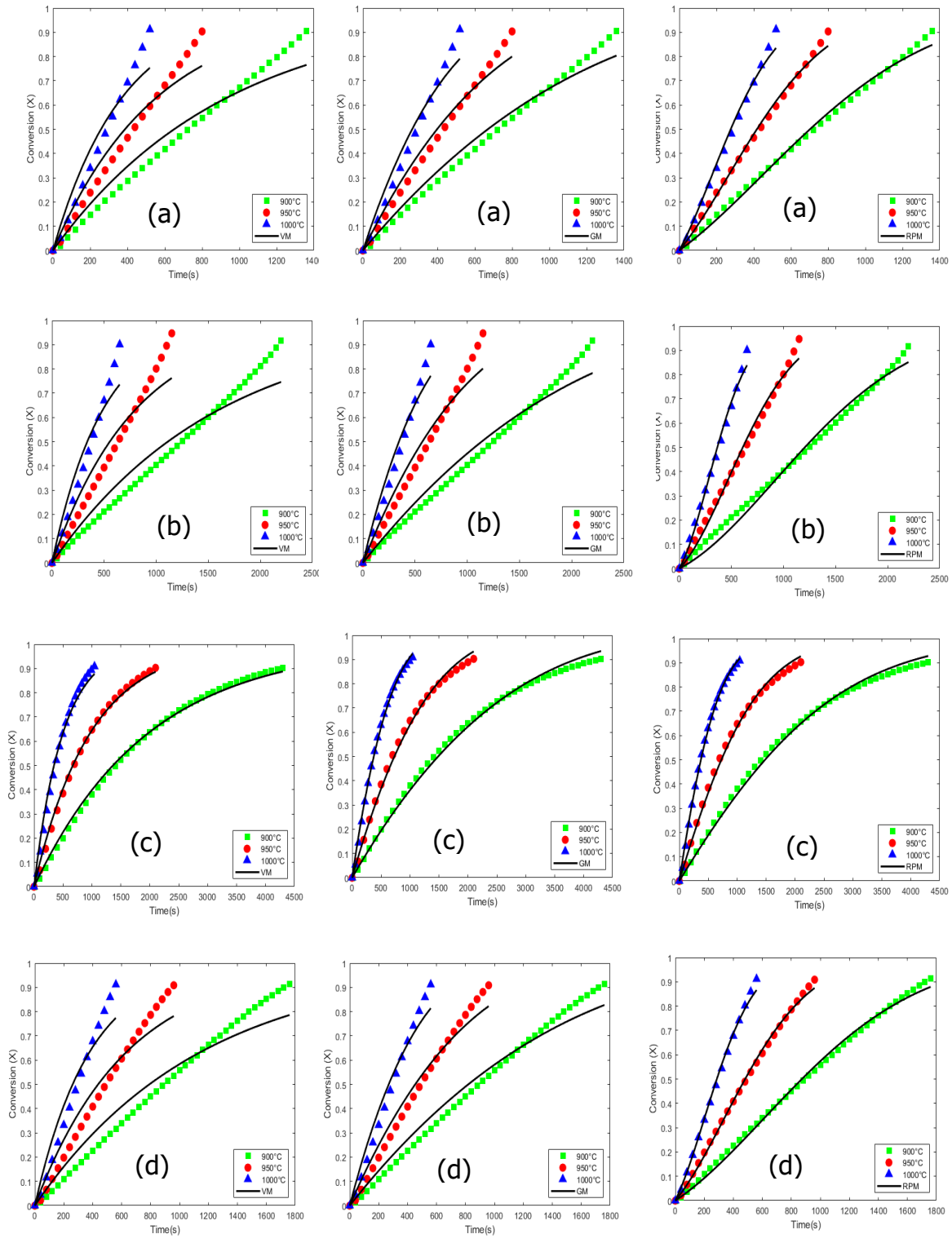

Figure 7.5: Fitting curves of experimental data and predicted values by the VM, GM and RPM models:(a) BC1, (b) BC2, (c) BC3 and (d) BC4.

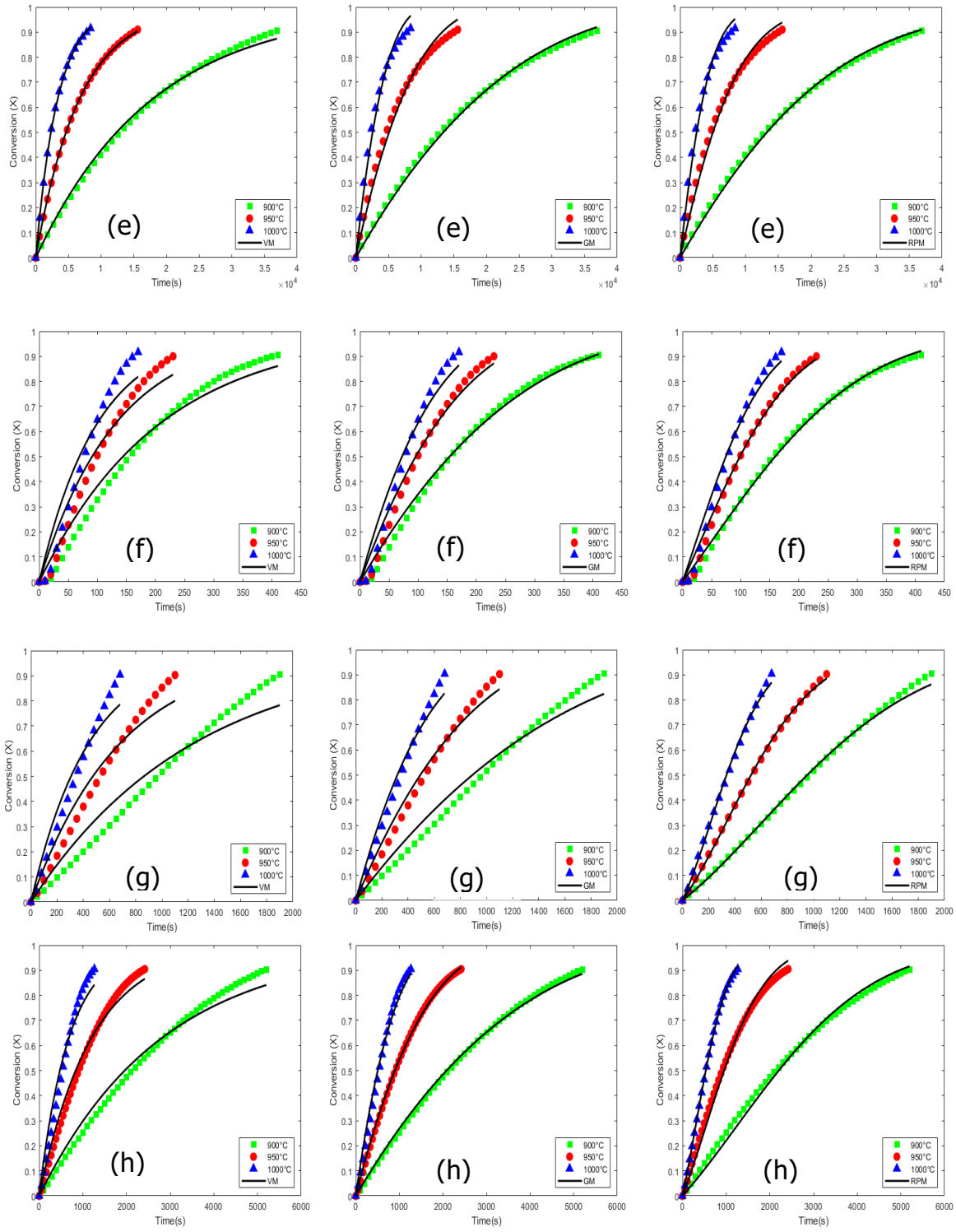

Figure 7.6: Fitting curves of experimental data and predicted values by the VM, GM and RPM models (e) CC, (f) HC, (g) BC1HCl and (h) HCHCl.

In comparison, experimental conversion profiles of CC were fitted by the VM indicating that coal char has a completely different mechanism compared to biomass chars. Table 7.3 presents the percentage errors between the experimental conversion values and those estimated by the kinetic models using Equation 5.16. A lower value of DEV(X)% means a better model to fit the experimental data. The results show that relative errors corresponding to the RPM are the lowest of all models except for CC and demineralised hydrochar (HCHCl) as shown in Table 7.3.

Table 7.1: Kinetic parameters obtained by VM, GM and RPM models for the char samples in isothermal CO_2 gasification.

Sample	VM		GM		RPM		
	E (kJ/mol)	A_0 (s^{-1})	E (kJ/mol)	A_0 (s^{-1})	E (kJ/mol)	A_0 (s^{-1})	ψ
BC1	125.2	559.2	123.7	354.9	124.9	210.7	7.7
BC2	153.6	6510.7	153.2	4575.2	155.6	1902.5	23.6
BC3	179.9	55547.8	180.0	39183.1	180.3	37949.1	1.3
BC4	142.4	2760.3	142.3	1986.2	143.9	1036.4	11.7
CC	193.6	26903.2	188.7	11385.6	190.3	13550.8	1.0
HC	114.0	733.4	114.9	568.2	116.2	479.4	2.9
BC1HCl	126.6	506.7	126.1	351.7	126.5	187.8	8.1
HCHCl	184.1	70615.2	183.0	44891.3	183.7	27694.8	5.7

Table 7.2: Activation energy values of chars in literature for isothermal CO_2 gasification.

Material	Temperature (°C)	Kinetic model	*E* (kJ/mol)	Reference
Herbaceous and wooden residues	850-1000	RPM	129.8-180.3	[114]
Barapukurian bituminous coal	800-1100	VM, GM and RPM	171.2-173.7	[139]
Bituminous coal	1050-1150	GM	125-207.6	[222]
Food waste	850-950	VM, GM and RPM	155-164.3	[193]
Pinus densiflora	850-1050	VM, GM and RPM	134-172	[223]

Table 7.3: Deviation between the predicted values by the kinetic models (VM, GM and RPM) and the experimental conversion data in isothermal CO_2 gasification.

Sample	*DEV (X)* (%)		
	VM	GM	RPM
BC1	15.03	10.10	3.77
BC2	16.17	11.15	3.49
BC3	4.02	3.10	2.99
BC4	15.02	9.79	2.41
CC	2.24	5.69	4.60
HC	12.72	7.24	4.76
BC1HCl	13.71	8.44	2.06
HCHCl	9.02	3.28	3.45

7.3 Kinetic analysis of non-isothermal CO_2 gasification

Biomass and coal chars were tested in non-isothermal conditions at different heating rates to study dynamic temperature impact on their reactivity and to measure kinetic parameters at these conditions. Thermogravimetric mass loss and first derivative thermogravimetric rate of mass loss curves are shown in Figure 7.7. As seen in TGA and DTG profiles, both mass loss trends and DTG peaks shifted to higher temperatures as the heating rate rises from 5 to 15°C/min. Also, the peak rate of mass loss becomes steeper as the heating rate increases, confirming the effect of temperature on the gasification process. Similar to the observed performance of hydrochar (HC) in isothermal tests, the chemical reactions started and completed earlier compared to the other char samples. However, woody chars (BC1 and BC2) exhibited higher DTG peaks compared to HC. This reflects their higher fixed carbon content and lower ash contents as shown in proximate analysis results in Table 6.3. Of the samples examined, coal char (CC) and BC3 samples demonstrated a very slow reaction rates, and CC did not even reach complete conversion for all heating rates. This behaviour is explained below.

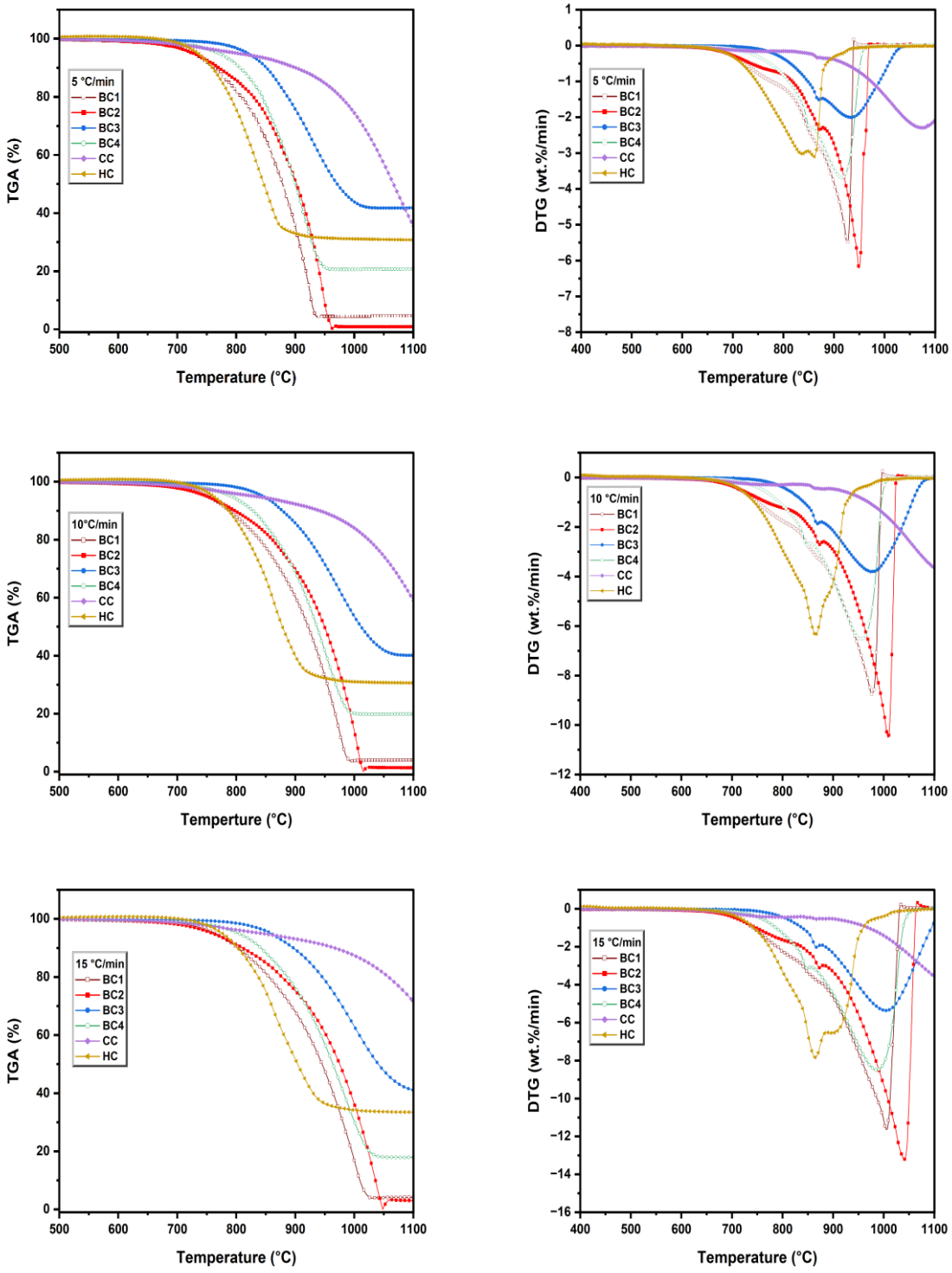

Figure 7.7: Thermal analysis profiles of non-isothermal CO_2 gasification of chars at different heating rate, TGA mass loss curves left and derivative TGA are right curves.

The non-isothermal CO_2 gasification comprises of three stages. The first stage is when the temperature below the initial gasification temperature (T_i) also known as onset temperature. At this stage the mass loss remains constant, which provides a baseline to determine T_i. Once mass loss deviates from the identified baseline, the second stage is reached, which ends at the final gasification temperature (T_f), known as offset temperature. The mass loss trend then subsequently returns to the baseline. The final stage represents the end of the gasification reaction above T_f, where only unconverted carbon and residual ash remain. The measurement of the gasification characteristic parameters and kinetic parameters (Section 7.4) is based on the second stage where most of the carbon is converted during the gasification process [92,129,133]. The gasification characteristic temperatures (T_i and T_f) are determined according to the standards ASTM E2550 [224] and ISO 11358-1 [225] using TGA and DTG profiles by identifying a threshold of 0.02% mass loss and baseline. These gasification parameters including T_i, T_m (maximum DTG_{peak} temperature), T_f can be used to assist material reactivity at similar conditions [129]. Additionally, the non-isothermal char gasification reactivity can be further evaluated using the comprehensive gasification characteristic index S [92]. A higher value of this index means high gasification reactivity [129]. It is calculated by the following equation:

$$S = \frac{(dx/dt)_{max}.(dx/dt)_{mean}}{T_i^2 T_f} \tag{7.1}$$

Where $(dx/dt)_{max}$ is the maximum experimental reaction rate and $(dx/dt)_{mean}$ is the mean experimental reaction rate for different heating rates.

Table 7.4 summarises the gasification characteristic parameters of the six chars with results reported as averages from duplicate and triplicate experiments. The experimental errors are given as standard deviations, which are provided in Appendix E. It can be seen that gasification characteristic parameters increase as the heating rate increases, which is in agreement with reported findings in literature [129,133]. The lower characteristic temperatures (T_i,T_m and T_f) and higher S indices for (BC1-BC4) and HC indicate that their

overall gasification reactivity is significantly higher than CC. This is consistent with the isothermal gasification experiment results presented in Chapter 6. Notably, HC demonstrates the lowest characteristic temperatures in the range of (637 to 999°C) which indicates superior thermal reactivity. However, BC1 and BC2 show higher reaction rates (dx/dt_{max}) and mass loss rates (DTG_{peak}) with values ranged from 0.058 to 0.132 min^{-1} and 5.50 to 13.45 wt.%/min, respectively. This outcome is reflected in the calculated S values. Overall, the char reactivities can be ranked from high to low as BC1, HC, BC2, BC4, BC3 and CC based on the gasification comprehensive reactivity index S.

Table 7.4: Non-isothermal gasification parameters of different chars at different heating rates.

Sample	Heating rate (°C /min)	T_i (°C)	T_m (°C)	T_f (°C)	DTG_{peak} (wt.%/min)	dx/dt_{max} (min^{-1})	dx/dt_{mean} (min^{-1})	S ($x10^{-13}$)	m_{ash} (%)
BC1	5	652.7	926.4	933.6	5.5	0.057	0.007	10.4	4.5
	10	667.5	978.4	988.6	8.8	0.092	0.014	29.9	4.0
	15	680.7	1009.2	1018.6	12.1	0.129	0.021	58.8	4.2
BC2	5	679.8	952.8	968.3	6.4	0.064	0.007	10.1	0.9
	10	692.6	1008.5	1025.1	10.5	0.105	0.014	30.5	1.4
	15	703.1	1038.8	1060.6	13.5	0.132	0.021	53.7	3.0
BC3☆	5	726.3	933.7	1027.6	2.0	0.035	0.007	4.6	41.4
	10	745.9	975.9	1078.0	3.8	0.064	0.014	15.3	40.1
	15	756.9	1005.0	1105.7	5.4	0.091	0.021	30.9	40.9
BC4	5	705.2	914.3	957.3	3.7	0.047	0.007	7.04	20.8
	10	708.6	956.6	1006.3	6.5	0.082	0.014	23.1	19.9
	15	716.0	985.9	1047.8	8.5	0.104	0.021	41.4	17.9
CC☆☆	5	847.6	1077.7	1103.6	2.3	0.039	0.007	3.6	34.4
	10	876.6	1101.5	1103.2	3.7	0.094	0.014	15.8	58.0
	15	904.4	1100.8	1104.0	3.6	0.125	0.021	29.6	70.7
HC	5	637.6	852.4	921.3	3.1	0.046	0.007	8.9	30.8
	10	662.1	865.0	971.0	6.3	0.092	0.014	30.9	30.6
	15	673.9	865.0	999.3	7.8	0.119	0.021	56.0	33.5

☆: T_f at heating rate 15°C/min is the last recorded temperature.

☆☆: T_f for all heating rate is the last recorded temperature.

7.4 Kinetic analysis of non-isothermal char gasification

Kinetic models (VM, GM and RPM) were applied to fit the experimental data and measure activation energy and pre-exponential factor using Equations 5.2-5.5 and Equation 5.17. Fitting the calculated reaction rate (dx/dt) and conversion (X) to the experimental reaction rate and conversion data were carried out in MATLAB and can be found in Appendix F and Appendix G.

Results are shown in Figure 7.8, Figure 7.9 and Table 7.5. As shown, activation energies and pre-exponential factors derived from non-isothermal CO_2 gasification tests are significantly higher than those obtained from isothermal CO_2 gasification (see Table 7.1) for all samples. Taking BC1 for example, the measured activation energy from VM, GM and RPM are 208.7, 195.2 and 174.2 kJ/mol, respectively. These are approximately 1.7, 1.6, and 1.4 times higher than their corresponding measured values under isothermal tests (125.2, 123.7, and 124.9 kJ/mol, respectively). Also, the pre-exponential factor under isothermal conditions significantly increases from (559.2, 354.9, and 210.7 s^{-1}) to (1.8×10^{8}, 3.6×10^{7}, and 2.2×10^{6} s^{-1}) in non-isothermal conditions. In contrast, the structural parameter for BC2, BC3, BC4, and HC significantly decreases in non-isothermal gasification. While similar findings have been reported by Wang et al. in their isothermal and non-isothermal CO_2 gasification studies of agricultural and coal [92,114], both studies did not explore the effect of these conditions on the kinetic parameters obtained from VM, GM, and RPM. Most kinetic investigations in literature using these models have focused on either isothermal or non-isothermal conditions, with only a few studies considered the effect of these conditions on the kinetic parameters. For instance, Czerski et al. [226] compared activation energies and pre-exponential factors using an nth-order model under both conditions. Tran et al.[227] also made a similar comparison but using the distributed activation energy model (DAEM) in non-isothermal gasification. This work, however, provides a direct comparison of VM, GM and RPM parameters under isothermal and non-isothermal conditions. It also extends the understanding of the reaction kinetics by including hydrothermally carbonised char which has different physicochemical properties.

Deviation between calculated reaction rate and experimental data was measured using Equation 5.22, the results in Table 7.6 indicate that GM was the best fitting model for (BC1,BC2 and BC4) with values of 7.17,7.81 and 4.29%,respectively, while RPM was better suited to samples BC3 and HC with values of 2.21 and 3.17%, respectively. This implies that gasification conditions play a significant role in reaction kinetics. Additionally, the obtained kinetic parameters (Table 7.5) were used to calculate char conversion Equations 5.19-5.21 at the three heating rates. The results are shown in Figure 7.10. It clear that char conversion was reduced and gasification reaction rate was increased (Figure 7.8 and Figure 7.9) as heating rates increased.

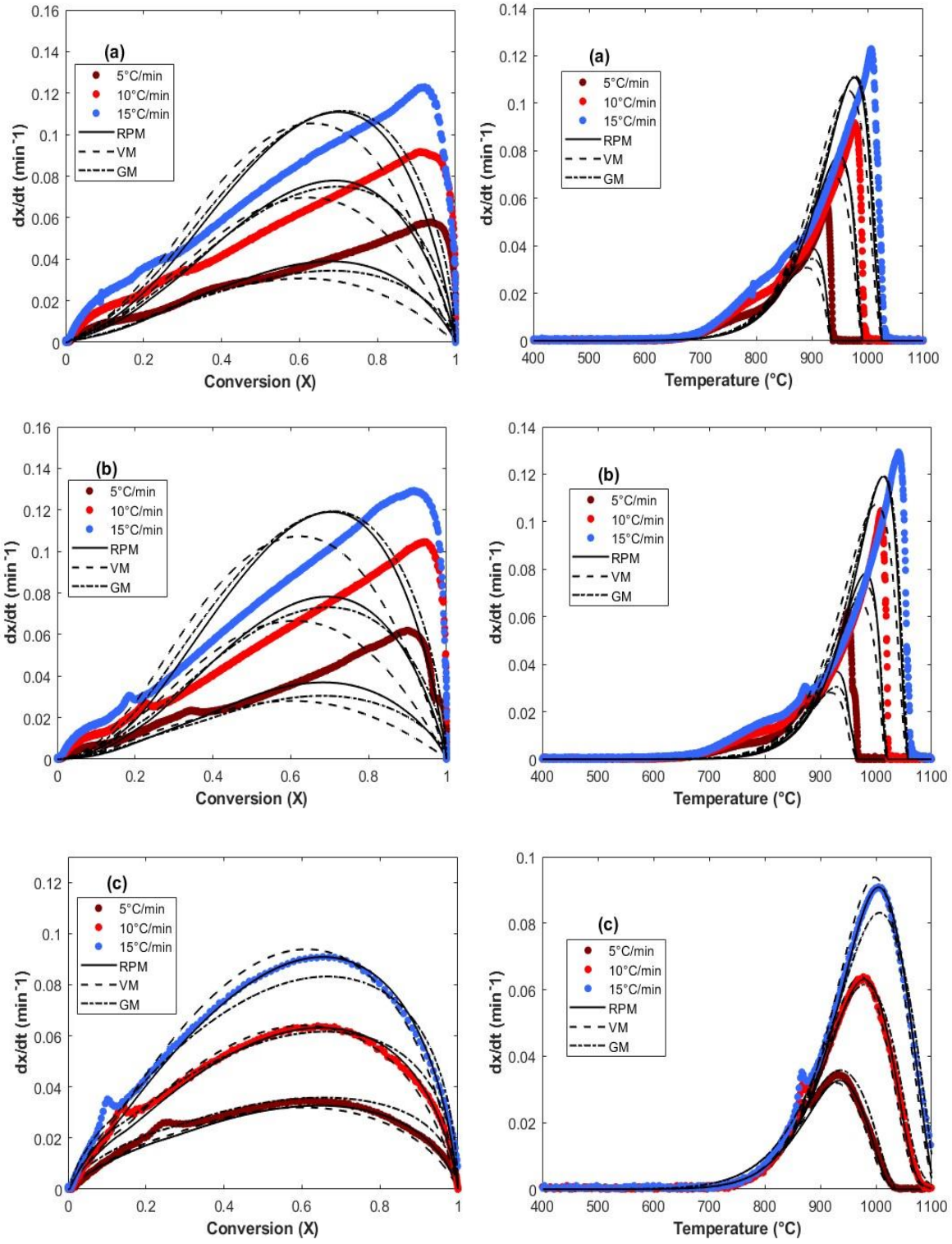

Figure 7.8: Fitting curves of experimental reaction rate data and predicted values by the VM, GM and RPM models:(a) BC1, (b) BC2 and (c) BC3.

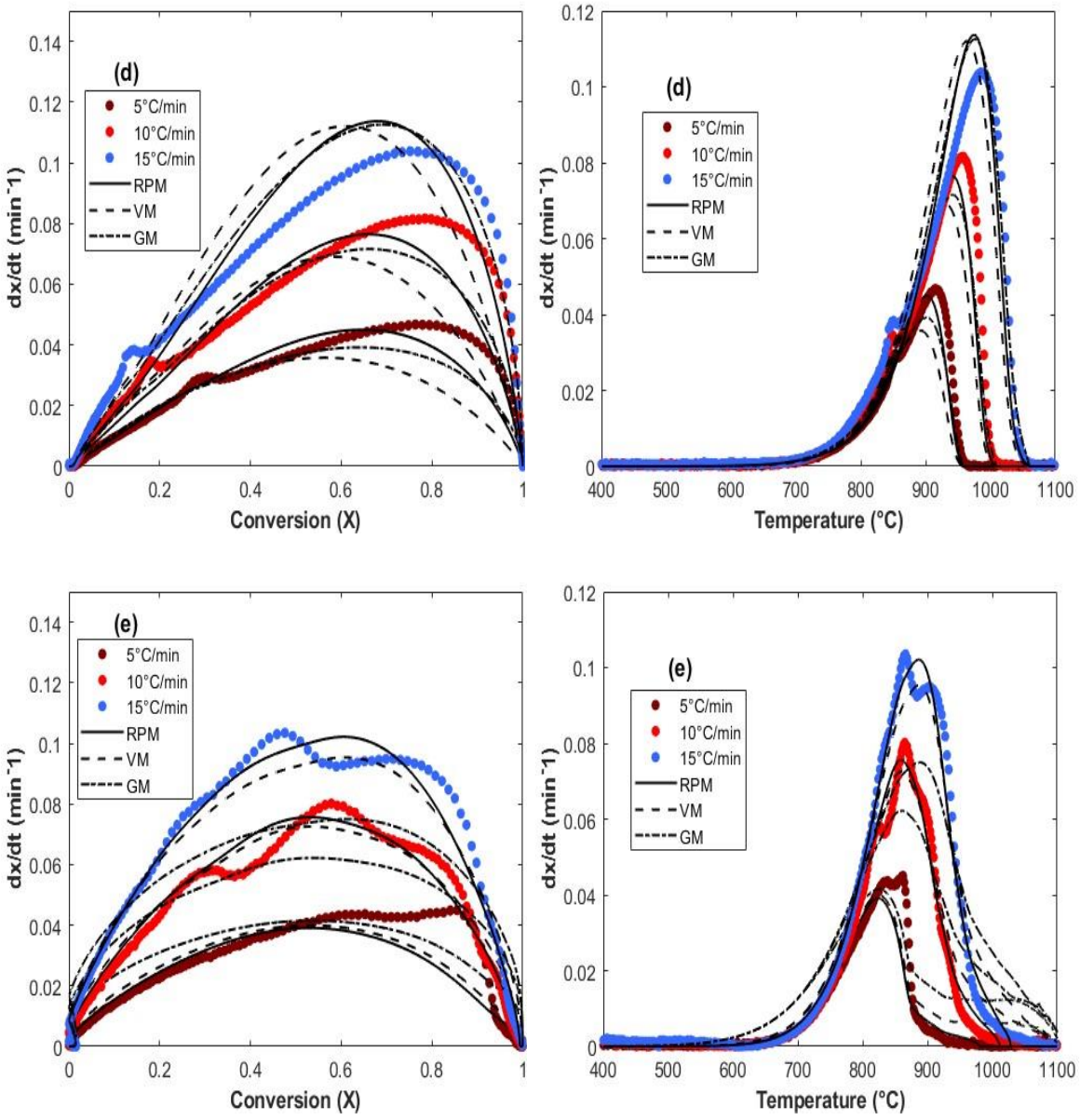

Figure 7.9: Fitting curves of experimental reaction rate data and predicted values by the VM, GM and RPM models:(d) BC4 and (e) HC.

Table 7.5: Kinetic parameters obtained by VM, GM and RPM models for the char samples in non-isothermal CO_2 gasification.

Sample	VM			GM			RPM			
	E (kJ/mol)	A_0 (s^{-1})	R^2	E (kJ/mol)	A_0 (min^{-1})	R^2	E (kJ/mol)	A_0 (min^{-1})	ψ	R^2
BC1	208.7	1.8e+08	0.77	195.2	3.6e+07	0.87	174.2	2.2e+06	7.7	0.84
BC2	214.9	1.9e+08	0.71	214.7	1.4e+08	0.83	190.8	6.2e+06	10.0	0.81
BC3	203.4	5.6e+07	0.99	158.6	5.1e+05	0.99	192.4	1.6e+07	0.5	0.99
BC4	209.7	2.0e+08	0.89	187.4	1.2e+07	0.97	164.8	9.2e+05	7.4	0.96
HC	177.4	2.4e+07	0.96	120.2	3.6e+04	0.86	196.3	2.0e+08	0.2	0.98

Table 7.6: Deviation between the predicted values by the kinetic models (VM, GM and RPM) and the experimental reaction rate data in non-isothermal CO_2 gasification.

Sample	*DEV (dx/dt)* (%)		
	VM	GM	RPM
BC1	9.56	7.17	7.89
BC2	10.16	7.81	8.19
BC3	2.54	2.81	2.21
BC4	7.71	4.29	4.98
HC	4.47	8.76	3.17

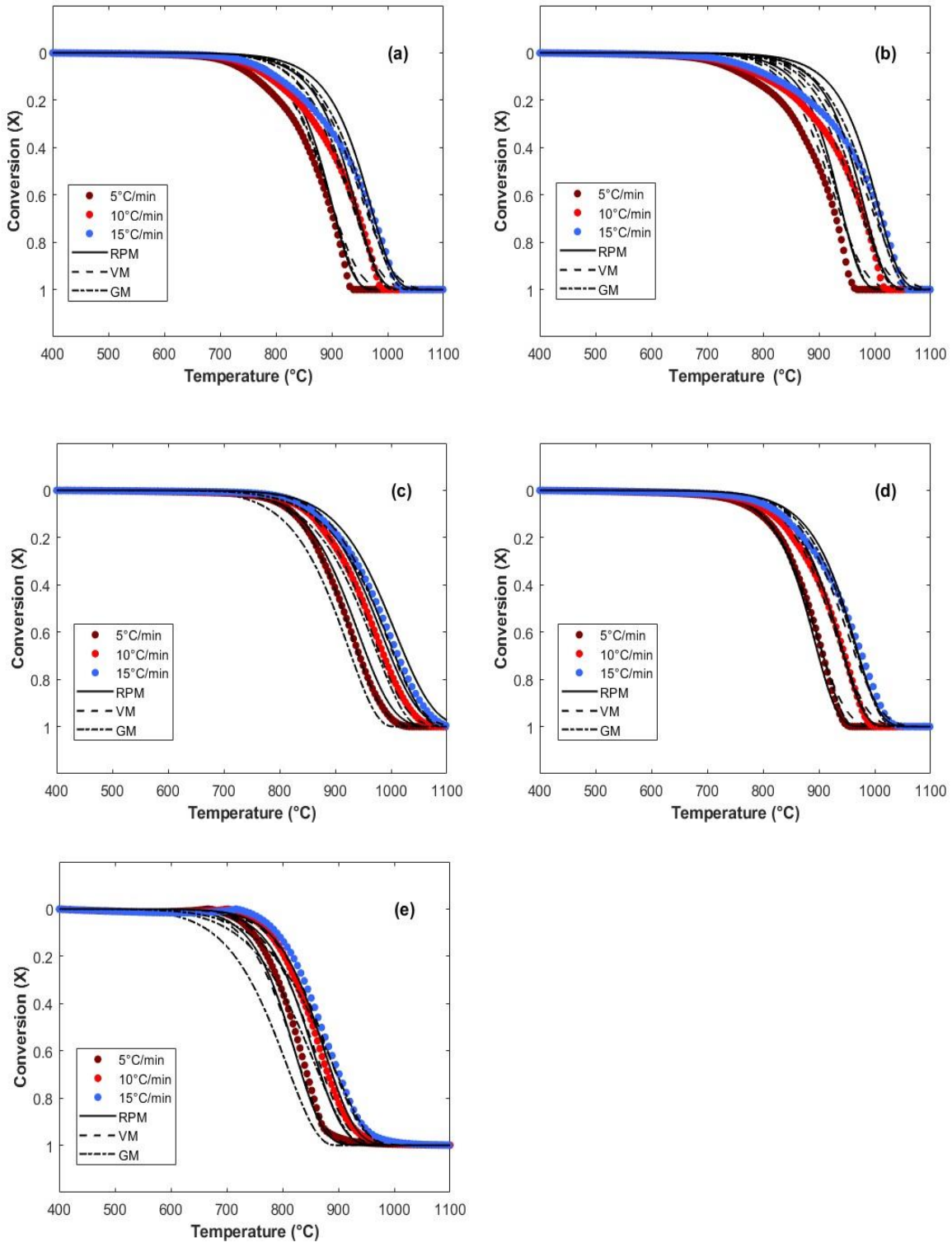

Figure 7.10: Fitting curves of experimental conversion data and predicted values by the VM, GM and RPM models:(a) BC1, (b) BC2, (c) BC3, (d) BC4 and (e) HC.

7.5 Chapter summary

Three kinetic models, namely, VM, GM and RPM were used to describe CO_2 gasification of the different samples by fitting experimental data with models in isothermal and non-isothermal conditions. Non-isothermal CO_2 gasification experiments were conducted at three heating rates (5,10 and 15°C/min) to investigate dynamic temperature impact on chars' reactivity and results show that:

a. The reaction rate constant values were significantly increased when the reaction temperature increased from 900°C to 1000°C for all the kinetic models.
b. The RPM model provides the most optimal fit for isothermal gasification data of the biomass chars and hydrochar under investigation at all temperatures. CC show an acceptable fit to the VM indicating that coal char has a completely different mechanism compared to biomass chars.
c. The RPM model was reduced to the GM model for the demineralised hydrochar at 900°C and 950°C, which suggests that the reaction mechanism of HC is different after demineralisation.
d. In non-isothermal gasification, increasing the heating rate moves mass loss trends and DTG peaks to higher temperature zones.
e. As heating rate increases, gasification characteristic parameters increase and char conversion decreases.
f. The gasification comprehensive reactivity index S indicates that the char reactivities can be ranked from high to low as BC1, HC, BC2, BC4, BC3 and CC.
g. Kinetic parameters including (activation energy and pre- exponential factor) under non-isothermal CO_2 gasification testing are significantly higher than those obtained from isothermal CO_2 gasification. Conversely, the structural parameter (ψ) is significantly lower under non-isothermal conditions.
h. In non-isothermal gasification, the GM was the best fit model for (BC1, BC2 and BC4), while RPM had a better fit for samples BC3 and HC.

Chapter 8 CO_2 gasification experimental results from Macro-TGA

8.1 Introduction

This chapter presents the results of CO_2 gasification from the fixed bed Macro-TGA reactor that was developed specifically for this research project. The conventional TGA was upscaled as detailed in Chapter 4 to investigate the reverse Boudouard reaction performance under more representative industrial conditions. In this system, a larger sample size of biochar (BC1) was used to evaluate its reactivity and reaction kinetics at different gasification temperatures. The results were compared to TGA data from smaller samples (~ 15 mg), as discussed in Chapter 5, to examine the influence of scale on material behaviour. Another set of experiments discussed the effect of changing the surface area exposed to CO_2 molecules, using pellets of different sizes. The influence of surface area on the CO_2 gasification behaviour is explained by real-time mass loss measurement and confirmation of this mass change using the corresponding gas composition analysis. Finally, gas compositions were analysed through a simple calculation of the gas analysis results.

8.2 Stability evaluation of the Macro-TGA balance system

Accuracy and functionality testing of the constructed thermobalance system are essential to produce a mass loss measurement. Prior to the gasification experiments, initial trials were performed to identify the most stable setup to provide reliable mass reading. In this test set, the balance stability was examined using two ceramic rods of different diameters to hold an unloaded crucible inside the chamber. The first rod was relatively thin (a 3 mm diameter) and the second was 12 mm diameter with a block support as described in Section 4.3.1.2. The tests were caried out in cold and hot conditions, and each test was repeated three times to ensure the repeatability of the examined setup, as shown in the following sections. In addition, one single test was carried out using a known reference weight to confirm chosen setup accuracy. It should be noted that balance readings were always smoothed using a moving average method in Origin software for clarity and to reduce noise, while retaining the experiment's trends. The smoothing interval was fixed at 100 data points for all runs. Figure 8.1 shows the effect of smoothing by comparing raw and smoothed data for three balance readings using the 3 mm ceramic rod.

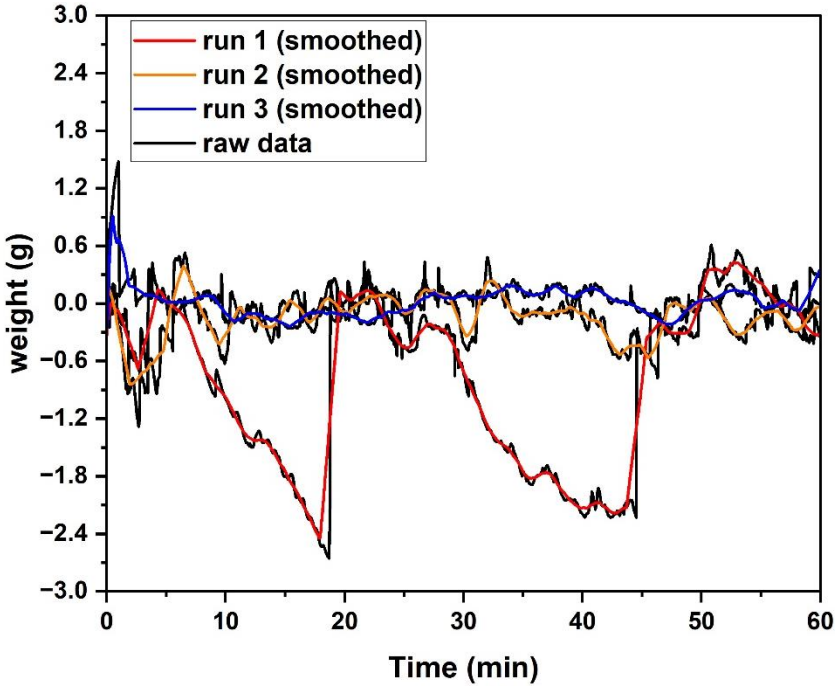

Figure 8.1: An example showing the effect of applying a moving average over 100 data points on the balance readings for three cold condition runs using the 3 mm ceramic rod.

8.2.1 Stability under cold (unheated) conditions

This test was conducted under ambient laboratory conditions in the absence of heat and gas flow inside the reactor for an hour. The balance was turned on and zeroed, and the mass was recorded using the connected SDL logging software. During all tests the lab extraction system was turned on to simulate the real experiment environment, and to get an indication of the vibration-induced noise from the system. The results from the two configurations are significantly different. When the thinner rod was used, a variation between 0.9 to -2.4 g was observed, as shown in Figure 8.2. This overestimated reading is nearly half of a typical sample size, 5 g, i.e. the proposed mass for the gasification experiments. It is not surprising that the surrounding noise affect the mass reading accuracy. However, achieving an acceptable error is crucial to avoid misinterpreting of the mass loss from the gasification experiments. The measured fluctuation was deemed acceptable in the second and third runs whereas first run was significantly more noisy. The unstable mass reading was attributed to the laboratory environment and size of the ceramic rod. Figure 8.3 shows the balance reading after replacing the rod with 12 mm rod. The results of all the three runs were steadier when compared to the 3 mm rod. This indicates that the mass and wider diameter of the rod provides less noise from the extraction fan and the movement around the rig.

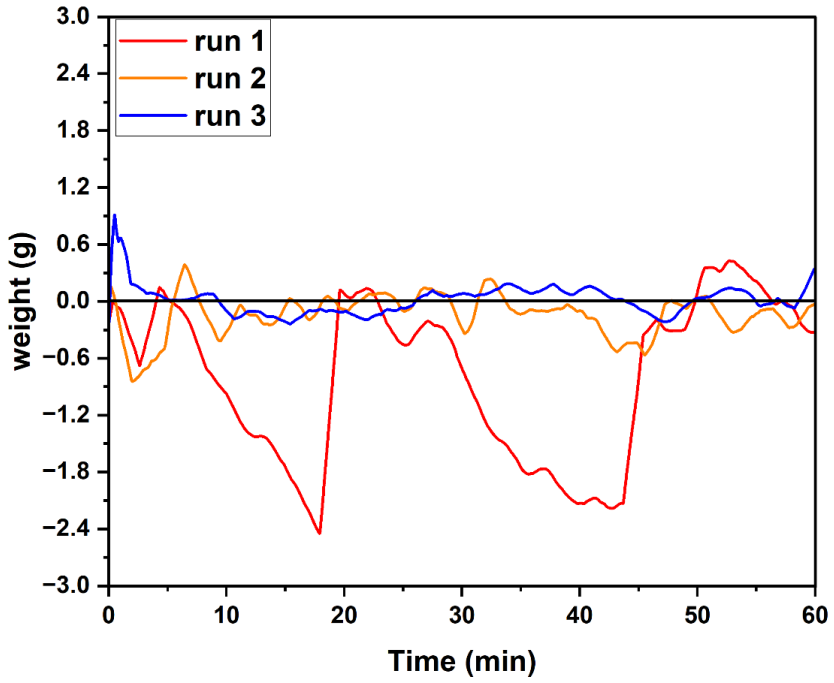

Figure 8.2: Stability of the balance using the 3 mm ceramic rod (Cold run with no gas flow and no sample).

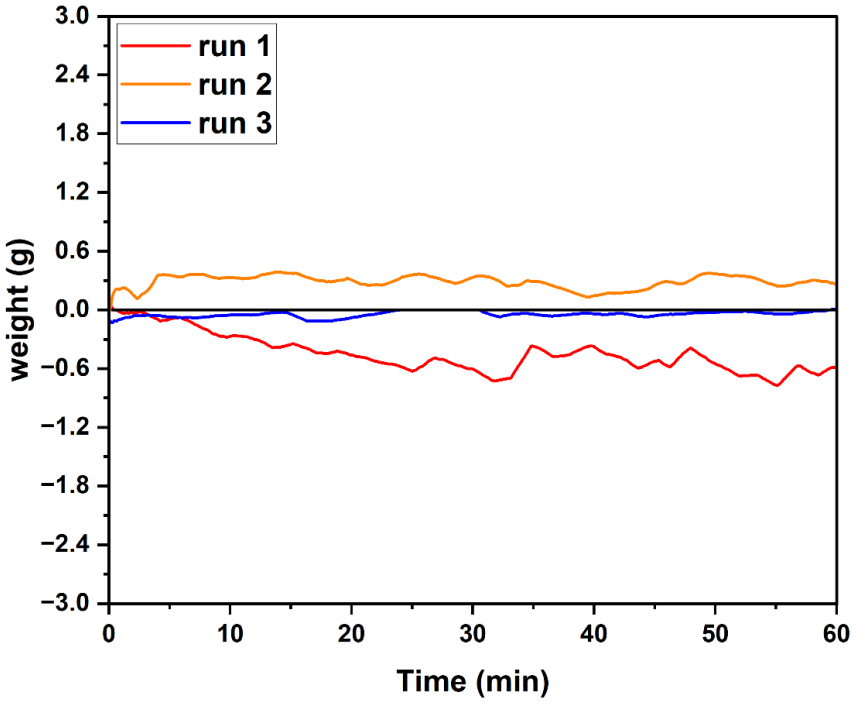

Figure 8.3: Stability of the balance using the 12 mm ceramic rod (Cold run with no gas flow and no sample).

8.2.2 Stability under hot conditions and gas flow

In order to examine the impact of high-temperature conditions on the weight measurement, heat and gas flow were introduced to the system. The furnace was heated to 900°C, and the reactor was then purged continuously by preheated 3.5 L/min N_2 at the same temperature. The mass reading was recorded for an hour under steady isothermal conditions. From the observation of the trials of 3 mm rod, the instability of the weight measurement was significantly increased as can be seen in Figure 8.4. This fluctuation likely occurs due to the introduction of heat, gas flow and thermal expansion of the furnace heating elements which can make instability more prevalent. The deviation of mass readings was between 2.8 and -3 g. In contrast, 12 mm rod provided a more stable reading across the three trials, and the deviation was within 0.3 and -0.5 g as shown in see Figure 8.5.

From this pre-gasification experimental work, it was decided that using 12 mm ceramic rod would be more effective against external and internal noise of the Macro-TGA setup.

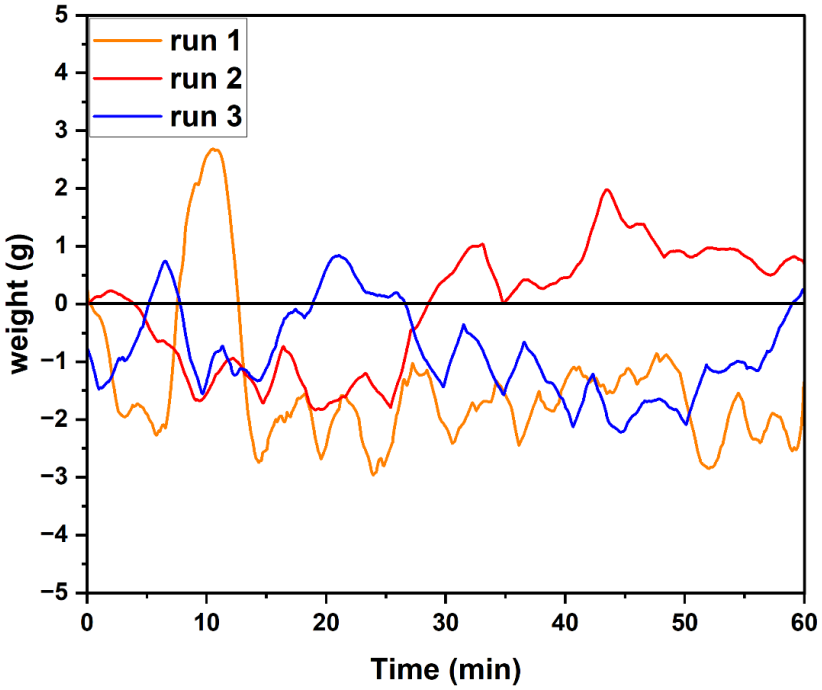

Figure 8.4: Stability of the balance using the 3 mm ceramic rod (Isothermal hot run at 900°C, 3.5 L/min N_2 and no sample).

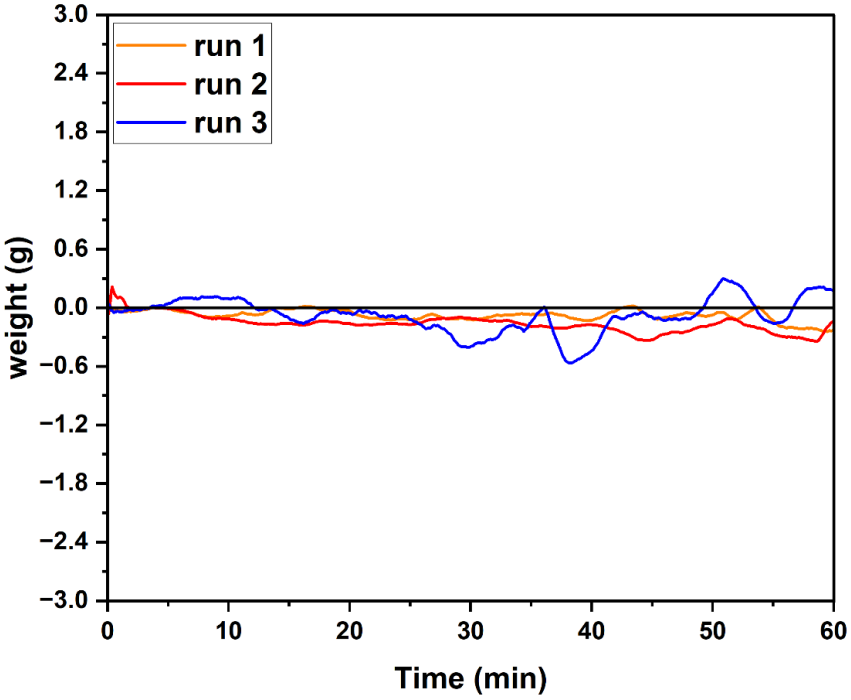

Figure 8.5: Stability of the balance using the 12 mm ceramic rod (Isothermal hot run at 900°C, 3.5 L/min N_2 and no sample).

8.2.3 Testing the system using a known mass

To further confirm the stability of the selected setup, thermobalance was tested using known stainless steel reference mass loaded into the crucible to simulate the presence of a char sample. As such the sample mass should not be subject to any chemical reactions and the mass reading should be constant during the test. The furnace temperature was set to 850°C and the gas flow rate was set to 3.5 L/min of N_2. Once the temperature reached 850°C, N_2 was then replaced by 1.91 L/min CO_2 flow. The flow was then kept at this condition for 40 minutes. The balance reading was recorded from the start of the experiment as shown Figure 8.6. Although only a single run was recorded, it can be seen that the balance data showed a steady measurement of the stainless-steel test mass in both isothermal and non-isothermal heating. This confirmed that the selected setup was satisfactorily stable to be used for the CO_2 gasification experiments in the Macro-TGA.

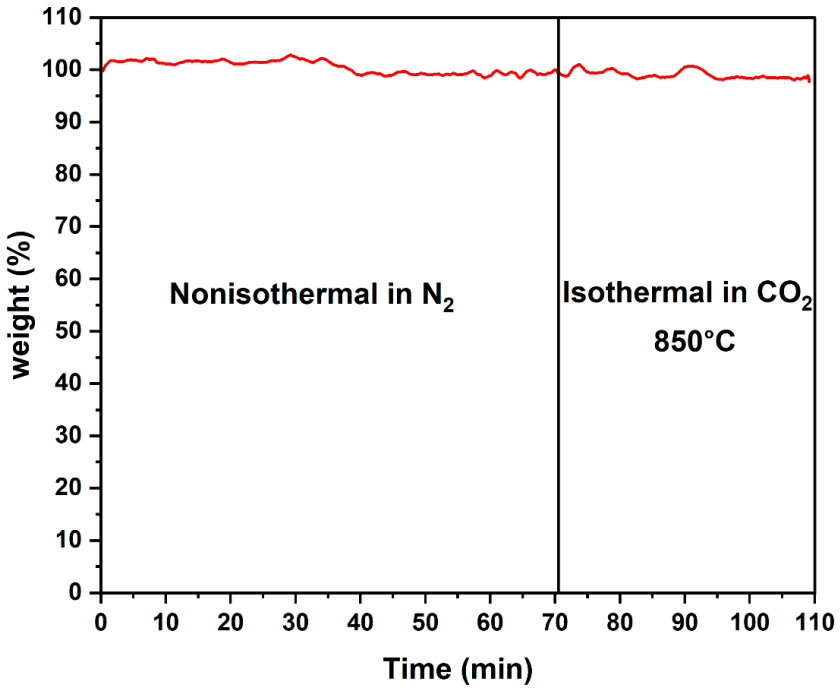

Figure 8.6: Testing the stability of the balance using a known mass at 850°C, 12 mm ceramic rod (3.5 L/min N_2, 1.91 L/min CO_2)

8.3 Measuring CO_2 gasification reactivity in the Macro-TGA

A conventional (micro-scale) TGA has precise control of experimental conditions and is suitable for the determination of intrinsic reactivity (Regime I) [1]. In contrast, industrial gasifiers usually have more variables controlling the reaction rate and/or less well-controlled conditions. This can result in differences between lab-scale studies and real-world gasification processes. In this PhD, the Macro-TGA was used to investigate whether biochar behaviour in a larger scale thermobalance will vary measurably from that observed in the conventional (micro) TGA.

BC1 was tested at different temperatures ranging from 850°C to 1000°C in the Macro-TGA. Tests were conducted in duplicate at 850°C-950°C, whereas only a single run was performed at 1000°C due to the furnace failure. The real-time mass loss curves (Figure 8.7(a, c, e and g)) demonstrate that reaction rate is increased as gasification temperature increases, which has been seen in the Micro-TGA results. Consequently, the time required to complete the reaction was reduced from 220 minutes at 850°C to 60 minutes at 1000°C. This highlights the sensitivity of the reverse Boudouard reaction to gasification temperature due to its endothermic nature. The undulations visible at the end of char conversion at 850°C and 1000°C (Figure 8.7(a, g)) are likely caused by balance reading error, as their corresponding gas composition curves (Figure 8.7(b, h)) show stable reading at these points.

The gas profiles demonstrate a temperature influence, since CO_2 conversion and CO formation indicate a proportional relationship with increasing temperature as shown in Figure 8.7(b, d, f and h). This finding is in agreement with literature regarding the temperature effect on CO_2 consumption and CO yield [150,228]. As can be seen, CO profiles show a maximum concentration at the initial conversion with values of 12.8, 27.84, 32.8 and 29.81% at 850°C, 900°C, 950°C and 1000°C, respectively. A study carried out by Ofuani and Bhoi [150], suggests that the initial peak of CO produced can be attributed to the available carbon active sites on the char surface. These active sites facilitate rapid carbon consumption when CO_2 is first introduced into the gasifier, thus a

high initial CO production. As gasification progresses, CO yield values steadily decrease at different rates for temperatures of 850°C to 950°C, while at 1000°C the CO curve shows a plateau at last third of the conversion, suggesting another mechanism occurs as shown in Figure 8.7(h). The reaction completed when no further mass loss occurred as confirmed by stabilisation in gas composition. The reaction time varied with temperature, as a result, it took approximately 220, 150, 90 and 60 minutes at 850°C, 900°C, 950°C and 1000°C, respectively.

The CO_2 gasification reactivity of BC1 at different temperatures in Macro-TGA was compared to the reactivity derived from Micro-TGA using the $R_{0.5}$ index (Equation 3.15). The comparison results in Figure 8.8 illustrate a significant difference of $R_{0.5}$ values between the two apparatus. It can be seen that Micro-TGA produced higher indices compared to Macro-TGA, and these differences increase as gasification temperature increases. One potential reason is that the sample size used in Macro-TGA, 5 g, involves a thickness of the char bed which is relatively lower in the Micro-TGA setup. This introduces a diffusion barrier to gas-solid reaction and consequently a reduction in the reaction rate [229]. These findings highlight the role of the physical characteristics of the char, such as sample size and available surface area, on the reactivity of CO_2 gasification at larger, more realistic scales.

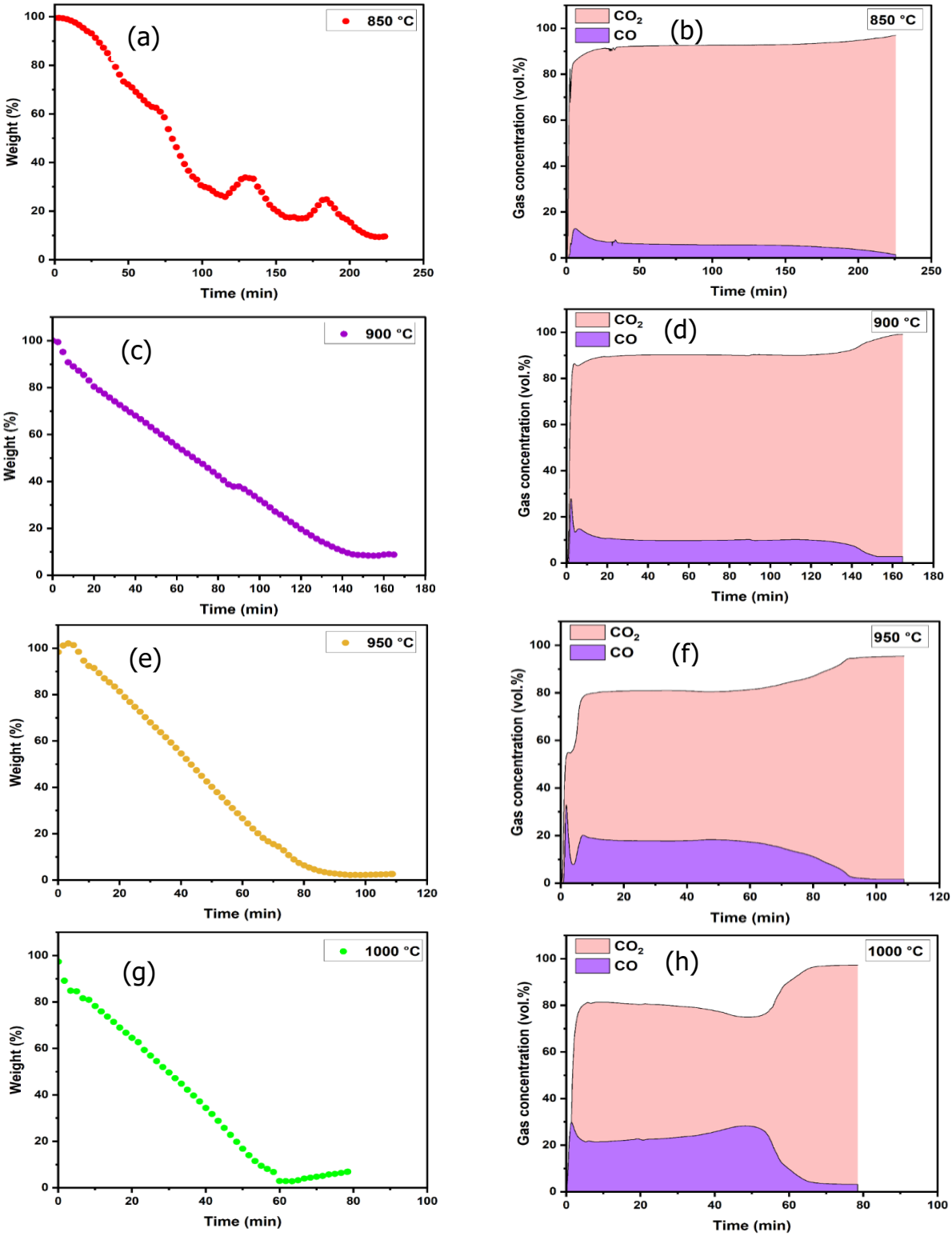

Figure 8.7: Real-time mass loss and gas composition profiles for CO_2 gasification of BC1 (a), (b) at 850°C, (c), (d) 900°C, (e), (f) at 950°C and (g), (h) at 1000°C.

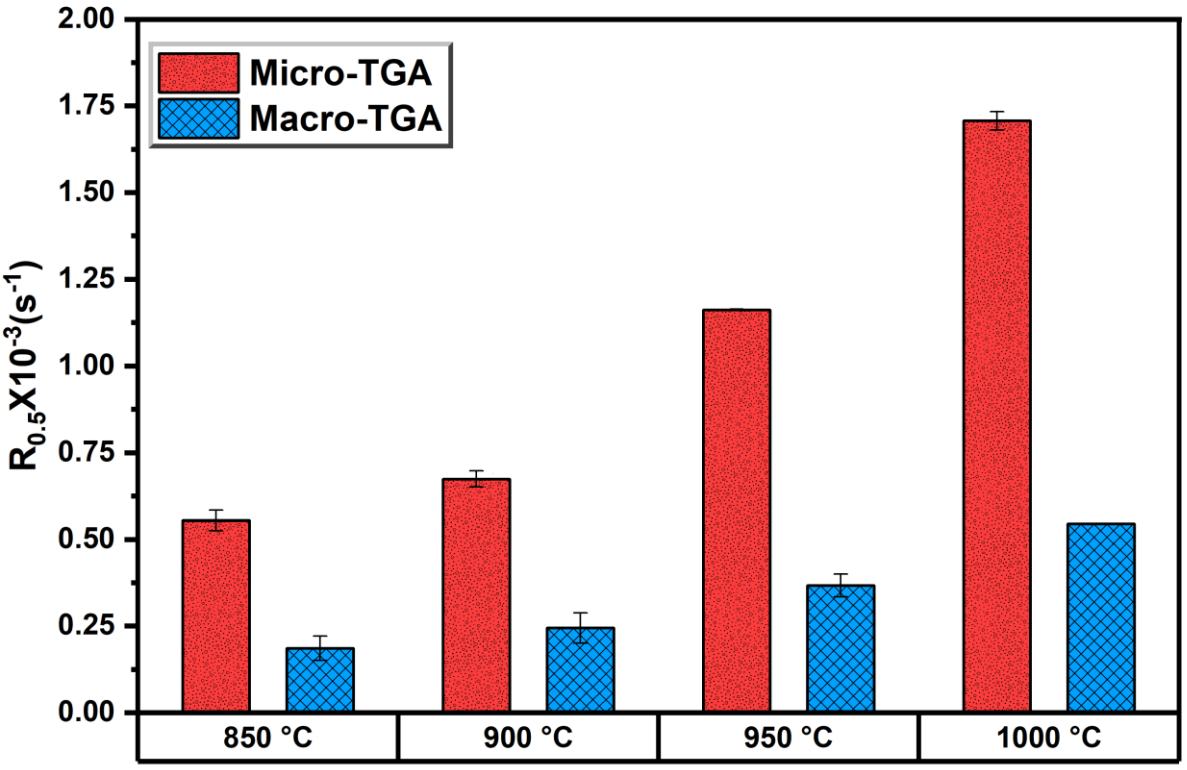

Figure 8.8: Comparison of the CO_2 gasification reactivity, $R_{0.5}$, measured from Micro-TGA and macro-TGA mass loss data for sample BC1.

8.4 Scale Effects on CO_2 Gasification kinetics

The kinetic study of CO_2 gasification of the BC1 sample was performed using the conversion profiles derived from Macro-TGA runs to confirm whether the reaction mechanism was consistent with that observed for BC1 in Chapter 6. Similarly, VM, GM and RPM were implemented to predict the experimental conversion of BC1 at 900°C to 1000°C. The linearised forms of the three kinetic models using experimental conversion data range between 0 to 0.9 are shown in Figure 8.9. Among the three models, the RPM generated the highest R^2 values of 0.966 to 0.9873. The reaction rate constants; k_{VM}, k_{GM} and k_{RPM}; were obtained from the slopes of these linearised forms. As shown in Figure 8.10, the reaction rate constants for BC1 in Macro-TGA were significantly lower than Micro-TGA by more than 70% for all the three models at all gasification temperatures. For example, the reaction rate constants values obtained from Micro-TGA were 1.48×10^{-3}, 1.1×10^{-3} and 0.58×10^{-3} s^{-1} at temperature of 900°C for VM, GM, and RPM models, respectively, while constant values from Macro-TGA were dropped to 0.29×10^{-3}, 0.21×10^{-3} and 0.16×10^{-3} s^{-1}.

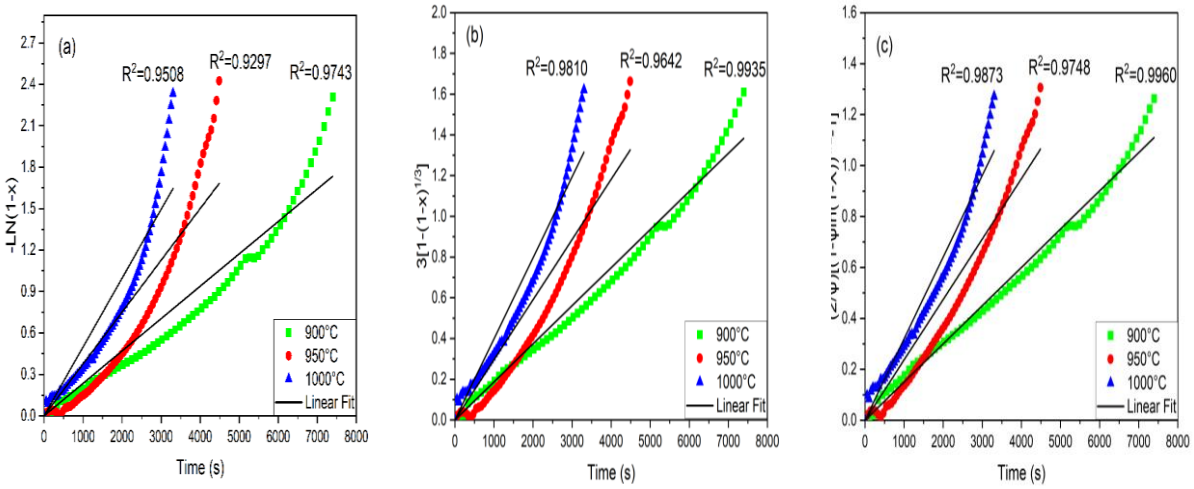

Figure 8.9: Linearisation of the VM model (a), GM model (b) and RPM model (c) using experimental conversion data in Macro-TGA 900°C, 950°C and 1000°C.

The reaction rate constants were then used to produce Arrhenius plots as shown Figure 8.11. In literature, the linearity of Arrhenius relation is used to explain whether the reaction is dominated by the surface chemistry of the char or limited by the pore diffusion [125,222,230].

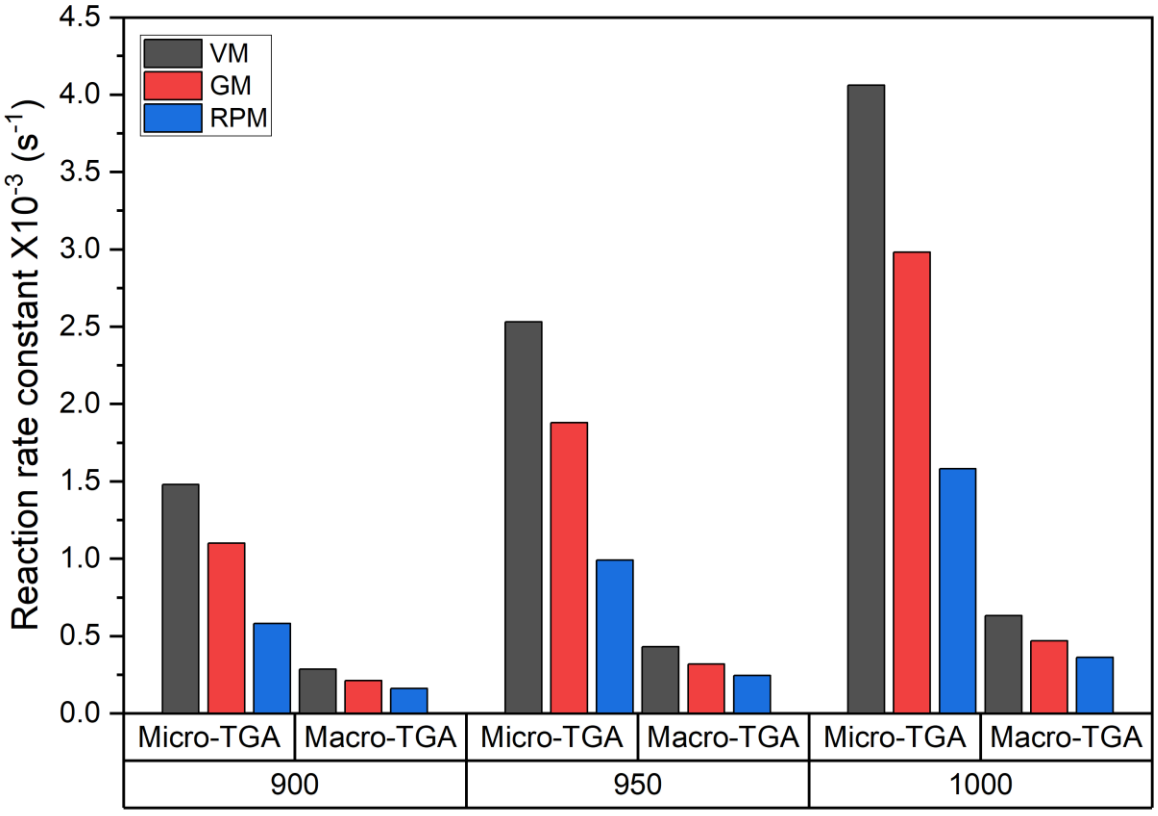

Figure 8.10: Comparison of reaction rate constant obtained from VM, GM and RPM models for sample BC1 using Micro-TGA and Macro-TGA.

In the Micro-TGA setup, the linearity of Arrhenius plots (Figure 7.4(a)) suggests that the reaction may occur in Regime I (chemical control), although this is not definitive as explained in Section 7.2. In contrast, the gradient of Arrhenius curves from the Macro-TGA results implies that the reaction may be affected by another mechanism, as shown in Figure 8.11. In a study of steam gasification of woody char in Macro-TGA conducted by Setptien et al. [68], they reported that the reaction is chemically controlled below

800°C and above this temperature the reaction was undergoing a transformation to a pore diffusion regime. In their work this was indicated from the reduction of the activation energy from 272 to 135 kJ/mol from the Arrhenius curve. The kinetic parameters are presented in Table 8.1. All three models indicate a decrease in activation energy values from Micro-TGA (123.6-125.2 kJ/mol) to Macro-TGA (98.8-99 kJ/mol) over gasification temperatures range. The pre-exponential factors also significantly dropped from (210.7-559.2 s^{-1}) in Micro-TGA to (4.1-7.2 s^{-1}) in Macro-TGA. Furthermore, the kinetic models were used to fit the experimental data as shown in Figure 8.12), and the deviation (as defined in Equation 5.16) between experimental conversion data and calculated conversion from the models are 14.63, 9.82 and 7.51% for VM, GM and RPM, respectively, suggesting that RPM is still best choice to explain gasification reaction of BC1 at those temperatures.

Table 8.1: Kinetic parameters obtained by VM, GM, and RPM models for BC1 sample in Macro-TGA.

Kinetic model	E (kJ/mol)	A_0(s^{-1})	DEV%
VM	98.8	7.2	14.63
GM	98.9	5.3	9.82
RPM	99.0	4.1	7.51

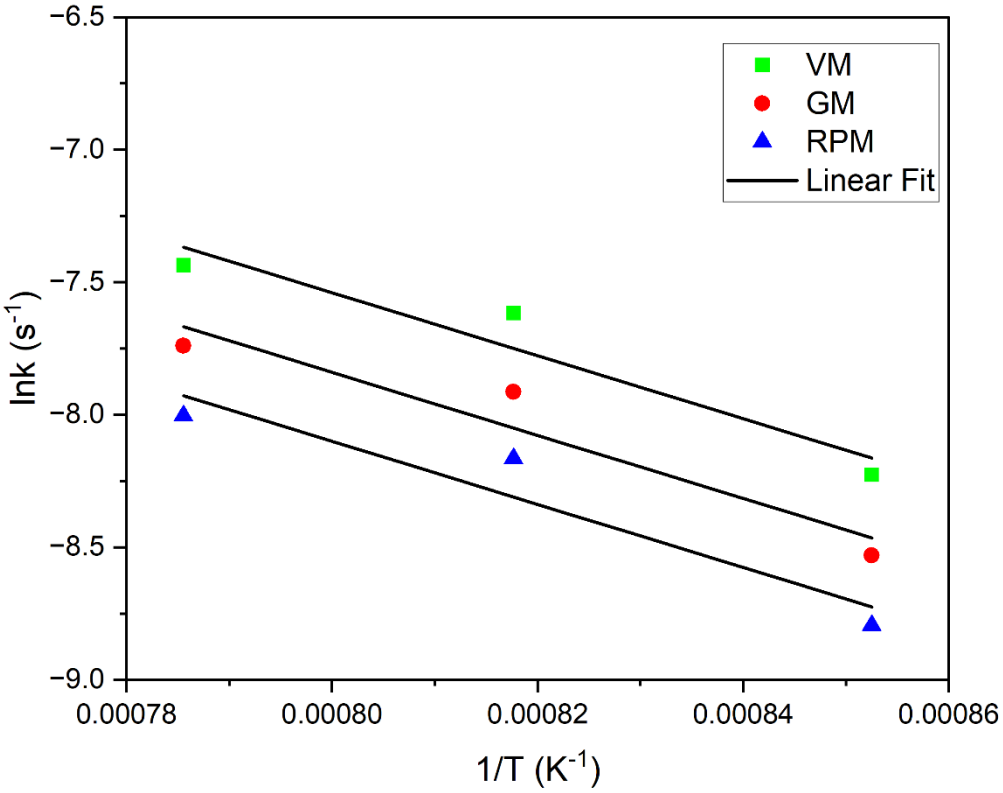

Figure 8.11: Arrhenius plots of BC1 tests in the Macro-TGA.

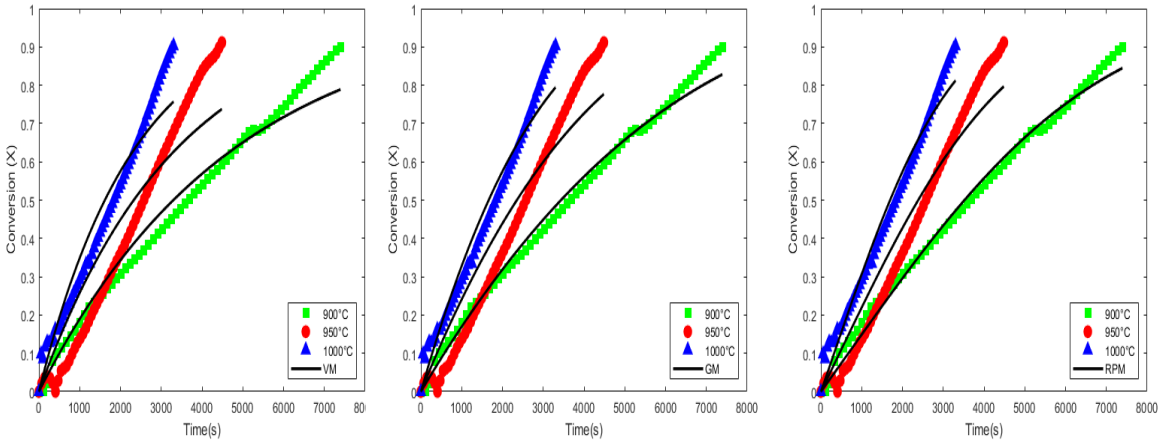

Figure 8.12: Nonlinear fitting curves of VM, GM and RPM to the experimental conversion data at 900°C and 950°C.

8.5 Influence of exposed surface area on CO_2 gasification in Macro-TGA

This section describes the results of changing one physical property to assess its impact on CO_2 gasification performance in the Macro-TGA thermobalance reactor. The available surface area for CO_2 reaction is the key variable in this experimental work, evaluated to test the hypothesis in this PhD that it is not the dominant factor controlling gasification reactivity. Therefore, the geometry of the pulverised BC1 was modified through a pelletisation (densification) process as described in Section 3.5.3. In this technique, the fine particles are compacted together reducing the void between them and consequently reducing the porosity of the char [231,232]. Thereby, the available surface area for the reactant gas CO_2 will be significantly reduced.

Three different external surface areas were established to distinguish between the variation of restriction degree for CO_2 molecules reaching the active sites within the char. A high surface area of char powder (Mixture P), moderate surface area (Pellet A), and finally low surface area (Pellet B). The geometries and compaction levels of the samples were used to measure their surface area ($S_{exposed}$) with the assumption that pellets have low porosity, as displayed in Table 8.2.

The reactivity of Mixture P, Pellet A and Pellet B was tested at two temperatures (900°C, 950°C) in the Macro-TGA system. In the gasification test, 5 g was used as the initial loaded mass in the crucible for each sample. This explains the different number of pellets used for Pellet A (12 mm diameter), Pellet B (16 mm diameter). The placement of three samples inside the crucible is shown in Figure 8.13. Mixture P was loaded to a height of >14 mm, allowing for maximum exposure of its fine particles to the CO_2 flow. Pellet A and Pellet B were placed in a flat position to ensure that both circular ends and half of the lateral surfaces were exposed to the gas flow. Although the height of cylindrical pellets varies for both Pellet A and Pellet B, the surface area exposed to the CO_2 flow ($S_{exposed}$) is always higher for Pellet A. It should be noted that only a single test was conducted for each sample at each temperature due to the breakdown of the furnace at the end of the PhD project.

Table 8.2: Surface area calculations for assumption of Mixture P, Pellet A and Pellet B.

Sample	Surface area	Gas-solid interaction	Exposed surface area $S_{exposed}$ (m^2)	Remark
Mixture P	High	High, pores structure allows both external and internal surfaces accessibility	S_{BET} X mass loaded	S_{BET} is assumed to be similar as S_{BET} of BC1=211 m^2/g
Pellet A	Moderate	Moderate, compaction reduces porosity and 3 pellets increase total external surface	$3 \times (\frac{\pi d_A h_a}{2} + \frac{\pi d_A^2}{2})$	$d_A = 12mm$ $h_A = 16.28 \text{ to } 25.32mm$
Pellet B	Low	Low; compacting reduces porosity and 2 pellets result in lower total external surface exposure	$2 \times (\frac{\pi d_B h_B}{2} + \frac{\pi d_B^2}{2})$	$d_B = 16mm$, $h_B = 11 \text{ to } 21.71mm$

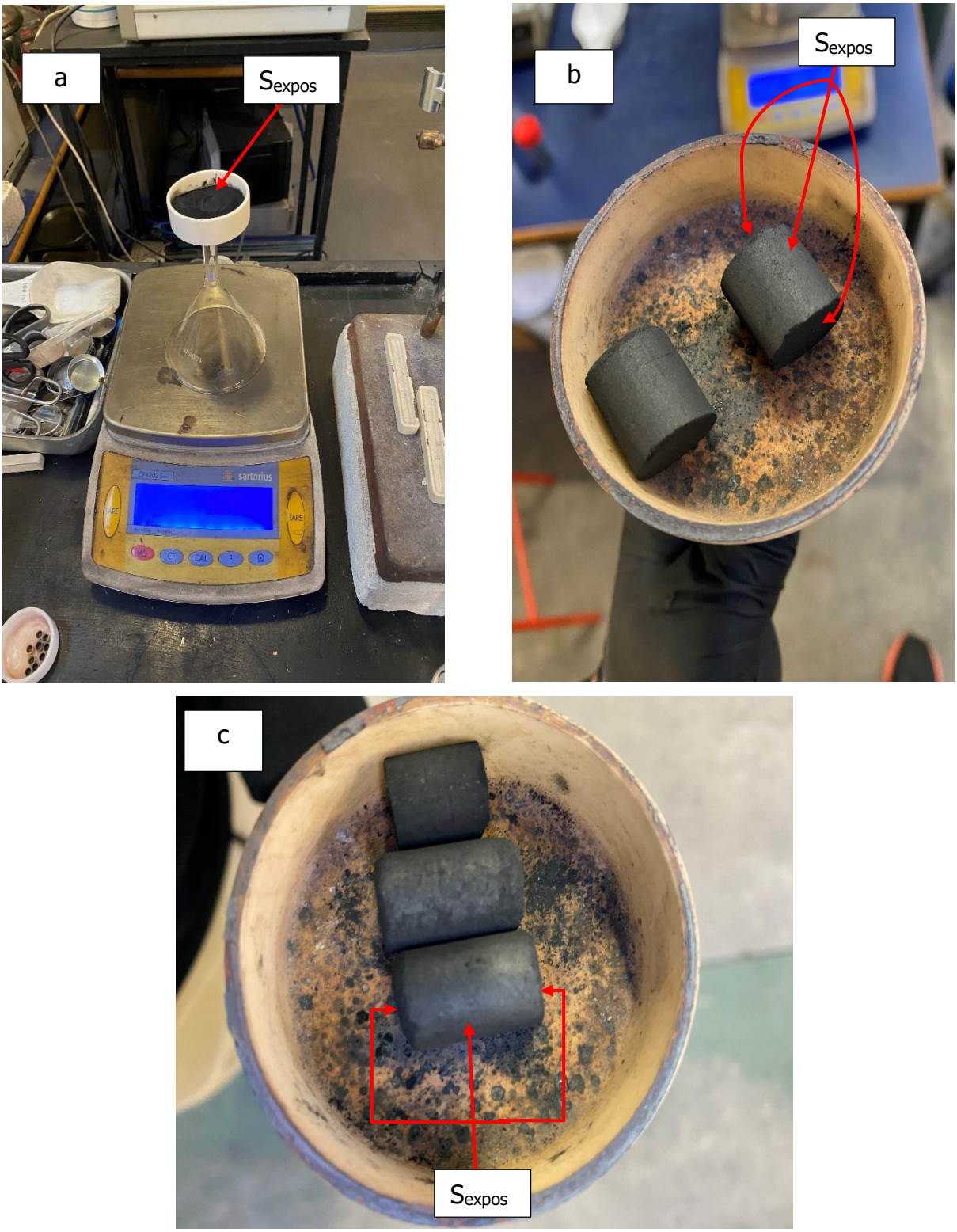

Figure 8.13: The shape of the powder char (a), Pellet B (b) and Pellet A (c) in the crucible.

The mass loss and corresponding gas composition profiles of CO_2 gasification of Mixture P, Pellet A and Pellet B samples at 900°C and 950°C are shown in Figure 8.14, Figure 8.15 and Figure 8.16, respectively. The mass loss curve of Mixture P at 900°C (Figure 8.14 (a)) shows a faster conversion over the reaction time compared to those for Pellet A and Pellet B (Figure 8.15 (a) and Figure 8.16 (a)). This is consistent with the high surface area availability for CO_2 molecules which provide more chance to directly contact the char particles. While pelletisation decreases the overall accessibility of the active sites, the available cylindrical surfaces still provide sufficient contact with CO_2 for moderate reactivity, as shown by Pellet A in Figure 8.15 (a). The reduction in gas-solid contact and internal mass diffusion limitation affects the reactivity of Pellet B as shown by its slowest mass loss.

The gas composition profiles at 900°C support the observation of the balance recorded mass loss, as presented in Figure 8.14 (b), Figure 8.15 (b) and Figure 8.16 (b). All samples show a maximum CO yield at the initial stage of the reaction, 21.68 to 28.64 %, followed by a decline in CO concentration as the reaction progresses. The gasification of Mixture P showed a higher level of reactivity than the pelletised samples, as evidenced by the more rapid formation of CO and consumption of CO_2. CO yield from Pellet A sharply dropped suggesting a reaction limitation most likely caused by limited gas-solid interactions. Pellet B released CO slowly but continuously, indicating a slower gasification process. Also, the reaction needed around 110, 130 and 170 minutes for Mixture P, Pellet A and Pellet B, respectively, as seen in the balance and gas analysers readings (Figure 8.14 (a),(b); Figure 8.15 (a), (b); and Figure 8.16 (a),(b)). The results imply that CO concentration and reaction duration curves can explain the difference in reaction rate [233]. These findings suggest that external surface area has a significant influence in the reactivity of the char samples at 900°C.

However, the reactivity index, $R_{0.5}$, values show different trends of sample reactivity at 900°C as shown in Table 8.3. The powdered char has a slightly lower $R_{0.5}$ value than Pellet A with 0.327×10^{-3} and 0.419×10^{-3} s^{-1}, respectively. This inconsistency is because $R_{0.5}$ represents the reaction rate at 50% char conversion rather than the entire reaction period. Also, the remaining unreacted carbon portion of Pellet A is quite high with a value of 18.01%, which means that incomplete reaction has occurred. This may be due to accumulation of ash on the pellet surfaces leading to pore diffusion limitation. Furthermore, the smaller diameter and the use of 3 pellets of Pellet A in the crucible led to denser packing compared to Pellet B, thus minimising voids between particles and limiting CO_2 contact. These findings suggest that surface area has a significant influence on the reactivity of the char samples at 900°C. Therefore, at this temperature the reactivities of the three samples are ranked as Mixture P> Pellet A> Pellet B.

Table 8.3: CO_2 gasification reactivity index ($R_{0.5}$) for the powder char and the pellets at 900 and 950°C.

Temperature (°C)	Sample	$R_{0.5}\times10^{-3,}$ (s^{-1})	Residual (%)
900	Mixture P	0.327	2.86
	Pellet A	0.419	18.01
	Pellet B	0.254	7.88
950	Mixture P	0.357	0.56
	Pellet A	0.359	26.63
	Pellet B	0.390	2.53

Increasing the gasification temperature to 950°C significantly reduces overall reaction time as shown in Figure 8.14 (c), Figure 8.15 (c) and Figure 8.16 (c). Mixture P and Pellet A show a higher reaction rate at the initial stage followed by a fluctuation and a steady mass loss. This fluctuation in the balance reading could be just an external disturbance as this does not appear in the corresponding output gas curves as shown in Figure 8.14 (d) and Figure 8.15 (d). Pellet B shows more improvement as the reaction time reduced from 170 minutes at 900°C to 100 minutes at 950°C, which is broadly similar to Mixture P. This is supported by their identical $R_{0.5}$ values (0.357 and 0.390×10^{-3} s^{-1}). Thus, the role of $S_{exposed}$ on CO_2 gasification at 950°C has less impact and other factors may have influenced the reaction. The visualisation of gas profiles at 950°C (see Figure 8.14 (d), Figure 8.15 (d) and Figure 8.16 (d)) show that CO concentration is higher than that at 900°C at the initial conversion but dropped close to the baseline concentration sooner. This demonstrates that raising gasification temperature improves char sample reactivity leading to faster consumption of char particles. In the case of Pellet A, as mentioned above, the diffusion limitation at 950°C is more pronounced, leaving higher residual mass of 26.63% and reduction in $R_{0.5}$. Despite this, the mass loss gas composition profiles show that the reaction time is about 100 minutes for the three samples (Figure 8.14 (c), (d); Figure 8.15 (c), (d); and Figure 8.16 (c),(d)).

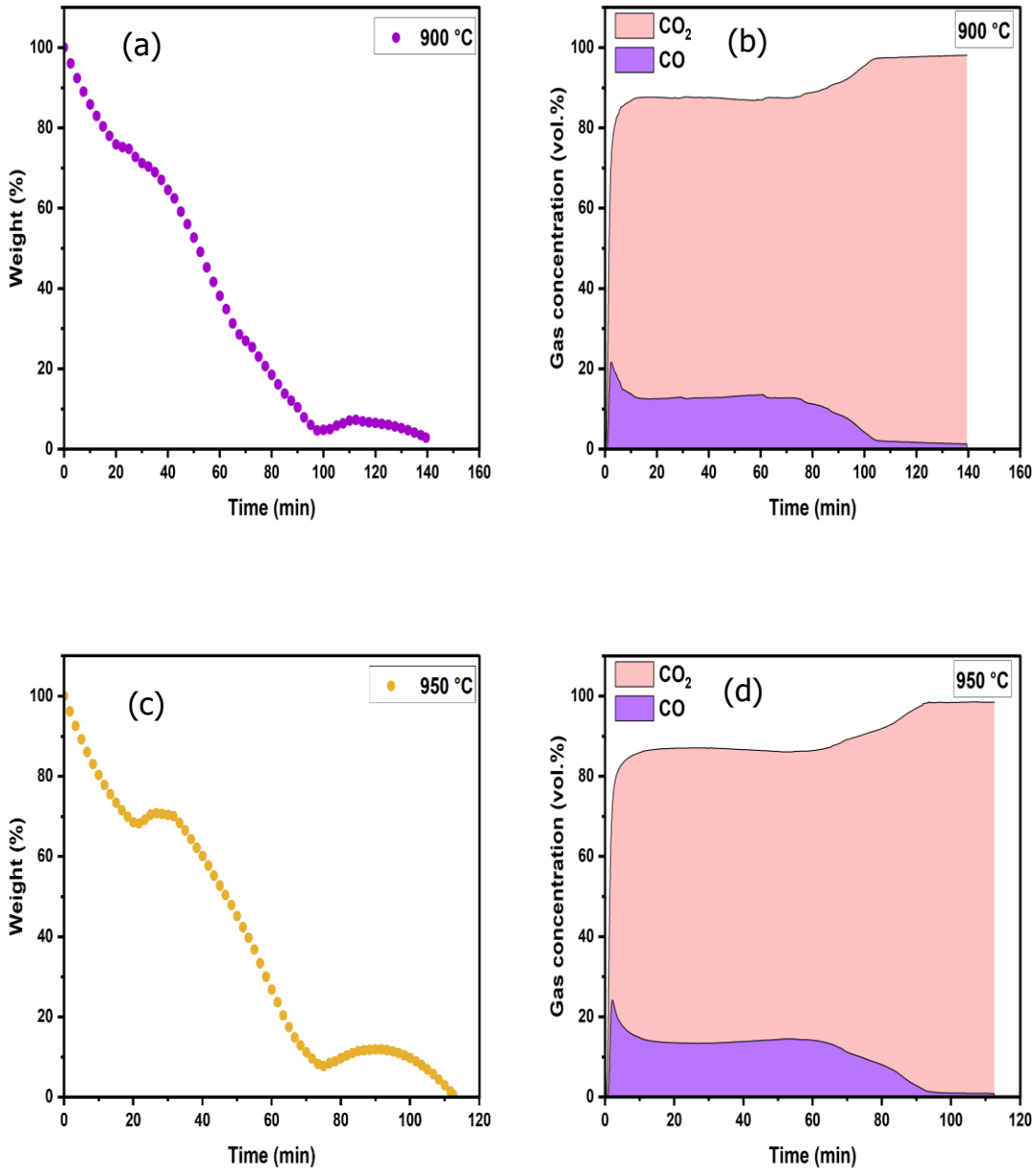

Figure 8.14: Real-time mass loss and gas composition profiles for CO_2 gasification of Mixture P (a), (b) at 900°C and (c), (d) at 950°C.

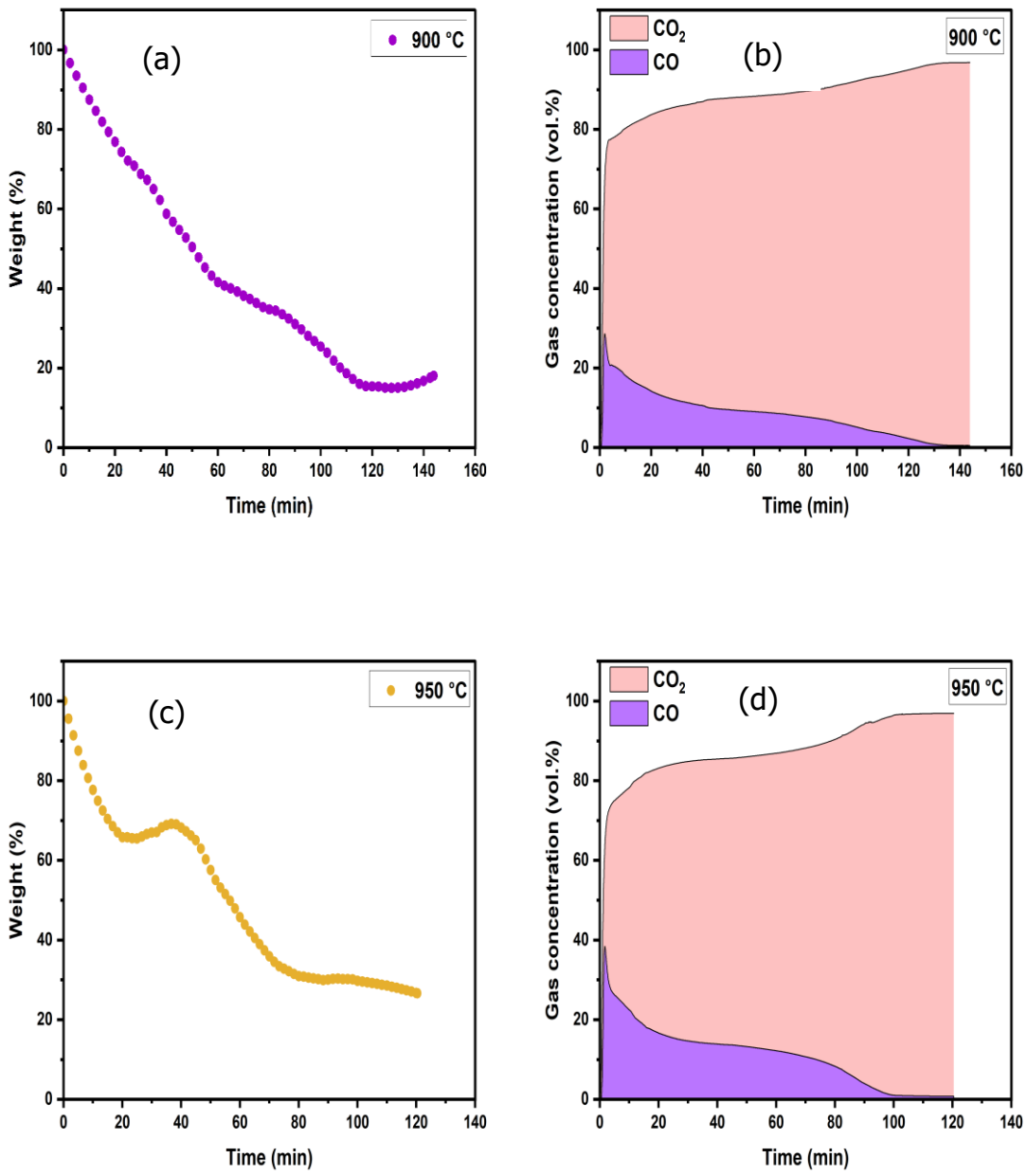

Figure 8.15: Real-time mass loss and gas composition profiles for CO_2 gasification of Pellet A (a), (b) at 900°C and (c), (d) 950°C.

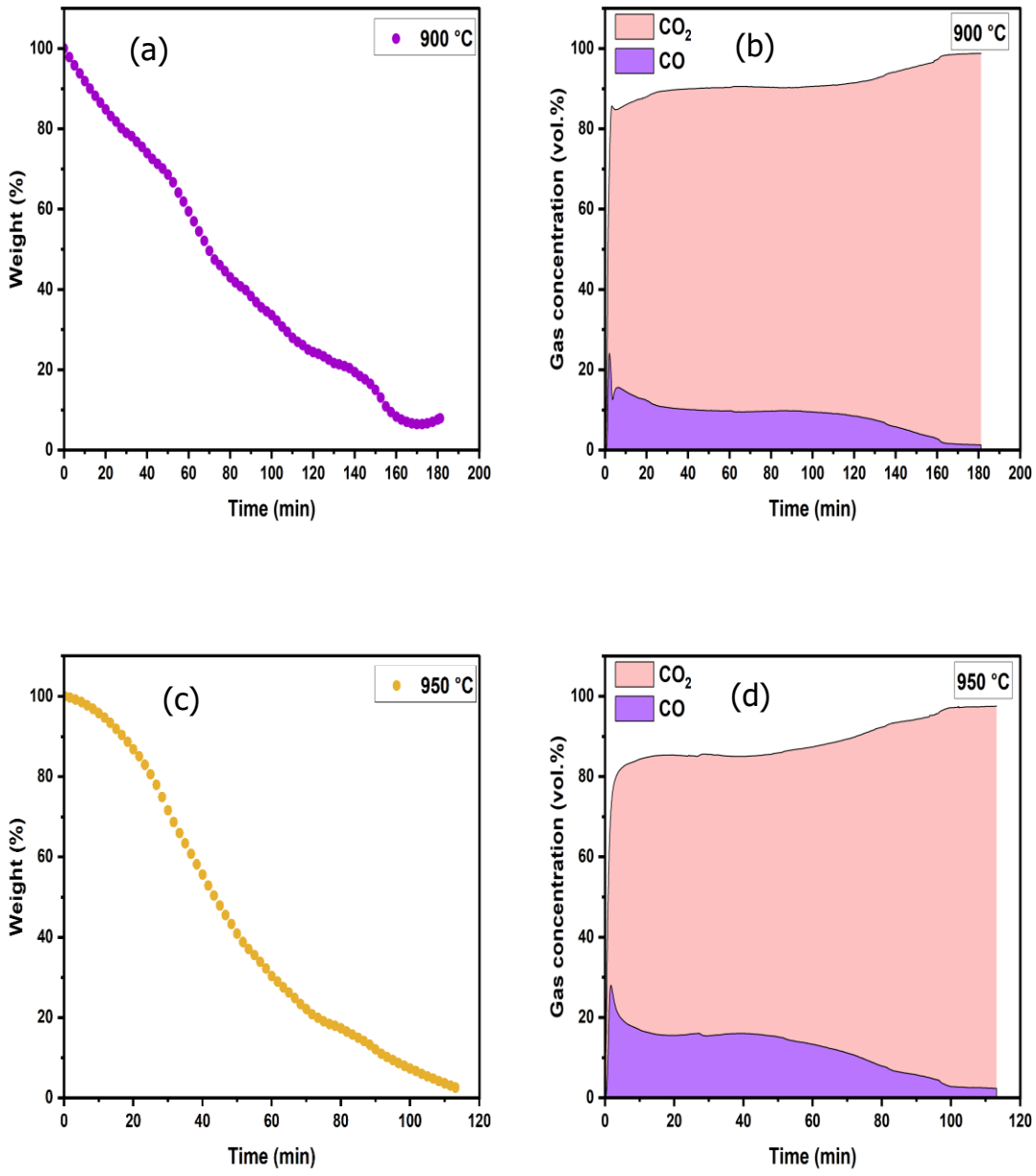

Figure 8.16: Real-time mass loss and gas composition profiles for CO_2 gasification of Pellet B (a), (b) at 900°C and (c), (d) 950°C.

8.6 Characterisation of gas composition

The efficiency of Macro-TGA in this project was assisted by evaluating the output gas composition data in real-time of the CO_2 gasification experiments. The calculations of CO yield and CO_2 conversion are based on integrated areas under the curves at each run at 298 K, using following equations [233], [234]:

$$Y_{CO} = \frac{\int CO\ dt\ (\% * \min) * CO_2 \text{ flow rate} \left(\frac{ml}{\min}\right)}{\text{Molar volume} \left(\frac{ml}{mmol}\right) * 5(g)} \tag{8.1}$$

$$n_{CO_{2,supplied}} = \frac{CO_2 \text{ flow rate} \left(\frac{ml}{\min}\right) * Gasification\ time\ (min)}{\text{Molar volume} \left(\frac{ml}{mmol}\right)} \tag{8.2}$$

$$C_{CO_2} = \frac{\int CO\ dt\ \ (\% * \min)}{\int CO + CO_2\ dt\ (\% * \min)} \times 100 \tag{8.3}$$

$Y_{CO}\ (mmol/g)$ and $C_{CO_2}(\%)$, represent the CO yield and CO_2 conversion$(\%)$, respectively. Molar volume is 24.4 ml/mmol at SATP and CO_2 flow rate is 1910 ml/min. $n_{CO_{2,supplied}}$ is the total number of moles of CO_2 that have been supplied to the system during the gasification test in $mmol$.

Table 8.4 summaries the calculation results for gas compositions of CO_2 gasification experiments in Macro-TGA. Overall trends of CO yield show a linear increase as the gasification temperature increases. For example, BC1, CO yield increased from 187 mmol/g at 850°C to 228.7 mmol/g at 900°C, but the yield slightly decreases at 950°C and 1000°C with 219.8 and 221.1 mmol/g, respectively. This reduction may be related to diffusion limitation as discussed in Section 8.4. Despite this, CO_2 conversion efficiency shows a strong correlation with the temperature. Hence it increases from 5.7% at 850°C to 18.7% at 1000°C. This reduction illustrates the complexity of the process in larger scale.

The effect of the reducing surface area on gasification performance is clearly shown at lower temperatures. Hence, CO yield of Mixture P at 900°C is significantly higher than the two pellet samples with 37.6% difference from Pellet A. Also, the powdered char consumed more CO_2 than Pellet A and Pellet B with values of 9.3, 5.9 and 8.4%, conversion respectively. This is further evidence of the surface area influence of char reactivity at low temperatures. CO yield and CO_2 conversion of Pellet A and Pellet B are almost identical at 950°C with values ranging from (196.7 to 198.9 mmol/g) and (11.1 to 11.7%), respectively. It was mentioned that at this temperature the remaining unreacted amount of Pellet A was 26.63%, so it may be an indication of a potential measurement error as the calculation is based on integration areas. The CO_2 supplied to the system was higher than required to maintain the slight positive pressure within the reactor; it should be noted that optimisation of the process was not an objective in the current study.

Table 8.4: Gas characterisation of CO_2 gasification experiments from Macro-TGA.

Sample	Temperature	Y_{co}	CO_2	CCO_2	CO
			supplied	conversion	max
	°C	mmol/g	mmol	%	vol.%
BC1	850	187.0	16982.7	5.7	12.8
	900	228.7	12410.9	9.3	27.8
	950	219.8	8186.6	14.0	32.8
	1000	221.1	5907.6	18.7	29.8
Mixture P	900	192.5	10498.2	9.3	21.7
	950	174.2	8466.3	10.4	24.2
Pellet A	900	120.1	10830.5	5.9	28.6
	950	196.7	9062.0	11.1	38.4
Pellet B	900	103.5	13633.8	8.4	24.1
	950	198.9	8516.4	11.7	28.1

8.7 Chapter summary

The results show that char performance is significantly affected by scale-up in the Macro-TGA reactor compared to the conventional (Micro) TGA. Thus, reactivity of material cannot be explained by only using a lab-based Micro-TGA apparatus. It was found that biochar reactivity was significantly lower than the measured reactivity from the Micro-TGA in all cases. Also, the kinetic study revealed that the reaction mechanism in Macro-TGA was affected by diffusion limitation above 950°C. As the gasification temperature increased, the reaction rate significantly increased. This is a common finding between the typical Micro-TGA and the Macro-TGA in this thesis. The influence of the available surface area has been investigated, and the results show that the reaction accelerates as the exposed surface area to the CO_2 flow was higher at low temperatures; whereas at higher temperature gasification process is dominated by other factors.

Chapter 9 Conclusions and Future work

9.1 Conclusions

This thesis investigated the influence of char physical and chemical properties on its reactivity during the reverse Boudouard reaction. A hypothesis was formulated as a basis of this PhD, which proposed that CO_2 gasification reactivity of char is not primarily controlled by surface area but rather by surface chemistry as it influences active sites and consequently controls the reaction mechanisms. The char properties such as pore structure, functional groups and inorganic mineral content were characterised using several advanced analytical techniques. Moreover, the kinetic modelling was carried out to understand the reaction mechanisms under different thermal conditions. The study also evaluated the potential use of thermochemical gasification as a CO_2 utilisation pathway by comparing its energy demand with some known CCUS methods. Although the measurement of the reaction's heat requirements was performed using a thermogravimetric apparatus, the results provide useful insights into the reaction's performance at elevated temperatures. In addition, a gasifier was developed to handle larger char samples and contribute to the understanding of the surface area characteristics impact on CO_2 gasification.

In this study, six biomass and coal derived chars were investigated under isothermal CO_2 gasification and their reactivities were examined against their properties. The key findings from this work are listed below:

- Biochars have much better CO_2 gasification reactivity compared to coal chars and are strong candidates for consideration in a carbon utilisation reaction to produce CO for the synthesis of platform chemicals. The shorter reaction time at lower temperatures will result in lower energy requirements to carry out the carbon utilisation reaction compared to other materials.
- According to physicochemical properties of chars there is more than one parameter controlling CO_2 gasification reactivity of chars at high temperature (900°C, 950°C

and 1000°C). While the pore structure of chars is indeed a significant characteristic, it appears that porosity alone does not exert the primary influence on gasification reactivity. This conclusion is supported by the findings of the analytical techniques, which indicate that the types of inorganic elements present and their distribution on the surface may be more closely associated with the observed variations in reactivity.

- The impact of demineralisation treatment on hydrochar was stronger than biochar, suggesting that the dominant factor of HC reactivity is the presence of the minerals and their catalytic effect.
- The reduction in the ash content by demineralisation of the chars reduces the strong CO_2 chemisorption and also relates to the rate of reaction. The results suggest minerals play a role in the mechanism by which CO_2 combines with carbon on the surface of the chars but there is some variation on its importance depending on the sample.
- The surfaces of the highest reactivity chars (HC and BC1) showed a wide range of functional chemical groups such as carbonyl, ester and carboxyl groups. However, it was less clear what role the sp^2/sp^3 bonding played for all the chars; although both HC and BC1 did correspond with lower sp^2 bonding, which is in agreement with other literature findings.
- The CO_2 chemisorption procedure can be used as an evaluation tool to predict different char reactivities, i.e. gasification reactivity is well correlated with CO_2 strong chemisorption C_{str}.
- In non-isothermal gasification, increasing the heating rate moves mass loss trends and DTG peaks to higher temperature zones. It also results in higher gasification characteristic parameters but lower char conversion.
- Heat requirement per unit mass of CO_2 confirms that biomass materials have more visible benefits than coal on the efficiency of CO_2 utilisation via the reverse Boudouard reaction. This indicates that the reactivity of carbonaceous material determines their suitability for CCU applications.

The kinetic modelling of CO_2 gasification was performed under isothermal and non-isothermal conditions using the VM, GM, and RPM models. The key findings are as follows:

- The reaction rate constant values were significantly increased when the reaction temperature increased from 900°C to 1000°C for all the kinetic models.
- In isothermal gasification, the RPM model was the best fit model for biomass chars and hydrochar conversion profiles while coal char shows an acceptable fit to the VM. This indicates that coal char has a completely different mechanism compared to biomass chars.
- The reaction mechanism of hydrochar has changed after acid leaching as the best fit model shifted from RPM to GM at 900 °C and 950 °C.
- The values of kinetic parameters measured under non-isothermal CO_2 gasification testing are significantly higher than those obtained from isothermal CO_2 gasification. Conversely, the structural parameter (ψ) is significantly lower under non-isothermal conditions.
- In non-isothermal gasification, the GM was the best fit model for (BC1, BC2 and BC4), while RPM had a better fit for samples BC3 and HC.

The measurement of char reactivity in CO_2 atmospheres at high temperatures using Micro-TGA is limited by the use of unrepresentative sample sizes (milligrams), which may not correspond to the overall reaction behaviour in an industrial application. Therefore, this study contributes to the understanding of the reactivity by developing a Macro-TGA to address this limitation. The newly developed Macro-TGA gasifier can carry out CO_2 gasification experiments using 5 g char samples under higher gas flow and allows for a direct evaluation of surface area effects.

The stability of the Macro-TGA system, along with the comparison of CO_2 gasification reactivity and kinetic parameters derived from both Micro-TGA and Macro-TGA experiments were studied in Chapter 8. The key findings from this experimental part of the study are summarised below:

- The accuracy of mass loss measurements in the Macro-TGA was significantly influenced by the design of the thermobalance setup. Increasing the diameter of the supporting ceramic rod to 12 mm improved system stability and decreased the fluctuations in the balance readings.
- In comparison to the reverse Boudouard reactivity results obtained using the traditional Micro-TGA, the reactivity measured in the Macro-TGA was significantly lower. This suggests that the mass of the gasified sample has a great influence on reaction performance. The reactivity indices of biochar (BC1) decreased by about 65% in the Macro-TGA at gasification temperatures (850-1000 °C). This demonstrates that a thicker char bed results in lower reactivity, likely due to restricted diffusion of CO_2 into deeper layers which consequently reduces the overall reaction rate.
- A notable influence of gasification temperature on char reactivity and CO yield was observed. The total reaction time for BC1 decreased from 220 minutes at 850 °C to 60 minutes at 1000 °C. This indicates that increasing gasification temperature in the Macro-TGA reduced or eliminated reaction constraints whether related to heat and mass transfer or to the accessibility of char active sites. Despite this, the CO profile at 1000°C showed at last third of the conversion.
- To further investigate the scale-up effects associated with using larger sample masses, kinetic parameters were measured using VM, GM and RPM kinetic models. The RPM model successfully predicted char conversion trends even for 5g samples in the Macro-TGA. In addition to the previously observed scale-up effects, the reaction rate constants for BC1 reduced by more than 70% in the Macro-TGA compared to those obtained from the Micro-TGA. The gradient of the Arrhenius plots derived from the Macro-TGA data suggests that the gasification reaction may be governed by a different mechanism compared to the Micro-TGA. This is supported by the lower values of activation energies and pre-exponential factors in these conditions.

- CO production profiles of BC1 showed sharp initial peaks across all temperatures with a slight increase in the yield at 1000 °C may indicate the contribution of an additional reaction mechanism at higher temperatures.
- CO_2 conversion efficiency showed a strong correlation with the temperature; however, the total CO yields slightly decreased at 950°C and 1000°C. This reduction illustrates the complexity of the process in larger scale.

Furthermore, the Macro-TGA gasifier was used to investigate the effect of exposed surface area on CO_2 gasification reactivity. Three char samples with different external surface area were tested: Mixture P, Pellet A and Pellet B. The main conclusions are as follows:

- Reducing exposed surface area by compacting char fine particles into pellets decreased the overall CO_2 gasification reactivity at 900°C. At this temperature, the mass loss profile and CO evaluation of Mixture P stabilised after 110 minutes compared to 130 and 170 minutes for Pellet A and Pellet B, respectively.
- Despite the slightly higher $R_{0.5}$ of Pellet A (0.419×10^{-3} s^{-1}) compared to Mixture P (0.327×10^{-3} s^{-1}), however, it retained 18.01% unconverted residue possibly due to ash accumulation causing pore blockage that leads to incomplete conversion.
- At 950 °C, the effect of surface area was negligible, as gasification temperature became the dominant factor influencing the reactivity. This finding is demonstrated by the reduction of the reaction time for Pellet B by 70 minutes compared to 900°C and the increase in $R_{0.5}$ value to $0.357\times10^{-3}\ s^{-1}$ which is close to that of Mixture P $0.390\times10^{-3}\ s^{-1}$ despite its lower surface area.
- Similar to the observation for BC1, Mixture P, Pellet A and Pellet B also exhibited a maximum CO yield at the early stage of the reaction then followed by a decrease in CO concentrations as the reaction progressed. Also, the amount of CO_2 converted increases as the gasification temperature increases.

9.2 Potential directions for future work

In the current PhD thesis, different mechanisms of CO_2 gasification have been investigated to find a link between char material reactivity and its properties as well as the reaction conditions. However, there is significant potential for further investigation with this apparatus. Further suggestions of future work are listed below:

- The chars used in this study were derived from commercial sources, these include recovered wood biochars, sewage sludge biochars, coal char and hydrothermally carbonised char from digested food waste. Future work could include feedstocks such as biomass or coal char and follow a systemic investigation where the char is produced from a variety of conditions (e.g., hydrothermal carbonisation, fast pyrolysis, slow pyrolysis). This will provide a clearer interpretation of how the original structure, as a baseline, influences the char reactivity.
- The role of char surface chemistry on the gasification reactivity was examined using a simple chemisorption method to estimate the amount of adsorbed CO_2 molecules on the char surface in the Micro-TGA. However, there are different advanced analytical techniques can be used to precisely quantify CO_2 chemisorption capacity on the carbon-based material such as Temperature Programmed Desorption (TPD) and Fourier Transform Infrared Spectroscopy (FTIR).
- In this study, the influence of inorganic compounds was examined by acid leaching char samples to isolate their effects on gasification reactivity. A recommended direction for future work is to further modify char surface chemistry to enhance gas–solid interactions. The modification involves activation treatments through doping with AAEMs or tuning functional groups to enhance the affinity of char particles with CO_2 and improve reaction rates.
- This study has investigated gasification reactivity and reaction kinetics in the Macro-TGA rig under 100% CO_2 concentration to examine the pure effect of CO_2 on the char reactivity without interference of side reactions. However, further experimental work should be conducted in varying CO_2 concentrations to better

reflect real flue gas conditions. It could examine the process by mixing CO_2 with an inert gas or even a reactive gas such as N_2 and H_2O, respectively. This would improve the industrial relevance of gasification method as a CCU pathway.

- The Macro-TGA was operated under laminar flow conditions to ensure system stability; however, this was found to influence gas mixing within the reactor. Computational Fluid Dynamics (CFD) can be employed to analyse flow dynamics, as well as heat and mass transfer effects on larger samples. In particular, simulations would allow flexibility in varying parameters such as gasifying agent flow rate, process temperature, and solid bed configuration. This would provide a robust understanding of the Macro-TGA's performance in the current design and help to optimise gasification process conditions by improving the design and validating it as a later step.
- A feasibility study based on Saudi Arabia's target of net zero emissions in 2060 is recommended. This should include a Life Cycle Assessment (LCA) of CO_2 gasification and MSW utilisation in Saudi Arabia to reduce their environmental impact under the kingdom's Circular Carbon Economy framework (CCE).

References

[1] IPCC. Climate Change 2023: Synthesis Report. 2023.

[2] NASA. What Is Climate Change? 2018. https://science.nasa.gov/climate-change/what-is-climate-change/ (accessed April 20, 2025).

[3] How do greenhouse gases actually warm the planet? 2022. https://www.unep.org/news-and-stories/story/how-do-greenhouse-gases-actually-warm-planet (accessed April 14, 2025).

[4] He C, Ji M, Grieneisen ML, Zhan Y. A review of datasets and methods for deriving spatiotemporal distributions of atmospheric CO_2. Journal of Environmental Management 2022;322:116101. https://doi.org/10.1016/j.jenvman.2022.116101.

[5] Kamkeng ADN, Wang M, Hu J, Du W, Qian F. Transformation technologies for CO_2 utilisation: Current status, challenges and future prospects. Chemical Engineering Journal 2021;409:128138. https://doi.org/10.1016/J.CEJ.2020.128138.

[6] UNFCCC. The Paris Agreement. United Nations Framework Convention on Climate Change 2015. https://unfccc.int/process-and-meetings/the-paris-agreement (accessed April 15, 2025).

[7] Kikstra JS, Nicholls ZRJ, Smith CJ, Lewis J, Lamboll RD, Byers E, Sandstad M, Meinshausen M, Gidden MJ, Rogelj J, Kriegler E, Peters GP, Fuglestvedt JS, Skeie RB, Samset BH, Wienpahl L, Van Vuuren DP, Van Der Wijst KI, Al Khourdajie A. The IPCC Sixth Assessment Report WGIII climate assessment of mitigation pathways: from emissions to global temperatures. Geoscientific Model Development 2022;15:9075–109. https://doi.org/10.5194/gmd-15-9075-2022.

[8] Betts RA, Jones CD, Keeling R, Knight JR, Pope JO, Sandford C. Mauna Loa carbon dioxide forecast for 2020 - Atmospheric CO_2 rise now exceeding IPCC 1.5°C scenarios 2025. https://www.metoffice.gov.uk/research/climate/seasonal-to-decadal/long-range/forecasts/co2-forecast (accessed April 14, 2025).

[9] Lan X, Keeling R. Trends in CO_2 - NOAA Global Monitoring Laboratory 2025. https://gml.noaa.gov/ccgg/trends/mlo.html (accessed April 14, 2025).

[10] IEA. Greenhouse Gas Emissions from Energy Data Explorer 2022. https://www.iea.org/data-and-statistics/data-tools/greenhouse-gas-emissions-from-energy-data-explorer (accessed April 15, 2025).

[11] IEA. CO_2 Emissions in 2023. vol. 24. 2023.

[12] Olivier JGJ, Schure KM, Peters JAHW. Trends in global CO_2 and total greenhouse gas emissions 2017.

[13] Zhang Z, Pan SY, Li H, Cai J, Olabi AG, Anthony EJ, Manovic V. Recent advances in

carbon dioxide utilization. Renewable and Sustainable Energy Reviews 2020;125. https://doi.org/10.1016/J.RSER.2020.109799.

[14] Nath F, Mahmood MN, Yousuf N. Recent advances in CCUS: A critical review on technologies, regulatory aspects and economics. Geoenergy Science and Engineering 2024;238:212726. https://doi.org/10.1016/j.geoen.2024.212726.

[15] Hong WY. A techno-economic review on carbon capture, utilisation and storage systems for achieving a net-zero CO_2 emissions future. Carbon Capture Science & Technology 2022;3:100044. https://doi.org/10.1016/J.CCST.2022.100044.

[16] Nagireddi S, Agarwal JR, Vedapuri D. Carbon Dioxide Capture, Utilization, and Sequestration: Current Status, Challenges, and Future Prospects for Global Decarbonization. ACS Engineering Au 2023;4:22–48. https://doi.org/10.1021/ACSENGINEERINGAU.3C00049.

[17] Rowaihy F, Hamieh A, Odeh N, Hejazi M, Al-Juaied M, Afifi AM, Hoteit H. Decarbonizing Saudi Arabia energy and industrial sectors: Assessment of carbon capture cost. Carbon Capture Science & Technology 2025;14:100375. https://doi.org/10.1016/J.CCST.2025.100375.

[18] Gabrielli P, Gazzani M, Mazzotti M. The Role of Carbon Capture and Utilization, Carbon Capture and Storage, and Biomass to Enable a Net-Zero-CO_2 Emissions Chemical Industry. Industrial & Engineering Chemistry Research 2020;59:7033–45. https://doi.org/10.1021/acs.iecr.9b06579.

[19] Zhang Z, Pan SY, Li H, Cai J, Olabi AG, Anthony EJ, Manovic V. Recent advances in carbon dioxide utilization. Renewable and Sustainable Energy Reviews 2020;125:109799. https://doi.org/10.1016/j.rser.2020.109799.

[20] Madejski P, Chmiel K, Subramanian N, Kuś T. Methods and Techniques for CO_2 Capture: Review of Potential Solutions and Applications in Modern Energy Technologies. Energies 2022, Vol 15, Page 887 2022;15:887. https://doi.org/10.3390/EN15030887.

[21] Carbon Capture, Utilisation and Storage - Energy System - IEA 2024. https://www.iea.org/energy-system/carbon-capture-utilisation-and-storage (accessed November 26, 2023).

[22] Fu L, Ren Z, Si W, Ma Q, Huang W, Liao K, Huang Z, Wang Y, Li J, Xu P. Research progress on CO_2 capture and utilization technology. Journal of CO_2 Utilization 2022;66:102260. https://doi.org/10.1016/j.jcou.2022.102260.

[23] Gulzar A, Gulzar A, Ansari MB, He F, Gai S, Yang P. Carbon dioxide utilization: A paradigm shift with CO_2 economy. Chemical Engineering Journal Advances 2020;3:100013. https://doi.org/10.1016/J.CEJA.2020.100013.

[24] International Energy Agency (IEA) 2019. Putting CO_2 to Use. Paris 2019. https://www.iea.org/reports/putting-co2-to-use.

[25] Kim C, Yoo CJ, Oh HS, Min BK, Lee U. Review of carbon dioxide utilization technologies and their potential for industrial application. Journal of CO_2 Utilization 2022;65:102239. https://doi.org/10.1016/J.JCOU.2022.102239.

[26] Saravanan A, Senthil kumar P, Vo DVN, Jeevanantham S, Bhuvaneswari V, Anantha Narayanan V, Yaashikaa PR, Swetha S, Reshma B. A comprehensive review on different approaches for CO_2 utilization and conversion pathways. Chemical Engineering Science 2021;236:116515. https://doi.org/10.1016/J.CES.2021.116515.

[27] Okoye-Chine CG, Otun K, Shiba N, Rashama C, Ugwu SN, Onyeaka H, Okeke CT. Conversion of carbon dioxide into fuels—A review. Journal of CO_2 Utilization 2022;62:102099. https://doi.org/10.1016/J.JCOU.2022.102099.

[28] Nimmas T, Wongsakulphasatch S, Chanthanumataporn M, Vacharanukrauh T, Assabumrungrat S. Thermochemical transformation of CO_2 into high-value products. Current Opinion in Green and Sustainable Chemistry 2024;47:100911. https://doi.org/10.1016/J.COGSC.2024.100911.

[29] Turakulov Z, Kamolov A, Norkobilov A, Variny M, Díaz-Sainz G, Gómez-Coma L, Fallanza M. Assessing various CO_2 utilization technologies: a brief comparative review. Journal of Chemical Technology and Biotechnology 2024;99:1291–307. https://doi.org/10.1002/JCTB.7606.

[30] Hasan MMF, Rossi LM, Debecker DP, Leonard KC, Li Z, Makhubela BCE, Zhao C, Kleij A. Can CO_2 and Renewable Carbon Be Primary Resources for Sustainable Fuels and Chemicals? ACS Sustainable Chemistry & Engineering 2021;9:12427–30. https://doi.org/10.1021/ACSSUSCHEMENG.1C06008.

[31] Huang J, Zhang H, Tan Q, Li L, Xu R, Xu Z, Li X. Enhanced conversion of CO_2 into O_2-free fuel gas via the Boudouard reaction with biochar in an atmospheric plasmatron. Journal of CO_2 Utilization 2021;45:101429. https://doi.org/10.1016/J.JCOU.2020.101429.

[32] Wang T. An overview of IGCC systems. In: Wang T, Stiegel GBT-IGCC (IGCC) T, editors. Integrated Gasification Combined Cycle (IGCC) Technologies, Woodhead Publishing; 2017, p. 1–80. https://doi.org/https://doi.org/10.1016/B978-0-08-100167-7.00001-9.

[33] Yang L, Ge X. Biogas and Syngas Upgrading. Advances in Bioenergy, vol. 1, Elsevier; 2016, p. 125–88. https://doi.org/10.1016/bs.aibe.2016.09.003.

[34] Redko A, Redko O, DiPippo R. Industrial waste heat resources. Low-Temperature Energy Systems with Applications of Renewable Energy, Academic Press; 2020, p. 329–62. https://doi.org/10.1016/b978-0-12-816249-1.00009-1.

[35] IEA. How much CO_2 does Saudi Arabia emit? 2022. https://www.iea.org/countries/saudi-arabia/emissions (accessed April 17, 2025).

[36] The General Authority for Statistics GASTAT. Per Capita Daily Waste Collection In Saudi Arabia During The Period 2010-2018. 2018.

[37] Saudi Vision 2030 2025. https://www.vision2030.gov.sa/en (accessed April 18, 2025).

[38] SGI. Saudi and Middle East Green Initiatives 2021. https://www.greeninitiatives.gov.sa/about-sgi/ (accessed April 18, 2025).

[39] SABIC. Creating the World's Largest Carbon Capture and Utilization Plant 2015. https://www.sabic.com/en/newsandmedia/stories/our-world/creating-the-worlds-largest-carbon-capture-and-utilization-plant (accessed April 18, 2025).

[40] Aramco. Carbon capture, utilization, and storage 2025. https://www.aramco.com/en/what-we-do/energy-innovation/advancing-energy-solutions/carbon-capture-utilization-and-storage (accessed April 18, 2025).

[41] Abdel Daiem MM, Said N. Energetic, economic, and environmental perspectives of power generation from residual biomass in Saudi Arabia. Alexandria Engineering Journal 2022;61:3351–64. https://doi.org/10.1016/j.aej.2021.08.049.

[42] Nizami A-S, Rehan M, Ismail I, Ouda O. Waste Biorefinery in Makkah: A Solution to Convert Waste produced during Hajj and Umrah Seasons into Wealth. 15th Scientific Symposium for the Research of Hajj, Umrah and Madinah Visit 2015. https://doi.org/10.13140/RG.2.1.4303.6560.

[43] Basu P. Gasification theory. Biomass Gasification, Pyrolysis and Torrefaction: Practical Design and Theory. Third, Academic Press; 2018, p. 211–62. https://doi.org/10.1016/B978-0-12-812992-0.00007-8.

[44] Adams P, Bridgwater T, Lea-Langton A, Ross A, Watson I. Biomass Conversion Technologies. Greenhouse Gas Balances of Bioenergy Systems 2018:107–39. https://doi.org/10.1016/B978-0-08-101036-5.00008-2.

[45] Demirbaş A, Arin G. An overview of biomass pyrolysis. Energy Sources 2002;24:471–82. https://doi.org/10.1080/00908310252889979.

[46] Al-Farraji A, Marsh R, Steer J. A Comparison of the Pyrolysis of Olive Kernel Biomass in Fluidised and Fixed Bed Conditions. Waste and Biomass Valorization 2017;8:1273–84. https://doi.org/10.1007/S12649-016-9670-6/FIGURES/12.

[47] Busto M, Nardi F, Dosso L, Badano JM, Tarifa EE, Vera CR. Review of Gasification of Thermoplastics and Thermosets. Processes 2025;13:647. https://doi.org/10.3390/PR13030647/S1.

[48] Basu P. Design of biomass gasifiers. Biomass Gasification, Pyrolysis and Torrefaction: Practical Design and Theory. Third Edit, Academic Press; 2018, p. 263–329. https://doi.org/10.1016/B978-0-12-812992-0.00008-X.

[49] Dutta A, Acharya B. Production of bio-syngas and biohydrogen via gasification.

Handbook of Biofuels Production: Processes and Technologies 2011:420–59. https://doi.org/10.1533/9780857090492.3.420.

[50] Golden T, Reed B, Das A. Handbook of Biomass Downdraft Gasifier Engine Systems. SERI US Department of Energy 1988:148.

[51] Chopra S, Jain AK. A Review of Fixed Bed Gasification Systems for Biomass. E-Journal - Internationale Kommission Für Agrartechnik 2007;9:1–23.

[52] Di Blasi CD, Signorelli G, Portoricco G. Countercurrent Fixed-Bed Gasification of Biomass at Laboratory Scale. Industrial and Engineering Chemistry Research 1999;38:2571–81. https://doi.org/10.1021/IE980753I.

[53] Belgiorno V, De Feo G, Della Rocca C, Napoli RMA. Energy from gasification of solid wastes. Waste Management 2003;23:1–15. https://doi.org/10.1016/S0956-053X(02)00149-6.

[54] Nuamah A, Malmgren A, Riley G, Lester E. Biomass Co-Firing. Comprehensive Renewable Energy 2012;5:55–73. https://doi.org/10.1016/B978-0-08-087872-0.00506-0.

[55] Patra TK, Sheth PN. Biomass gasification models for downdraft gasifier: A state-of-the-art review. Renewable and Sustainable Energy Reviews 2015;50:583–93. https://doi.org/10.1016/J.RSER.2015.05.012.

[56] Inayat M, Shahbaz M, Naqvi SR, Sulaiman SA. Advance strategies for tar elimination from biomass gasification techniques. Bioenergy Resources and Technologies 2021:61–88. https://doi.org/10.1016/B978-0-12-822525-7.00010-X.

[57] Lever T, Haines P, Rouquerol J, Charsley EL, Van Eckeren P, Burlett DJ. ICTAC nomenclature of thermal analysis (IUPAC Recommendations 2014). Pure and Applied Chemistry 2014;86:545–53. https://doi.org/10.1515/pac-2012-0609.

[58] Ahluwalia VK. Thermogravimetric Analysis. Instrumental Methods of Chemical Analysis, Springer Nature Switzerland; 2023, p. 81–9. https://doi.org/10.1007/978-3-031-38355-7_11.

[59] Riley JT, Marsh M. Macro thermogravimetric analyzers: Versatile and underutilized analytical instruments. Journal of Testing and Evaluation 2021;49:4357–63. https://doi.org/10.1520/JTE20200706.

[60] Long Y, Zhou H, Meng A, Li Q, Zhang Y. Interactions among biomass components during co-pyrolysis in (macro)thermogravimetric analyzers. Korean Journal of Chemical Engineering 2016;33:2638–43. https://doi.org/10.1007/S11814-016-0102-X/METRICS.

[61] Loganathan S, Valapa RB, Mishra RK, Pugazhenthi G, Thomas S. Chapter4: Thermogravimetric Analysis for Characterization of Nanomaterials. Thermal and Rheological Measurement Techniques for Nanomaterials Characterization, vol. 3, Elsevier Inc.; 2017, p. 67–108. https://doi.org/10.1016/B978-0-323-46139-

9.00004-9.

[62] Wu S, Li Z. Experimental and modeling study on centimeter pine char combustion in fast-heating Macro TGA. Proceedings of the Combustion Institute 2023;39:3497–508. https://doi.org/10.1016/j.proci.2022.08.080.

[63] Cortazar M, Lopez G, Alvarez J, Arregi A, Amutio M, Bilbao J, Olazar M. Experimental study and modeling of biomass char gasification kinetics in a novel thermogravimetric flow reactor. Chemical Engineering Journal 2020;396:125200. https://doi.org/10.1016/J.CEJ.2020.125200.

[64] Rezaei H. Physical and thermal characterization of ground bark and ground wood particles [PhD thesis]. University of British Columbia, 2017. https://doi.org/10.1016/j.renene.2018.06.038.

[65] Acharya B, Pradhan RR, Dutta A, Acharya B, Pradhan RR, Dutta A. Qualitative and kinetic analysis of torrefaction of lignocellulosic biomass using DSC-TGA-FTIR. AIMS Energy 2015 4:760 2015;3:760–73. https://doi.org/10.3934/ENERGY.2015.4.760.

[66] Tapasvi D, Khalil R, Skreiberg Ø, Tran KQ, Grønli M. Torrefaction of Norwegian birch and spruce: An experimental study using macro-TGA. Energy and Fuels 2012;26:5232–40. https://doi.org/10.1021/EF300993Q/ASSET/IMAGES/LARGE/EF-2012-00993Q_0005.JPEG.

[67] Castro C, Gonçalves M, Longo A, Vilarinho C, Ferreira M, Ribeiro A, Pacheco N, Teixeira JC. Influence of Temperature in the Thermo-Chemical Decomposition of Below-Stoichiometric RDF Char—A Macro TGA Study. Energies 2023;16. https://doi.org/10.3390/en16073064.

[68] Septien S, Escudero Sanz FJ, Salvador S, Valin S. Steam gasification of char from wood chips fast pyrolysis: Development of a semi-empirical model for a fluidized bed reactor application. Biomass and Bioenergy 2015;77:64–74. https://doi.org/10.1016/j.biombioe.2015.03.011.

[69] Khalil RA, Mészáros E, Grønli MG, Várhegyi G, Mohai I, Marosvölgyi B, Hustad JE. Thermal analysis of energy crops: Part I: The applicability of a macro-thermobalance for biomass studies. Journal of Analytical and Applied Pyrolysis 2008;81:52–9. https://doi.org/10.1016/J.JAAP.2007.08.004.

[70] Hu Q, He X, Yao Z, Dai Y, Wang CH. Gaseous production kinetics and solid structure analysis during isothermal conversion of biomass pellet under different atmospheres. Journal of the Energy Institute 2021;98:53–62. https://doi.org/10.1016/j.joei.2021.06.009.

[71] Wretborn T. Pyrolysis of Wood Chips : Influence of Pyrolysis Conditions on Charcoal Yield and Charcoal Reactivity [Dissertation]. Luleå University of Technology, 2016.

[72] Orang N, Tran H. Effect of feedstock moisture content on biomass boiler operation.

PEERS Conference 2014 2014;14:909–21.

[73] Zhang S, Wu M, Bie X, Qian Z, Li Q, Zhang Y, Zhou H. Deciphering interactions between biomass components during CO_2 gasification: Insights from thermogravimetric behavior, gas production, and char reactivity. Fuel 2024;371:131974. https://doi.org/10.1016/j.fuel.2024.131974.

[74] Hedayati A, Lestander TA, Rudolfsson M, Thyrel M, Öhman M. Fate of phosphorus and potassium in single-pellet thermal conversion of forest residues with a focus on the char composition. Biomass and Bioenergy 2021;150. https://doi.org/10.1016/j.biombioe.2021.106124.

[75] Meng A, Chen S, Long Y, Zhou H, Zhang Y, Li Q. Pyrolysis and gasification of typical components in wastes with macro-TGA. Waste Management 2015;46:247–56. https://doi.org/10.1016/j.wasman.2015.08.025.

[76] Zhang S, Yu S, Li Q, Mohamed BA, Zhang Y, Zhou H. Insight into the relationship between CO_2 gasification characteristics and char structure of biomass. Biomass and Bioenergy 2022;163:106537. https://doi.org/10.1016/j.biombioe.2022.106537.

[77] Wang L, Skreiberg Ø, Smith-Hanssen N, Jayakumari S, Jahrsengene G, Rørvik S, Turn S. Investigation of the Properties and Reactivity of Biocarbons at High Temperature in a Mixture of CO/CO_2. Chemical Engineering Transactions 2022;92:697–702. https://doi.org/10.3303/CET2292117.

[78] Tapasvi D. Experimental and Simulation Studies on Biomass Torrefaction and Gasification [PhD thesis]. Norwegian University of Science and Technology, 2015.

[79] Baraket N, Brandelet B, Trouvé G, Rogaume Y. Study of the memory effect of PCDD/F during the combustion of several biomasses in a moving grate boiler. Environmental Science and Pollution Research 2022;29:72639–54. https://doi.org/10.1007/s11356-022-20774-1.

[80] Balme Q, Lemont F, Rousset F, Sedan J, Charvin P, Bondroit J, Marias F. Design, calibration and testing of a new macro-thermogravimetric analyzer. Journal of Thermal Analysis and Calorimetry 2018;132:1439–47. https://doi.org/10.1007/s10973-018-7118-x.

[81] Higman C, van der Burgt M. The Thermodynamics of Gasification. Gasification, Gulf Professional Publishing; 2008, p. 11–31. https://doi.org/10.1016/b978-0-7506-8528-3.00002-x.

[82] Bockhorn H. Gasification kinetics. In: Editor(s): Michael S. Blinderman AYK, editor. Underground Coal Gasification and Combustion, Woodhead Publishing; 2018, p. 213–52. https://doi.org/10.1016/B978-0-08-100313-8.00007-4.

[83] Ergun S. Kinetics of the Reaction of Carbon with Carbon Dioxide. Journal of Physical Chemistry 1956;60:480–5. https://doi.org/10.1021/J150538A022.

[84] Pang S. Fuel flexible gas production: Biomass, coal and bio-solid wastes. Fuel Flexible Energy Generation: Solid, Liquid and Gaseous Fuels, Woodhead Publishing; 2016, p. 241–69. https://doi.org/10.1016/B978-1-78242-378-2.00009-2.

[85] Marsh H, Diez MA, Kuo K. Specific Reactivities of Pure Carbon of Diverse Origins. Fundamental Issues in Control of Carbon Gasification Reactivity, Springer, Dordrecht; 1991, p. 205–20. https://doi.org/10.1007/978-94-011-3310-4_11.

[86] Huo W, Zhou Z, Chen X, Dai Z, Yu G. Study on CO_2 gasification reactivity and physical characteristics of biomass, petroleum coke and coal chars. Bioresource Technology 2014;159:143–9. https://doi.org/10.1016/j.biortech.2014.02.117.

[87] Jing X, Wang Z, Yu Z, Zhang Q, Li C, Fang Y. Experimental and kinetic investigations of CO_2 gasification of fine chars separated from a pilot-scale fluidized-bed gasifier. Energy and Fuels 2013;27:2422–30. https://doi.org/10.1021/EF4002296/ASSET/IMAGES/LARGE/EF-2013-002296_0008.JPEG.

[88] Jing X, Wang Z, Zhang Q, Yu Z, Li C, Huang J, Fang Y. Evaluation of CO_2 Gasification Reactivity of Different Coal Rank Chars by Physicochemical Properties. Energy and Fuels 2013;27:7287–93. https://doi.org/10.1021/EF401639V.

[89] Lv P, Bai Y, Yang X, Gao M, Bao W, Li F. Impacts of char structure evolution and inherent alkali and alkaline earth metallic species catalysis on reactivity during the coal char gasification with CO_2/H_2O. International Journal of Energy Research 2018;42:3633–42. https://doi.org/10.1002/er.4111.

[90] Phounglamcheik A, Vila R, Kienzl N, Wang L, Hedayati A, Broström M, Ramser K, Engvall K, Skreiberg Ø, Robinson R, Umeki K. CO_2 Gasification Reactivity of Char from High-Ash Biomass. ACS Omega 2021;6:34115–28. https://doi.org/10.1021/ACSOMEGA.1C05728/ASSET/IMAGES/LARGE/AO1C05728_0010.JPEG.

[91] Tong W, Liu Q, Yang C, Cai Z, Wu H, Ren S. Effect of pore structure on CO_2 gasification reactivity of biomass chars under high-temperature pyrolysis. Journal of the Energy Institute 2020;93:962–76. https://doi.org/10.1016/j.joei.2019.08.007.

[92] Wang G, Zhang J, Hou X, Shao J, Geng W. Study on CO_2 gasification properties and kinetics of biomass chars and anthracite char. Bioresource Technology 2015;177:66–73. https://doi.org/10.1016/j.biortech.2014.11.063.

[93] Xu M, Wu Y, Nan D, Lu Q, Yang Y. Effects of gaseous agents on the evolution of char physical and chemical structures during biomass gasification. Bioresource Technology 2019;292:121994. https://doi.org/10.1016/j.biortech.2019.121994.

[94] Huang Y, Yin X, Wu C, Wang C, Xie J, Zhou Z, Ma L, Li H. Effects of metal catalysts on CO_2 gasification reactivity of biomass char. Biotechnology Advances 2009;27:568–72. https://doi.org/10.1016/j.biotechadv.2009.04.013.

[95] Pacioni TR, Soares D, Di Domenico M, Alves JLF, Virmond E, Moreira R de FPM, José HJ. Kinetic modeling of CO_2 gasification of biochars prepared from Brazilian agro-industrial residues: effect of biomass indigenous mineral content. Biomass Conversion and Biorefinery 2023;13:6675–88. https://doi.org/10.1007/S13399-021-01671-Y/TABLES/5.

[96] Roncancio R, Gore JP. CO_2 char gasification: A systematic review from 2014 to 2020. Energy Conversion and Management: X 2021;10. https://doi.org/10.1016/J.ECMX.2020.100060.

[97] Yin R, Liu R, Wu J, Wu X, Sun C, Wu C. Influence of particle size on performance of a pilot-scale fixed-bed gasification system. Bioresource Technology 2012;119:15–21. https://doi.org/10.1016/J.BIORTECH.2012.05.085.

[98] Luo S, Xiao B, Hu Z, Liu S, Guan Y, Cai L. Influence of particle size on pyrolysis and gasification performance of municipal solid waste in a fixed bed reactor. Bioresource Technology 2010;101:6517–20. https://doi.org/10.1016/J.BIORTECH.2010.03.060.

[99] Inayat M, Sulaiman SA, Kumar A, Guangul FM. Effect of fuel particle size and blending ratio on syngas production and performance of co-gasification. Journal of Mechanical Engineering and Sciences 2016;10:2187–99. https://doi.org/10.15282/jmes.10.2.2016.21.0205.

[100] Mani T, Mahinpey N, Murugan P. Reaction kinetics and mass transfer studies of biomass char gasification with CO_2. Chemical Engineering Science 2011;66:36–41. https://doi.org/10.1016/J.CES.2010.09.033.

[101] Hernández JJ, Aranda-Almansa G, Bula A. Gasification of biomass wastes in an entrained flow gasifier: Effect of the particle size and the residence time. Fuel Processing Technology 2010;91:681–92. https://doi.org/10.1016/J.FUPROC.2010.01.018.

[102] Gómez-Barea A, Ollero P, Fernández-Baco C. Diffusional Effects in CO_2 Gasification Experiments with Single Biomass Char Particles. 1. Experimental Investigation. Energy and Fuels 2006;20:2202–10. https://doi.org/10.1021/EF050365A.

[103] Leng L, Xiong Q, Yang L, Li H, Zhou Y, Zhang W, Jiang S, Li H, Huang H. An overview on engineering the surface area and porosity of biochar. Science of the Total Environment 2021;763:144204. https://doi.org/10.1016/j.scitotenv.2020.144204.

[104] Zhao H, Cao Y, Orndorff W, Pan WP. Gasification characteristics of coal char under CO_2 atmosphere. Journal of Thermal Analysis and Calorimetry 2014;116:1267–72. https://doi.org/10.1007/S10973-013-3627-9/TABLES/4.

[105] Lahijani P, Zainal ZA, Mohammadi M, Mohamed AR. Conversion of the greenhouse gas CO_2 to the fuel gas CO via the Boudouard reaction: A review. Renewable and Sustainable Energy Reviews 2015;41:615–32.

https://doi.org/10.1016/J.RSER.2014.08.034.

[106] Thommes M, Kaneko K, Neimark A V, Olivier JP, Rodriguez-reinoso F, Rouquerol J, Sing KSW. Physisorption of gases , with special reference to the evaluation of surface area and pore size distribution (IUPAC Technical Report). Journal of Pure & Applied Chemistry 2015;87:1051–69. https://doi.org/10.1515/pac-2014-1117.

[107] Kinashi K, Kambe Y, Misaki M, Koshiba Y, Ishida K, Ueda Y. Reporting physisorption data for gas/solid systems with special reference to the determination of surface area and porosity (Recommendations 1984). Journal of Pure & Applied Chemistry 1985;57:603–19. https://doi.org/10.1002/pola.26338.

[108] Shurtz RC, Fletcher TH. Coal Char-CO_2 Gasification Measurements and Modeling in a Pressurized Flat-Flame Burner. Energy and Fuels 2013;27:3022–38. https://doi.org/10.1021/EF400253C.

[109] Rollinson AN, Karmakar MK. On the reactivity of various biomass species with CO_2 using a standardised methodology for fixed-bed gasification. Chemical Engineering Science 2015;128:82–91. https://doi.org/10.1016/J.CES.2015.02.007.

[110] Zou X, Ding L, Liu X, Guo Q, Lu H, Gong X. Study on effects of ash on the evolution of physical and chemical structures of char during CO_2 gasification. Fuel 2018;217:587–96. https://doi.org/10.1016/J.FUEL.2017.12.009.

[111] Gupta A, Thengane SK, Mahajani S. CO_2 gasification of char from lignocellulosic garden waste: Experimental and kinetic study. Bioresource Technology 2018;263:180–91. https://doi.org/10.1016/J.BIORTECH.2018.04.097.

[112] Jiao W, Wang Z, Jiao W, Li L, Zuo Z, Li G, Hao Z, Song S, Huang J, Fang Y. Influencing factors and reaction mechanism for catalytic CO_2 gasification of sawdust char using K-modified transition metal composite catalysts: Experimental and DFT studies. Energy Conversion and Management 2020;208:112522. https://doi.org/10.1016/j.enconman.2020.112522.

[113] Zhang Y, Hara S, Kajitani S, Ashizawa M. Modeling of catalytic gasification kinetics of coal char and carbon. Fuel 2010;89:152–7. https://doi.org/10.1016/J.FUEL.2009.06.004.

[114] Wang G, Zhang J, Shao J, Liu Z, Wang H, Li X, Zhang P, Geng W, Zhang G. Experimental and modeling studies on CO_2 gasification of biomass chars. Energy 2016;114:143–54. https://doi.org/10.1016/J.ENERGY.2016.08.002.

[115] Htet TT, Yan Z, Spooner S, Degirmenci V, Meijer K, Li Z. Gasification and physical-chemical characteristics of carbonaceous materials in relation to HIsarna ironmaking process. Fuel 2021;289:119890. https://doi.org/10.1016/j.fuel.2020.119890.

[116] Kan T, Strezov V, Evans TJ. Lignocellulosic biomass pyrolysis: A review of product properties and effects of pyrolysis parameters. Renewable and Sustainable Energy

Reviews 2016;57:1126–40. https://doi.org/10.1016/j.rser.2015.12.185.

[117] Li X, Zhang H, Liu MJ, Zhi LF, Bai J, Bai ZQ, Li W. Investigation of coal-biomass interaction during co-pyrolysis by char separation and its effect on coal char structure and gasification reactivity with CO_2. Journal of Fuel Chemistry and Technology 2020;48:897–907. https://doi.org/10.1016/S1872-5813(20)30062-1.

[118] Li X, He J, Liu M, Bai J, Bai Z, Li W. Interaction between Coal and Biomass during Co-Gasification: A Perspective Based on the Separation of Blended Char. Processes 2022, Vol 10, Page 286 2022;10:286. https://doi.org/10.3390/PR10020286.

[119] Fryda LE, Panopoulos KD, Kakaras E. Agglomeration in fluidised bed gasification of biomass. Powder Technology 2008;181:307–20. https://doi.org/10.1016/J.POWTEC.2007.05.022.

[120] Sakawa M, Sakurai Y, Hara Y. Influence of coal characteristics on CO_2 gasification. Fuel 1982;61:717–20. https://doi.org/10.1016/0016-2361(82)90245-9.

[121] Wang Q, Wang E, Li K, Husnain N, Li D. Synergistic effects and kinetics analysis of biochar with semi-coke during CO_2 co-gasification. Energy 2020;191:116528. https://doi.org/10.1016/J.ENERGY.2019.116528.

[122] Perander M, DeMartini N, Brink A, Kramb J, Karlström O, Hemming J, Moilanen A, Konttinen J, Hupa M. Catalytic effect of Ca and K on CO_2 gasification of spruce wood char. Fuel 2015;150:464–72. https://doi.org/10.1016/j.fuel.2015.02.062.

[123] Xu K, Hu S, Su S, Xu C, Sun L, Shuai C, Jiang L, Xiang J. Study on Char Surface Active Sites and Their Relationship to Gasification Reactivity. Energy and Fuels 2012;27:118–25. https://doi.org/10.1021/ef301455x.

[124] Molina A, Montoya A, Mondragón F. CO_2 strong chemisorption as an estimate of coal char gasification reactivity. Fuel 1999;78:971–7. https://doi.org/10.1016/S0016-2361(98)00220-8.

[125] Tremel A. Reaction Kinetics of Solid Fuels during Entrained Flow Gasification [PhD thesis]. Technische Universität München, 2012.

[126] Chen H, Yang H, Ju F, Wang J, Zhang S. The influence of pressure and temperature on coal pyrolysis/gasification. Asia-Pacific Journal of Chemical Engineering, vol. 2, 2007, p. 203–12. https://doi.org/10.1002/apj.42.

[127] Liu H, Kaneko M, Luo C, Kato S, Kojima T. Effect of pyrolysis time on the gasification reactivity of char with CO_2 at elevated temperatures. Fuel 2004;83:1055–61. https://doi.org/10.1016/S0016-2361(03)00142-X.

[128] Schneider C, Walker S, Phounglamcheik A, Umeki K, Kolb T. Effect of calcium dispersion and graphitization during high-temperature pyrolysis of beech wood char on the gasification rate with CO_2. Fuel 2021;283:118826. https://doi.org/10.1016/j.fuel.2020.118826.

[129] Tian H, Hu Q, Wang J, Chen D, Yang Y, Bridgwater A V. Kinetic study on the CO_2 gasification of biochar derived from Miscanthus at different processing conditions. Energy 2021;217:119341. https://doi.org/10.1016/j.energy.2020.119341.

[130] Xu T, Wang G wei, Zhang J liang, Song T fei, Xu R sheng. Non-isothermal study of gasification process of coal char and biomass char in CO_2 condition. Journal of Iron and Steel Research International 2017;24:985–90. https://doi.org/10.1016/S1006-706X(17)30144-9.

[131] Liu M, Zhang C, Bai J, Wang X, Xing L, Li X, Han B, Kong L, Bai Z, Li H, Li W. Comparative study on the effects of heating rate on char gasification behaviors by thermogravimetric analyzer and high-temperature stage microscope under non-isothermal condition. Fuel 2023;343:127972. https://doi.org/10.1016/j.fuel.2023.127972.

[132] Liu M, Bai J, Kong L, Bai Z, He C, Li W. The correlation between coal char structure and reactivity at rapid heating condition in TGA and heating stage microscope. Fuel 2020;260:116318. https://doi.org/10.1016/j.fuel.2019.116318.

[133] Lahijani P, Mohammadi M, Mohamed AR. Catalytic CO_2 gasification of rubber seed shell-derived hydrochar: reactivity and kinetic studies. Environmental Science and Pollution Research 2019;26:11767–80. https://doi.org/10.1007/s11356-019-04613-4.

[134] Qambrani NA, Rahman MM, Won S, Shim S, Ra C. Biochar properties and eco-friendly applications for climate change mitigation, waste management, and wastewater treatment: A review. Renewable and Sustainable Energy Reviews 2017;79:255–73. https://doi.org/10.1016/j.rser.2017.05.057.

[135] Masoumi S, Borugadda VB, Nanda S, Dalai AK. Hydrochar: A Review on Its Production Technologies and Applications. Catalysts 2021;11:939. https://doi.org/10.3390/catal11080939.

[136] Yuliansyah AT, Putri CO, Clarasinta BD, Nonaka M. TGA investigation of CO_2 gasification of hydrothermally treated biomass (corn cob-coconut shell mixture). International Journal of Technology 2019;10:1166–73. https://doi.org/10.14716/ijtech.v10i6.3641.

[137] Ulbrich M, Preßl D, Fendt S, Gaderer M, Spliethoff H. Impact of HTC reaction conditions on the hydrochar properties and CO_2 gasification properties of spent grains. Fuel Processing Technology 2017;167:663–9. https://doi.org/10.1016/j.fuproc.2017.08.010.

[138] Wei X, Liu P, Huang S, Li X, Wu Y, Wu S. Hydrothermal carbonization characteristics and mechanism of penicillin mycelial residues and CO_2 gasification performance of hydrochars. Biomass and Bioenergy 2024;183:107130. https://doi.org/10.1016/j.biombioe.2024.107130.

[139] Shahabuddin M, Kibria MA, Bhattacharya S. Gasification kinetics of Barapukurian

coal char using carbon dioxide and steam reactants. Chemical Papers 2022;76:4459–70. https://doi.org/10.1007/S11696-022-02186-0/FIGURES/14.

[140] Ren L, Yang J, Gao F, Yan J. Laboratory Study on Gasification Reactivity of Coals and Petcokes in CO_2/Steam at High Temperatures. Energy and Fuels 2013;27:5054–68. https://doi.org/10.1021/EF400373Y.

[141] McEnaney B. Active Sites in Relation to Gasification of Coal Chars. Fundamental Issues in Control of Carbon Gasification Reactivity, Springer, Dordrecht; 1991, p. 175–203. https://doi.org/10.1007/978-94-011-3310-4_10.

[142] Bikane K. Reaction Kinetics and Structural Evolution of Pyrolysis and Gasification Chars [PhD]. Imperial College London, 2020.

[143] Sean Connolly T, Co A, Schwiderke E, Van Heiningen ARP. Carbon dioxide gasification of kraft black liquor char in a laboratory char bed reactor. AIChE Annual Meeting, Conference Proceedings, 2006.

[144] Zhang Y, Geng P, Zheng Y. Exploration and practice to improve the kinetic analysis of char-CO_2 gasification via thermogravimetric analysis. Chemical Engineering Journal 2019;359:298–304. https://doi.org/10.1016/J.CEJ.2018.11.122.

[145] Tanner J, Bhattacharya S. Kinetics of CO_2 and steam gasification of Victorian brown coal chars. Chemical Engineering Journal 2016;285:331–40. https://doi.org/10.1016/j.cej.2015.09.106.

[146] Shaofeng L, Shiyong W. CO_2 gasification reaction kinetics of shenfu coal chars at elevated temperatures. Journal of China Coal Society 2010;35:670–5.

[147] Kajitani S, Hara S, Matsuda H. Gasification rate analysis of coal char with a pressurized drop tube furnace. Fuel 2002;81:539–46. https://doi.org/10.1016/S0016-2361(01)00149-1.

[148] Yuan S, Chen XL, Li J, Wang FC. CO_2 gasification kinetics of biomass char derived from high-temperature rapid pyrolysis. Energy and Fuels 2011;25:2314–21. https://doi.org/10.1021/EF200051Z/ASSET/IMAGES/LARGE/EF-2011-00051Z_0007.JPEG.

[149] Alauddin ZABZ, Lahijani P, Mohammadi M, Mohamed AR. Gasification of lignocellulosic biomass in fluidized beds for renewable energy development: A review. Renewable and Sustainable Energy Reviews 2010;14:2852–62. https://doi.org/10.1016/J.RSER.2010.07.026.

[150] Ofuani N, Bhoi P. Carbon Dioxide Gasification of Biochar: A Sustainable Way of Utilizing Captured CO_2 to Mitigate Greenhouse Gas Emission. Sustainability 2024;16:5044. https://doi.org/10.3390/su16125044.

[151] Snape CE, Meredith W, McKechnie J, West H, Rodgers S, Stephens L, Gill A, Riley P, Alce J. BEIS GGR Innovation Phase 1 Project Bio-waste to Biochar (B to B) via Hydrothermal Carbonisation and Post-Carbonisation Final Report. 2022.

[152] (BSI) BSI. Solid biofuels —Solid biofuels. Determination of moisture content. Oven dry method. Moisture in general analysis sample, BS EN ISO 18134-3-2015 2015.

[153] (BSI) BSI. Solid biofuels — Determination of ash content, BS EN ISO 18122-2015 2015.

[154] (BSI) BSI. Solid biofuels — Determination of the content of volatile matter, BS EN ISO 18123:2015 2009:5–11.

[155] Sarkar DK. Chapter3: Fuels and Combustion. Thermal Power Plant: Design and Operation, 2015, p. 91–137. https://doi.org/10.1016/b978-0-12-801575-9.00003-2.

[156] Lawal AI, Aladejare AE, Onifade M, Bada S, Idris MA. Predictions of elemental composition of coal and biomass from their proximate analyses using ANFIS, ANN and MLR. International Journal of Coal Science and Technology 2021;8:124–40. https://doi.org/10.1007/s40789-020-00346-9.

[157] Krotz L. Micro vs. macro analysis using the FlashSmart Elemental Analyzer. 2023.

[158] Thermo FlashSmart CHNS/O Elemental Analyzer. 2020.

[159] Leco. Organic Application Note: Sulfur and Carbon in Coal , Coke , and Graphite. 2007.

[160] Kolosionis A, Kastanaki E, Veksha A, Wang H, He C, Lisak G, Giannis A. The Effects of Washing Techniques on Thermal Combustion Properties of Sewage Sludge Chars. International Journal of Environmental Research 2021;15:285–97. https://doi.org/10.1007/S41742-021-00312-6.

[161] X-5000 Energy Dispersive X-ray Fluorescence Analyzer - HORIBA n.d. https://www.horiba.com/int/scientific/products/detail/action/show/Product/x-5000-1135/ (accessed July 17, 2025).

[162] Limbeck A, Bonta M, Nischkauer W. Improvements in the direct analysis of advanced materials using ICP-based measurement techniques. Journal of Analytical Atomic Spectrometry 2017;32:212–32. https://doi.org/10.1039/C6JA00335D.

[163] Ruiz-De-Cenzano M, Rochina-Marco A, Ruiz J, Cervera ML, De La Guardia M. A comparative study on sample preparation procedures for supplementary foods by ICP-OES: Green chemistry considerations. Analytical Methods 2015;7:3637–44. https://doi.org/10.1039/C5AY00397K.

[164] Rabb SA, Olesik JW. Assessment of high precision, high accuracy Inductively Coupled Plasma-Optical Emission Spectroscopy to obtain concentration uncertainties less than 0.2% with variable matrix concentrations. Spectrochimica Acta Part B: Atomic Spectroscopy 2008;63:244–56. https://doi.org/10.1016/J.SAB.2007.11.034.

[165] Nasrollahzadeh M, Atarod M, Sajjadi M, Sajadi SM, Issaabadi Z. Plant-Mediated

Green Synthesis of Nanostructures: Mechanisms, Characterization, and Applications. vol. 28. 1st ed. Elsevier Ltd.; 2019. https://doi.org/10.1016/B978-0-12-813586-0.00006-7.

[166] (BSI) BSI. Determination of the specific surface area of solids by gas adsorption — BET method, BS ISO 9277:2022 2022.

[167] (BSI) BSI. Method of determining specific surface area of coal, BS ISO 23604:2022 2022.

[168] (BSI) BSI. Pore size distribution and porosity of solid materials by mercury porosimetry and gas adsorption, Part 2: Analysis of nanopores by gas adsorption, BS ISO 15901-2:2022 2022.

[169] Brunauer S, Emmett P. H, Teller E. Adsorption of Gases in Multimolecular Layers. Journal of the American Chemical Society 1938;60:309–19.

[170] de Boer JH, Lippens BC, Linsen BG, Broekhoff JCP, van den Heuvel A, Osinga TJ. The t-curve of multimolecular N_2-adsorption. Journal of Colloid And Interface Science 1966;21:405–14. https://doi.org/10.1016/0095-8522(66)90006-7.

[171] Barrett EP, Joyner LG, Halenda PP. The Determination of Pore Volume and Area Distributions in Porous Substances. I. Computations from Nitrogen Isotherms. Journal of the American Chemical Society 1951;73:373–80. https://doi.org/10.1021/JA01145A126.

[172] Magee RW. Evaluation of the External Surface Area of Carbon Black by Nitrogen Adsorption. Rubber Chemistry and Technology 1995;68:590–600. https://doi.org/10.5254/1.3538760.

[173] Herbert J. The Behaviour of Mineral Matter from Pulverised Coal Injection in the Blast Furnace Raceway [PhD thesis]. Cardiff University, School of Engineering, 2019.

[174] Rietveld HM. A profile refinement method for nuclear and magnetic structures. Journal of Applied Crystallography 1969;2:65–71. https://doi.org/10.1107/s0021889869006558.

[175] PDF-5+ Powder Diffraction File Database. International Centre for Diffraction Data (ICDD) n.d. https://www.icdd.com/pdf-5/ (accessed May 1, 2025).

[176] Djerdj I. Rietveld Refinement in the Characterization of Crystalline Materials. 2019. https://doi.org/10.3390/books978-3-03897-528-1.

[177] Reed S. Introduction to Energy Dispersive X-ray Spectrometry. Electron Probe Microanalysis 1995:1–12.

[178] Fairley N, Fernandez V, Richard-Plouet M, Guillot-Deudon C, Walton J, Smith E, Flahaut D, Greiner M, Biesinger M, Tougaard S, Morgan D, Baltrusaitis J. Systematic and collaborative approach to problem solving using X-ray photoelectron

spectroscopy. Applied Surface Science Advances 2021;5:100112. https://doi.org/10.1016/J.APSADV.2021.100112.

[179] Mathias J. Advantages & Disadvantages of XPS Spectroscopy Testing & Analysis 2019. https://www.innovatechlabs.com/newsroom/2012/advantages-disadvantages-xps-testing-analysis/?utm_source=chatgpt.com (accessed July 17, 2025).

[180] Mettler Toledo. Thermal Analysis System DMA 1 - METTLER TOLEDO. n.d.

[181] Takarada T, Tamai Y, Tomita A. Reactivities of 34 coals under steam gasification. Fuel 1985;64:1438–42. https://doi.org/10.1016/0016-2361(85)90347-3.

[182] Steer J, Greenslade M, Marsh R. A comparison of laboratory coal testing with the blast furnace process and coal injection. Metals 2021;11. https://doi.org/10.3390/met11091476.

[183] Resbond® 940HT alumina adhesive. Final Advanced Materials n.d. https://www.final-materials.com/gb/alumina-ceramic-adhesive/575-resbond-940ht-adhesif-alumine.html#/285-volume_l-047_l (accessed July 18, 2025).

[184] White FM. VISCOUS FLUID FLOW. Second Edi. McGraw-Hill, New York ISBN: 0070697124; 1992.

[185] Economical Gas Mass Flow meters For Clean Gases with Optional Integral Display n.d. https://www.omega.co.uk/pptst/FMA1700A_1800A.html (accessed July 31, 2024).

[186] NIST Chemistry WebBook, SRD 69. National Institute of Standards and Technology 2025. https://webbook.nist.gov/chemistry/name-ser/ (accessed July 18, 2025).

[187] Simple Data Logger weight recording software (SDL) n.d. https://www.smartlux.com/sdl/documentation/ (accessed August 1, 2024).

[188] Betancur M, Natalia Arenas C, Daniel Martínez J, Victoria Navarro M, Murillo R. CO_2 gasification of char derived from waste tire pyrolysis: Kinetic models comparison. Fuel 2020;273:117745. https://doi.org/10.1016/j.fuel.2020.117745.

[189] Ge Z, Cao X, Zha Z, Ma Y, Zeng M, Wu Y, Hou Z, Zhang H. Establishment of correlation between reaction kinetics and carbon structures in the char gasification process. Carbon Resources Conversion 2023;6:67–75. https://doi.org/10.1016/J.CRCON.2023.02.002.

[190] Sircar I, Sane A, Wang W, Gore JP. Experimental and modeling study of pinewood char gasification with CO_2. Fuel 2014;119:38–46. https://doi.org/10.1016/j.fuel.2013.11.026.

[191] Fermoso J, Arias B, Pevida C, Plaza MG, Rubiera F, Pis JJ. Kinetic models comparison for steam gasification of different nature fuel chars. Journal of Thermal Analysis and Calorimetry 2008;91:779–86. https://doi.org/10.1007/s10973-007-8623-5.

[192] Zuo H, Geng W, Zhang J, Wang G. Comparison of kinetic models for isothermal CO_2 gasification of coal char-biomass char blended char. International Journal of Minerals, Metallurgy and Materials 2015;22:363–70. https://doi.org/10.1007/S12613-015-1081-3.

[193] Izaharuddin AN, Paul MC, Yoshikawa K, Theppitak S, Dai X. Comprehensive Kinetic Modeling Study of CO_2 Gasification of Char Derived from Food Waste. Energy and Fuels 2020;34:1883–95. https://doi.org/10.1021/acs.energyfuels.9b03937.

[194] Ishida M, Wen CY. Comparison of zone-reaction model and unreacted-core shrinking model in solid-gas reactions-I isothermal analysis. Chemical Engineering Science 1971;26:1031–41. https://doi.org/10.1016/0009-2509(71)80017-9.

[195] Lopez G, Alvarez J, Amutio M, Arregi A, Bilbao J, Olazar M. Assessment of steam gasification kinetics of the char from lignocellulosic biomass in a conical spouted bed reactor. Energy 2016;107:493–501. https://doi.org/10.1016/j.energy.2016.04.040.

[196] Szekely J, Evans JW. A structural model for gas-solid reactions with a moving boundary. Chemical Engineering Science 1970;25:1091–107. https://doi.org/10.1016/0009-2509(70)85053-9.

[197] Bhatia SK, Perlmutter DD. A Rondom Pore Model for Fluid-Solid Reactions: I. Isothermal, Kinetic Control. AIChE Journal 1980;26:379–86. https://doi.org/10.1007/978-3-319-89554-3.

[198] Bhatia SK, Perlmutter DD. A Random Pore Model for Fluid-Solid Reactions : II. Diffusion and Transport Effects. AIChE Journal 1981;27:247–54.

[199] Wang G, Zhang J, Zhang G, Ning X, Li X, Liu Z, Guo J. Experimental and kinetic studies on co-gasification of petroleum coke and biomass char blends. Energy 2017;131:27–40. https://doi.org/10.1016/j.energy.2017.05.023.

[200] Schmidt HP, Bucheli T, Kammann C, Glaser B, Abiven S, Leifeld J, Soja G, Hagemann N. European Biochar Certificate - Guidelines for a Sustainable Production of Biochar. European Biochar Foundation (EBC) 2023;10.

[201] Al-Ghouti MA, Da'ana DA. Guidelines for the use and interpretation of adsorption isotherm models: A review. Journal of Hazardous Materials 2020;393:122383. https://doi.org/10.1016/j.jhazmat.2020.122383.

[202] Müller FJ, Fuchs J, Fanjul Cuesta M, Oblanca Gutiérrez A, Pratschner S, Müller S, Winter F. CO_2 conversion to CO by fluidized bed biomass gasification: Analysis of operational parameters. Journal of CO_2 Utilization 2024;81:102706. https://doi.org/10.1016/J.JCOU.2024.102706.

[203] Kowalczyk P, Furmaniak S, Terzyk AP, Corrente NJ, Neimark A V. Surface area and porosity analysis in nanoporous carbons by atomistic pore domain model. Carbon 2024;229:119510. https://doi.org/10.1016/J.CARBON.2024.119510.

[204] Khasraw D. Fundamental understanding on the use of different carbon sources in the HIsarna alternative ironmaking process [PhD thesis]. University of Warwick, 2021.

[205] Trueman C. GEOCHEMISTRY/Inorganic. Encyclopedia of Analytical Science: Second Edition 2005:171–81. https://doi.org/10.1016/B0-12-369397-7/00240-5.

[206] Wajima T. Effects of Step-Wise Acid Leaching with HCl on Synthesis of Zeolitic Materials from Paper Sludge Ash. Minerals 2020, Vol 10, Page 402 2020;10:402. https://doi.org/10.3390/MIN10050402.

[207] Czerski G, Śpiewak K, Grzywacz P, Wierońska-Wiśniewska F. Assessment of the catalytic effect of various biomass ashes on CO_2 gasification of tire char. Journal of the Energy Institute 2021;99:170–7. https://doi.org/10.1016/J.JOEI.2021.09.003.

[208] Morgan DJ. Comments on the XPS Analysis of Carbon Materials. C 2021, Vol 7, Page 51 2021;7:51. https://doi.org/10.3390/C7030051.

[209] Zhang F, Wu Q. Functional Materials Development from Kitchen Waste. Procedia Environmental Sciences 2012;16:70–4. https://doi.org/10.1016/j.proenv.2012.10.010.

[210] Luo Y, Lan Y, Liu X, Xue M, Zhang L, Yin Z, He X, Li X, Yang J, Hong Z, Naushad M, Gao B. Hydrochar effectively removes aqueous Cr(VI) through synergistic adsorption and photoreduction. Separation and Purification Technology 2023;317:123926. https://doi.org/10.1016/j.seppur.2023.123926.

[211] Qiu M, Liu L, Ling Q, Cai Y, Yu S, Wang S, Fu D, Hu B, Wang X. Biochar for the removal of contaminants from soil and water: a review. Biochar 2022;4:1–25. https://doi.org/10.1007/S42773-022-00146-1/FIGURES/7.

[212] Goel C, Mohan S, Dinesha P. CO_2 capture by adsorption on biomass-derived activated char: A review. Science of the Total Environment 2021;798:149296. https://doi.org/10.1016/j.scitotenv.2021.149296.

[213] Masoumi S, Borugadda VB, Nanda S, Dalai AK. Hydrochar: A review on its production technologies and applications. Catalysts 2021;11:939. https://doi.org/10.3390/catal11080939.

[214] Qambrani NA, Rahman MM, Won S, Shim S, Ra C. Biochar properties and eco-friendly applications for climate change mitigation, waste management, and wastewater treatment: A review. Renewable and Sustainable Energy Reviews 2017;79:255–73. https://doi.org/10.1016/J.RSER.2017.05.057.

[215] Guo S, Jiang Y, Liu T, Zhao J, Huang J, Fang Y. Investigations on interactions between sodium species and coal char by thermogravimetric analysis. Fuel 2018;214:561–8. https://doi.org/10.1016/j.fuel.2017.11.069.

[216] Li Z, Feng S, Yang X, Lyu H, Wei S, Shen B. A review of biomass porous carbon for carbon dioxide adsorption from flue gas: Physicochemical properties and

performance. Fuel 2025;387:134318. https://doi.org/10.1016/j.fuel.2025.134318.

[217] Font-Palma C, Cann D, Udemu C, García O. Review of Cryogenic Carbon Capture Innovations and Their Potential Applications. C 2021, Vol 7, Page 58 2021;7:58. https://doi.org/10.3390/C7030058.

[218] Patil SC, Fahim STM, Lee JH, Gilliard-AbdulAziz KL. Electrothermal Carbon Capture and Utilization—A Review. ACS Energy Letters 2024:371–92. https://doi.org/10.1021/ACSENERGYLETT.4C02851/ASSET/IMAGES/LARGE/NZ4C02851_0013.JPEG.

[219] Song Q, Wang X, Gu C, Li H, Huo J. Study on CO_2 gasification kinetics of biomass char based on pore structure analysis: Theoretical modelling of structural parameter ψ in random pore model. International Journal of Energy Research 2021;45:4429–42. https://doi.org/10.1002/ER.6113.

[220] Wang G, Ren S, Zhang J, Ning X, Liang W, Zhang N, Wang C. Influence mechanism of alkali metals on CO_2 gasification properties of metallurgical coke. Chemical Engineering Journal 2020;387:124093. https://doi.org/10.1016/J.CEJ.2020.124093.

[221] Liu Z, Wang G, Zhang J, Lee J-Y, Wang H, Sun M, Wang C. Study on CO_2 Gasification Reactivity and Structure Characteristics of Carbonaceous Materials from the Corex Furnace. Energy & Fuels 2018;32:6155–66. https://doi.org/10.1021/acs.energyfuels.8b00072.

[222] Kim YT, Seo DK, Hwang J. Study of the Effect of Coal Type and Particle Size on Char–CO_2 Gasification via Gas Analysis. Energy & Fuels 2011;25:5044–54. https://doi.org/10.1021/ef200745x.

[223] Seo DK, Lee SK, Kang MW, Hwang J, Yu T-U. Gasification reactivity of biomass chars with CO_2. Biomass and Bioenergy 2010;34:1946–53. https://doi.org/10.1016/j.biombioe.2010.08.008.

[224] ASTM standard E2550-21. Standard Test Method for Thermal Stability by Thermogravimetry. ASTM International 2017;11:5. https://doi.org/10.1520/E2550-11.2.

[225] INTERNATIONAL STANDARD ISO 11358-1. Plastics — Thermogravimetry (TG) of polymers 2022;2022.

[226] Czerski G, Grzywacz P, Śpiewak K. Comparison of CO_2 gasification of coal in isothermal and non-isothermal conditions. E3S Web of Conferences 2019;108. https://doi.org/10.1051/e3sconf/201910802017.

[227] Tran KQ, Bui HH, Luengnaruemitchai A, Wang L, Skreiberg Ø. Isothermal and non-isothermal kinetic study on CO_2 gasification of torrefied forest residues. Biomass and Bioenergy 2016;91:175–85. https://doi.org/10.1016/J.BIOMBIOE.2016.05.024.

[228] Hu Y, Yu H, Zhou F, Chen D. A comparison between CO_2 gasification of various biomass chars and coal char. The Canadian Journal of Chemical Engineering 2019;97:1326–31. https://doi.org/10.1002/CJCE.23417.

[229] Mandapati RN, Daggupati S, Mahajani SM, Aghalayam P, Sapru RK, Sharma RK, Ganesh A. Experiments and kinetic modeling for CO_2 gasification of Indian coal chars in the context of underground coal gasification. Industrial and Engineering Chemistry Research 2012;51:15041–52. https://doi.org/10.1021/ie3022434.

[230] Tomaszewicz M, Łabojko G, Tomaszewicz G, Kotyczka-Morańska M. The kinetics of CO_2 gasification of coal chars. Journal of Thermal Analysis and Calorimetry 2013;113:1327–35. https://doi.org/10.1007/s10973-013-2961-2.

[231] Wystalska K, Kwarciak-Kozłowska A, Włodarczyk R. Influence of Technical Parameters of the Pyrolysis Process on the Surface Area, Porosity, and Hydrophobicity of Biochar from Sunflower Husk Pellet. Sustainability (Switzerland) 2023;15. https://doi.org/10.3390/su15010394.

[232] Reed T, Das A. A Survey of Biomass Gasification Volume II – Principles of Gasification. Golden, Colorado, United States: 1979.

[233] Quan C, Zhang J, Tang Z, Magdziarz A, Wu C, Gao N. Investigation on the influence of inherent AAEMs on gasification reactivity of solid digestate char. Fuel 2023;335:127015. https://doi.org/10.1016/j.fuel.2022.127015.

[234] Zhu Y, Li B, Miao J, Sun S, Wang Y, Zhao X, Chen B, Wu C. Achieving zero CO_2 emissions from integrated biomass gasification with CO_2 capture and utilization (IGCCU). Chemical Engineering Journal 2023;474:145767. https://doi.org/10.1016/J.CEJ.2023.145767.

[235] Fecht S. How Exactly Does Carbon Dioxide Cause Global Warming? Lamont-Doherty Earth Observatory. Columbia University, Climate School 2021. https://lamont.columbia.edu/news/how-exactly-does-carbon-dioxide-cause-global-warming (accessed March 21, 2022).

[236] Lindsey R. Climate Change: Atmospheric Carbon Dioxide 2024. https://www.climate.gov/news-features/understanding-climate/climate-change-atmospheric-carbon-dioxide (accessed April 15, 2025).

[237] International Energy Forum-IEF. Creating Demand For Captured Carbon : The Unsolved Puzzle 2021:1–7. https://www.ief.org/news/creating-demand-for-captured-carbon-the-unsolved-puzzle (accessed August 30, 2023).

[238] Lindstad T, Syvertsen M, Ishak RJ, Arntzen HB, Grontvedt PO. THE INFLUENCE OF ALKALIS ON THE BOUDOUARD REACTION 2004;6:261–71. https://doi.org/10.1007/BF02997045.

[239] Sikarwar VS, Zhao M, Fennell PS, Shah N, Anthony EJ. Progress in biofuel production from gasification. Progress in Energy and Combustion Science

2017;61:189–248. https://doi.org/10.1016/j.pecs.2017.04.001.

[240] Zhang Y, Wan L, Guan J, Xiong Q, Zhang S, Jin X. A Review on Biomass Gasification: Effect of Main Parameters on Char Generation and Reaction. Energy and Fuels 2020;34:13438–55. https://doi.org/10.1021/ACS.ENERGYFUELS.0C02900/ASSET/IMAGES/ACS.ENERGYFUELS.0C02900.SOCIAL.JPEG_V03.

[241] Lee SY, Sankaran R, Chew KW, Tan CH, Krishnamoorthy R, Chu D-T, Show P-L. Waste to bioenergy: a review on the recent conversion technologies. BMC Energy 2019 1:1 2019;1:1–22. https://doi.org/10.1186/S42500-019-0004-7.

[242] Kumari G, Karmee SK. Thermochemical routes applying biomass: a critical assessment. Handbook of Biofuels 2022:435–51. https://doi.org/10.1016/B978-0-12-822810-4.00022-1.

[243] Tian Z, Mbayachi VB, Dai W, Khalil M, Ayejoto DA. Thermal Analysis Methods. Advanced Diagnostics in Combustion Science, Springer Nature Singapore; 2023. https://doi.org/10.1007/978-981-99-0546-1_3.

[244] Liu Y, Qu J, Wu X, Zhang K, Zhang Y. Reaction kinetics and internal diffusion of Zhundong char gasification with CO_2. Frontiers of Chemical Science and Engineering 2021;15:373–83. https://doi.org/10.1007/s11705-020-1949-2.

[245] Marsh H. A tribute to Philip L. Walker. Carbon 1991;29:703–4. https://doi.org/10.1016/0008-6223(91)90004-3.

[246] Lin Y, Ma X, Peng X, Yu Z, Fang S, Lin Y, Fan Y. Combustion, pyrolysis and char CO_2-gasification characteristics of hydrothermal carbonization solid fuel from municipal solid wastes. Fuel 2016;181:905–15. https://doi.org/10.1016/J.FUEL.2016.05.031.

Appendices

Appendix A: Risk Assessment for Macro-TGA system

Risk Assessment Form

IMPORTANT: Before carrying out the assessment, please read the Guidance Notes

1. General Information

Department	ENGIN	**Building**	Combustion lab
Name of Assessor	Ahmed Alsawadi	**Date of Original Assessment**	23rd April 2024

Status of Assessor: Supervisor ☐ Postgraduate ☒ Undergraduate ☐ Technician ☐ Other:

2. Brief Description of Procedure/Activity including its Location and Duration

Testing using laboratory scale gasification rig. The system consists of six sections: a gasifier (a vertical tube reactor for gasification tests of biomass chars in a CO_2 atmosphere at 850-1000°C), which contains a ceramic crucible placed at the top of a ceramic rod with a balance underneath, a gas delivery system, a heating system, a tar trap system, product gas analysis, and data acquisition system. The testing will take place in the combustion lab, west building, from May 2024 to December 2024.

3. Persons at Risk

Are they...		Notes
Staff ☐	Trained ☐	
Students ☒	Competent ☒	
Visitor ☐	Inexperienced ☐	
Contractor ☐	Disabled ☐	

4. Level of Supervision

	Notes
None ☒ Constant ☐ Periodic ☐ Training Required ☐	

5. Will Protective Equipment Be Used? Please give ***specific*** details of PPE

Head ☐ Eye ☒ Ear ☐ Body ☒ Hand ☒ Foot ☒	Safety shoes, gloves, goggles, and lab coat

6. Is the Environment at Risk? Notes

Yes ☐ No ☒	An extraction fan will be used, there are limited fumes generation, and the area is well-ventilated. Additionally, the experimental rig will be contained within a fume hood to ensure safe operation

7. Will Waste be generated? If 'yes' please give details of disposal

Yes ☒ No ☐	The gases from the gasification experiments will be analysed and then expelled from the lab using the extraction fan. Solid residues will be discarded in the combustion laboratory bin. Liquid byproducts, such as tar, will be disposed of in designated containers.

8. Hazards involved

Work Activity / Item of Equipment / Procedure / Physical Location	**Hazard**	**Control Measures and Consequence of Failure**	**Likelihood (0 to 5)**	**Severity (0 to 5)**	**Level of Risk**
High temperature surfaces: pipes, furnace, preheater	Burns	Thermal gloves will be worn when handling hot materials.	2	1	2
Using electrical equipment	Electric shock	All electrical equipment will be PAT tested.	1	2	2
Gas cylinders	Explosion	Cylinders will be used in accordance with cylinder regulations.	1	3	3

Moving around testing area	Trips/slips	Working area will be maintained tidy, any trip hazards will be identified and removed	1	1	1

9. Chemical Safety (COSHH Assessment)

Hazard	**Control Measures**	**Likelihood (0 to 5)**	**Severity (0 to 5)**	**Level of Risk**
Production of Carbon dioxide Carbon Monoxide, Hydrogen and Hydrocarbon, risk of asphyxiation, poison or fire.	Ensure area is well ventilated during experimentation by turning the extraction on, personal gas monitor to be worn (CO detector), lab gas monitor, masks to be worn.	1	3	3
Carbon Dioxide, Nitrogen	Stored in pressurised cylinder, used in accordance with cylinder regulations.	1	3	3
Isopropanol	Stored in suitable labelled container, gloves to be worn.	2	1	2

Scoring Criteria for Likelihood (chance of the hazard causing a problem)
0 – Zero to extremely unlikely, 1 – Very Unlikely, 2 – Unlikely, 3 – Likely, 4 – Very Likely, 5 – Almost certain to happen

Scoring Criteria for Severity of injury (or illness) resulting from the hazard
0 – No injury, 1 – First Aid is adequate, 2 – Minor injury, 3 – "Three day" injury, 4 – Major injury, 5 – Fatality or disabling injury

10. Source(s) of information used to complete the above

11. Further Action

Highest Level of Risk Score	**Action to be taken**
0 to 5 ☒	No further action needed
6 to 11 ☐	Appropriate additional control measures should be implemented

12 to 25☐	Additional control measures **MUST** be implemented. Work **MUST NOT** commence until such measures are in place. If work has already started it must **STOP** until adequate control measures are in place.

12. Additional Control Measures – Likelihood and Severity are the values with the additional controls in place

Work Activity / Item of Equipment / Procedure / Physical Location	Hazard and Existing Control Measures	Additional Controls needed to Reduce Risk	Likelihood (0 to 5)	Severity (0 to 5)	Level of Risk

After the implementation of new control measures the procedure/activity should be re-assessed to ensure that the level of risk has been reduced as required.

13. Action in the Event of an Accident or Emergency

Report to supervisor / manager and emergency shutdown of apparatus, switch off power and close all gas valves.

14. Arrangements for Monitoring the Effectiveness of Control

Ad-hoc visual checks and regular inspection of equipment and procedures.

Appendix B: N_2 physical adsorption analysis:

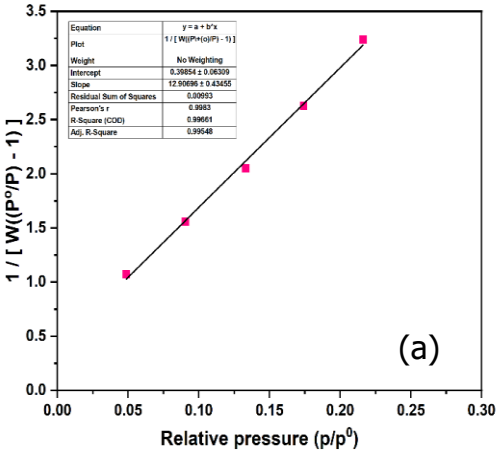

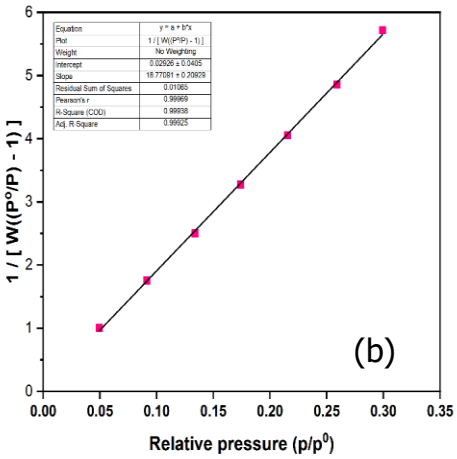

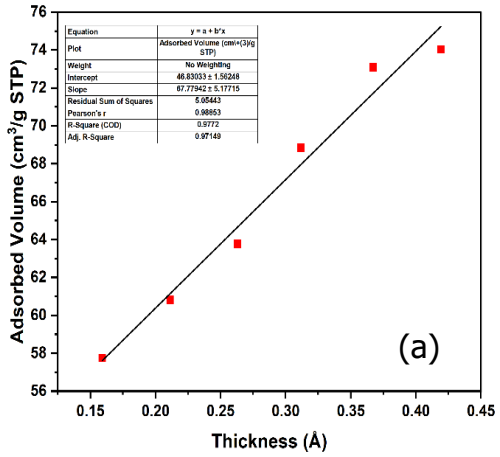

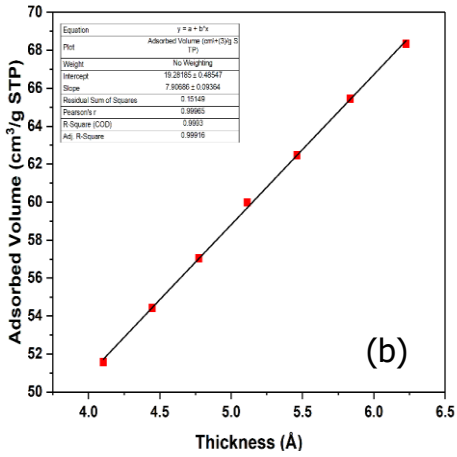

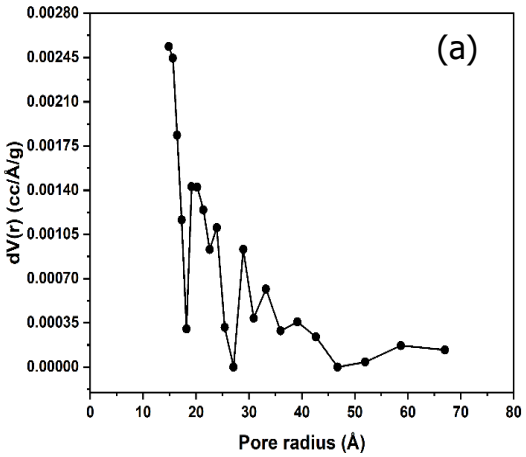

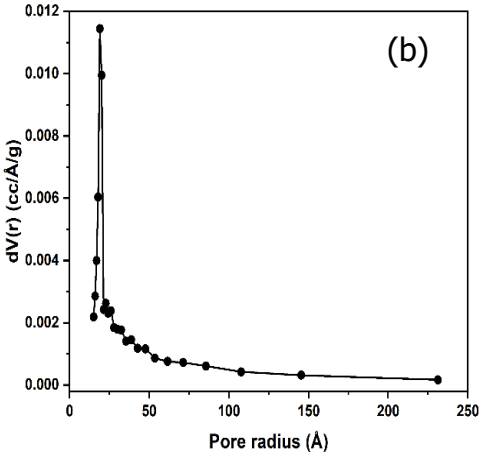

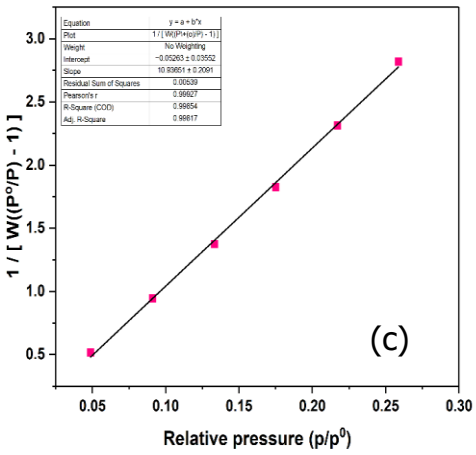
Equation y = a + b*x
Plot 1 / [W((P°/P) - 1)]
Weight No Weighting
Intercept -0.05263 ± 0.03552
Slope 10.93651 ± 0.2091
Residual Sum of Squares 0.00539
Pearson's r 0.99827
R-Square (COD) 0.99654
Adj. R-Square 0.99617
1 / [W((P°/P) - 1)]
Relative pressure (p/p0)
(c)

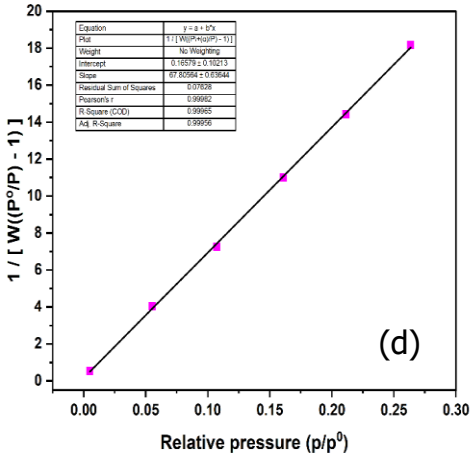
Equation y = a + b*x
Plot 1 / [W((P°/P) - 1)]
Weight No Weighting
Intercept 0.16579 ± 0.00213
Slope 67.80564 ± 0.03644
Residual Sum of Squares 0.07628
Pearson's r 0.99982
R-Square (COD) 0.99965
Adj. R-Square 0.99956
1 / [W((P°/P) - 1)]
Relative pressure (p/p0)
(d)

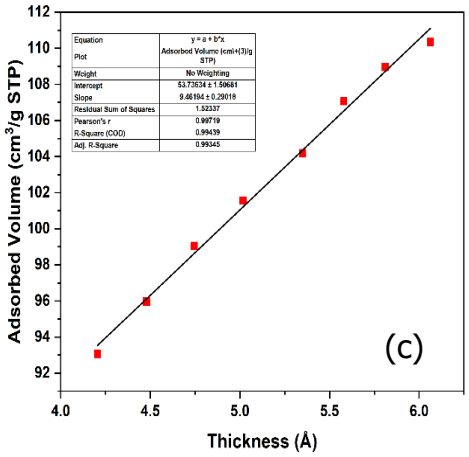
Equation y = a + b*x
Plot Adsorbed Volume (cm³/g STP)
Weight No Weighting
Intercept 53.73634 ± 1.50681
Slope 9.46194 ± 0.29018
Residual Sum of Squares 1.52337
Pearson's r 0.99719
R-Square (COD) 0.99439
Adj. R-Square 0.99345
Adsorbed Volume (cm³/g STP)
Thickness (Å)
(c)

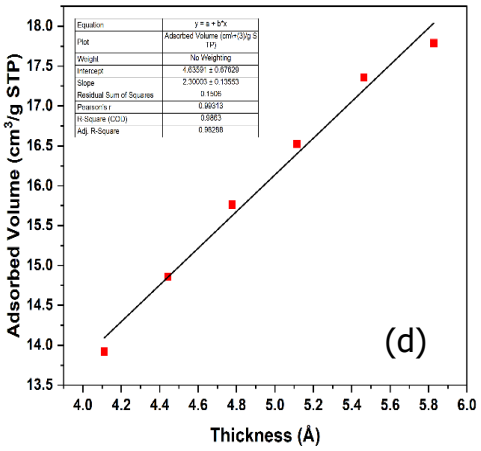
Equation y = a + b*x
Plot Adsorbed Volume (cm³/g STP)
Weight No Weighting
Intercept 4.63591 ± 0.87629
Slope 2.30003 ± 0.13593
Residual Sum of Squares 0.1506
Pearson's r 0.99313
R-Square (COD) 0.9863
Adj. R-Square 0.98268
Adsorbed Volume (cm³/g STP)
Thickness (Å)
(d)

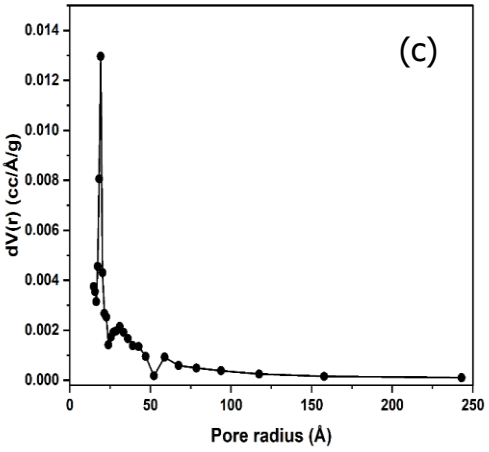
dV(r) (cc/Å/g)
Pore radius (Å)
(c)

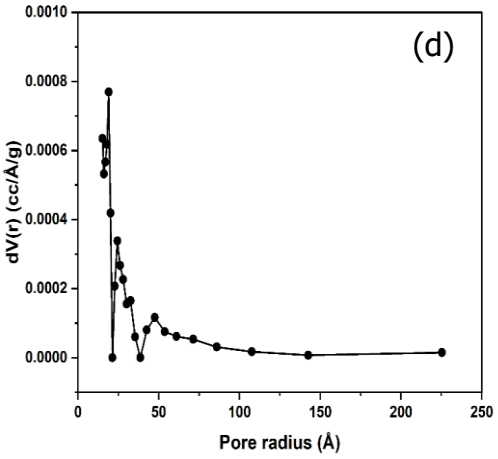
dV(r) (cc/Å/g)
Pore radius (Å)
(d)

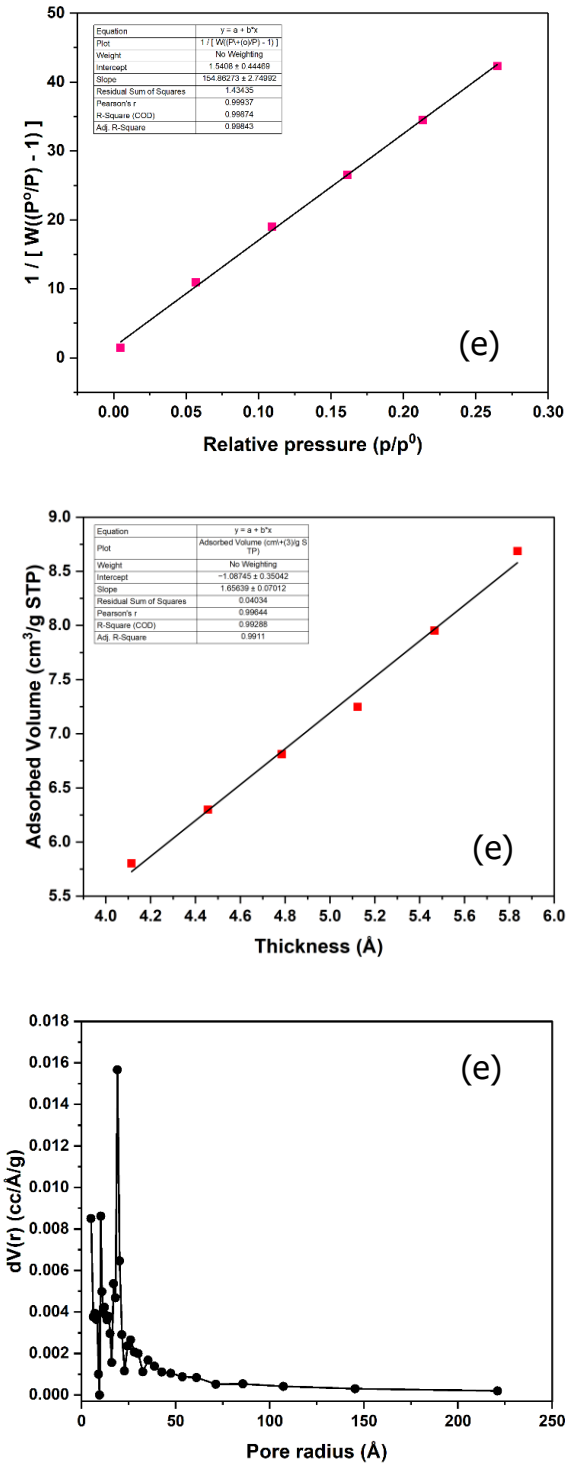

Figure B.1: Multi-Point BET linear plot, t-plot curve and BJH pore size distribution for (a) BC2, (b) BC3, (c) BC4, (d) CC and (e) HC, respectively.

Appendix C: Standard deviations of proximate and ultimate analysis

Sample	Proximate analysis (wt.%, d)			Ultimate analysis (wt.%, d, daf)				
	V	A	FC[a]	C	H	O[a]	N	S
BC1	0.2	0.39	0.53	0.6	0.05	0.93	0.29	0.004
BC2	0.16	0.04	0.14	0.3	0.05	0.29	0.04	0.001
BC3	0.22	0.3	0.14	0.11	0.01	0.07	0.05	0.036
BC4	2.0	0.54	1.58	0.9	0.03	0.65	0.22	004
CC	0.16	1.1	1.32	0.18	0.01	0.13	0.05	0.001
HC	0.63	0.47	0.49	0.13	0.0	0.16	0.03	0.016
BC1HCl	1.1	0.01	1.1	0.02	0.05	0.08	0.005	-
HCHCl	0.83	0.03	0.81	0.17	0.01	0.23	0.06	0.0

Appendix D: MATLAB code for fitting kinetic models (VM, GM and RPM) to experimental conversion data under isothermal CO_2 gasification:

```
% Volumetric model (VM)
clc
clear
M=xlsread('BC1fitting.xlsx','Sheet4'); %input data for gasification at
900°C.
y1=M(:,1);x1=M(:,2);
plot(x1,y1,'s','Color',[0 0
0],'MarkerEdgeColor','g','MarkerSize',8,'MarkerFaceColor','g')
hold on
M=xlsread('BC1fitting.xlsx','Sheet5'); %input data for gasification at
950°C.
y2=M(:,1);x2=M(:,2);
plot(x2,y2,'o','Color',[0 0
0],'MarkerEdgeColor','r','MarkerSize',8,'MarkerFaceColor','r')
hold on
M=xlsread('BC1fitting.xlsx','Sheet6'); %input data for gasification at
1000°C.
y3=M(:,1);x3=M(:,2);
plot(x3,y3,'^','Color',[0 0
0],'MarkerEdgeColor','b','MarkerSize',8,'MarkerFaceColor','b')
hold on
%%
ft=inline('1-exp(-a1(1)./10000*x1)','a1','x1');
a1=nlinfit(x1,y1,ft,[0.001]); %initial guess for reaction rate
constant>0.
n=length(y1);y11=zeros(n,1);
for i=1:n
    y11(i,1)=1-exp(-a1(1)/10000*x1(i,1));
end
%1
s_1=0;s_2=0;
for i=1:n-1
s_1=s_1+y1(i,1)^2;
s_2=s_2+(y11(i,1)-y1(i,1))^2;
end
R1=(s_1-s_2)/s_1
%
ft=inline('1-exp(-a2(1)./10000*x2)','a2','x2');
a2=nlinfit(x2,y2,ft,[0.001]); %initial guess for reaction rate
constant>0.
n=length(y2);y22=zeros(n,1);
for i=1:n
    y22(i,1)=1-exp(-a2(1)/10000*x2(i,1));
end
%2
s_2=0;
for i=1:n-1
```

```
s_2=s_2+(y22(i,1)-y2(i,1))^2;
end
R2=(s_1-s_2)/s_1
%
ft=inline('1-exp(-a3(1)./10000*x3)','a3','x3');
a3=nlinfit(x3,y3,ft,[0.001]); %initial guess for reaction rate
constant>0.
n=length(y3);y33=zeros(n,1);
for i=1:n
    y33(i,1)=1-exp(-a3(1)/10000*x3(i,1));
end
%3
s_2=0;
for i=1:n-1
s_2=s_2+(y33(i,1)-y3(i,1))^2;
end
R3=(s_1-s_2)/s_1
plot(x1,y11,'k',x2,y22,'k',x3,y33,'k','LineWidth',2)
xlabel('Time(s)')
ylabel('Conversion (X)')
legend('900°C','950°C','1000°C','VM','Location','SouthEast')


% Grain model model (GMM)
clc
clear
M=xlsread('BC1fitting.xlsx','Sheet4'); %input data for gasification at
900°C.
y1=M(:,1);x1=M(:,2);
plot(x1,y1,'s','Color',[0 0
0],'MarkerEdgeColor','g','MarkerSize',8,'MarkerFaceColor','g')
hold on

M=xlsread('BC1fitting.xlsx','Sheet5'); %input data for gasification at
950°C.
y2=M(:,1);x2=M(:,2);
plot(x2,y2,'o','Color',[0 0
0],'MarkerEdgeColor','r','MarkerSize',8,'MarkerFaceColor','r')
hold on

M=xlsread('BC1fitting.xlsx','Sheet6'); %input data for gasification at
1000°C.
y3=M(:,1);x3=M(:,2);
plot(x3,y3,'^','Color',[0 0
0],'MarkerEdgeColor','b','MarkerSize',8,'MarkerFaceColor','b')
hold on
%%
ft=inline('1-(1-a1(1)./10000*x1./3).^3','a1','x1');
a1=nlinfit(x1,y1,ft,[0.001]); %initial guess for reaction rate
constant>0.
n=length(y1);y11=zeros(n,1);
for i=1:n
```

```
    y11(i,1)=1-(1-a1(1)/10000*x1(i,1)./3)^3;
end
%1

s_1=0;s_2=0;
for i=1:n-1
s_1=s_1+y1(i,1)^2;
s_2=s_2+(y11(i,1)-y1(i,1))^2;
end
R1=(s_1-s_2)/s_1
%
ft=inline('1-(1-a2(1)./10000*x2./3).^3','a2','x2');
a2=nlinfit(x2,y2,ft,[0.001]); %initial guess for reaction rate
constant>0.
n=length(y2);y22=zeros(n,1);
for i=1:n
    y22(i,1)=1-(1-a2(1)/10000*x2(i,1)./3)^3;
end
%2
s_2=0;
for i=1:n-1
s_2=s_2+(y22(i,1)-y2(i,1))^2;
end
R2=(s_1-s_2)/s_1
%
ft=inline('1-(1-a3(1)./10000*x3./3).^3','a3','x3');
a3=nlinfit(x3,y3,ft,[0.001]); %initial guess for reaction rate
constant>0.
n=length(y3);y33=zeros(n,1);
for i=1:n
    y33(i,1)=1-(1-a3(1)/10000*x3(i,1)./3)^3;
end
%3
s_2=0;
for i=1:n-1
s_2=s_2+(y33(i,1)-y3(i,1))^2;
end
R3=(s_1-s_2)/s_1

plot(x1,y11,'k',x2,y22,'k',x3,y33,'k','LineWidth',2)
xlabel('Time(s)')
ylabel('Conversion (X)')
legend('900°C','950°C','1000°C','GM','Location','SouthEast')


% Random pore model (RPM)
clc
clear
M=xlsread('BC1fitting.xlsx','Sheet4'); %input data for gasification at
900°C.
y1=M(:,1);x1=M(:,2);
```

```
plot(x1,y1,'s','Color',[0 0
0],'MarkerEdgeColor','g','MarkerSize',8,'MarkerFaceColor','g')
hold on

M=xlsread('BC1fitting.xlsx','Sheet5'); %input data for gasification at
950°C.
y2=M(:,1);x2=M(:,2);
plot(x2,y2,'o','Color',[0 0
0],'MarkerEdgeColor','r','MarkerSize',8,'MarkerFaceColor','r')
hold on

M=xlsread('BC1fitting.xlsx','Sheet6'); %input data for gasification at
1000°C.
y3=M(:,1);x3=M(:,2);
plot(x3,y3,'^','Color',[0 0
0],'MarkerEdgeColor','b','MarkerSize',8,'MarkerFaceColor','b')
hold on
%%
ft=inline('1-exp(-
a1(1)./10000*x1.*(1+a1(1)./10000*x1.*1/4))','a1','x1');
a1=nlinfit(x1,y1,ft,[0.001,1]); %initial guess for reaction rate
constant and structural parameter>0.
n=length(y1);y11=zeros(n,1);
for i=1:n
    y11(i,1)=1-exp(-a1(1)/10000*x1(i,1)*(1+a1(1)/10000*x1(i,1)*1/4));
end
%1

s_1=0;s_2=0;
for i=1:n-1
s_1=s_1+y1(i,1)^2;
s_2=s_2+(y11(i,1)-y1(i,1))^2;
end
R1=(s_1-s_2)/s_1
%

ft=inline('1-exp(-
a2(1)./10000*x2.*(1+a2(1)./10000*x2.*1/4))','a2','x2');
a2=nlinfit(x2,y2,ft,[0.001,1]); %initial guess for reaction rate
constant and structural parameter>0.
n=length(y2);y22=zeros(n,1);
for i=1:n
    y22(i,1)=1-exp(-a2(1)/10000*x2(i,1)*(1+a2(1)/10000*x2(i,1)*1/4));
end
%2
s_2=0;
for i=1:n-1
s_2=s_2+(y22(i,1)-y2(i,1))^2;
end
R2=(s_1-s_2)/s_1
%
```

```
ft=inline('1-exp(-
a3(1)./10000*x3.*(1+a3(1)./10000*x3.*1/4))','a3','x3');
a3=nlinfit(x3,y3,ft,[0.001,1]); %initial guess for reaction rate
constant and structural parameter>0.
n=length(y3);y33=zeros(n,1);
for i=1:n
    y33(i,1)=1-exp(-a3(1)/10000*x3(i,1)*(1+a3(1)/10000*x3(i,1)*1/4));
end
%3

s_2=0;
for i=1:n-1
s_2=s_2+(y33(i,1)-y3(i,1))^2;
end
R3=(s_1-s_2)/s_1

plot(x1,y11,'k',x2,y22,'k',x3,y33,'k','LineWidth',2)
xlabel('Time(s)')
ylabel('Conversion (X)')
legend('900°C','950°C','1000°C','RPM','Location','SouthEast')
```

Appendix E: Standard deviations of non-isothermal gasification parameters of different chars at different heating rates:

Sample	Heating rate	T_i	T_m	T_f	DTG	dx/dt_{max}	dx/dt_{mean}	S	m_{ash}
	(°C /min)	(°C)	(°C)	(°C)	(wt.%/min)	(min^{-1})	(min^{-1})		(%)
BC1	5	1.10	0.06	0.69	0.01	2.4E-05	8.5E-07	4.0E-15	0.37
	10	1.13	2.51	1.66	0.10	1.9E-03	1.7E-06	7.8E-14	0.93
	15	1.12	5.17	4.84	0.20	3.1E-03	3.8E-06	1.5E-13	0.47
BC2	5	1.13	3.97	3.92	0.25	3.1E-03	3.4E-06	5.8E-14	0.71
	10	0.13	0.88	0.88	0.30	3.4E-03	6.9E-18	9.8E-14	0.11
	15	1.91	4.53	2.63	0.09	1.5E-03	3.8E-06	1.7E-14	0.43
BC3	5	9.44	1.66	5.89	0.10	1.0E-03	3.9E-18	2.7E-14	4.01
	10	3.69	1.07	0.49	0.06	1.1E-04	1.7E-06	1.9E-14	1.16
	15	1.10	1.73	2.37	0.06	1.0E-03	1.4E-17	1.8E-14	0.11
BC4	5	1.31	0.22	1.54	0.02	5.5E-05	8.5E-07	2.2E-15	0.47
	10	0.67	0.70	1.74	0.02	4.3E-04	1.7E-06	1.2E-14	0.04
	15	0.26	1.36	0.32	0.03	9.7E-04	6.9E-18	4.4E-14	0.44
CC	5	4.9	4.15	0.26	0.02	3.0E-03	2.2E-18	3.4E-14	0.22
	10	0.7	1.42	0.15	0.11	1.1E-02	1.0E-05	1.6E-13	0.87
	15	11.8	1.51	0.60	0.97	1.6E-02	4.7E-05	2.7E-13	5.73
HC	5	3.12	12.25	2.57	0.07	2.0E-03	1.6E-06	3.1E-14	1.06
	10	0.35	0.20	4.79	0.10	2.0E-03	9.7E-06	8.0E-14	2.53
	15	1.88	0.23	5.15	0.04	2.3E-03	3.8E-06	1.6E-13	0.89

Appendix F: MATLAB code for fitting kinetic models (VM, GM and RPM) to experimental gasification reaction rate data under non-isothermal CO_2 gasification:

```
%% Kinetic study for non-isothermal CO2 gasification (reaction rate) %%
% Load Data
clc
clear
data = readmatrix('data.xlsx', 'Sheet', 'BC3');

% Extract columns for each heating rate
T1 = data(:, 1); X1 = data(:, 2); dxdt1 = data(:, 3);
T2 = data(:, 4); X2 = data(:, 5); dxdt2 = data(:, 6);
T3 = data(:, 7); X3 = data(:, 8); dxdt3 = data(:, 9);

% Define a function to clean data and adjust X values
clean_and_adjust_data = @(T, X, dxdt) deal( ...
    T(T > 0 & X >= 0 & dxdt > 0), ...                    % Keep valid T
    min(max(X(T > 0 & X >= 0 & dxdt > 0), 0), 1), ...    % Cap X to
[0,1]
    dxdt(T > 0 & X >= 0 & dxdt > 0));                    % Keep valid
dx/dt

% Clean and adjust data for each heating rate
[T1, X1, dxdt1] = clean_and_adjust_data(T1, X1, dxdt1);
[T2, X2, dxdt2] = clean_and_adjust_data(T2, X2, dxdt2);
[T3, X3, dxdt3] = clean_and_adjust_data(T3, X3, dxdt3);

% Add end points to ensure smooth curves
add_zero_point = @(T, X, dxdt) deal([T; T(end)], [X; 1], [dxdt; 0]);
[T1, X1, dxdt1] = add_zero_point(T1, X1, dxdt1);
[T2, X2, dxdt2] = add_zero_point(T2, X2, dxdt2);
[T3, X3, dxdt3] = add_zero_point(T3, X3, dxdt3);

% Combine data for global fitting
all_T = [T1; T2; T3];
all_X = [X1; X2; X3];
all_dxdt = [dxdt1; dxdt2; dxdt3];

% Define the universal gas constant
R = 8.314; % J/(mol*K)

% Define the Random Pore Model (RPM)
rpm_model = @(params, X, T) ...
    params(1) .* exp(-params(2) ./ (R .* T)) .* ...
    (1 - X) .* sqrt(max(0, 1 - params(3) .* log(max(1e-6, 1 - X))));

% Define the Volumetric Model (VM)
vm_model = @(params, X, T) ...
    params(1) .* exp(-params(2) ./ (R .* T)) .* (1 - X);
```

```
% Define the Grain Model (GM)
gm_model = @(params, X, T) ...
    params(1) .* exp(-params(2) ./ (R .* T)) .* (1 - X).^(2/3);

% Initial guesses for parameters
initial_params_rpm = [1e7, 170000, 0.1]; % [A0, E, psi] for RPM
initial_params_vm = [1e5, 150000];       % [A0_vm, E_vm] for VM
initial_params_gm = [1e5, 200000];       % [A0_gm, E_gm] for GM

% Optimization options
options = optimset('Display', 'iter', 'TolFun', 1e-9, 'TolX', 1e-9,
'MaxIter', 5000);

% Perform global fitting for RPM
disp('Performing Global Fitting for RPM...');
[params_rpm, ~] = lsqcurvefit(@(params, X) rpm_model(params, X,
all_T), ...initial_params_rpm, all_X, all_dxdt, [], [], options);

% Perform global fitting for VM
disp('Performing Global Fitting for VM...');
[params_vm, ~] = lsqcurvefit(@(params, X) vm_model(params, X, all_T),
...
    initial_params_vm, all_X, all_dxdt, [], [], options);

% Perform global fitting for GM
disp('Performing Global Fitting for GM...');
[params_gm, ~] = lsqcurvefit(@(params, X) gm_model(params, X, all_T),
...
    initial_params_gm, all_X, all_dxdt, [], [], options);

% Calculate R² for RPM
fitted_dxdt_rpm = rpm_model(params_rpm, all_X, all_T);
SS_res_rpm = sum((all_dxdt - fitted_dxdt_rpm).^2);
SS_tot_rpm = sum((all_dxdt - mean(all_dxdt)).^2);
R2_rpm = 1 - (SS_res_rpm / SS_tot_rpm);

% Calculate R² for VM
fitted_dxdt_vm = vm_model(params_vm, all_X, all_T);
SS_res_vm = sum((all_dxdt - fitted_dxdt_vm).^2);
SS_tot_vm = sum((all_dxdt - mean(all_dxdt)).^2);
R2_vm = 1 - (SS_res_vm / SS_tot_vm);

% Calculate R² for GM
fitted_dxdt_gm = gm_model(params_gm, all_X, all_T);
SS_res_gm = sum((all_dxdt - fitted_dxdt_gm).^2);
SS_tot_gm = sum((all_dxdt - mean(all_dxdt)).^2);
R2_gm = 1 - (SS_res_gm / SS_tot_gm);

% Calculate Deviation (DEV) Function
calculate_deviation = @(dxdt_exp, dxdt_calc) 100 * sqrt(mean((dxdt_exp
- dxdt_calc).^2)) / max(dxdt_exp);
```

```
% Calculate DEV for each model
dev_rpm = calculate_deviation(all_dxdt, fitted_dxdt_rpm);
dev_vm = calculate_deviation(all_dxdt, fitted_dxdt_vm);
dev_gm = calculate_deviation(all_dxdt, fitted_dxdt_gm);

% Display Final Results with Optimized Parameters, R², and DEV
fprintf('\nFinal Results:\n');
fprintf('\nGlobal Optimized Parameters for RPM:\n');
fprintf('A0: %.3e 1/min\n', params_rpm(1));
fprintf('E: %.3f J/mol (%.3f kJ/mol)\n', params_rpm(2), params_rpm(2)
/ 1000);
fprintf('psi: %.3f\n', params_rpm(3));
fprintf('Global Fit R² (RPM): %.4f\n', R2_rpm);
fprintf('DEV (RPM): %.4f%%\n', dev_rpm);

fprintf('\nGlobal Optimized Parameters for VM:\n');
fprintf('A0_vm: %.3e 1/min\n', params_vm(1));
fprintf('E_vm: %.3f J/mol (%.3f kJ/mol)\n', params_vm(2), params_vm(2)
/ 1000);
fprintf('Global Fit R² (VM): %.4f\n', R2_vm);
fprintf('DEV (VM): %.4f%%\n', dev_vm);

fprintf('\nGlobal Optimized Parameters for GM:\n');
fprintf('A0_gm: %.3e 1/min\n', params_gm(1));
fprintf('E_gm: %.3f J/mol (%.3f kJ/mol)\n', params_gm(2), params_gm(2)
/ 1000);
fprintf('Global Fit R² (GM): %.4f\n', R2_gm);
fprintf('DEV (GM): %.4f%%\n', dev_gm);

% Plot the experimental vs. fitted data for all heating rates
figure;

% Plot Experimental Data and Model Fittings
% Define a step size for skipping data points
step = 10; % Plot every 5th point (adjust this value as needed)

% Heating Rate 1 (5°C/min)
scatter(X1(1:step:end), dxdt1(1:step:end), 36, [0.5, 0, 0],
'filled','o', 'DisplayName', '5°C/min');
hold on;
plot(X1, rpm_model(params_rpm, X1, T1), 'k-', 'LineWidth', 1.5,
'DisplayName', '');
plot(X1, vm_model(params_vm, X1, T1), 'k--', 'LineWidth', 1.5,
'DisplayName', '');
plot(X1, gm_model(params_gm, X1, T1), 'k-.', 'LineWidth', 1.5,
'DisplayName', '');

% Heating Rate 2 (10°C/min)
scatter(X2(1:step:end), dxdt2(1:step:end),  36, [1, 0,
0],'filled','o', 'DisplayName', '10°C/min');
```

```
plot(X2, rpm_model(params_rpm, X2, T2), 'k-', 'LineWidth', 1.5,
'DisplayName', 'RPM');
plot(X2, vm_model(params_vm, X2, T2), 'k--', 'LineWidth', 1.5,
'DisplayName', 'VM');
plot(X2, gm_model(params_gm, X2, T2), 'k-.', 'LineWidth', 1.5,
'DisplayName', 'GM');

% Heating Rate 3 (15°C/min)
scatter(X3(1:step:end), dxdt3(1:step:end), 36, [0.2, 0.4, 1],
'filled','o', 'DisplayName', '15°C/min');
plot(X3, rpm_model(params_rpm, X3, T3), 'k-', 'LineWidth', 1.5,
'DisplayName', '');
plot(X3, vm_model(params_vm, X3, T3), 'k--', 'LineWidth', 1.5,
'DisplayName', '');
plot(X3, gm_model(params_gm, X3, T3), 'k-.', 'LineWidth', 1.5,
'DisplayName', '');

% Customize Legend
legend({'5°C/min', '', '', '', ...
        '10°C/min', '', '', '', ...
        '15°C/min', 'RPM', 'VM', 'GM'}, ...
        'Location', 'Best');

% Add Labels, legend
xlabel('Conversion (X)', 'FontWeight', 'bold');
ylabel('dx/dt (min^-1)', 'FontWeight', 'bold');
grid off;

% Set y-axis limit
ylim([0 0.13]);
yticks([0 0.02 0.04 0.06 0.08 0.10 0.12 0.14]);
box on;

% Add text at a desired position
text(0.1, 0.12, '(c)', 'FontSize', 14, 'FontWeight', 'bold'); % Adjust
the position as needed

% Customize frame thickness and axis appearance
ax = gca; % Get current axes
ax.FontSize = 12; %Set font size for ticks

% Convert temperature from K to °C
T1_C = T1 - 273.15;
T2_C = T2 - 273.15;
T3_C = T3 - 273.15;

% Define a step size for skipping data points
step = 10; % Plot every 10th point (adjust this value as needed)

% Plot dx/dt vs T (in °C) for each heating rate with model fits
figure;
```

```
% Heating Rate 1 (5°C/min)
scatter(T1_C(1:step:end), dxdt1(1:step:end), 36, [0.5, 0, 0],
'filled','o', 'DisplayName', '5°C/min');
hold on;
plot(T1_C, rpm_model(params_rpm, X1, T1), 'k-', 'LineWidth', 1.5,
'DisplayName', '');
plot(T1_C, vm_model(params_vm, X1, T1), 'k--', 'LineWidth', 1.5,
'DisplayName', '');
plot(T1_C, gm_model(params_gm, X1, T1), 'k-.', 'LineWidth', 1.5,
'DisplayName', '');

% Heating Rate 2 (10°C/min)
scatter(T2_C(1:step:end), dxdt2(1:step:end), 36, [1, 0,
0],'filled','o', 'DisplayName', '10°C/min');
plot(T2_C, rpm_model(params_rpm, X2, T2), 'k-', 'LineWidth', 1.5,
'DisplayName', '');
plot(T2_C, vm_model(params_vm, X2, T2), 'k--', 'LineWidth', 1.5,
'DisplayName', '');
plot(T2_C, gm_model(params_gm, X2, T2), 'k-.', 'LineWidth', 1.5,
'DisplayName', '');

% Heating Rate 3 (15°C/min)
scatter(T3_C(1:step:end), dxdt3(1:step:end), 36, [0.2, 0.4, 1],
'filled','o', 'DisplayName', '15°C/min');
plot(T3_C, rpm_model(params_rpm, X3, T3), 'k-', 'LineWidth', 1.5,
'DisplayName', '');
plot(T3_C, vm_model(params_vm, X3, T3), 'k--', 'LineWidth', 1.5,
'DisplayName', '');
plot(T3_C, gm_model(params_gm, X3, T3), 'k-.', 'LineWidth', 1.5,
'DisplayName', '');

% Customize Legend
legend({'5°C/min', '', '', '', ...
        '10°C/min', '', '', '', ...
        '15°C/min', 'RPM', 'VM', 'GM'}, ...
        'Location', 'Best');
 % Add labels, legend
xlabel('Temperature (°C)', 'FontWeight', 'bold');
ylabel('dx/dt (min^-1)', 'FontWeight', 'bold');
legend('Location', 'Best');

% Set x-axis limits to 400°C to 1100°C
xlim([400, 1100]);
grid off;
box on;
% Add text at a desired position
text(500, 0.08, '(c)', 'FontSize', 14, 'FontWeight', 'bold'); % Adjust
the position as needed

% Customize frame thickness and axis appearance
ax = gca; % Get current axes
ax.FontSize = 12; %Set font size for ticks
```

Appendix G: MATLAB code for fitting kinetic models (VM, GM and RPM) to experimental conversion data under non-isothermal CO_2 gasification:

```
%% Kinetic study for non-isothermal CO2 gasification (conversion)%%
% Load Data
clc
clear
data = readmatrix('data2.xlsx', 'Sheet', 'BC3');

% Extract relevant columns for each heating rate
T_5K = data(:,1) ;
X_exp_5K = data(:,2);
T_10K = data(:,4) ;
X_exp_10K = data(:,5);
T_15K = data(:,7) ;
X_exp_15K = data(:,8);

% Ensure experimental conversion values do not exceed 1
X_exp_5K = min(X_exp_5K, 1);
X_exp_10K = min(X_exp_10K, 1);
X_exp_15K = min(X_exp_15K, 1);

% Flip experimental conversion
X_exp_5K_flipped = 1 - X_exp_5K;
X_exp_10K_flipped = 1 - X_exp_10K;
X_exp_15K_flipped = 1 - X_exp_15K;

% Kinetic parameters for RPM, VM, and GM
A0_RPM = data(1,10); E_RPM = data(1,11); psi_RPM = data(1,12);
A0_VM = data(1,13); E_VM = data(1,14);
A0_GM = data(1,15); E_GM = data(1,16);
R = 8.314; % Universal gas constant in J/mol/K

% Define RPM model for Conversion X
RPM_model = @(T, T0, A0_RPM, E_RPM, psi_RPM, beta) ...
    1 - max(0,exp(-(A0_RPM .* (R .* T.^2) ./ (beta .* E_RPM) .* exp(-
E_RPM ./ (R .* T)))) ...
    .* max(0, 1 + (A0_RPM .* psi_RPM ./ 4) .* (R .* T.^2) ./ (beta .*
E_RPM) .* exp(-E_RPM ./ (R .* T))));

% Define VM model for Conversion X
VM_model = @(T, T0, A0_VM, E_VM, beta) ...
    1 - max(0,exp(-A0_VM .* (R .* T.^2) ./ (beta .* E_VM) .* exp(-E_VM
./ (R .* T))));

% Define GM model for Conversion X
GM_model = @(T, T0, A0_GM, E_GM, beta) ...
    1 - max(0, (1 - A0_GM .* (R .* T.^2) ./ (3 * beta .* E_GM) .*
exp(-E_GM ./ (R .* T)))).^3;

% Define heating rates (beta) in K/min
```

```
beta_5K = 5;
beta_10K = 10;
beta_15K = 15;


% Initial temperatures (T0) in Celsius
T0_5K = data(1,3);
T0_10K = data(1,6);
T0_15K = data(1,9);

% Calculate X for RPM model and flip the values
X_RPM_5K = RPM_model(T_5K, T0_5K, A0_RPM, E_RPM, psi_RPM, beta_5K);
X_RPM_10K = RPM_model(T_10K, T0_10K, A0_RPM, E_RPM, psi_RPM,
beta_10K);
X_RPM_15K = RPM_model(T_15K, T0_15K, A0_RPM, E_RPM, psi_RPM,
beta_15K);
X_RPM_5K_flipped = 1 - X_RPM_5K;
X_RPM_10K_flipped = 1 - X_RPM_10K;
X_RPM_15K_flipped = 1 - X_RPM_15K;

% Calculate X for VM model and flip the values
X_VM_5K = VM_model(T_5K, T0_5K, A0_VM, E_VM, beta_5K);
X_VM_10K = VM_model(T_10K, T0_10K, A0_VM, E_VM, beta_10K);
X_VM_15K = VM_model(T_15K, T0_15K, A0_VM, E_VM, beta_15K);
X_VM_5K_flipped = 1 - X_VM_5K;
X_VM_10K_flipped = 1 - X_VM_10K;
X_VM_15K_flipped = 1 - X_VM_15K;

% Calculate X for GM model and flip the values
X_GM_5K = GM_model(T_5K, T0_5K, A0_GM, E_GM, beta_5K);
X_GM_10K = GM_model(T_10K, T0_10K, A0_GM, E_GM, beta_10K);
X_GM_15K = GM_model(T_15K, T0_15K, A0_GM, E_GM, beta_15K);
X_GM_5K_flipped = 1 - X_GM_5K;
X_GM_10K_flipped = 1 - X_GM_10K;
X_GM_15K_flipped = 1 - X_GM_15K;

% Convert temperatures to Celsius for plotting
T_5K_C = T_5K - 273.15;
T_10K_C = T_10K - 273.15;
T_15K_C = T_15K - 273.15;

% Plot Experimental and Calculated Conversion
figure;
% Define a step size for skipping data points
step = 10; % Plot every 10th point (adjust this value as needed)

% Plot 5 K/min
scatter(T_5K_C(1:step:end), X_exp_5K_flipped(1:step:end), 36, [0.5, 0,
0], 'filled', 'o', 'DisplayName', 'Exp (5 °C/min)');
hold on;
plot(T_5K_C, X_RPM_5K_flipped, 'k-', 'LineWidth', 1.5, 'DisplayName',
'RPM (5 °C/min)');
```

```
plot(T_5K_C, X_VM_5K_flipped, 'k--', 'LineWidth', 1.5, 'DisplayName',
'VM (5 °C/min)');
plot(T_5K_C, X_GM_5K_flipped, 'k-.', 'LineWidth', 1.5, 'DisplayName',
'GM (5 °C/min)');
% Plot 10 K/min
scatter(T_10K_C(1:step:end), X_exp_10K_flipped(1:step:end), 36, [1, 0,
0], 'filled', 'o', 'DisplayName', 'Exp (10 °C/min)');
plot(T_10K_C, X_RPM_10K_flipped, 'k-', 'LineWidth', 1.5,
'DisplayName', 'RPM (10°C/min)');
plot(T_10K_C, X_VM_10K_flipped, 'k--', 'LineWidth', 1.5,
'DisplayName', 'VM (10 °C/min)');
plot(T_10K_C, X_GM_10K_flipped, 'k-.', 'LineWidth', 1.5,
'DisplayName', 'GM (10 °C/min)');

% Plot 15 K/min
scatter(T_15K_C(1:step:end), X_exp_15K_flipped(1:step:end), 36, [0.2,
0.4, 1], 'filled', 'o', 'DisplayName', 'Exp (15 °C/min)');
plot(T_15K_C, X_RPM_15K_flipped, 'k-', 'LineWidth', 1.5,
'DisplayName', 'RPM (15 °C/min)');
plot(T_15K_C, X_VM_15K_flipped, 'k--', 'LineWidth', 1.5,
'DisplayName', 'VM (15 °C/min)');
plot(T_15K_C, X_GM_15K_flipped, 'k-.', 'LineWidth', 1.5,
'DisplayName', 'GM (15 °C/min)');
% Customize Legend
legend({'5°C/min', '', '', '', ...
        '10°C/min', '', '', '', ...
        '15°C/min', 'RPM', 'VM', 'GM'}, ...
        'Location', 'Best');

% Customize plot
xlabel('Temperature (°C)','FontWeight', 'bold');
ylabel('Conversion (X)','FontWeight', 'bold');
ylim([0 1]);
legend('Location', 'Best');
grid off;
% Set y-axis limit
ylim([0 1.2]);
box on;
% Add text at a desired position
text(1000, 1, '(c)', 'FontSize', 14, 'FontWeight', 'bold'); % Adjust
the position as needed

% Customize frame thickness and axis appearance
ax = gca; % Get current axes
ax.FontSize = 12; %Set font size for ticks

% Adjust Y-axis tick labels to reverse direction
yticks([0 0.2 0.4 0.6 0.8 1]); % Set consistent ticks
yticklabels({'1', '0.8', '0.6', '0.4', '0.2', '0'}); % Reverse tick
labels
% Set x-axis limits to 400°C to 1100°C
xlim([400, 1100]);
```